FINAL REPORT

Antimony(V) Adsorption by Variable-Charge Minerals

SERDP Project ER-1741

October 2013

Michael Essington
University of Tennessee

SERDP
DOD ▪ EPA ▪ DOE

REPORT DOCUMENTATION PAGE

Form Approved
OMB No. 0704-0188

1. REPORT DATE *(DD-MM-YYYY)*	**2. REPORT TYPE**	**3. DATES COVERED** *(From - To)*
06/08/2013	Draft	Jan 2010 - Aug 2013

4. TITLE AND SUBTITLE

Antimony(V) Adsorption by Variable-Charge Minerals

5a. CONTRACT NUMBER
W912HQ-10-C-0006

5b. GRANT NUMBER

5c. PROGRAM ELEMENT NUMBER

6. AUTHOR(S)

Essington, Michael, E

5d. PROJECT NUMBER
ER-1741

5e. TASK NUMBER

5f. WORK UNIT NUMBER

7. PERFORMING ORGANIZATION NAME(S) AND ADDRESS(ES)

University of Tennessee
103 Morgan Hall
2621 Morgan Circle
Knoxville, TN 37996-4540

8. PERFORMING ORGANIZATION REPORT NUMBER

9. SPONSORING / MONITORING AGENCY NAME(S) AND ADDRESS(ES)

SERDP Program Office
Dr. Andrea Leeson
901 North Stuart Street
Suite 303
Arlington, VA 22203

10. SPONSOR/MONITOR'S ACRONYM(S)
SERDP

11. SPONSOR/MONITOR'S REPORT NUMBER(S)

12. DISTRIBUTION / AVAILABILITY STATEMENT

Approved for public release; distribution is unlimited

13. SUPPLEMENTARY NOTES

14. ABSTRACT

This research describes the adsorption of Sb(V) by the surface-reactive minerals that are common to soils and sediments. The results indicate that Sb(V) retention is strongly dependent on pH. Depending on the adsorbent, Sb(V) adsorption is also influenced by the ionic strength (salinity) and the presence of ligands (SO_4 and PO_4) that compete for adsorption sites. In general, Sb(V) is immobilized in strongly acidic environments, and by Fe- and Mn-rich phases (but not by Al-rich phases). The research findings also indicate that the addition of PO_4-based fertilizer amendments to immobilize lead in shooting range soils will potentially enhance Sb(V) mobility and bioaccessibility. Geochemical models that predict the distribution of Sb(V) between soluble and adsorbed phases as a function of pH and ionic environment were successfully developed. However, the application of these models to predict behavior in Sb(V)-affected environments will require site-specific chemical information and calibration.

15. SUBJECT TERMS
Adsorption, Surface Complexation, Adsorption Competition, Gibbsite, Kaolinite, Goethite, Birnessite

16. SECURITY CLASSIFICATION OF:			**17. LIMITATION OF ABSTRACT**	**18. NUMBER OF PAGES**	**19a. NAME OF RESPONSIBLE PERSON**
a. REPORT	**b. ABSTRACT**	**c. THIS PAGE**			Michael E. Essington
U	U	U	UU	190	**19b. TELEPHONE NUMBER** *(include area code)* (865)974-7266

Standard Form 298 (Rev. 8-98)
Prescribed by ANSI Std. Z39.18

Table of Contents

List of Tables

List of Figures

List of Acronyms

ATR-IR: attenuated total reflectance-infrared
BET: Baunauer-Emmett-Teller
CIP: common intersection point
EXAFS: extended x-ray absorption fine structure
ICP-AES: inductively couple plasma-atomic emission spectroscopy
IEP: isoelectric point
SCM: surface complexation model
TLM: triple layer model
TOTH: total hydrogen
XRD: x-ray diffraction

Keywords

Antimony
Antimonate
Phosphate
Sulfate
Adsorption
Adsorption Edge
Adsorption Isotherm
Adsorption Mechanism
Adsorption Competition
Surface Complexation
Triple Layer Model
Gibbsite
Kaolinite
Goethite
Birnessite

Abstract

Background. Antimony (Sb) is a co-contaminant with lead (Pb) in shooting range soils at DoD installations throughout the United States. This element is a specified contaminant of interest in the FY2010 SERDP Statement of Need. The *in-situ* immobilization of Pb in shooting range soils may be accomplished through the application of phosphate (PO_4). However, the impact of this treatment on the mobility and bioaccessibility of Sb is unknown. Further, the ability to predict Sb fate and behavior in contaminated soils, or as influenced by treatment technologies, has not been suitably developed. In soil, Sb commonly exists in the Sb(V) oxidation state as the hydroxyanion $Sb(OH)_6^-$. This anionic species is derived through the hydrolysis of antimonic acid ($Sb(OH)_5^0$, a weak acid). As such, the principal mechanisms of retention in soils are anion exchange (weak outer-sphere electrostatic adsorption) and ligand exchange (strong inner-sphere covalent adsorption) by variable-charge soil minerals, such as iron (Fe), aluminum (Al), and manganese (Mn) oxyhydroxides. Available research findings suggest that Sb(V) is associated with Fe oxyhydroxides in soils, and that PO_4 amendments can enhance Sb(V) mobility and bioaccessibility. **Objectives.** The objectives are to: (1) determine the mechanisms and thermodynamics of Sb(V) adsorption by hydrous Fe, Al, and Mn oxyhydroxides (goethite, gibbsite, kaolinite, and birnessite) as a function of ionic environment, pH, temperature, and Sb(V) concentrations; (2) quantify the competitive effects of PO_4 and SO_4 on Sb(V) adsorption; and (3) develop and evaluate the capability of chemical models to predict Sb(V) adsorption within the holistic framework of a complex chemical environment. **Technical Approach.** A series of laboratory-based experiments were performed to determine the Sb(V) adsorption mechanisms, and the tenacity and reversibility of the adsorption processes. Adsorption edge studies were used to assess the mechanisms of Sb(V) retention by reactive soil minerals as a function of several environmental variables, including pH, ionic strength (I_s, controlled by KNO_3), and the presence of competing ligands (PO_4 and SO_4). Adsorption isotherms were developed as a function of Sb(V) concentration, pH, and temperature to assess the thermodynamics of Sb(V) adsorption. The data accumulated from these experimental activities, including the identified adsorption mechanisms, were then used to develop mechanistic predictive models that combine aqueous speciation and surface complexation (adsorption) phenomenon. The chemical modeling activity resulted in mechanistic parameters that described Sb(V) retention and that are transferable; they can be used to predict Sb(V) fate and behavior in any soil environment (given that soil chemical information are available). **Results.** The aluminol group (≡AlOH) is the reactive surface functional group on kaolinite and gibbsite. The aluminol group has relatively low affinity for Sb(V), and retention is both pH- and ionic strength-dependent. Kaolinite exhibits the lowest capacity to retain Sb(V) (1.48 mmol kg^{-1} adsorbed Sb(V) at pH 5.5), with minimal adsorption (~0 % of added Sb(V)) in pH > 7 suspensions. In pH < 4 suspensions, adsorption increases to approximately 50 % of the added Sb(V) in 0.1 I_s, and to 80 % in 0.01 I_s. Similarly, Sb(V) retention by gibbsite is pH- and I_s-dependent (4.32 mmol kg^{-1} adsorbed Sb(V) at pH 5.5), with between 0 % and 10 % of the added Sb(V) retained in pH > 9 suspensions. In pH < 4 suspensions, retention increases to approximately 80 % of the added Sb(V) in 0.1 I_s, and to > 90 % in 0.01 I_s. The ionic strength-dependency of Sb(V) adsorption by kaolinite and gibbsite indicates that the weak, electrostatic retention of Sb(V) is an important mechanism. However, in strongly acidic suspensions (pH < 5 to 6), Sb(V) adsorption is irreversible, suggesting strong covalent bonding. The mechanistic interpretation of the adsorption edge results are supported by the adsorption isotherm results and

surface electrostatics. In pH 8 suspensions, Sb(V) adsorption is exothermic, indicating that the predominate retention mechanism is anion exchange. In pH 5.5 suspensions, there is an endothermic component to the adsorption process, indicating covalent bonding by the aluminol functional group. Antimonate adsorption generates a negative shift in surface charge and an increase in proton adsorption, both of which are consistent with covalent bonding. Both sulfate and phosphate interfere with Sb(V) retention on kaolinite and gibbsite. The ferrol group (≡FeOH) on goethite has a high capacity to retain Sb(V) (88.5 mmol kg^{-1} adsorbed Sb(V) at pH 5.5). Adsorption by goethite is pH-dependent, independent of ionic strength, and generally irreversible. Approximately 40 % of the added Sb(V) is retained by goethite in pH 10 suspensions, increasing to 100 % when pH < 6. Antimonate adsorption is endothermic in both pH 5.5 and 8 suspensions and adsorption generates a negative shift in goethite surface charge, indicating covalent bonding by the ferrol functional group. Antimonate adsorption by goethite is not impacted by sulfate. However, phosphate strongly inhibits Sb(V) retention. Like the ferrol group on goethite, the manganol group (≡MnOH) on birnessite is a scavenger for Sb(V) (14.8 mmol kg^{-1} adsorbed Sb(V) at pH 5.5). Adsorption by birnessite is pH- and ionic strength-dependent. Approximately 10 % (low I_s) to 20 % (high I_s) of the added Sb(V) was retained by birnessite in pH > 9 suspensions, increasing to 100 % when pH < 5. Antimonate adsorption generates a negative shift in birnessite surface charge, indicating covalent bonding by the manganol functional group. Antimonate adsorption by birnessite is not impacted by either sulfate or phosphate. The experimental findings suggest that the retention of Sb(V) by kaolinite and gibbsite occurs via a combination of electrostatic and covalent bonding mechanisms; whereas, retention by goethite and birnessite occurs predominately by covalent mechanisms. Antimonate adsorption by all surfaces, as a function of pH and ionic strength, was successfully predicted by employing the triple-layer surface complexation model that considered both outer-sphere [≡SOH_2^+–$Sb(OH)_6^-$] and inner-sphere [≡$SOSb(OH)_5^-$] adsorption mechanisms. In general, however, the models generated for single ligand systems required reoptimization to successfully predict adsorption in the competitive ($Sb(OH)_6$ and SO_4 or $Sb(OH)_6$ and PO_4) systems. **Benefits.** This research specifically addresses deficiencies in the scientific literature by providing an improved understanding of Sb(V) adsorption behavior by reactive soil and sediment components, and by developing the capabilities to predict Sb(V) mobility and bioavailability. The research results will help establish technically-defensible clean-up goals and priorities at DoD facilities, and will improve public and DoD site manager confidence in the management of contaminated environments. This research describes the adsorption of Sb(V) by the surface-reactive minerals that are common to soils and sediments. The results indicate that Sb(V) retention is strongly dependent on pH. Depending on the adsorbent, Sb(V) adsorption is also influenced by the ionic strength (salinity) and the presence of ligands (SO_4 and PO_4) that compete for adsorption sites. In general, Sb(V) is immobilized in strongly acidic environments, and by Fe- and Mn-rich phases (but not by Al-rich phases). The research findings also indicate that the addition of PO_4-based fertilizer amendments to immobilize lead in shooting range soils will potentially enhance Sb(V) mobility and bioaccessibility. Geochemical models that predict the distribution of Sb(V) between soluble and adsorbed phases as a function of pH and ionic environment were successfully developed. However, the application of these models to predict behavior in Sb(V)-affected environments will require site-specific chemical information and calibration.

Objective

This research addresses the FY 2010 SERDP Statement of Need on, "Mechanisms of Contaminant Interaction with Soil and its Impact on the Bioavailability of Contaminants" (ERSON-10-03). The research provides an improved understanding of the mechanisms and permanence of the binding of antimony (Sb) (a contaminant of interest in the SON) by soil components through a combination of laboratory-scale studies and computer modeling activities. This research is predicated on the recognition that a mechanistic understanding of bioavailability processes, and the development of scientifically-based mechanistic predictive models, is needed to assess the risk associated with contaminated soils and sediments (National Research Council, 2003). Antimony is a toxin having no known biological function, and a common co-contaminant with lead in shooting range soils and soils subjected to military training activities. These environments are present at DoD installations throughout the United States. Antimony is bound to soil particles via adsorption processes. However, there is a paucity of scientific evidence and technical information concerning the adsorption behavior of Sb in the environment. Thus, the evaluation of soil treatment technologies, such as those using phosphate amendments to stabilize lead, remains a challenge. Unlike many other metal toxins (e.g., lead and arsenic), the mechanisms (chemical reactions) that impact bioaccessibility, and distribute Sb between mobile and immobile components of the soil environment, are not well-understood. Yet, knowledge of these mechanisms (specific bonding mechanisms, chemical reactions and associated equilibrium constants) is required for predicting the long-term fate and behavior of Sb in the environment. This research seeks to provide a clear and holistic understanding of Sb behavior under various chemical conditions, to provide technical information that may be employed to assess treatment strategies, and to predict bioaccessibility through the development of predictive chemical models.

The objectives of this research were fulfilled through a series of hypothesis-driven tasks designed to enhance the conceptual and numerical understanding of Sb(V) fate and behavior in chemically-complex environments. The following hypotheses and associated project tasks and subtasks were resolved in the research:

1. **The adsorption characteristics of Sb(V) by hydrous Al, Fe, and Mn oxyhydroxides will establish the mechanisms and quantitative parameters needing to assess treatment strategies and predict bioaccessibility.**

   Task 1 Antimony(V) adsorption edge determinations for gibbsite, kaolinite, goethite, and birnessite
   Task 2 Antimony(V) adsorption isotherm determinations at temperatures of 278K, 288K, 298K, and 308K (gibbsite, kaolinite, and goethite)
   Task 3 Electrostatics at the solid-solution interface for gibbsite, kaolinite, goethite, and birnessite

2. **Phosphate and sulfate will compete with Sb(V) for adsorption sites on reactive soil minerals; the competitive effect will differ with competing ligand, initial saturation of the surfaces, and pH.**

Task 4 Competitive adsorption in preadsorbed ligand systems for gibbsite, kaolinite, goethite, and birnessite

Task 5 Competitive adsorption with direct ligand competition for gibbsite, kaolinite, goethite, and birnessite

3. Surface complexation models (SCMs) may be employed to determine the distribution of Sb(V) between adsorbed and solution phases, thereby providing a molecular-level prediction of Sb fate and behavior in chemically-complex environments.

Task 6 Surface complexation modeling of antimony(V) adsorption in non-competitive systems and competitive systems

Background

Antimony is a naturally occurring trace element found with a median soil concentration estimated at 1 mg kg^{-1} (ranging < 0.2 to 10 mg kg^{-1}) (Helmke, 1999; Filella et al., 2002a). Higher Sb concentrations in soil are directly correlated to anthropogenic sources, mainly mining and smelter areas, shooting ranges, and along roadsides due to the presence of Sb in dust from brake pads and tires (Filella et al., 2002a; Scheinost et al., 2006; Li and Thornton, 1993; Crecelius et al., 1975; Nriagu and Pacyna, 1988; Nriagu, 1989). In the past, the major industrial use of Sb was as an additive to strengthen lead in the production of alloys; now, Sb is mainly used as a flame retardant (Carlin, 2000). There has been increasing concern regarding the environmental behavior of Sb compounds (Filella et al., 2002a, b). It is listed as a priority pollutant by the U.S. Environmental Protection Agency (USEPA, 2004; Flynn et al., 2003) and as a priority metal according to the Department of Defense (Salatas et al., 2004). Antimony has no known biological function, has high acute toxicity, and is known to induce chronic health effects (Schnorr et al., 1995; Gebel et al., 1997). The World Health Organization and the USEPA have set drinking water guidelines of 20 μg L^{-1} and 6 μg L^{-1} (WHO, 2006; USEPA, 2004).

Antimony is a metalloid that exists in nature in the –III, 0, III, and V oxidation states. Both Sb(III) and Sb(V) are common to natural environments, with the Sb(III) species reportedly more toxic than Sb(V) forms (Bencze, 1994). However, Sb(V) is thermodynamically stable in oxic and suboxic soils; when O_2, Fe(III), and Mn(IV) are present (Fig. 1) (Takayanagi and Cossa, 1997; Andreae et al., 1981). Antimony redox equilibrium may be described by the reaction (Filella and May, 2003): $Sb(OH)_3^0 + 3H_2O = Sb(OH)_6^- + 3H^+ + 2e^-$ (log K= –25.15). Based on this oxidation reaction, the theoretical activity ratio of $Sb(OH)_6^-$ to $Sb(OH)_3^0$ is 10^{23} at pH 7 and pE 13.6 (oxic conditions). In natural oxic waters (freshwater, seawater, estuarine), the concentration ratio of Sb(V) to Sb(III) is considerably smaller (in general, Sb(III) is detected), although Sb(V) still predominates (Filella et al., 2002a; Mitsunobu et al., 2006). In oxic systems, Sb(V) (antimonate) aqueous speciation is controlled by the hydrolysis reaction (Filella and May, 2003; Accornero et al., 2008): $Sb(OH)_5^0 + H_2O = Sb(OH)_6^- + H^+$ (log K_a = –2.85). Thus, at pH values greater than 2.85 the hydroxyanion $Sb(OH)_6^-$ species predominates (Fig. 1). Studies have shown that Sb(III) is quickly oxidized to Sb(V) in oxic soils (Thanabalasingam and Pickering, 1990; Belzile et al., 2001; Quentel et al., 2004; Leuz et al., 2006). Furthermore, Sb(V) is generally the only Sb oxidation state found in oxic soils and sediments (Takaoka et al., 2005; Mitsunobu et al., 2006; Scheinost et al., 2006; Ritchie et al., 2013). In the few studies that investigate Sb(III) oxidation, it has been shown that oxidation occurs rapidly when in the presence of peroxide (H_2O_2) and

Fe(III) and Mn(IV) oxyhydroxides (Belzile et al., 2001; Watkins et al., 2006; Leuz et al., 2006; Xu et al., 2011). Belzile et al. (2001) confirmed that Sb(III) was completely oxidized by amorphous Fe(III) oxyhydroxides within 5 days and by Mn(IV) oxyhydroxides within 3 days. Similar results were seen by Leuz et al. (2006) for goethite [FeOOH]. Relative to health concerns, the oxidation of Sb(III) to Sb(V) is desired, as Sb(III) is considered more toxic to organisms than Sb(V); however, Sb(V) displays greater solubility and environmental mobility than Sb(III).

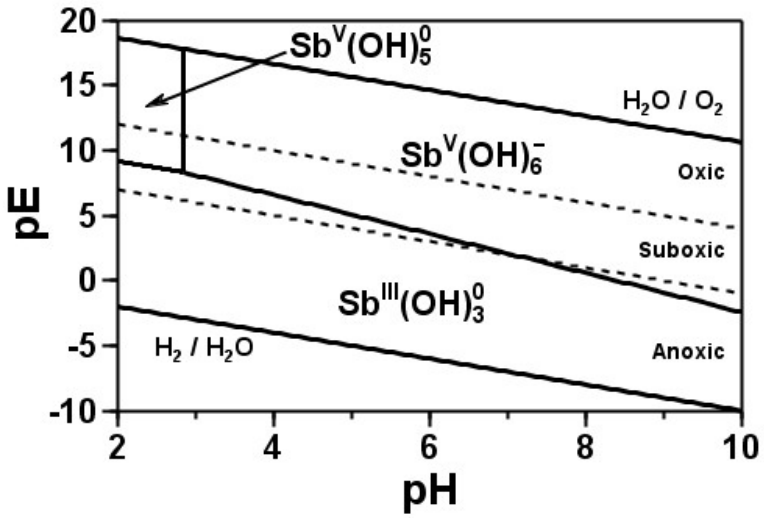

Figure 1. The redox speciation of antimony (Sb). The oxic, suboxic, and anoxic regions are also shown. The diagram illustrates that Sb(V) species predominate in oxic (O_2 present) and suboxic (Fe(II)–Fe(III) and Mn(II)–Mn(IV) couples control pE) environments. The diagram also shows that the $Sb(OH)_6^-$ species predominates in the pH range commonly observed in soils (pH 4 to 9).

As a contaminant, Sb is commonly found in association with lead (Pb). Localized shooting activities are a major source of Pb and Sb contamination in many locations worldwide, through the weathering of spent bullets. These bullets corrode and release metals and metalloids into the soil. Lead bullets have a core composed of ~ 95% Pb and ~2 to 5% Sb. Other elements that may be present include arsenic (As), bismuth (Bi), gold (Au), selenium (Se), silver (Ag), and tellurium (Te) depending on Pb quality (Johnson et al., 2005; Kilgour et al., 2008). Antimony is a co-contaminant with Pb (Kilgour et al., 2008; Clausen and Korte, 2009), as both elements are present in the bullet fragments. Indeed, Sb concentrations in soils affected by military training activities and at civilian shooting ranges can reach 100,000 mg kg^{-1} (Scheinost et al., 2006); although commonly reported Sb concentrations at civilian shooting ranges are substantially lower, ranging from < 517 mg kg^{-1} to < 17,500 mg kg^{-1} (Basunia and Landesberger, 2001; Knechtenhofer et al., 2003; Johnson et al., 2005; Mitsunobu et al., 2006; Spuller et al., 2007; Kilgour et al., 2008; Clausen and Korte, 2009). Still, these shooting range soil Sb concentrations far exceed those of uncontaminated soils, by several orders of magnitude, resulting in elevated

pore water Sb concentrations (Clausen and Korte, 2009; Lewis et al., 2010). In addition, Sb and Pb concentrations exhibit a strong linear correlation in shooting range soils (Kilgour et al., 2008)

Antimony(V) exists as a ligand in aqueous environments [$Sb(OH)_6^-$]. As such, it may potentially bind to variable charged surfaces, specifically those that develop positive surface charge. Oxides and oxyhydroxides of Al, Fe, and Mn are ubiquitous in soils and have a pH dependent surface charge, making them an important component in both metal and ligand adsorption. The ≡AlOH and ≡FeOH surface sites on variable-charge minerals (e.g., gibbsite and goethite) develop net positive charge when solution pH is less than 8 to 9 (Essington, 2003). Only a few studies have investigated the adsorption of Sb(V) on naturally occurring minerals and soils, even though many papers have noted a correlation between the presence of Fe oxyhydroxides and Sb mobility (Mok and Wai, 1990; Chen et al., 2003; Gal et al., 2006; Martínez-Lladó et al., 2011). In general, Sb has been found to be relatively immobile in soil. Under acidic to slightly alkaline pH (2.5 to ~8) and oxic soil conditions, the $Sb(OH)_6^-$ ligand binds strongly to Fe oxyhydroxides, such as goethite and hematite [Fe_2O_3], as well as Al oxyhydroxides, ferrous and ferric sulfates (Ambe, 1987; Xu et al., 2001; Johnson et al., 2005; Leuz et al., 2006; Mitsunobu et al., 2006 and 2009), and clay minerals (Xi et al., 2011). With increasing pH from ~3, Sb retention decreases with a concomitant increase in mobility (Crecelius et al., 1975; Legoux et al., 1992; Xu et al., 2001; Nakamura et al., 2006; McComb et al., 2007; Rakshit et al., 2011). Other studies have also shown low mobility of the Sb(V) bound to oxides and indicated that there may potentially be inner-sphere complexation (Lintschinger et al., 1998; Knechtenhofer et al., 2003; Basunia and Landsberger, 2001; Mitsunobu et. al., 2009; Rakshit et al., 2011; Xi et al., 2011). Xi et al. (2011) found that the adsorption of Sb(V) by the edge ≡AlOH sites on bentonite was endothermic, which suggests an inner-sphere surface complexation mechanism (Journey et al., 2010). Scheinost et al. (2006) and Mitsunobu et. al. (2006) used EXAFS to investigate Sb speciation in shooting range and mine-affected soils that ranged in pH from 3.1 to ~8. They determined that only two Sb species were present: Sb(V) adsorbed by or coprecipitated in Fe oxides, and Sb(0) in unweathered bullet fragments. Mitsunobu et. al. (2010) used EXAFS to show that Sb(V) formed inner-sphere surface complexes on, and was incorporated into the structures of, ferrihydrite and goethite. Using EXAFS, Scheinost et al. (2006), Ilgen and Trainor (2012), and Ritchie et al. (2013) concluded that Sb(V) retention resulted from the formation of two types of inner-sphere surface complexes on Al and Fe oxides: monodentate-mononuclear and bidentate-binuclear. Using ATR-IR spectroscopy, McComb et al. (2007) concluded that Sb(V) adsorption onto amorphous Fe(III) oxide occurred via both inner- and outer-sphere mechanisms in the pH 3 to 8 range.

The use of mineral amendments to immobilize metals at contamination sites has become increasingly popular. There have been numerous studies investigating the effect of PO_4 on Pb mobilization (Melamed and Ma, 2008). Addition of PO_4 to immobilize soil Pb has the advantage of being an *in situ* method and thereby decreasing remediation costs and risk of worker exposure. Although the literature is replete with studies that examine the competitive adsorption of PO_4 and arsenate or selenate, there has been only limited investigation into the effects of PO_4 on Sb(V) adsorption. Kilgour et al. (2008) observed increases in Sb(V) leaching and bioaccessibility in shoot range soils treated with triple superphosphate, relative to untreated. Xi et al. (2011) observed that PO_4, and to a lesser degree SO_4, reduced the retention of Sb(V) by bentonite in pH 6 systems, and Biver et al. (2011) found that PO_4 and carbonate (HCO_3 and CO_3) effectively desorbed Sb(V) from hydrous metal (Al and Fe) oxides, clay minerals, and Sb(V)-contaminated sediments, relative to the desorption effectiveness of SO_4, nitrate (NO_3), and chloride. It is

generally assumed that the geochemical behavior and toxicity of Sb is similar to As (Wilson et al., 2004; Tighe et al., 2005a, b). In turn, arsenate behavior is similar to that of PO_4. Concentration of porewater As has been shown to increase in the presence of PO_4 (Kaplan and Knox, 2004). This increase is not the result of dissolution of minor contaminants in the PO_4, but a result of competition between the oxyanions, PO_4 and arsenate. Phosphate amendments can also influence contaminant mobility by increasing the pH of soil solution; thereby, potentially decreasing the retention of Sb(V). Direct evidence of the influence of PO_4 on Sb solubilization from shooting range soil was reported by Spuller et al. (2007). They observed the mobilization of Sb with additions of Ca- and NH_4-phosphates, and attributed the response to a competitive displacement process.

The state of Sb in Pb munitions-contaminated DoD soils, and the chemical factors affecting Sb behavior, can be hypothesized from information available in the scientific literature. Both thermodynamic and experimental evidence suggest that Sb in soil exists in the Sb(V) oxidation state. As a species, Sb(V) occurs as the hydroxyanion, $Sb(OH)_6^-$, which dominates Sb(V) solution chemistry when soil solution pH is greater than 2.85. This aqueous species is derived from the monoprotic, weak Lowry-Brønsted acid, $Sb(OH)_5^0$. Because $Sb(OH)_6^-$ is a weak acid anion ($Sb(OH)_5^0$ is a weak acid), it may potentially participate in both inner-sphere and outer-sphere surface complexation by variable-charge soil minerals (Fe-, Mn-, and Al-oxyhydroxides). The adsorption edge (adsorbed Sb versus pH) of Sb(V) by variable-charge minerals (increasing retention with decreasing pH) suggests that inner-sphere complexation is an important retention mechanism. Similarly, direct spectroscopic evidence also tends to support this conclusion. It has also been noted that the soil retention of Sb(V) is directly correlated to the Fe oxyhydroxide content of soil, and that the surface-bound Sb(V) is difficult to desorb, particularly from acidic soil. Phosphate stabilization of Pb in munitions-affected soil tends to reduce Sb(V) adsorption, enhancing mobility and bioaccessibility. Because PO_4 is strongly retained by variable-charge minerals by inner-sphere adsorption mechanisms, it is theorized that that the added PO_4 directly, and effectively, competes with Sb(V) for adsorption sites. However, despite the available evidence, knowledge of Sb(V) behavior in complex contaminated soil systems remains limited, and the ability to predict the mobility and bioaccessibility of Sb(V) in these environments has yet to be demonstrated.

The rational that underlies this research is the need to understand the processes affecting Sb adsorption by soil minerals, and to establish the ability to predict Sb(V) adsorption in the absence or presence of competing ligands. The specific objectives of this research are to:

1. Determine the mechanisms and thermodynamics of antimony adsorption by hydrous aluminum, iron, and manganese oxyhydroxides (gibbsite, kaolinite, goethite, and birnessite) as a function of ionic environment, pH, temperature, and antimony concentrations.

2. Quantify the competitive effects of phosphate and other soil anions on antimony adsorption.

3. Develop and evaluate the capability of chemical models to predict antimony adsorption within the holistic framework of a complex chemical environment.

Materials and Methods

Preparation of Solutions

All chemicals used were of analytical grade or better, and the solutions were prepared using CO_2-free Type-1 deionized water (18Ω). A 0.01 *M* potassium hexahydrate antimonate stock solution was prepared from solid $KSb(OH)_6$ (obtained from Sigma Aldrich). Potassium phosphate and potassium sulfate stock solutions, each 0.01 *M*, were prepared from salts of KH_2PO_4 and K_2SO_4. Background electrolyte solutions of 0.1 and 0.01 *M* potassium nitrate were prepared from solid KNO_3. All pH adjustments were made using certified 0.5, 0.1, or 0.01 *M* solutions of nitric acid (HNO_3) and potassium hydroxide (KOH).

Analytical

The elemental content of all solutions was determined with a Spectro CIROS inductively coupled argon plasma-atomic emission spectrometer (ICP-AES) (Fitchburg, MA) using commercially available ICP standards. For the adsorption edge studies the solutions were analyzed for Sb, P, and S. The method detection limits for these elements ranged from 0.01 to 0.1 mg L^{-1}, depending on background electrolyte composition. The solutions were also analyzed for Al (gibbsite and kaolinite systems), Fe (goethite systems), and Mn (birnessite systems) to evaluate mineral dissolution during the course of the experiments. The quantities of soluble Al, Fe, and Mn found in the equilibrium solutions were either at or below method detection limits (0.01 mg L^{-1}).

The pH measurements were performed under CO_2-free conditions in a N_2 glove box. All pH measurements were obtained using an Accumet Excel XL 25 dual channel pH/ion meter (Fisher Scientific, Pittsburg, PA) and a Ross Sure-Flow combination pH electrode. Calibration of the pH electrode was performed using pH 4, 7, and 10 commercially-available buffers. The surface area of the adsorbent minerals was determined by 5 point Baunauer-Emmett-Teller (BET) N_2 adsorption isotherms using a Beckman Coulter SA3100 surface area analyzer (Brea, CA). The particle size distribution of the adsorbents was determined using a Beckman Coulter LS 13 320 laser diffraction particle size analyzer (Brea, CA). X-ray diffraction (XRD) was used to verify the mineralogy of the adsorbents. The XRD patterns were generated by a Bruker AXS D8 Advance with K760 generator (Madison, WI) using Cu Kα radiation and a Ni filter. The XRD patterns were compared to Joint Committee on Powder Diffraction Standards files for solids identification.

Preparation of Solids

Alumina hydrate (SF-4) was obtained from Alcan Chemicals (Beachwood, OH). X-ray diffraction confirmed that the composition of the SF-4 was monoclinic gibbsite without detectable impurities (Fig. 2). The gibbsite was treated with 0.01 *M* NaOH for 30 minutes to remove poorly crystalline $Al(OH)_3$ (Sarkar et al, 1999). The treated gibbsite was centrifuge washed with Type-1 water to remove NaOH; this process was repeated until the suspension pH was approximately 7. The gibbsite was freeze-dried and stored at ambient temperatures (20-22°C).

A well-crystallized Georgia kaolinite (KGa-1b) from the Source Clays Repository of The Clay Minerals Society (West Lafayette, IN) (Fig. 2) was prepared using the method from Mattigod et al. (1985). Kaolinite was suspended in Type-1 water and dispersed in a blender for 45 minutes. The suspension pH was increased to pH 9.5 with 0.1 *M* NaOH. The less than 20 μm size fraction was obtained using Stokes' Law sedimentation. The collected size fraction was centrifuge washed with Type-1 water until neutral suspension pH was obtained. The kaolinite was freeze-dried and stored at ambient temperatures.

Goethite (FeOOH) was synthesized using the method of Schwertmann and Cornell (2000). A 1.0 *M* $Fe(NO_3)_3$ solution was created by dissolving anhydrous $Fe(NO_3)_3$ in Type-1 water. A 100-mL volume of 1.0 *M* $Fe(NO_3)_3$ solution was placed in a 2-L polyethylene flask. A 180-mL volume of 5 *M* KOH was then rapidly added with vigorous stirring, yielding a red-brown precipitate. The solution was then quickly diluted to a 2-L volume using Type-1 water to quench the reaction. The flask was sealed and placed in a 70°C oven for 60 h. The precipitate was then washed and centrifuged with 1 m*M* HCl until pH 5, then with 1 m*M* KNO_3 until all traces of chloride ion were removed (determined by a silver nitrate test). The goethite was stored in the 1 m*M* KNO_3 suspension at ambient temperature. The precipitate was determined by XRD to be goethite (poorly crystalline) without any detectable impurities (Fig. 2).

Birnessite (δ-MnO_2) was synthesized using the method of McKenzie (1971). A 1.0 *M* $KMnO_4$ solution was brought to a boil. To this was slowly added 165-mL of 12.1 *M* HCl. The suspension was boiled for an additional 10 min following the HCl addition. The resulting precipitate was centrifuge washed with 1 m*M* HCl until pH 5 was obtained. The solid was then centrifuge washed with 1 m*M* KNO_3 until all traces of chloride ion were removed as determined by a silver nitrate test. The solid was then stored in the 1 m*M* KNO_3 suspension at ambient temperature. The precipitate was determined by XRD to be poorly crystalline birnessite without any detectable impurities (Fig. 2).

The specific surface area and particle size characteristics of the solids are presented in Table 1.

Adsorption Edge Determinations

Antimony(V) adsorption by gibbsite and kaolinite (≡AlOH surface functional groups) and goethite (≡FeOH and $\equiv Fe_3OH$ surface functional groups) was examined as a function of pH and background electrolyte (KNO_3) concentration (ionic strength). Adsorption edge experiments were performed in duplicate and in 2-L flat bottomed water-jacketed glass reaction vessels with recirculating water held at a constant temperature of 298 K (25°C). All experiments were conducted in a CO_2-free environment in a N_2 filled glove box to eliminate the influence of CO_2. The solid-to-solution ratio for gibbsite and kaolinite was 10 g L^{-1}; and for goethite was 5 g L^{-1} due to its higher adsorptive capacity (complete removal of Sb(V) from the equilibrating solutions throughout the pH range studied was observed when goethite was used at 10 g L^{-1}). The minerals were suspended in a background electrolyte solution of either 10 or 100 m*M* KNO_3 with aid of a Teflon-coated, magnetic stir bar and mechanical stir plate. Nitric acid was employed to lower the suspension pH to 3.5 and was allowed to fully hydrate overnight in an N_2 environment to insure CO_2 removal. After a minimum 15 h equilibration, the suspension pH was increased to pH 9.5 with additions of 0.5 *M* KOH. When the solution pH was stable, a volume of the adsorptive 10 m*M* $KSb(OH)_6$ was added to yield a 50 μmol L^{-1} solution of Sb(V) in the gibbsite and kaolinite systems, and a 500 μmol L^{-1} solution in the goethite systems. The suspension was allowed to

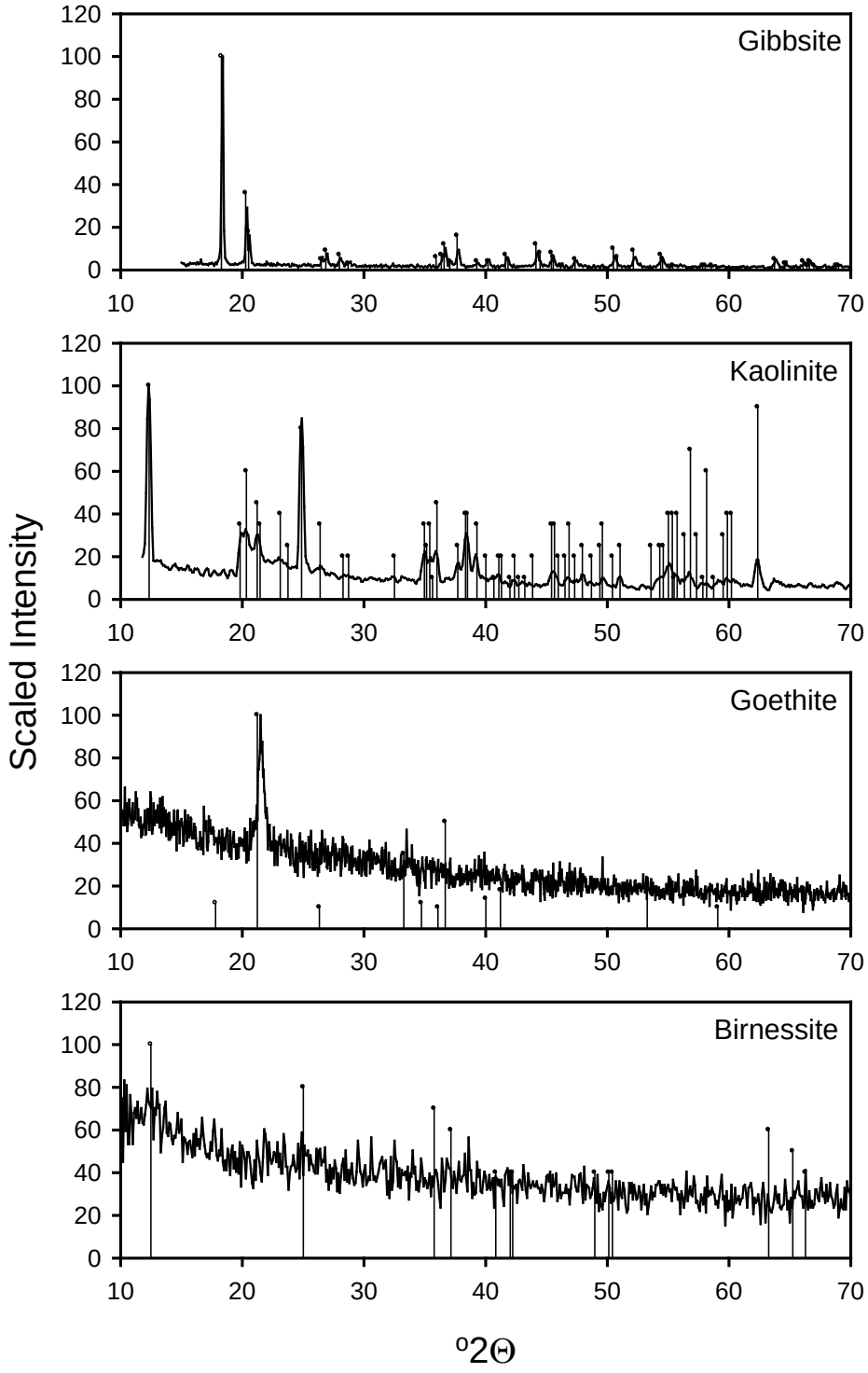

Figure 2. X-ray diffraction patterns of absorbents. The vertical bars represent reference peak locations obtained from the Joint Committee on Powder Diffraction Standards files for the solids.

equilibrate for a minimum of 1 h after Sb(V) introduction (preliminary kinetic studies were employed to determine the required equilibration period). Following the equilibration period, the solution pH was recorded and a 15-ml aliquot of suspension was removed with a polypropylene syringe. The sample was passed through a 0.45-μm membrane syringe filter and stored under refrigeration in a 15-ml polypropylene centrifuge tube for analysis by ICP-AES. Once the pH was recorded and the sample removed, an aliquot of a HNO_3 solution was added to lower the suspension pH by approximately 0.2 pH units. The suspension was again equilibrated at the new pH value, sampled, and the pH lowered. This process was repeated until a suspension pH of approximately 3.5 was achieved.

Upon the completion of the adsorption experiment, the reversibility of the adsorption process (desorption) was investigated by incrementally increasing the suspension pH. As with the adsorption portion of the experiment (described above), the pH of the suspension was increased using aliquots of a KOH solution to achieve stepped pH changes of approximately 0.2 pH units. At each step the pH was recorded and a 15-ml suspension aliquot was removed with a polypropylene syringe. The suspension was passed through a 0.45 μm membrane syringe filter and stored under refrigeration for analysis. Preliminary kinetic studies indicated that an 8-h period was required to achieve desorption equilibrium following each incremental pH change.

All adsorption-desorption experiments were repeated to examine SO_4 and PO_4 retention behavior using an aliquot of 0.01*M* K_2SO_4 or KH_2PO_4 to achieve an initial 50 μmol L^{-1} solution adsorbate concentrations in the gibbsite and kaolinite systems, and 500 μmol L^{-1} solution adsorbate concentrations in the goethite systems. The concentration of adsorbed Sb(V), SO_4, or PO_4 was computed as the difference between the mass of ligand added and the mass in solution at equilibrium, divided by the mass of solid.

The adsorption of Sb(V), SO_4, and PO_4 by birnessite as a function of pH and ionic strength was investigated using a batch procedure. All studies were performed in duplicate, with a blank (no solid) for each pH increment. Birnessite suspensions of 5 g L^{-1} were created in 50-mL polypropylene tubes with 0.125-g solid and 25-mL of either 10 m*M* or 100 m*M* KNO_3. Birnessite suspensions were prepared in an N_2-filled glove box to insure a CO_2-free environment. To achieve a pH range between 3.5 and 10, each tube was individually adjusted with HNO_3 or KOH. The tubes were then shaken, and allowed to stabilize for 30 min before volumes of either 10 m*M* $KSb(OH)_6$, 10 m*M* K_2SO_4, or 10 m*M* KH_2PO_4 were added to each tube to yield an initial ligand concentration of 80 μmol L^{-1}. The tubes were then shaken on a platform shaker for 24 h at ambient temperature (20 to 22°C). Following the equilibration, the tubes were returned to the CO_2-free, N_2 environment for pH determinations using a calibrated (pH 4, 7, and 10 buffers) combination pH electrode. The supernatant was removed from the tubes and filtered through a 0.20-μm nylon syringe filter and analyzed by ICP-AES for total Sb, S, or P. The concentration of adsorbed Sb(V), SO_4, or PO_4 was computed as the difference between the mass of ligand added and the mass in solution at equilibrium, divided by the mass of solid.

Adsorption Isotherm Determinations

The adsorption of Sb(V) by gibbsite, kaolinite, and goethite was determined as a function of Sb(V) concentration, pH (pH 5.5 or 8), and temperature (5, 15, 25, or 35 ± 1°C). Each adsorption experiment was performed in duplicate. All adsorption isotherm studies were performed in 1-L flat bottomed water jacketed glass reaction vessels in CO_2-free, N_2 environments. Temperature control was achieved using a recirculating water bath that continually pumped constant

temperature water through the jacket of the glass beaker. Mineral suspensions were prepared in 10 m*M* KNO_3, placed in the reaction vessel, and the pH initially adjusted with additions of either HNO_3 or KOH. The solid-to-solution ratios for the suspensions were 10 g L^{-1} for gibbsite and kaolinite and 5 g L^{-1} for goethite. Each mineral suspension system was paired with a blank (mineral free) system, otherwise treated identically to the suspensions. The suspensions were continuously agitated during each experiment using a magnetic stirring bar.

Following the initial pH adjustment, the mineral suspension and blank were brought to the desired temperature and allowed to equilibrate for 16 h. The suspension pH was then readjusted as needed and duplicate 15 mL aliquots where removed for background Sb(V) analysis. The pH of the suspension was determined using a Thermo Orion pH meter (Thermo Fisher Scientific, Waltham, MA) and a Thermo Orion Ross Series combination electrode. Calibration of the pH electrode was performed using commercially available buffer solutions (pH 4, 7, and 10 at 25°C with an accuracy of ±0.01 pH units, adjusted for temperature) and at the temperature of the study. A volume of 10 m*M* $KSb(OH)_6$ was then added to the suspension and blank to achieve the lowest isotherm initial Sb concentration (C_{in} value). The system was allowed to equilibrate for a 2 h period, during which the suspension pH was constantly monitored and adjusted as needed. Following this equilibration, the suspension pH was recorded and duplicate 15 mL aliquots were removed, passed through a 0.45-µm membrane syringe filter, and analyzed for the equilibrium Sb concentration (C_{eq} value) using ICP-AES. A second volume of 10 m*M* $KSb(OH)_6$ was then added to the suspension and blank to achieve the next higher isotherm C_{in} value. The system was allowed to equilibrate for an additional 2 h period, sampled, filtered, and analyzed for Sb C_{eq}. The Sb(V) addition, 2 h equilibration, and sampling for C_{eq} was repeated to achieve incrementally higher C_{in} values and a total of 6 isotherm points.

Data generated from the blank solutions were the initial concentrations (C_{in}, µmol L^{-1}) of Sb(V) for each increment of Sb addition, and from the suspensions were the equilibrium Sb(V) solution concentrations (C_{eq}, µmol L^{-1}) for the 2 h equilibrium samples. The concentration of adsorbed Sb(V) (q, µmol kg^{-1}) was determined by difference:

$$q = \frac{V_l (C_{in} - C_{eq})}{m_s} \quad [1]$$

where V_l is the volume of the suspension and m_s is the mass of the solid. Adsorption isotherms were generated by plotting q vs. C_{eq} for each system and each combination of pH and temperature. The adsorption data were also evaluated by plotting K_d vs. q, where K_d (L kg^{-1}) is the distribution coefficient (= q/C_{eq}).

Adsorption isotherms are empirically described by mathematical functions (isotherm models) whose adjustable parameters are generally taken to have physical meaning. The Freundlich model and both the one- and two-site Langmuir models were used to describe the Sb(V) adsorption isotherms. The Freundlich isotherm model is:

$$q = K_F C_{eq}^N \quad [2]$$

where K_F and N are positive-valued adjustable parameters and N is constrained to lie between 0 and 1. The Freundlich parameters are not normally interpreted to have physical meaning. However, K_F is an intensity parameter, as it is numerically equal to q when C_{eq} is unity, and N is

a measure of inflection in the curve that fits the isotherm data. The parameter N has also been shown to provide a measure of adsorption site heterogeneity (Sposito, 1980). As N approaches 0, surface site heterogeneity increases, indicating a broad distribution of adsorption site types. Conversely, as N approaches 1, the surface site homogeneity increases, indicating a narrow distribution of adsorption site types. Equation [2] may be rearranged into a linear function:

$$\log q = \log K_F + N \log C_{eq} \quad [3]$$

where a plot of log q versus log C_{eq} will be linear if the Freundlich model describes the adsorption data. The Freundlich parameters, K_F and N, were obtained using linear regression analysis of log q vs. log C_{eq} plots and Eq. [3].

The one-site Langmuir isotherm model is:

$$q = \frac{bK_L C_{eq}}{1 + K_L C_{eq}} \quad [4]$$

which may be rearranged to generate an alternate Langmuir equation:

$$K_d = bK_L - qK_L \quad [5]$$

A plot of K_d versus q will be linear if the Langmuir model describes the adsorption data. In Eqs. [4] and [5], b is described as the adsorption maxima (in units of q), and K_L is the Langmuir constant (in units of inverse C_{eq}) (Essington, 2003). The Langmuir isotherm parameters, K_L and b were obtained using the linear regression analysis of K_d vs. q plots and Eq. [5].

As the equilibrium solution becomes infinitely dilute in the adsorptive (as the surface excess of an adsorbate approaches zero), the Langmuir equation reduces to a linear isotherm:

$$\lim_{C_{eq} \to 0} q = K_{ad} C_{eq} \quad [6]$$

where K_{ad} is the adsorption constant ($K_{ad} = bK_L$), or the Henry's Law constant when gas adsorption is considered (Kinniburgh, 1986). Under the limiting conditions of infinite dilution (Eq. [6]), the solution and adsorbed phases are effectively in their infinite dilution reference states, and K_{ad} may be viewed as a true equilibrium constant for the adsorption reaction (Journey et al., 2010).

The two-site Langmuir isotherm model is:

$$q = \frac{b_1 K_1 C_{eq}}{1 + K_1 C_{eq}} + \frac{b_2 K_2 C_{eq}}{1 + K_2 C_{eq}} \quad [7]$$

where b_1 and b_2 are described as the adsorption maxima (in units of q) of site types 1 and 2, and K_1 and K_2 are the associated Langmuir constants (Essington, 2003). In this formulation, site type 1 may be viewed as a high intensity–low capacity site, while site type 2 is a low intensity–high capacity site. The Langmuir isotherm parameters, K_1 and b_1, and K_2 and b_2, were obtained using the linear regression analysis of q vs. K_d plots and the interpolation procedure of Sposito (1982).

As the equilibrium solution becomes infinitely dilute in the adsorptive (as the surface excess of an adsorbate approaches zero), the Langmuir equation reduces to a linear isotherm with contributions from both adsorption site types:

$$\lim_{C_{eq}\to 0} q = K_{ad1}C_{eq} + K_{ad2}C_{eq} \quad [8]$$

where K_{ad1} and K_{ad2} are the adsorption constants for site types 1 and 2, representing the true equilibrium constant for the adsorption reaction at each site.

For each isotherm, the T of the adsorption study, and the values of K_{ad}, or K_{ad1} and K_{ad2}, determined from the Langmuir equation were used, in conjunction with the van't Hoff equation (Essington, 2003), to determine the enthalpy (ΔH_{ad}) and entropy (ΔS_{ad}) of adsorption:

$$\ln K_{ad} = -\frac{\Delta H_{ad}}{RT} + \frac{\Delta S_{ad}}{R} \quad [9]$$

where R is the molar gas constant (8.314 J K^{-1} mol^{-1}), and T is the temperature (K). The van't Hoff equation assumes that ΔH_{ad} and ΔS_{ad} are constant and independent of T (Essington et al., 2004); therefore, the variation in K_{ad} as a function of T may be used to compute ΔH_{ad} and ΔS_{ad}. Enthalpy values for each system were determined by linear plots of ln K_{ad} vs. T^{-1} according to Eq. [9], where ($-\Delta H_{ad}/R$) is the slope and ($\Delta S_{ad}/R$) is the intercept.

The sign and magnitude of ΔH_{ad} was used to provide information about the adsorption reaction (the heat of the reaction and the driving force) and the mechanism of Sb(V) retention (Journey et al., 2010). If ΔH_{ad} is large and positive, inner-sphere complexation is inferred. However, if ΔH_{ad} is small and positive, or negative, outer-sphere complexation is inferred. Positive ΔH_{ad} values are indicative of endothermic reactions, where adsorption K_{ad} values increase with increasing temperature. Endothermic reactions are generally thought to indicate inner-sphere adsorption mechanisms. Inner-sphere complexation requires the formation of covalent bond character, which requires energy. At higher temperatures, inner-sphere complexation is supported by "excited" ions in solution that provide energy for covalent bond formation. Conversely, negative ΔH_{ad} values are indicative of exothermic reactions, where adsorption K_{ad} values decrease with increasing temperature. Exothermic reactions indicate ion exchange (outer-sphere complexation). Outer-sphere complexation requires the formation of weak electrostatic bonds that require ions to exist in close proximity to one another on the surface. As temperatures increase, ions in solution become more mobile; therefore, electrostatic bond formation decreases.

The Gibb's free energy of formation (ΔG_{ad}) is a measure of the substance's ability to react and the extent of the reaction. The ΔG_{ad} is determined by

$$\Delta G_{ad} = -RT \ln K_{ad} \quad [10]$$

or

$$\Delta G_{ad} = \Delta H_{ad} - T\Delta S_{ad} \quad [11]$$

At constant temperature and pressure, negative ΔG_{ad} values indicate that the adsorption reaction is spontaneous and irreversible, while positive ΔG_{ad} values indicate that energy must be supplied in order for the reaction to proceed.

The driving force of the Sb(V) adsorption reaction was determined using the ΔS_{ad} and ΔH_{ad} values that were computed from the methods described above. As seen in Eq. [11], the degree to which $T\Delta S_{ad}$ contributes to the ΔG_{ad} value of the reaction determines the driving force of the reaction. Spontaneous, endothermic reactions would require a large positive value for $T\Delta S_{ad}$, resulting in a negative ΔG_{ad}. In general, reactions in which $T\Delta S_{ad}$ is a large contributor to ΔG_{ad} are said to be entropically driven (i.e., adsorb heat) and characteristic of endothermic (inner-sphere surface complexation) reactions. Reactions in which ΔH_{ad} is a large contributor to ΔG_{ad} are said to be enthalpically driven (i.e., release heat) and characteristic of exothermic (electrostatic) reactions.

Proton Adsorption and Zeta Potential

The region between the mineral surface and the bulk solution is called the solid-solution interface, and consists of various layers of charge density (Essington, 2003). The total net surface charge density on a particle (σ_p) is (Sposito, 1981):

$$\sigma_p = \sigma_s + \sigma_H + \sigma_{is} + \sigma_{os} = -\sigma_d \qquad [12]$$

where σ_s is the permanent structural charge density, σ_H is the proton surface charge resulting from the specific adsorption of proton and hydroxyl ions, σ_{is} is the inner-sphere charge resulting from specific ion adsorption, σ_{os} is the outer-sphere charge resulting from non-specific ion adsorption, and σ_d is the counterion diffuse ion swarm charge that exactly balances σ_p. Antimony(V) adsorption mechanisms, outer- vs. inner-sphere complexation, may be directly determined through electrokinetic experiments, and indirectly by potentiometric titrations.

Electrokinetic experiments measure the electric double layer potential at the shear plane between the solid and the bulk solution. This electric potential is known as the zeta potential (ζ). The ζ-potential is assumed to approximate the diffuse double layer potential (Goldberg et al., 2012). To measure the ζ-potential, the movement of a suspended charged particle is tracked under an applied electric field. The mobility of the particle is measured as electrophoretic mobility, which is related to ζ by the Smoluchowski equation:

$$\mu_E = \frac{\varepsilon\zeta}{\eta} \qquad [13]$$

where μ_E is the electrophoretic mobility (microns sec^{-1} per volt cm^{-1}), ε is the dielectric constant of solution, ζ is the zeta potential (mV), and η is the viscosity of the suspending liquid (poises). The electrophoretic mobility of a particle within an indifferent electrolyte will reflect the surface charge created by proton adsorption and desorption on mineral surface functional groups (in the absence of particle charge from of isomorphic substitution), as well as σ_{os} charge derived from the retention of the indifferent electrolyte. When a ligand other than the indifferent electrolyte is present, electrophoretic mobility will reflect the adsorption mechanism. Adsorption of an anionic ligand in the is-plane will decrease μ_E, while adsorption of the ligand in the os-plane will not affect μ_E, relative to the indifferent electrolyte. The electrophoretic mobility of a particle is also

influenced by ionic strength. Increased concentrations of electrolyte in the σ_d plane tend to shield the particle charge, decreasing the extent of charge influence in the solid-solution interface and decrease the response (particle movement) in an electric field (Yu, 1997).

Potentiometric titrations may be employed to indirectly characterize ligand adsorption mechanisms. Potentiometric titrations measure variation in σ_H as a function of pH by quantifying protonation and deprotonation reactions on surface functional groups. Variations in σ_H are determined by measuring proton concentration without the solid (blank) and measuring proton concentration when the solid is present, the difference is considered adsorbed proton per mass of solid (Q_h in $mmol_c\ kg^{-1}$). When an adsorbed ligand is present (in addition to the background electrolyte), the proton adsorption characteristics can be used to infer the ligand adsorption mechanism. Adsorption of a anionic ligand in the is-plane will increase Q_h in response to the addition of intrinsic negative surface charge (decreasing σ_{is}), while adsorption of a ligand in the os-plane will not have an effect on Q_h. Potentiometric titrations are used to indirectly measure adsorption because the initial protonation status of surface functional groups is unknown (Sposito, 2004); only changes in Q_h are quantified. Specific adsorption of a ligand in the is-plane will also displace water and hydroxyl ions from surface functional groups influencing σ_H. Further, the influence of an anionic ligand extends out from the surface and into the solid-solution interface, requiring additional protons to satisfy the charge, thus increasing Q_h.

Electrophoretic mobility and potentiometric titrations provide the evidence necessary to identify ligand adsorption mechanisms. In addition to variations in μ_E and Q_h, points of zero charge (pH_{pzc}) and common intersection points (CIP) of potentiometric titration curves obtained under differing ionic strength conditions may also indicate ligand retention mechanisms. When the electrophoretic mobility of a particle is zero, this is the point of zero charge: the pH at which the concentrations of negative and positive functional groups on a mineral surface are equal (Goldberg et al., 2012). When determined by electrophoretic mobility, the point of zero charge is known as the isoelectric point (IEP) (Appel et al., 2003). Ligand adsorption occurring in the is-plane will decrease the number of positive surface sites, shifting the point of zero charge (pH_{pzc}) to lower values (Goldberg and Kabengi, 2010). In a potentiometric titration, a CIP will occur when proton adsorption curves of varying ionic strength cross at a common pH. When the electrolytes are indifferent, the CIP is the point of zero salt effect (pH_{pzse}) and is equal to the pH_{pzc} (Avena et al., 1998; Appel et al., 2003). However, when the specific adsorption of a ligand occurs, pH_{pzse} is not equal to the pH_{pzc} (Sposito, 2004).

Batch proton adsorption studies were performed to examine the charging characteristics of gibbsite, kaolinite, goethite, and birnessite in the presence of background electrolyte (KNO_3), or adsorbed Sb(V), SO_4, or PO_4. The proton adsorption studies were conducted in 50-ml polypropylene tubes containing 0.25-g of gibbsite or kaolinite, or 0.125-g of goethite or birnessite. After a suspension containing the solids was placed in the tubes, the tubes were placed in a N_2-filled glove box to ensure a CO_2-free environment. A 25-ml volume of a swamping electrolyte was then added to each tube, yielding a solid-to-solution ratio of 10 g L^{-1} for gibbsite and kaolinite, or 5 g L^{-1} for goethite and birnessite. The swamping electrolyte solutions were: 10 m*M* or 100 m*M* KNO_3; 10 m*M* $KSb(OH)_6$; 10 m*M* K_2SO_4; 10 m*M* KH_2PO_4; 10 m*M* KNO_3 with 10 m*M* $KSb(OH)_6$ or 10 m*M* K_2SO_4 or 10 m*M* KH_2PO_4; and 100 m*M* KNO_3 with 10 m*M* $KSb(OH)_6$ or 10 m*M* K_2SO_4 or 10 m*M* KH_2PO_4. The suspension pH was adjusted in each tube individually with 0.005 ml to 0.15 ml aliquots of HNO_3 or KOH to achieve a pH range between 3.5 and 10. Blank tubes were prepared without solid under otherwise identical conditions. After pH adjustments were made, the tubes were capped and placed on a platform shaker for a 2 h

equilibration at ambient temperature (20 to 22°C). After equilibration, the solid and solution phases were separated by centrifugation and the tubes were placed back into the CO_2-free, N_2 environment. The supernatant of each tube was analyzed for pH with a Ross Sure-Flow combination electrode.

The variation in added acid or base concentration (total hydrogen, TOTH = $[H^+] - [OH^-]$; the free proton minus the free hydroxide concentrations) as a function of pH in the systems containing NO_3, Sb(V), or SO_4 in the absence of solid was fitted to an equation of the form:

$$\mathrm{TOTH} = a \times 10^{-\mathrm{pH}} - b \times 10^{-(14-\mathrm{pH})} + c \times \mathrm{pH} + d \qquad [14]$$

For systems containing PO_4, the TOTH relationship was:

$$\mathrm{TOTH} = a \times 10^{-\mathrm{pH}} - b \times 10^{-(14-\mathrm{pH})} + c \times \frac{10^{-\mathrm{pH}}}{\left(10^{-\mathrm{p}K_a} + 10^{-\mathrm{p}H}\right)} + d \times \mathrm{pH} + e \qquad [15]$$

where pK_a is the acid dissociation constant for the $H_2PO_4^-$ to HPO_4^{2-} reaction. In Eqs. [14] and [15] the adjustable paramters (*a* through *e*) take into account the ionic dissociation product of water (K_w), the proton activity coefficient, and the electrode liquid-junction potential. The concentration of adsorbed proton (Q_h), also termed the apparent net proton surface charge, is computed by subtracting the fitted blank (Eqs. [14] or [15]) from the suspension titration data:

$$Q_h = \left[c_A - c_B - \left([\mathrm{H}^+] - [\mathrm{OH}^-]\right)\right] \times \frac{V}{m_S} \qquad [16]$$

where c_A is the concentration of strong acid in the suspension, c_B is the concentration of strong base, V is the suspension volume, and m_S is the mass of solid. In the absence of structural charge (a valid assumption for the minerals), Q_h can be ascribed to represent the surface charge of the mineral.

Surface charging characteristics of gibbsite, kaolinite, goethite, and birnessite in various swamping electrolytes was also determined by microelectrophoresis using the Zeta-Meter System 4.0 (Zeta Meter, Staunton, VA). The suspensions for testing were prepared in 50-ml polypropylene tubes. After a volume of mineral suspension (gibbsite, kaolinite, goethite, or birnessite) was placed into the tubes, the tubes were placed in a N_2-filled glove box to ensure a CO_2-free environment. A volume of a swamping electrolyte was added to each tube to yield a solid-to-solution ratio of 0.2 g L^{-1} for gibbsite and kaolinite, and 0.15 g L^{-1} for goethite and birnessite. The suspension pH was adjusted in each tube individually with HNO_3 or KOH in order to achieve a pH range between 3.5 and 10. The tubes were removed from the glove box and shaken for 24 h to reach equilibrium at ambient temperature (20 to 22°C). The tubes were placed back into the CO_2-free, N_2 environment for pH determinations using a calibrated (pH 4, 7, and 10 buffers) combination pH electrode. Suspensions were then manually loaded into a GT-2 electrophoresis cell according to the Zeta-Meter 4.0 operating instructions. A minimum of 10 particles were tracked across a single scale of division for each suspension. An average ζ-potential (mV) reading was recorded for each suspension. The Zeta-Meter 4.0 unit automatically calculated the zeta potential in millivolts for aqueous systems using the Smoluchowski equation Eq. [13]. Zeta potential was then plotted as a function of pH. The impact of NO_3, Sb(V), SO_4,

and PO_4 on ζ-potential was determined by varying the swamping background electrolyte compositions to include $KSb(OH)_6$, K_2SO_4, and KH_2PO_4. The swamping electrolytes used were: 10 m*M* KNO_3; 100 m*M* KNO_3; 10 m*M* $KSb(OH)_6$; 10 m*M* K_2SO_4; 10 m*M* KH_2PO_4; 10 m*M* KNO_3 with 10 m*M* $KSb(OH)_6$, or 10 m*M* K_2SO_4, or 10 m*M* KH_2PO_4; 100 m*M* KNO_3 with 10 m*M* $KSb(OH)_6$, or 10 m*M* K_2SO_4, or 10 m*M* KH_2PO_4.

Competitive Antimony(V), Sulfate, and Phosphate Adsorption

A series of adsorption edge studies was performed to investigate the competitive effects of PO_4 and SO_4 on Sb(V) retention by gibbsite, kaolinite, goethite, and birnessite. The batch adsorption studies were conducted in 50-ml polypropylene tubes containing 0.25-g of gibbsite or kaolinite, or 0.125 g of goethite or birnessite. After the solids were placed in the tubes, the tubes were placed in a N_2-filled glove box to ensure a CO_2-free environment. A 25-ml volume of the background electrolyte (10 m*M* or 100 m*M* KNO_3) was added to each tube, yielding the solid-to-solution ratios of 10 g L^{-1} or 5 g L^{-1}. The suspension pH was adjusted in each tube individually with aliquots of HNO_3 or KOH to achieve a pH range between 3.5 and 9.5. After pH adjustments were made, the tubes were capped and shaken by hand and the pH was allowed to stabilize. Upon equilibration, an appropriate volume of the adsorptive solution (10 m*M* $KSb(OH)_6$, 10 m*M* K_2SO_4, or 10 m*M* KH_2PO_4) was added to the suspension to achieve initial concentrations of 50 μmol L^{-1} for gibbsite and kaolinite; 500 μmol L^{-1} for goethite; or 80 μmol L^{-1} for birnessite. The tubes were then recapped and sealed while in the CO_2-free environment and placed on a platform shaker for a minimum of 12 hours at ambient temperature (20 to 22°C). After equilibration, the solid and solution phases were separated by centrifugation. Before sampling the supernatant solution, the tubes were placed back into the CO_2-free, N_2 environment. The supernatant of each tube was analyzed for pH with a Ross Sure-Flow combination electrode, and then filtered through a 0.45-μm or 0.20-μm nylon syringe filter. All samples were refrigerated until analyzed by ICP-AES.

The batch adsorption edge studies employed four scenarios of introducing the adsorptives to the solids. In the first scenario, adsorption was investigated in single adsorptive systems involving singular additions of Sb(V), SO_4, or PO_4, followed by a 12 h equilibration. The second scenario involved the initial 12 h adsorption equilibration of Sb(V), followed by the additions of either SO_4 or PO_4 and an additional 12 h equilibration. The third scenario involved the initial adsorption of either SO_4 or PO_4, followed by the addition of Sb(V). The fourth scenario involved the simultaneous additions of either Sb(V) and SO_4, or Sb(V) and PO_4, and a 12 h equilibration.

The initial concentrations of Sb(V), PO_4, and SO_4 were determined in each adsorptive system through the analysis of control samples (no solid). The difference between the initial mass of ligand added to each tube and the equilibrium suspension mass of the ligands was defined as the adsorbed concentration (Eq. [1]). Adsorption edge plots (% adsorbed vs. pH) were then created.

Surface Complexation Modeling of Antimony(V), Sulfate, and Phosphate Adsorption

Adsorption is but one of many chemical processes occurring in natural environments that distribute matter between various species within and between the solid, solution, and gaseous phases. For environments at equilibrium, tools are available to predict these chemical processes (e.g., aqueous speciation and mineral precipitation). For ligands, such as antimonate, a

mechanistic prediction of adsorption by variable-charge surfaces can be achieved through the theoretical and thermodynamic framework of surface complexation models. Surface complexation models (SCMs) evolved in the 1970s (Davis et al., 1978) and are used to take into account the molecular features of adsorption and to aid in the indirect identification of specific surface species, chemical reactions, and charge balance at the solid-solution interface (Goldberg, 1992; Sposito, 2004). Further, if a mechanism of retention is known, an SCM can be employed to determine the specific equilibrium constant for the adsorption reaction.

There are several SCMs that can be applied to predict surface complexation, each differing on how they conceptualize the solid-solution interface (e.g., where adsorption occurs, how surface electrostatics are considered) and in the number and types of required parameters (Goldberg and Criscenti, 2008). However, there exists a set of fundamental concepts, or assumptions, to which all models adhere: adsorption takes place at one or more well-defined surface functional groups; a total concentration of sites for each type of surface functional group can be determined; and that a free energy of adsorption ($\Delta G°_{ads}$) can be defined for each adsorption reaction (Essington, 2003). Mathematically, this is the sum of the intrinsic and coulombic free energy terms ($\Delta G°_{ads} = \Delta G°_{int} + \Delta G°_{coul}$). Correspondingly, the adsorption constant for a specified adsorption reaction, K_{ads}, is a product of the intrinsic (K^{int}) and coulombic (K_{coul}) constants: $K_{ads} = K^{int}K_{coul}$. For example, consider the protolysis reaction that occurs at a singly-coordinated surface functional group on a hydrous metal oxide, where *S* represents the metal: $\equiv SOH^0 + H^+ = \equiv SOH_2^+$. The adsorption constant for this reaction is:

$$K_+ = \frac{[\equiv SOH_2^+]}{[\equiv SOH^0](H^+)} = K_+^{int} K_{coul} \qquad [17]$$

where the brackets represent concentrations and the parentheses activities. The coulombic constant, K_{coul}, is defined as:

$$K_{coul} = \exp\left(\frac{-F\Delta Z\psi_{(0)}}{RT}\right) \qquad [18]$$

where *F* is the Faraday constant, ΔZ is the net change in surface charge due to adsorption, $\psi_{(0)}$ is the surface potential relative to the reference potential of zero in the bulk solution, *R* is the natural gas constant, and *T* is temperature (in Kelvin). Substituting for K_{coul} and rearranging yields K_+^{int}:

$$K_+^{int} = \frac{[\equiv SOH_2^+]}{[\equiv SOH^0](H^+)} \exp\left(\frac{F\psi_{(0)}}{RT}\right) \qquad [19]$$

with $\Delta Z = 1$ for the surface protolysis reaction. The intrinsic equilibrium constant, K_+^{int}, is a true equilibrium constant that is independent of the composition of the adsorbed phase at a fixed ionic strength. Thus, it may be used to describe an adsorption process in any environment having an ionic strength similar to the one in which K_+^{int} was determined.

The SCM selected to describe Sb(V) (as well as phosphate and sulfate) adsorption by gibbsite, kaolinite, goethite, and birnessite was the 2-pK_a formulation of the triple layer model

(TLM) (Fig. 3). The protonation and deprotonation of surface functional groups is described by two reactions with corresponding pK_a values (2-pK_a formulation). The TLM allows for both inner- and outer-sphere adsorption of metal and ligand species, and the outer-sphere complexation of counter ions (K^+ and NO_3^-). The model treats the solid-solution interface as composed of two layers of constant capacitance enveloped by a third, diffuse layer (Fig. 3) (Essington, 2003). The surface potential of each plane is given by:

$$\sigma_{in} = C_1(\psi_{(0)} - \psi_{os}) \quad [20]$$

$$\sigma_d = C_2(\psi_d - \psi_{os}) = -(8RTI\varepsilon_0\varepsilon)^{0.5} \sinh\left(\frac{F\psi_d}{2RT}\right) \quad [21]$$

where C_1 and C_2 are the inner and outer layer capacitances, I is the ionic strength, ε_0 is the permittivity of vacuum, and ε is the dielectric constant of water. The TLM uses measured or experimentally estimated surface parameters for the adsorbents and intrinsic equilibrium constants for surface reactions.

The TLM formulation of the 2-pK_a SCM coupled with the q vs. pH adsorption edge data were used to develop a chemical model that described Sb(V), phosphate, and sulfate adsorption by gibbsite, kaolinite, goethite, and birnessite. The SCM computations were conducted using FITEQL 4.0 software (Herbelin and Westall, 1999). FITEQL 4.0 is a computer program that combines a nonlinear least-squares fitting routine with a chemical model that describes aqueous speciation and adsorption. The SCM requires a set of fixed parameters: values for surface parameters of the adsorbents (e.g., specific surface, site density, and capacitances), formation constants for all aqueous species, and intrinsic equilibrium constants that describe surface hydrolysis and background electrolyte adsorption. These values were obtained from literature sources, or were directly measured. The adsorbent surface parameters used in the application of the TLM are presented in Table 1. Surface protolysis constants (describing the formation of $\equiv SOH_2^+$ and $\equiv SO^-$), constants describing the outer-sphere complexation of the background electrolyte ($\equiv SOH_2^+$–NO_3^- and $\equiv SO^-$–K^+), and the equilibrium constants for the relevant aqueous speciation reactions are listed in Table 2.

The following surface complexation reactions where considered for describing Sb(V) adsorption:

$$\equiv SOH^0 + H^+ = \equiv SOH_2^+ \quad [22]$$

$$\equiv SOH^0 = \equiv SO^- + H^+ \quad [23]$$

$$\equiv SOH^0 + K^+ = \equiv SO^- - K^+ + H^+ \quad [24]$$

$$\equiv SOH^0 + H^+ + NO_3^- = \equiv SOH_2^+ - NO_3^- \quad [25]$$

$$\equiv SOH^0 + H^+ + Sb(OH)_6^- = \equiv SOH_2^+ - Sb(OH)_6^- \quad [26]$$

$$\equiv SOH^0 + H^+ + Sb(OH)_6^- = \equiv SOHSb(OH)_5^0 + H_2O \quad [27]$$

$$\equiv SOH^0 + Sb(OH)_6^- = \equiv SOSb(OH)_5^- + H_2O \quad [28]$$

$$2{\equiv}SOH^0 + Sb(OH)_6^- = (\equiv SO)_2Sb(OH)_4^- + 2H_2O \quad [29]$$

where $\equiv SOH^0$ represents a singly-coordinated, reactive surface hydroxyl site bound to metal ion *S* on the mineral surfaces (*S* = Al^{3+} on gibbsite and kaolinite; Fe^{3+} on goethite; or Mn^{4+} on birnessite). Equations [22] and [23] represent the surface protonation and deprotonation reactions that are responsible for the development of intrinsic surface charge. The outer-sphere surface complexation of ions from the background electrolyte is described in Eqs. [24] and [25]. The outer-sphere retention of Sb(V) is described by Eq. [26], where a water molecule (not shown) is present between the surface function group and adsorbed $Sb(OH)_6^-$. Equations [27] and [28] describe the monodentate-mononuclear inner-sphere surface complexation of Sb(V) where no water is present between the surface function group and adsorbed $Sb(OH)_6^-$. Equation [29] describes the bidentate-binuclear inner-sphere surface complexation of Sb(V). The location of the various adsorbed species on the mineral surfaces is depicted in Fig. 3.

The intrinsic equilibrium constants for the surface complexation reactions are:

$$K_{+}^{\text{int}} = \frac{[\equiv SOH_2^+]}{[\equiv SOH^0](H^+)} \exp\left(\frac{F\psi_{(0)}}{RT}\right) \quad [30]$$

$$K_{-}^{\text{int}} = \frac{[\equiv SO^-](H^+)}{[\equiv SOH^0]} \exp\left(\frac{-F\psi_{(0)}}{RT}\right) \quad [31]$$

$$K_{K^+}^{\text{int}} = \frac{[\equiv SO^- - K^+](H^+)}{[\equiv SOH^0](K^+)} \exp\left(\frac{F(\psi_{os} - \psi_{(0)})}{RT}\right) \quad [32]$$

$$K_{NO_3^-}^{\text{int}} = \frac{[\equiv SOH_2^+ - NO_3^-]}{[\equiv SOH^0](H^+)(NO_3^-)} \exp\left(\frac{F(\psi_{(0)} - \psi_{os})}{RT}\right) \quad [33]$$

$$K_{Sb(OH)_6^-}^{\text{int, os}} = \frac{[\equiv SOH_2^+ - Sb(OH)_6^-]}{[\equiv SOH^0](H^+)(Sb(OH)_6^-)} \exp\left(\frac{F(\psi_{(0)} - \psi_{os})}{RT}\right) \quad [34]$$

$$K_{Sb(OH)_6^-}^{\text{int, is1}} = \frac{[\equiv SOHSb(OH)_5^0]}{[\equiv SOH^0](H^+)(Sb(OH)_6^-)} \quad [35]$$

$$K_{Sb(OH)_6^-}^{\text{int, is2}} = \frac{[\equiv SOSb(OH)_5^-]}{[\equiv SOH^0](Sb(OH)_6^-)} \exp\left(\frac{-F\psi_{(0)}}{RT}\right) \quad [36]$$

$$K_{Sb(OH)_6^-}^{\text{int, is3}} = \frac{[(\equiv SO)_2Sb(OH)_4^-]}{[\equiv SOH^0]^2(Sb(OH)_6^-)} \exp\left(\frac{-F\psi_{(0)}}{RT}\right) \quad [37]$$

The total number of surface functional groups (mass balance) is:

$$[\equiv SOH]_T = [\equiv SOH^0] + [\equiv SOH_2^+] + [\equiv SO^-] + [\equiv SO^- - K^+] + [\equiv SOH_2^+ - NO_3^-] + [\equiv SOH_2^+ - Sb(OH)_6^-] + [\equiv SOHSb(OH)_5^0] + [\equiv SOSb(OH)_5^-] + 2[(\equiv SO)_2Sb(OH)_4^-] \quad [38]$$

which is also related to the surface site density (N_s, site nm^{-2}) by:

$$[\equiv SOH]_T = \frac{N_S S a 10^{18}}{N_A} \quad [39]$$

where S is the surface area in m^2 g^{-1}, a is the solid-to-solution ratio (g L^{-1}), and N_A is Avogadro's number (site mol^{-1}). The charge balance relationships are:

$$\sigma_0 + \sigma_{os} + \sigma_d = 0 \quad [40]$$

$$\sigma_0 = [\equiv SOH_2^+] - [\equiv SO^-] - [\equiv SO^- - K^+] + [\equiv SOH_2^+ - NO_3^-] + [\equiv SOH_2^+ - Sb(OH)_6^-] - [\equiv SOSb(OH)_5^-] - [(\equiv SO)_2Sb(OH)_4^-] \quad [41]$$

$$\sigma_{os} = [\equiv SO^- - K^+] - [\equiv SOH_2^+ - NO_3^-] - [\equiv SOH_2^+ - Sb(OH)_6^-] \quad [42]$$

where the relationships between the surface charge (σ) and surface potential (ψ) components are described in Eqs. [20] and [21]. Surface complexation models that describe the adsorption of phosphate and sulfate by the variable-charge minerals were developed similarly to that for Sb(V) by modifying Eqs. [26] through [29] and [34] through [42].

Surface complexation constants (log K^{int} values; Eqs. [34] through [37]) for the specified ligand adsorption reactions (Eqs. [26] through [29]) were optimized by FITEQL using the adsorption edge data (q vs. pH) at the two ionic strengths. Unless noted otherwise, the intrinsic constants were optimized for both ionic strength conditions simultaneously. A goodness-of-fit parameter is calculated by FITEQL and defined as the weighted sum of squares of residuals divided by the degrees of freedom (V_Y). This parameter incorporates the overall variance associated with the model predictions and the standard deviation in the experimental data (analytical error). Generally, the V_Y ranges between 0.1 and 20 when the user-defined chemical model adequately describes the ligand adsorption edge (when using the FITEQL default error parameters). The goal of the modeling was to find a chemical model for each ligand-mineral combination with the least number of surface species (simplest model) that generated the lowest values of V_Y, that was applicable to both ionic strength conditions, and that was consistent with the mechanistic interpretations of the experimental data.

Table 1. Solid and suspension properties used in the 2-pK_a triple layer surface complexation modeling of $Sb(OH)_6$, SO_4, and PO_4 adsorption by gibbsite, kaolinite, goethite, and birnessite.

	Mineral			
Parameter	Gibbsite	Kaolinite	Goethite	Birnessite
Formula	$Al(OH)_3$	$Al_2Si_2O_5(OH)_4$	FeOOH	MnO_2
Particle size, μm†				
Mean	2.55	2.94	3.59	ND
Median	2.06	1.95	3.15	ND
Mode	3.06	1.92	4.05	ND
Surface area, $m^2\ g^{-1}$‡	5.82	13.08	34.25	46.30
Site density, nm^{-2}§	8.0	0.55 (≡AlOH) 0.27 (≡SiOH)	3.45	12.5
Total site concentration, mmol L^{-1}¶	0.7732	0.1195 (≡AlOH) 0.0587 (≡SiOH)	0.98	4.805
Inner-layer capacitance, F m^{-2}§	1.1	1.0	0.905	2.4
Outer-layer capacitance, F m^{-2}§	0.2	0.2	0.2	0.2
Suspension density, g L^{-1}	10	10	5	5

†Laser diffraction; ND, not determined.

‡BET-N_2 gas adsorption.

§Site density and capacitance data from Catts and Langmuir (1986), Geelhoed et al. (1997), Sahai and Sverjensky (1997), and He et al. (1997).

¶Computed using Eq. [39].

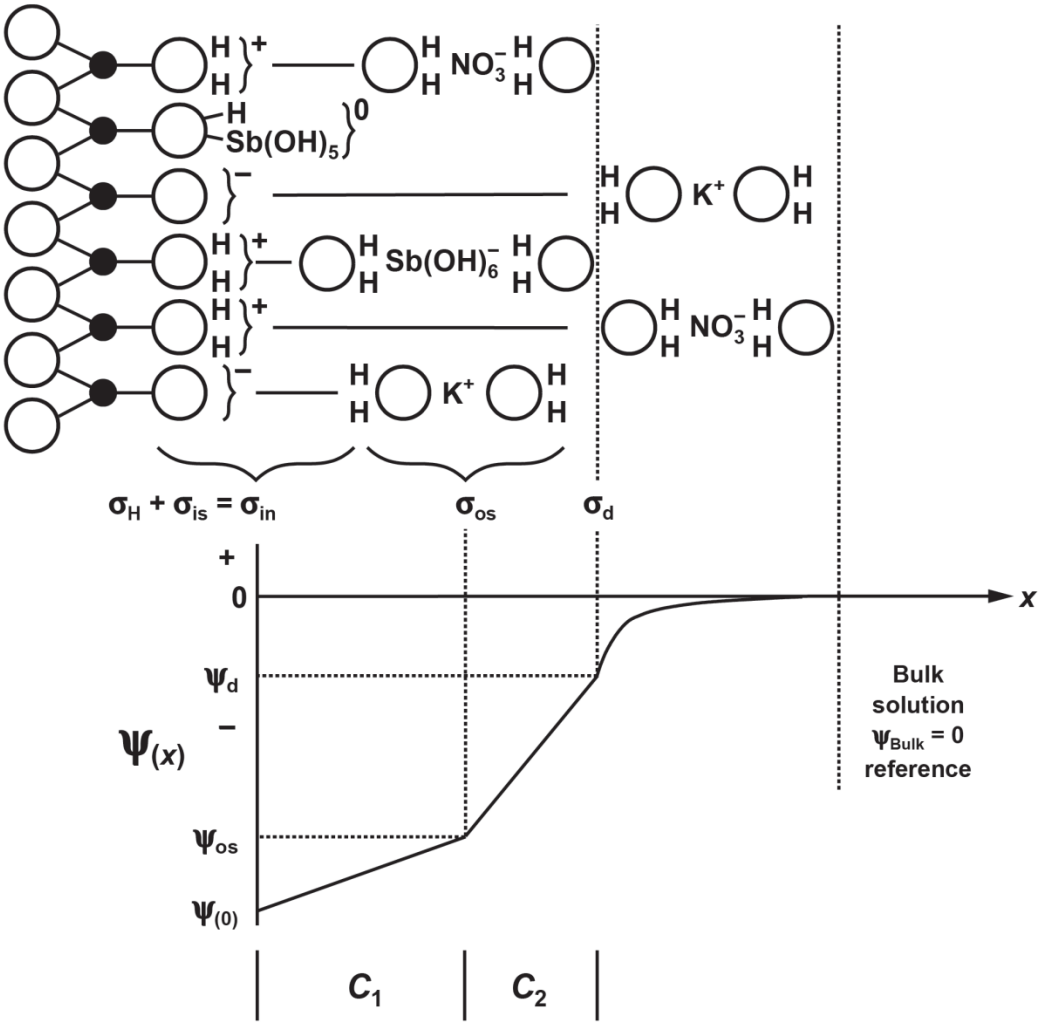

Figure 3. The solid-solution interface of a generic hydrous metal oxide surface as described by the triple layer surface complexation model. The top figure illustrates the location of inner-sphere surface species (e.g., $\equiv SOHSb(OH)_5^0$) that contribute to σ_{in}, and outer-sphere surface species (e.g., $\equiv SOH_2^+ – Sb(OH)_6^-$) that contribute to σ_{os}. The bottom figure illustrates the distribution of surface charge (ψ values) in the solid-solution interface (modified from Essington, 2003).

Table 2. Surface complexation and aqueous speciation reactions used in the 2-pK_a triple layer surface complexation modeling of $Sb(OH)_6$, SO_4, and PO_4 adsorption by gibbsite, kaolinite, goethite, and birnessite.

	log K^{int}†				
	Gibbsite	Kaolinite		Goethite	Birnessite
Surface complexation reaction	*S* = Al	*S* = Al	*S* = Si	*S* = Fe	*S* = Mn
$\equiv SOH^0 + H^+ = \equiv SOH_2^+$	8.50	7.89	2.00	7.00	–1.60
$\equiv SOH^0 = \equiv SO^- + H^+$	–12.50	–9.05	–6.80	–12.60	–5.60
$\equiv SOH^0 + H^+ + NO_3^- = \equiv SOH_2^+–NO_3^-$	7.50	7.90		8.97	1.24
$\equiv SOH^0 + K^+ = \equiv SO^–K^+ + H^+$	–13.50	–9.20	–3.50	–10.29	–2.34

Aqueous speciation reaction	log *K*‡
$Sb(OH)_6^- + H^+ = Sb(OH)_5^0 + H_2O$	2.85
$PO_4^{3-} + H^+ = HPO_4^{2-}$	12.35
$PO_4^{3-} + 2H^+ = H_2PO_4^-$	19.55
$PO_4^{3-} + 3H^+ = H_3PO_4^0$	21.70
$PO_4^{3-} + K^+ = KPO_4^{2-}$	1.37
$PO_4^{3-} + H^+ + K^+ = KHPO_4^-$	12.94
$PO_4^{3-} + 2H^+ + K^+ = KH_2PO_4^0$	19.97
$SO_4^{2-} + H^+ = HSO_4^-$	1.99
$SO_4^{2-} + K^+ = KSO_4^-$	0.85

†He et al. (1997) and Sahai and Sverjensky (1997).
‡Data from May and Murry (1991), Martell et al. (2004), and Accornero et al. (2008).

Results and Discussion

The only process in soils and sediments that restricts the mobility and bioaccessibility of antimony(V) (antimonate) is adsorption. Several experiments were performed to investigate the adsorption of antimonate by environmentally-relevant minerals as a function pH, ionic strength, antimonate concentration, temperature, and in the presence of competing anions. In addition to providing a characterization of antimonate adsorption behavior, the results may be interpreted to provide information on the mechanism of antimonate retention. The results are also used to develop chemical models that may be employed to predict antimonate behavior in chemically complex environments, such as soils and sediments. The experiments are briefly described below, as are how the results are interpreted to indicate retention mechanisms.

Antimonate ($Sb(OH)_6^-$) adsorption by gibbsite and kaolinite (≡AlOH groups), goethite (≡FeOH groups), and birnessite (≡MnOH groups) was examined as a function of pH and background electrolyte concentration (ionic strength, controlled by KNO_3). Adsorption as a function of pH (adsorption edge) can indicate the adsorption mechanism. Additional evidence can be gained by examining the influence of ionic strength on the adsorption edge. For outer-sphere complexation (anion exchange), increasing the ionic strength will decrease adsorption, as the counterions in the background electrolyte compete with antimonate for adsorption sites.

However, ionic strength will have little effect on inner-sphere adsorption (ligand exchange) because this mechanism involves the direct coordination of the ligand to a surface metal cation. In addition to examining the influence of pH and ionic strength on antimonate retention, adsorption reversibility is initiated by changing the pH of systems at equilibrium. An upward shift in pH should result in the release of adsorbed antimonate. It is hypothesized that hysteretic desorption behavior (antimonate is not released from the surface) connotes strong covalent (inner-sphere) bonding, while reversible and non-hysteretic desorption indicates weak, electrostatic (outer-sphere adsorption). The adsorption edge data are also required for the development of chemical models that predict adsorption behavior.

In addition to nitrate, which is a counter ion in the background electrolyte, sulfate and phosphate are common ligands in soils and sediments. These ligands will compete with antimonate for adsorption sites on hydrous metal oxyhydroxides, potentially enhancing antimonate mobility and bioaccessibility. The competitive effects of sulfate and phosphate on antimonate adsorption by gibbsite, kaolinite, goethite, and birnessite were examined as a function of pH, ionic strength, and the order of ligand addition in the binary systems. Competition for adsorption sites depends on a number of factors, including the relative affinities of the competing ligands for the surface, and the concentration of reactive surface sites. The reduction in antimonate retention when in competition with sulfate or phosphate may result from the direct competition for adsorption sites (competing inner-sphere ligands and a low abundance of sites) or from electrostatic effects of the change in surface charge that arises from the specific adsorption of sulfate or phosphate (high site abundance and outer-sphere antimonate retention).

The adsorption of antimonate by gibbsite, kaolinite, and goethite was examined as a function of concentration, temperature, and pH. Adsorption as a function of concentration (adsorption isotherm) is generally employed as a descriptive tool. The adsorption isotherm is a graph that relates the adsorbed concentration antimonate (the surface excess) to its concentration in the equilibrating solution. The isotherm is described mathematically using an adsorption isotherm model, such as the Langmuir equation, which provides a measure of the capacity of an adsorbent to retain antimonate (an adsorption maximum), as well as an adsorption intensity parameter. Because isotherm models are descriptive, they do not allow for a mechanistic interpretation. However, the intensity and capacity parameter may be combined, resulting in an adsorption constant. In the case of the Langmuir equation, the adsorption constant represents the slope of the isotherm at infinite dilution (as the surface excess approaches zero). The variation in the adsorption constant as a function of temperature can provide a general indication of adsorption mechanism; whether inner-sphere or outer-sphere complexation predominates. When the adsorption constant increases with increasing temperature (adsorption increases with temperature), the adsorption process is endothermic (heat is absorbed during adsorption), and inner-sphere complexation is indicated. When the adsorption constant decreases with increasing temperature (adsorption decreases with temperature), the process is exothermic (heat is released during adsorption), and outer-sphere complexation is indicated.

The surface charge characteristics of the hydrous metal oxyhydroxides were examined using electrophoretic mobility and proton adsorption as a function of pH, ionic strength, and the background electrolyte composition. The hydrous metal oxyhydroxides develop surface charge via protonation and deprotonation reactions, and through the specific adsorption of metals and ligands. The inner-sphere complexation of antimonate (an anion) will shift the surface charge of a mineral to more negative values (at a fixed pH), as well as shift the point of zero charge of the mineral to a lower value. Additionally, proton adsorption will increase to satisfy the additional

negative surface charge. Conversely, the outer-sphere complexation of antimonate will not influence the surface charging characteristic.

Surface complexation modeling employs a defined group of surface complexation and aqueous speciation reactions, coupled with a model of the electrostatics of the solid-solution interface, to predict an antimonate adsorption edge. The surface complexation reactions are formulated in accordance with the experimental results and interpretations (as described above). Ancillary information, such as spectroscopic evidence from the literature, may also be employed to aid in model development. A fitting routine is then used to optimize the adsorption reaction equilibrium constants and fit the predicted adsorption to the experimental adsorption edge. In general, the chemical model that provides the superior fit to the experimental data is assumed to be correct. The chemical models developed for single ligand systems are then tested by applying to binary ligand (antimonate-sulfate and antimonate-phosphate) adsorption edge data.

The antimonate adsorption results are described and discussed for each mineral separately. This is necessary because the surface reactivity of each mineral, the types and concentrations of reactive surface functional groups, the affinity of antimonate for the surfaces, and the types of surface complexes formed vary with mineral type. Further, experimental design was necessarily modified to account for these varying mineral characteristics. Therefore, the direct comparison of results between minerals is not recommended unless identical experimental conditions were employed.

Gibbsite

Adsorption Edge: Reversibility

The adsorption of antimonate by gibbsite is dependent on solution pH and ionic strength (Fig. 4). Antimonate adsorption is at a relative maximum in strongly acidic environments (pH < 4), and decreases with increasing pH to a minimum in strongly alkaline conditions (pH > 9). Increasing the ionic strength (KNO_3 concentration) depresses antimonate retention by gibbsite; primarily in the pH < 7 range (Fig. 5). Varying the adsorption and desorption equilibration periods (0.67 h to 2 h for adsorption and 2 h to 8 h for desorption) did not influence antimony retention in a consistent manner (i.e., increasing retention with increasing equilibration period). Indeed, the variance in antimonate retention displayed in Fig. 4 for differing equilibration periods is similar to that observed for replicate studies for a single equilibration period (Fig. 5). These findings suggest that antimonate adsorption equilibrium is achieved at a period of less than 1 h, consistent with the available literature for antimonate retention by soil and metal oxides (Ambe, 1987; Xi et al., 2010; Wang et al., 2012; Kameda et al., 2012; Fan et al., 2013). The pH-dependence of antimonate adsorption is similar to the observed by other investigators (Ambe et al., 1986; Ambe, 1987; Xu et al., 2001; Biver et al., 2011; Rakshit et al., 2011; Ilgen and Trainor, 2012), and for other anions (Essington, 2003). Increasing antimonate retention with decreasing pH is consistent with both inner-sphere and outer-sphere adsorption mechanisms. Increasing the proton concentration (decreasing pH) results in the protonation of reactive surface functional groups and generates positive surface charge:

$$\equiv AlOH^0 + H^+ = \equiv AlOH_2^+ \qquad [43]$$

Anions are then electrostatically attracted to the surface to form an outer-sphere surface complex (anion exchange):

$$\equiv AlOH_2^+ – NO_3^- + Sb(OH)_6^- = \equiv AlOH_2^+ – Sb(OH)_6^- + NO_3^- \quad [44]$$

Conversely, surface protonation generates surface-bound water, which may then be displaced by an adsorbate ligand to form an inner-sphere surface complex (ligand exchange):

$$\equiv AlOH_2^+ + Sb(OH)_6^- = \equiv AlOSb(OH)_5^- + H_2O + H^+ \quad [45]$$

All soluble anions may participate in anion exchange; however, only anions that are formed by weak acid dissociation may participate in ligand exchange (Essington, 2003). Because antimonate is a weak acid anion (pK_a = 2.85), inner-sphere complexation by variable-charge mineral surfaces is expected.

The decrease in antimonate adsorption by gibbsite with increasing ionic strength is not consistent with the recent findings of Rakshit et al. (2011). They observed that antimonate adsorption by gibbsite was unaffected by a one-hundred-fold change (from 0.001 *M* to 0.1 *M* KCl) in ionic strength, and concluded that antimonate retention occurred via inner-sphere mechanisms. Our findings suggest that there is weak, electrostatic character (outer-sphere adsorption) to the antimonate retention mechanism. This is evidenced by the reduction in retention when the background electrolyte concentration is increased from 0.01 *M* to 0.1 *M* KNO_3 (Fig. 5). However, the desorption edge data indicate that there is also a strong bonding component (inner-sphere adsorption) to the retention mechanism, particularly in acidic systems, consistent with the spectroscopic findings of Ilgen and Trainor (2012). As pH is increased from the minimum value of 3.5, antimonate does not readily desorb from the gibbsite surface until the solution pH exceeds approximately 6.5 (desorption is hysteretic). At pH values above 6.5, the slopes of the adsorption and desorption edges are similar, indicating that desorption becomes reversible as solution alkalinity increases (non-hysteretic). The reversibility of antimonate adsorption-desorption in the alkaline pH range was further tested by truncating the adsorption edge study to begin desorption at a pH of approximately 7 (Fig. 6). In this case, the adsorption and desorption edges are superimposed, indicating that the antimonate retention process is reversible in the alkaline range.

The adsorption-desorption edge data suggest that antimonate is retained by both strong and weak reaction mechanisms at the gibbsite surface. Strong, inner-sphere complexation mechanisms (ligand exchange) appear to predominate in acidic environments, while a weak outer-sphere mechanism (anion exchange) predominates in alkaline (although adsorption reversibility doesn't necessarily connote an outer-sphere mechanism). It is not uncommon for the predominant mechanism of ligand retention (anion versus ligand exchange) to differ as a function of soil solution properties, such as pH. For example, ligand exchange mechanisms may predominate in neutral to acidic systems, while anion exchange predominates in alkaline soils. This is the case for arsenate, molybdate, and sulfate retention by Fe- and Al-oxyhydroxides (Catalano et al., 2008; Goldberg et al., 2006; Mansour et al., 2009). It was also postulated by Leuz et al. (2006) that antimonate retention by goethite may involve greater anion exchange character when solution pH values exceed 6.

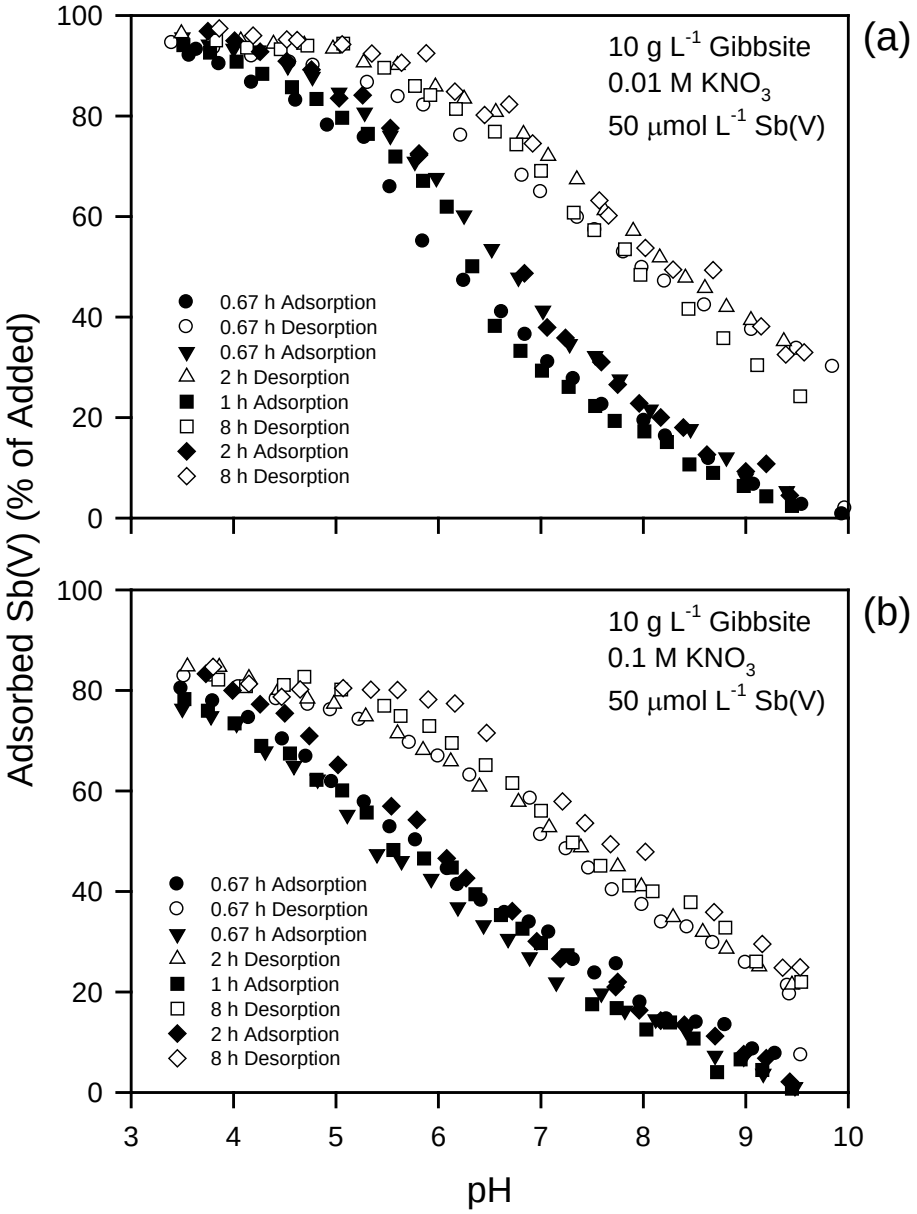

Figure 4. The adsorption and desorption of antimonate by gibbsite in (a) 10 m*M* KNO_3 and (b) 100 m*M* KNO_3 media as a function of pH and equilibration period.

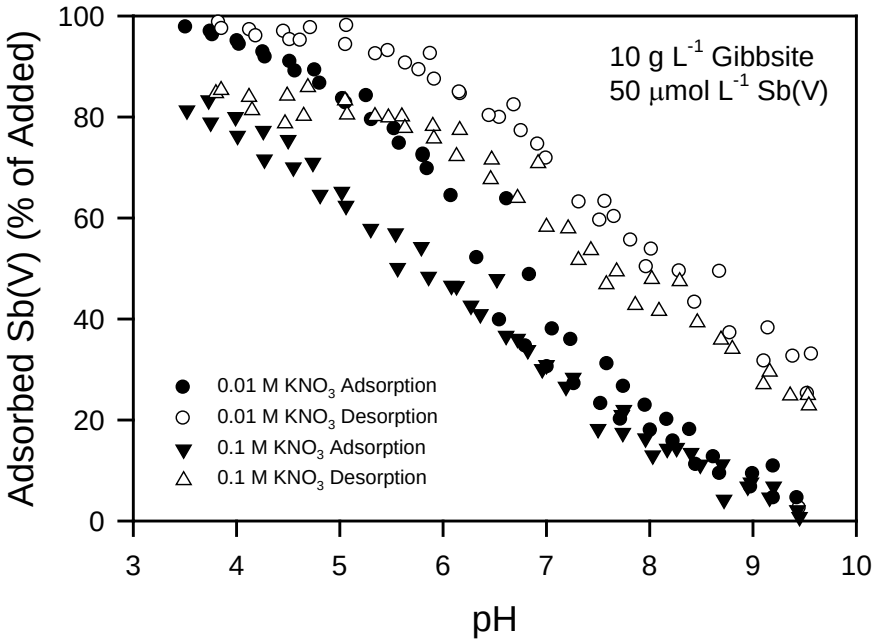

Figure 5. The adsorption and desorption of antimonate by gibbsite as a function of pH and ionic strength.

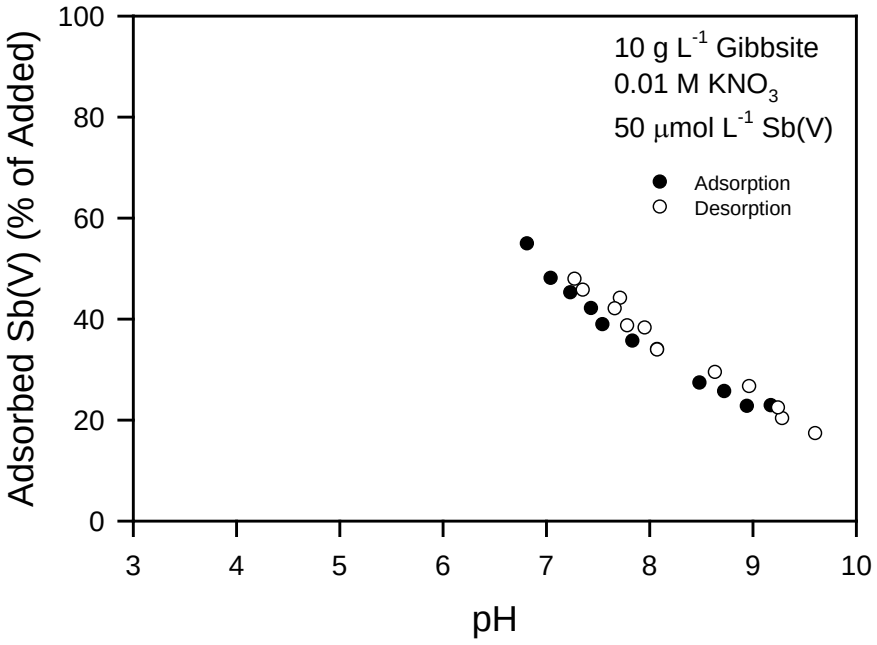

Figure 6. The adsorption and desorption of antimonate by gibbsite as a function of pH in 10 m*M* KNO_3 media. These data illustrate non-hysterestic (reversible) desorption behavior in the neutral to alkaline pH range.

The retention of sulfate and phosphate by gibbsite was examined for comparison to antimonate retention, as the mechanisms involved in the adsorption of sulfate and phosphate by hydrous Al oxyhydroxides have been well-established. Except in strongly acidic systems (pH < 4), sulfate is retained predominately by outer-sphere mechanisms (He et al., 1997; Karamalidis and Dzombak, 2010). Sulfate adsorption by gibbsite increases with decreasing pH, with a strong dependence on ionic strength (Fig. 7a). In addition, sulfate adsorption is reversible throughout the entire pH range studied (non-hysteretic; the adsorption and desorption edges overlap), differing from the desorption behavior of antimonate (Fig. 4). These findings are consistent with an anion exchange mechanism and the weak, electrostatic retention of sulfate. Sulfate retention is also depressed, relative to that of antimonate, throughout the entire pH range studied and particularly in the higher ionic strength systems (Fig. 8). Despite their similar acid pK_a values (1.99 for sulfate and 2.85 for antimonate; Table 2), the retention of antimonate by gibbsite is greater than that of sulfate, less affected by ionic strength, and hysteretic.

Phosphate is retained by inner-sphere surface complexation mechanisms throughout a broad pH range (Karamalidis and Dzombak, 2010). Phosphate is strongly retained by gibbsite (Fig. 7b) and shows no dependence on ionic strength, an observation that is consistent with the ligand exchange adsorption mechanism. Further, phosphate retention exceeds that of both antimonate and sulfate (Fig. 8). Phosphate adsorption is reversible in strongly alkaline systems (Fig. 7b), owing to the competitive effects of the hydroxide ion. The reversibility of phosphate adsorption in slightly alkaline to acidic systems could not be evaluated due to the strong and complete retention in this pH range.

Adsorption Edge: Competition

The adsorption of antimonate, sulfate, and phosphate by gibbsite in the batch systems (Fig. 9) is similar to that observed in the continuous titration (beaker) systems (Figs. 5 and 7). Ligand adsorption increases with decreasing pH, the retention of antimonate and sulfate decreased with increasing ionic strength, and the adsorption of phosphate is not influenced by the ionic media. Sulfate adsorption is less than that of antimonate throughout the pH 3 to 10 range, irrespective of ionic strength, and phosphate adsorption is complete at pH values below approximately 7.

The influence of ligand competition on the adsorption edge of antimonate, sulfate, and phosphate on gibbsite is quantitatively described by the equation (Essington, 2003):

$$q_{\%} = \frac{q_{\max}}{\{1 + \exp[-b(\mathrm{pH} - \mathrm{pH}_{50})]\}} \qquad [46]$$

where $q_{\%}$ is the adsorbed ligand concentration (expressed as a percentage of the total added), $q_{\max}$ is the adsorption maximum (as a percentage of the total), pH_{50} is the pH at which 50% of $q_{\max}$ is obtained, and b indicates the slope of the adsorption edge at pH_{50}. The influence of ionic strength on the adsorption of antimonate is primarily observed in the neutral to acidic pH range (Fig. 9a), where retention is decreased by approximately 10 % at $q_{\max}$ by increasing KNO_3 concentration. The application of Eq. [46] also demonstrates this finding (Table 4), as well as a 0.2 pH unit negative shift in the adsorption edge (pH_{50} value). The sulfate adsorption maximum is not influenced by ionic strength (Fig. 9b and Table 4); however, the adsorption edge shifts in the negative direction by approximately 1 pH unit (from 6.36 to 5.34) with increasing KNO_3

concentration. Neither the phosphate adsorption maximum nor the adsorption edge is influenced by the ionic medium (Fig. 9c and Table 5).

The inclusion of sulfate as a competing ligand reduces the retention of antimonate by gibbsite in the 0.01 *M* KNO_3 systems (Fig. 10a), but not in 0.1 *M* KNO_3 (Fig. 10b). In the low ionic strength systems, the addition of sulfate following the preadsorption of antimonate (preadsorbed Sb(V), S added) and the addition of sulfate and antimonate simultaneously (direct competition) results in an approximate 10 % reduction in antimonate adsorption by gibbsite at q_{max} (relative to antimonate adsorption without the addition of sulfate) (Fig 10a). However, the adsorption edge (pH_{50}) is not affected, remaining at approximately 6.9 (Table 4). The preadsorption of sulfate prior to the addition of antimonate decreases antimonate adsorption by approximately 20 % at q_{max}, relative to adsorption without sulfate. Correspondingly, the adsorption edge shifts to a lower value by approximately 0.4 pH units (from 6.9 to 6.5). Sulfate adsorption is reduced in both the preadsorbed antimonate and sulfate ligand systems, relative to adsorption in the absence of antimonate (Figs. 11a and b), as indicated by a negative shift in pH_{50} (from 6.4 to approximately 5.5) in 0.01 *M* KNO_3, and a reduction in q_{max} in 0.1 *M* KNO_3 (from 93.5 % to 57.2 % adsorbed) (Table 4). When added simultaneously, antimonate has only a minor impact on sulfate adsorption in 0.01 *M* KNO_3. Antimonate has a more pronounced impact on sulfate adsorption in the high ionic strength systems (Fig. 11b). In general, the impact of sulfate on antimonate adsorption by gibbsite is more pronounced in 0.01 *M* KNO_3, while that of antimonate on sulfate was more prominent in 0.1 *M* KNO_3.

The competitive adsorption findings indicate that antimonate and sulfate compete for adsorption sites on the gibbsite surface, and that the competitive effect is a function of the ionic environment (ionic strength and nitrate concentration) and the initial occupation of the adsorbed phase (preadsorbed ligand versus direct competition). The data suggest that both sulfate and antimonate participate in an inner-sphere surface complexation process in strongly acidic environments. This is evidenced for antimonate by the hysteretic desorption behavior in acidic systems (Fig. 5). If sulfate retention were solely outer-sphere in nature, the impact on antimonate adsorption would be negligible, as the concentration of reactive surface functional groups (773 μmol L^{-1}) far exceeds the concentration of added antimonate and sulfate (~ 100 μmol L^{-1}). The influence of sulfate on antimonate retention would be masked by the ionic strength effect (50 μmol L^{-1} sulfate versus 10 to 100 mmol L^{-1} nitrate). Further, the observation that antimonate has difficulty displacing preadsorbed sulfate also suggest an inner-sphere component to sulfate retention.

The inclusion of phosphate as a competing ligand reduces the retention of antimonate by gibbsite in both the 0.01 *M* KNO_3 and 0.1 *M* KNO_3 systems (Fig. 12). In the low ionic strength systems, the addition of phosphate shifts the antimonate adsorption edge (pH_{50}) from 6.88 to 6.18 in the preadsorbed antimonate system, and to approximately 5.3 in the preadsorbed phosphate and direct competition systems (indicating the antimonate is slightly more competitive with phosphate when preadsorbed). In the 0.1 *M* KNO_3 medium, phosphate has minimal impact on antimonate q_{max}; however, the adsorption edge is shifted from 6.67 to 5.43 in preadsorbed phosphate, and to 5.22 in direct competition. Phosphate adsorption by gibbsite is not influenced by antimonate (Fig. 13). The impact of phosphate relative to that of sulfate on antimonate adsorption by gibbsite in the direct competition systems is shown in Fig. 14.

The competitive adsorption findings indicate that phosphate is strongly preferred by the gibbsite ligand exchange sites, relative to antimonate. The inner-sphere complexation of phosphate species contributes negative charge to the gibbsite surface, reducing the outer-sphere

(electrostatic) complexation of antimonate. Greater proton concentration (lower pH) is required to overcome this effect; thus, the antimonate adsorption edge shifts to lower values. Further, only a fixed number of reactive surface functional groups are involved in the inner-sphere complexation of phosphate, as the total phosphate concentration is fixed (43 μmol L^{-1}) and phosphate adsorption is complete at pH values less than approximately 7. Thus, additional sites for the inner-sphere complexation of antimonate are created by protolysis ($\equiv AlOH_2^+$, Eq. [22]) which increases with decreasing pH, shifted the antimonate adsorption edge to lower values.

Table 3. The influence of ionic environment and competing ligand on the antimonate and sulfate adsorption maximum (q_{max}) and adsorption edge (pH_{50}) on gibbsite computed using Eq. [46].

Parameter	Ligand alone	Preadsorbed Sb(V) S added	Preadsorbed S Sb(V) added	Direct competition
		Sb(V) adsorption		
		0.01 *M* KNO_3		
q_{max} (se)†	103.6 (1.1)	96.36 (1.56)	81.06 (1.84)	90.61 (1.17)
b	–1.152	–0.832	–0.847	–0.853
pH_{50} (se)	6.88 (0.03)	6.86 (0.06)	6.50 (0.07)	6.88 (0.04)
		0.1 *M* KNO_3		
q_{max} (se)	93.13 (0.84)	107.4 (2.6)		102.9 (3.9)
b	–0.949	–0.867		–0.867
pH_{50} (se)	6.67 (0.04)	6.80 (0.08)		6.53 (0.12)
		S adsorption		
		0.01 *M* KNO_3		
q_{max} (se)	90.78 (1.55)	104.6 (3.2)	94.20 (3.29)	87.03 (1.58)
b	–1.423	–0.824	–1.047	–1.275
pH_{50} (se)	6.36 (0.05)	5.38 (0.09)	5.67 (0.09)	6.24 (0.05)
		0.1 *M* KNO_3		
q_{max}(se)	93.51 (7.52)	57.19 (5.52)		54.08 (5.75)
b	–1.086	–1.341		–1.035
pH_{50} (se)	5.34 (0.19)	5.65 (0.22)		5.39 (0.26)

†se is the standard error determined from the non-linear regression of Eq. [46] using the adsorption edge data in Figs. 10 and 11.

Table 4. The influence of ionic environment and competing ligand on the antimonate and phosphate adsorption maximum (q_{max}) and adsorption edge (pH_{50}) on gibbsite computed using Eq. [46].

Parameter	Ligand alone	Preadsorbed Sb(V) P added	Preadsorbed P Sb(V) added	Direct competition
		Sb(V) adsorption		
		0.01 *M* KNO_3		
q_{max} (se)†	103.6 (1.13)	104.7 (1.6)	99.26 (1.51)	103.4 (2.7)
b	–1.152	–1.219	–1.258	–1.122
pH_{50} (se)	6.88 (0.03)	5.99 (0.04)	5.73 (0.04)	5.59 (0.07)
		0.1 *M* KNO_3		
q_{max} (se)	93.13 (0.84)	91.84 (3.37)	97.06 (2.78)	103.0 (3.4)
b	–0.949	–1.302	–1.009	–0.855
pH_{50} (se)	6.67 (0.04)	6.18 (0.09)	5.43 (0.08)	5.22 (0.10)
		P adsorption		
		0.01 *M* KNO_3		
q_{max} (se)	98.88 (0.59)	99.08 (0.47)	97.10 (0.29)	99.59 (0.91)
b	–1.378	–1.248	–1.372	–1.218
pH_{50} (se)	9.14 (0.03)	8.88 (0.02)	8.89 (0.01)	8.87 (0.04)
		0.1 *M* KNO_3		
q_{max} (se)	100.3 (0.8)	100.1 (0.5)	99.7 (0.45)	98.35 (0.52)
b	–1.101	–1.636	–1.483	–1.590
pH_{50} (se)	9.40 (0.05)	8.54 (0.03)	8.79 (0.02)	8.69 (0.02)

†se is the standard error determined from the non-linear regression of Eq. [46] using the adsorption edge data in Figs. 12 and 13.

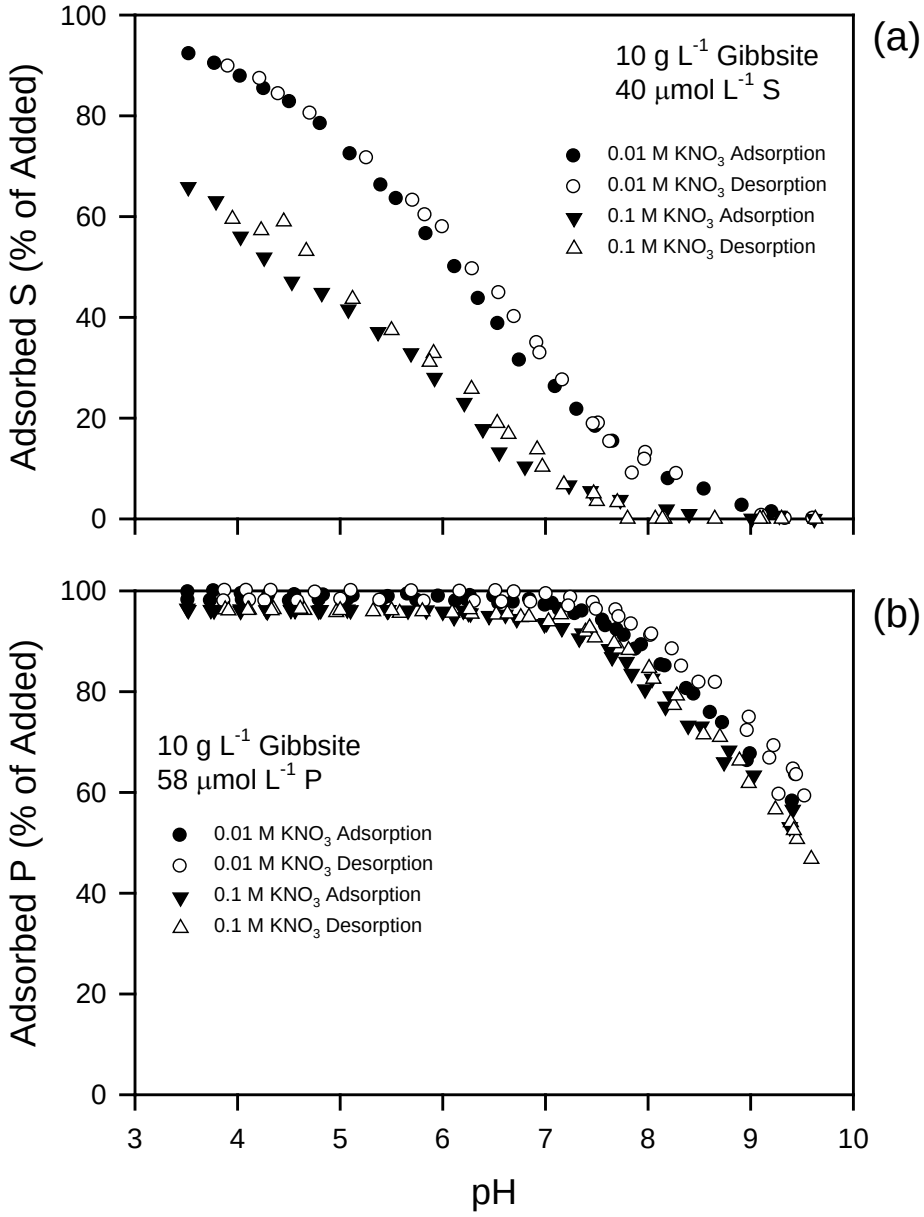

Figure 7. The adsorption and desorption of (a) sulfate and (b) phosphate by gibbsite as a function of pH and ionic strength.

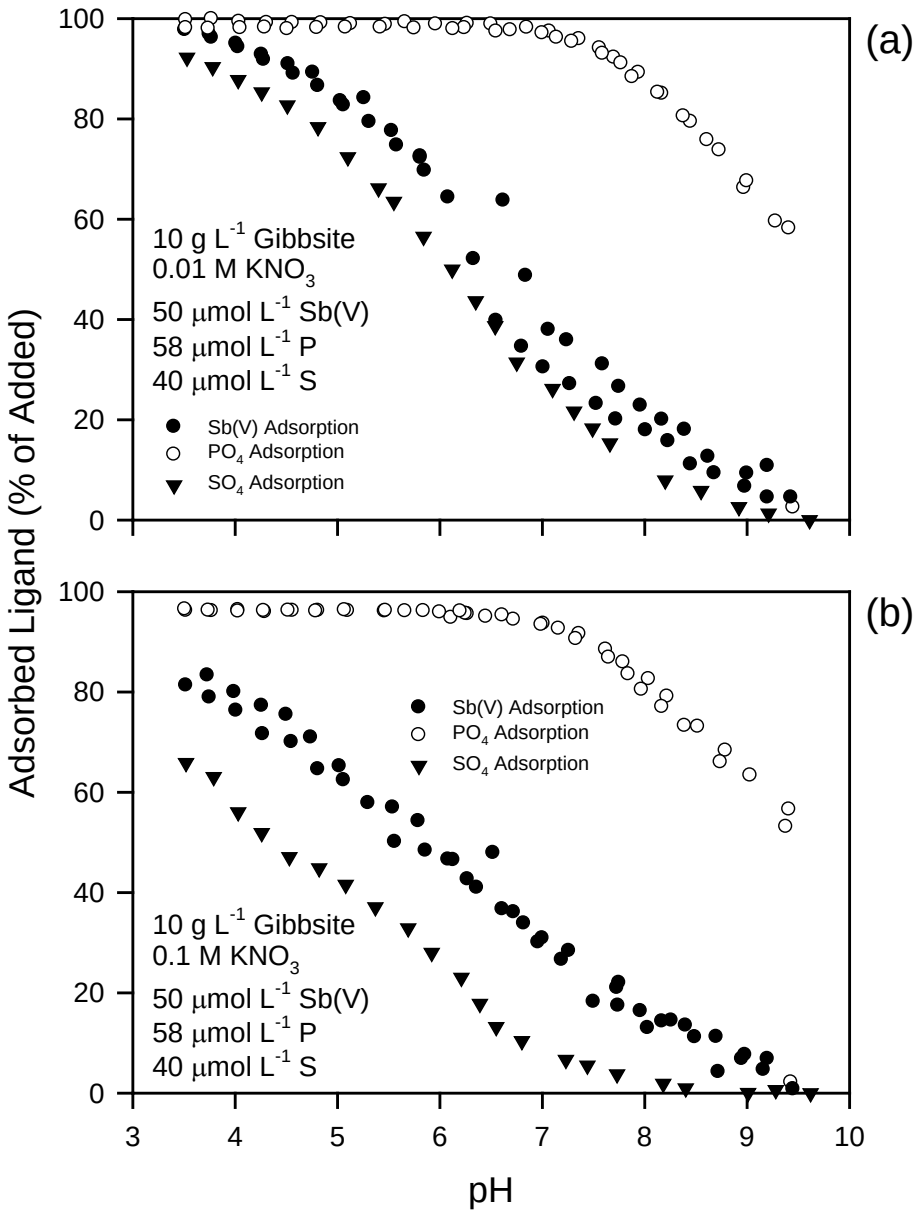

Figure 8. The adsorption antimonate, sulfate, and phosphate by gibbsite as a function of pH in (a) 10 m*M* KNO_3 and (b) 100 m*M* KNO_3 ionic media.

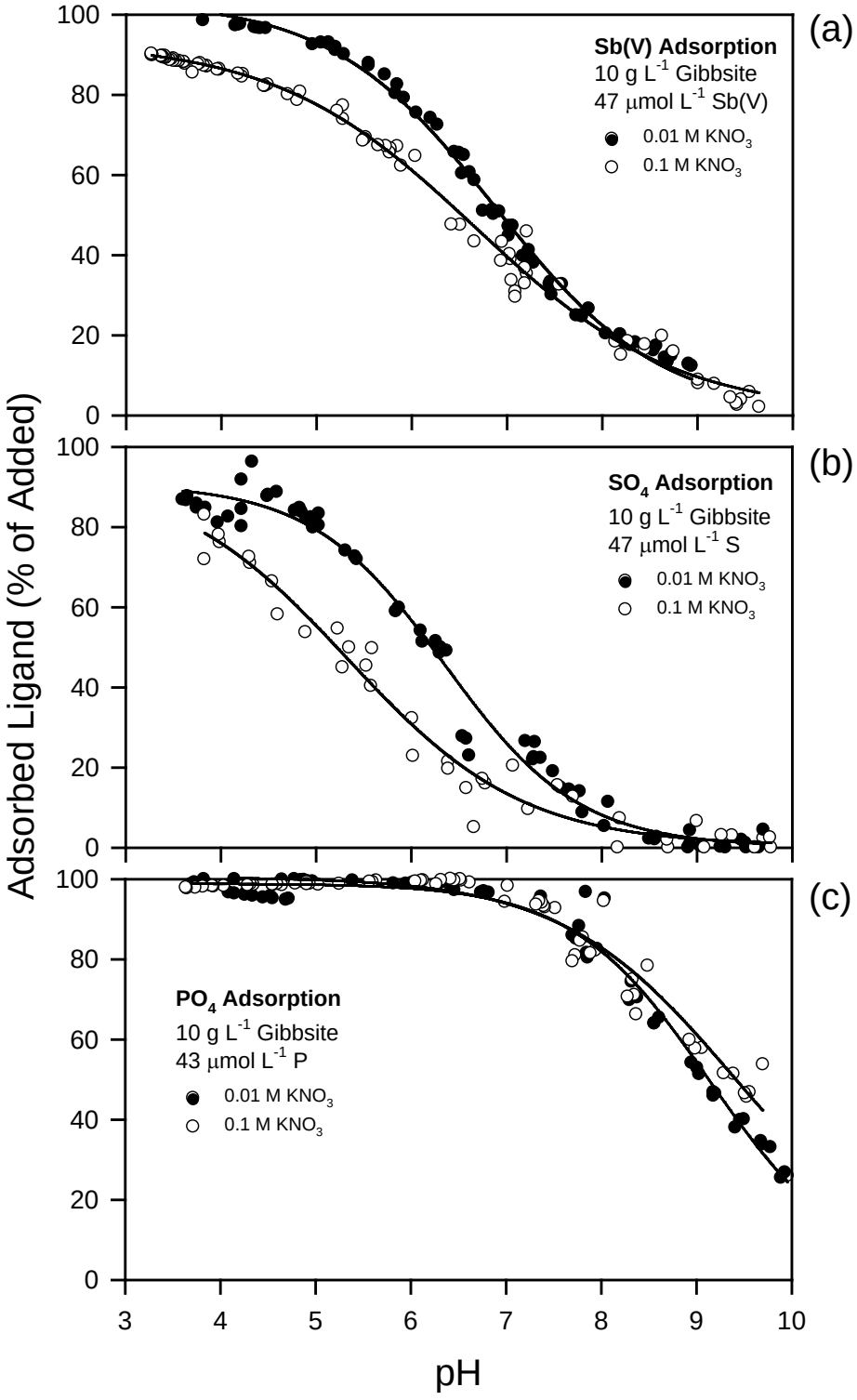

Figure 9. The adsorption of (a) antimonate, (b) sulfate, and (c) phosphate by gibbsite from batch equilibrium systems as a function of pH and ionic strength. The solid lines represent Eq. [46] using the parameters presented in Tables 3, and 4.

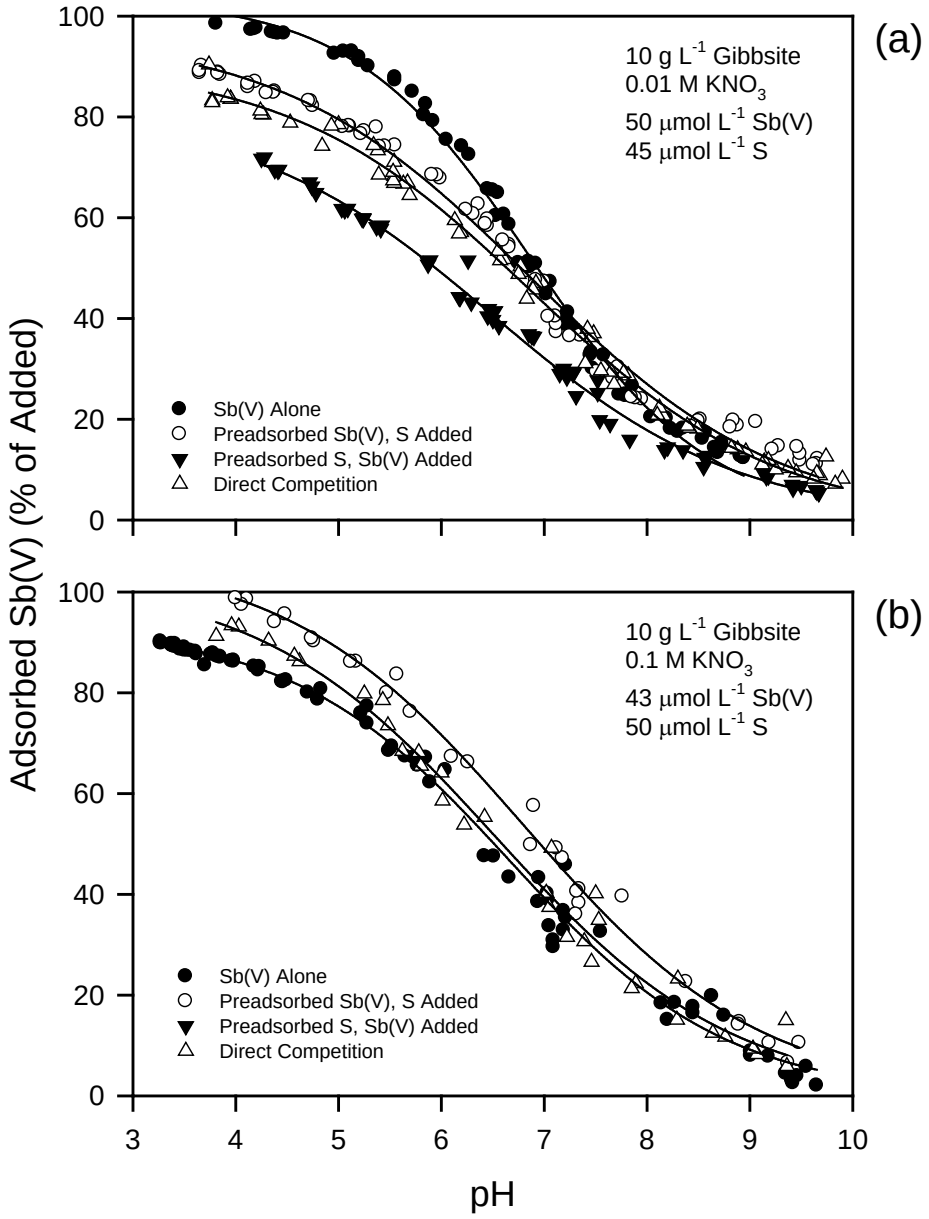

Figure 10. The competitive adsorption of antimonate by gibbsite in the presence of sulfate in (a) 10 m*M* KNO_3 and (b) 100 m*M* KNO_3 electrolyte media as a function of pH and method of sulfate addition. The solid lines represent Eq. [46] using the parameters presented in Table 3.

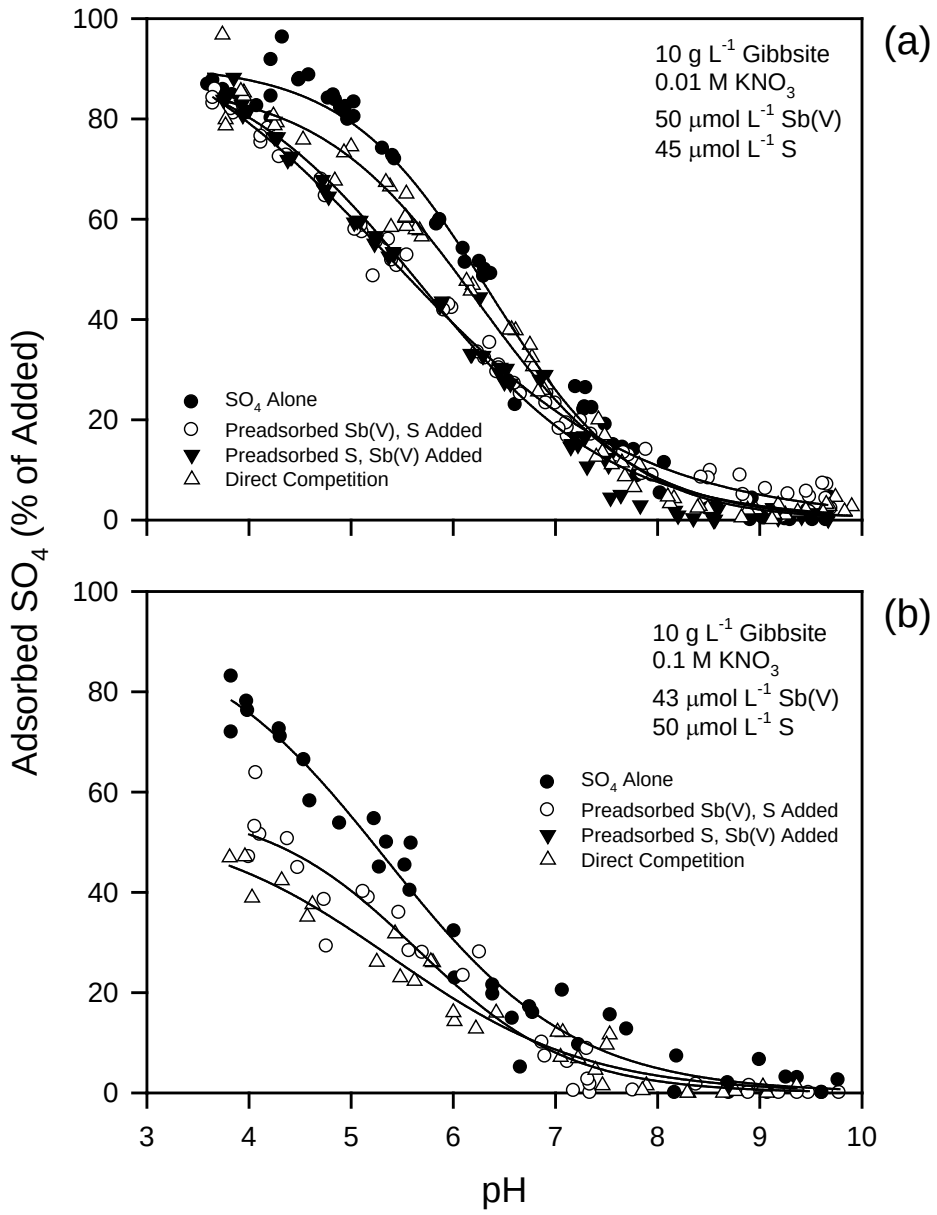

Figure 11. The competitive adsorption of sulfate by gibbsite in the presence of antimonate in (a) 10 m*M* KNO_3 and (b) 100 m*M* KNO_3 electrolyte media as a function of pH and method of antimonate addition. The solid lines represent Eq. [46] using the parameters presented in Table 3.

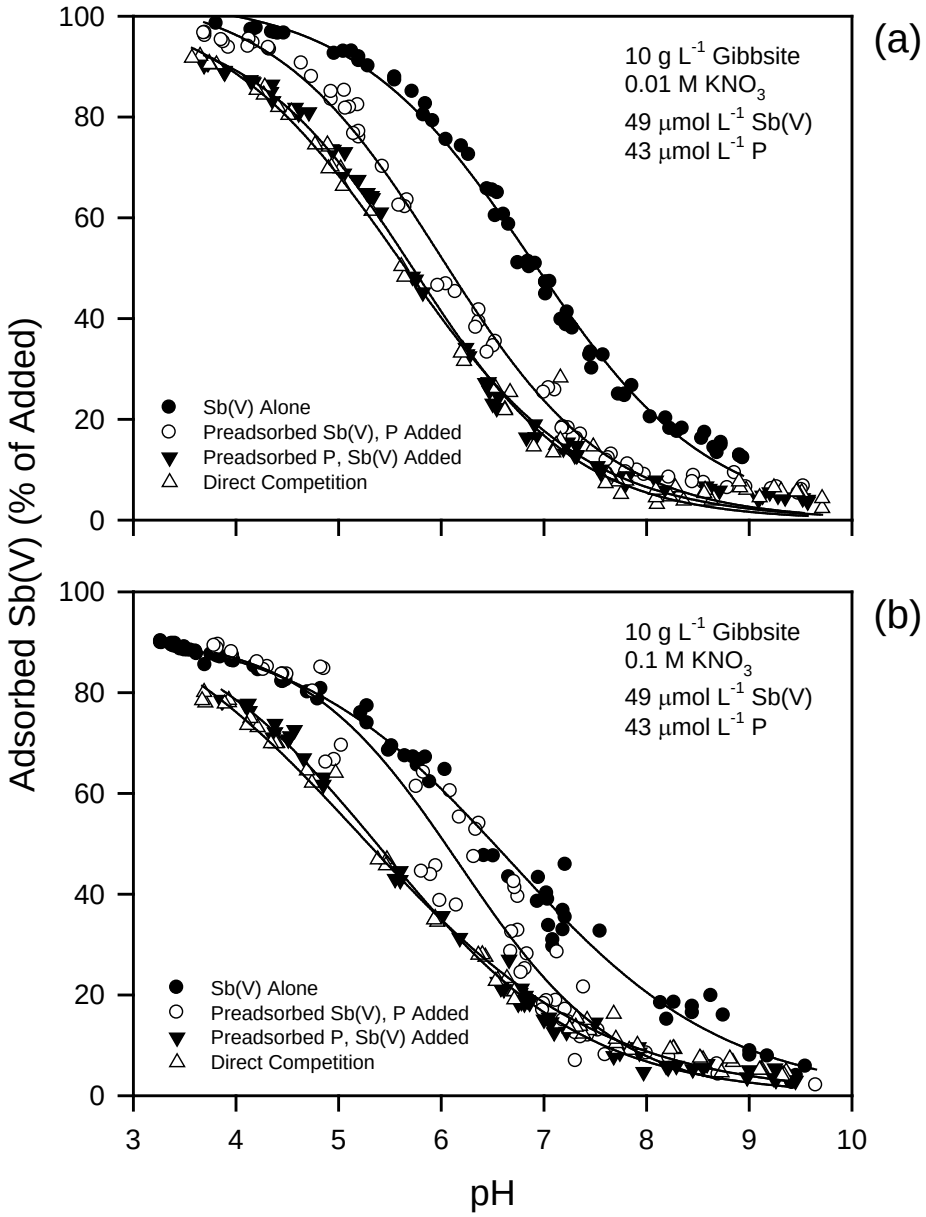

Figure 12. The competitive adsorption of antimonate by gibbsite in the presence of phosphate in (a) 10 m*M* KNO_3 and (b) 100 m*M* KNO_3 electrolyte media as a function of pH and method of phosphate addition. The solid lines represent Eq. [46] using the parameters presented in Table 4.

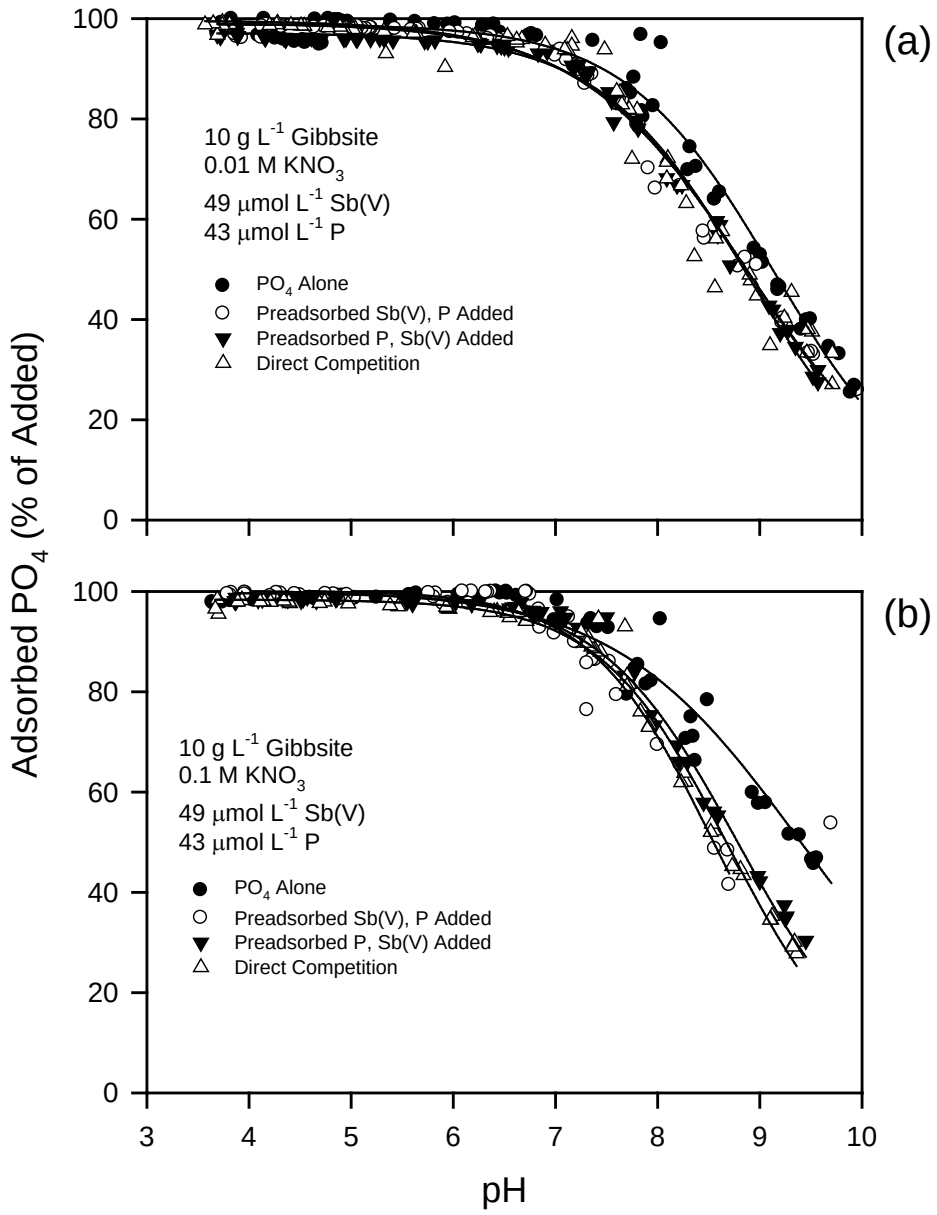

Figure 13. The competitive adsorption of phosphate by gibbsite in the presence of antimonate in (a) 10 m*M* KNO_3 and (b) 100 m*M* KNO_3 electrolyte media as a function of pH and method of antimonate addition. The solid lines represent Eq. [46] using the parameters presented in Table 4.

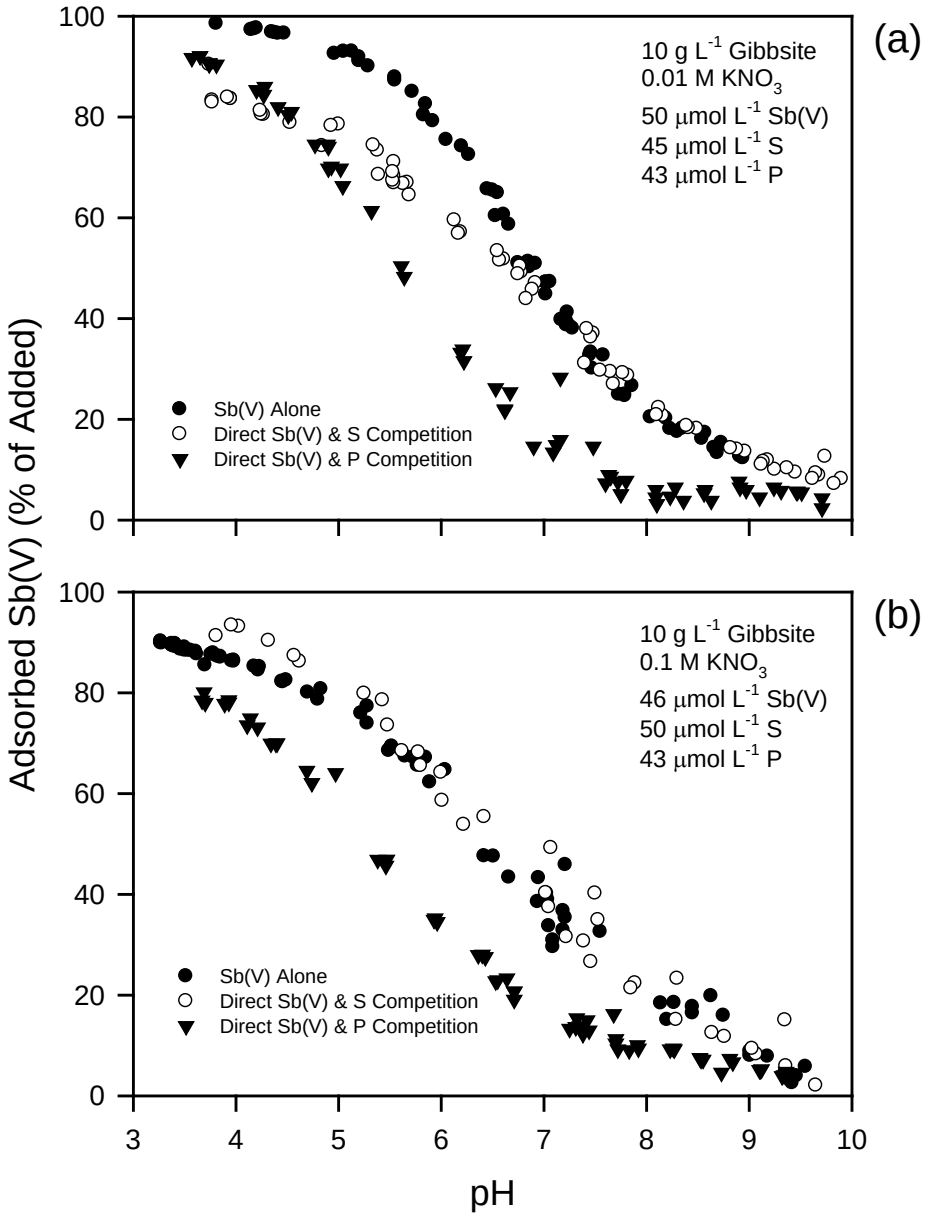

Figure 14. The competitive adsorption of antimonate by gibbsite in the presence of sulfate and phosphate in (a) 10 m*M* KNO_3 and (b) 100 m*M* KNO_3 electrolyte media as a function of pH for the direct ligand competition systems.

Adsorption Isotherms: Thermodynamics

The adsorption of antimonate by gibbsite in both pH 5.5 and 8, 0.01 *M* KNO_3 solutions is Langmuirian; adsorption intensity (isotherm slope) decreases with increasing surface coverage (Fig. 15a). The adsorption isotherms are linear in log-log space (Fig. 15b), indicating that the isotherms are appropriately described by the Freundlich isotherm model (Eq. [3]). Antimonate adsorption is strongly influenced by pH, as adsorption increases with increasing acidity, consistent with the adsorption edge findings described in the previous section (Fig. 5). On average, the K_F values for antimonate adsorption at pH 5.5 and 8 were 774 and 125, which represent the surface excess of antimonate (q, in μmol kg^{-1}) when C_{eq} is unity (Table 5). Adsorption of antimonate from pH 5.5 solutions does not appear to be particularly sensitive to temperature (Fig. 15b), and the Freundlich model isotherm parameters log K_F and N do not significantly differ as a function of temperature (Table 5). However, the influence of temperature on antimonate adsorption is evident in pH 8 systems, where retention tends to decrease with increasing temperature.

Plots of K_d vs. q indicate that the adsorption data may also be described by the two-site Langmuir model (Eq. [7]; Figs. 16 and 17). For all cases of pH and temperature, the K_d vs. q plot may be split into two linear segments, where each segment adheres to the Langmuir model (Eq. [5]). The linear segment at low q describes high intensity and low capacity antimonate adsorption; whereas at high q, low intensity and high capacity retention is described. The slope, and K_d and q intercept values obtained through the linear regression analysis of the isotherm segments in Figs. 16 and 17 were used to compute the two-site Langmuir isotherm parameters; K_1 and b_1, and K_2 and b_2, using the interpolation procedure of Sposito (1982) (Table 5). The K_1 and b_1 parameters describe antimonate adsorption by high intensity and low capacity sites (type 1), while K_2 and b_2 describe adsorption by low intensity and high capacity sites (type 2). The Henry's Law constants for the type 1 sites (K_{ad1}), generated from the Langmuir parameters K_1 and b_1 (Table 5), tend to increase with increasing temperature in the pH 5.5 and decrease with temperature in pH 8 systems (Fig. 18). However, K_{ad2} decreases with increasing temperature under both pH conditions. Both the enthalpy (ΔH_{ad}) and entropy (ΔS_{ad}) of adsorption were computed for antimonate adsorption using the van't Hoff equation (Eq. [9]), as applied to the ln K_{ad} vs. T^{-1} data in Fig. 18. For high intensity, low capacity adsorption (type 1 sites) in pH 5.5, ΔH_{ad} is positive (11.7 kJ mol^{-1}) and $T\Delta S_{ad}$ is large (29.19 kJ mol^{-1} at 298 K) relative to ΔH_{ad}, indicating that antimonate adsorption is endothermic and entropically driven (Table 6). However, for type 1 sites in pH 8, and for low intensity, high capacity adsorption (type 2 sites) in pH 5.5 and 8, ΔH_{ad} is negative and $T\Delta S_{ad}$ is small relative to ΔH_{ad}, indicating that antimonate adsorption is exothermic and enthalpically driven. For both site types, and for both pH conditions, the free energy of adsorption (ΔG_{ad}) is negative, indicating that antimonate adsorption is spontaneous.

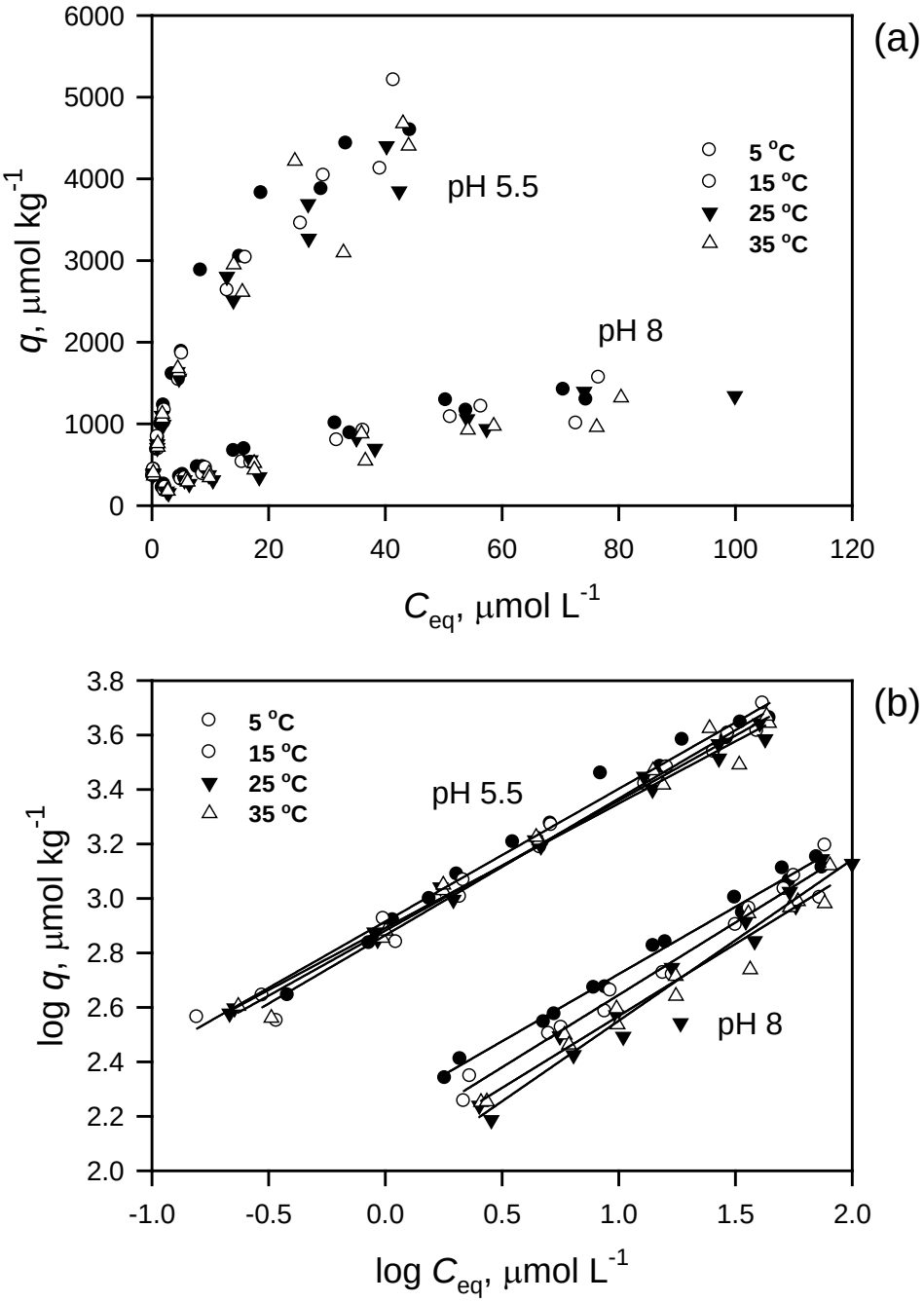

Figure 15. Adsorption isotherms, plotted in (a) normal space and (b) log-log space, illustrating the adsorption (q) of antimonate in 0.01 M KNO_3 by gibbsite (10 g L^{-1}) as a function equilibrium solution concentration (C_{eq}), pH, and temperature.

Table 5. Freundlich and two-site Langmuir isotherm parameters, and the Henry's Law constants (K_{ad} values) for the adsorption of antimonate by gibbsite.

	Freundlich parameters†			Two-site Langmuir parameters‡					
T, °C	log K_F	K_F	N	K_1	b_1	K_{ad1}	K_2	b_2	K_{ad2}
				pH 5.5					
5	2.915	822.2	0.487	0.5137	1330	683.1	0.0885	4134	365.9
15	2.865	732.8	0.502	0.7133	1618	1154	0.0269	6632	178.5
25	2.892	779.8	0.457	1.2163	1307	1590	0.0721	3709	267.3
35	2.882	762.1	0.478	0.5871	1769	1039	0.0209	7436	155.6
				pH 8					
5	2.229	169.4	0.494	0.3628	377.6	137.0	0.0331	1408	46.59
15	2.114	130.0	0.532	0.2115	429.3	90.82	0.0109	2539	27.69
25	1.959	90.99	0.592	0.1203	347.9	41.84	0.0121	2093	25.40
35	2.040	109.6	0.529	0.1634	414.9	67.80	0.0093	2201	20.42

†log K_F and N were obtained by linear regression analysis of Eq. [3]. Within pH, the log K_F and N do not significantly differ as a function of temperature at $P = 0.05$.

‡K_1 and b_1 (high intensity, low capacity adsorption), and K_2, and b_2 (low intensity, high capacity adsorption) were obtained by linear regression analysis of Eq. [5] and the data presented in Figs. 15 and 16, and by employing the method of Sposito (1982); $K_{ad1} = b_1K_1$ and $K_{ad2} = b_2K_2$. Units of K_1 and K_2 are L μmol^{-1}; b_1 and b_2 are μmol kg^{-1}; and K_{ad1} and K_{ad2} are L kg^{-1}.

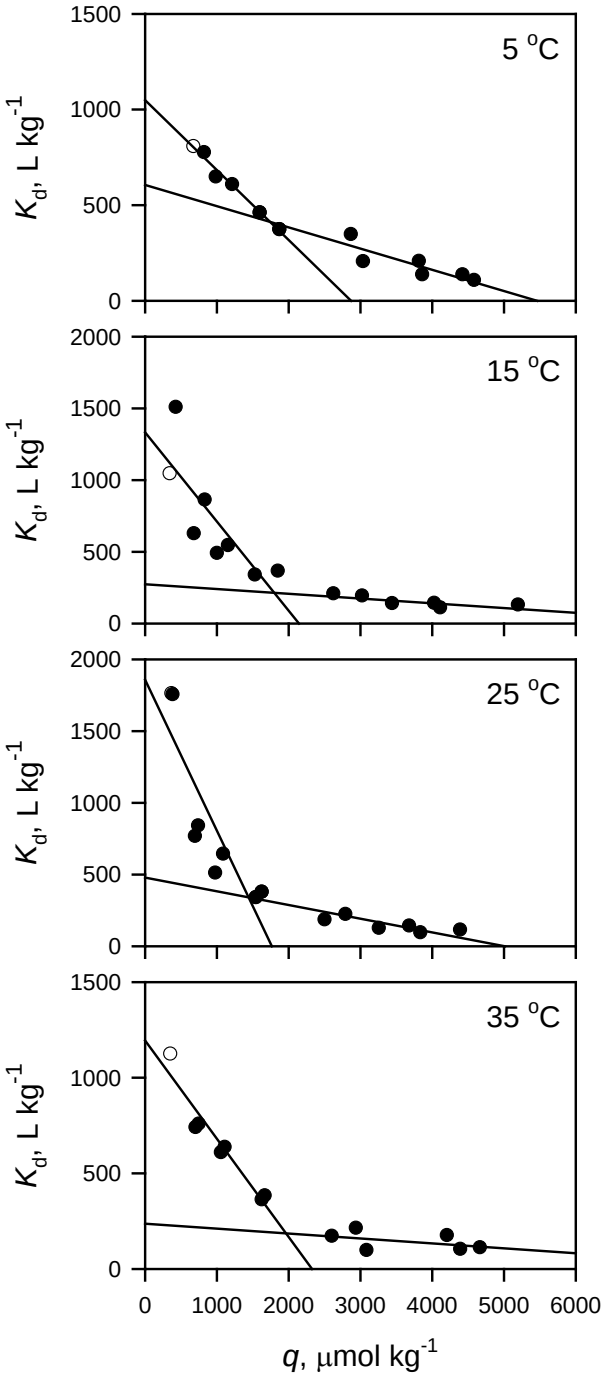

Figure 16. Application of the transformed version of the Langmuir model to K_d vs. q plots of the pH 5.5 antimonate adsorption isotherm data described in Fig. 15a. The adsorption of antimonate by gibbsite is described by two separate Langmuir isotherm equations (Table 5).

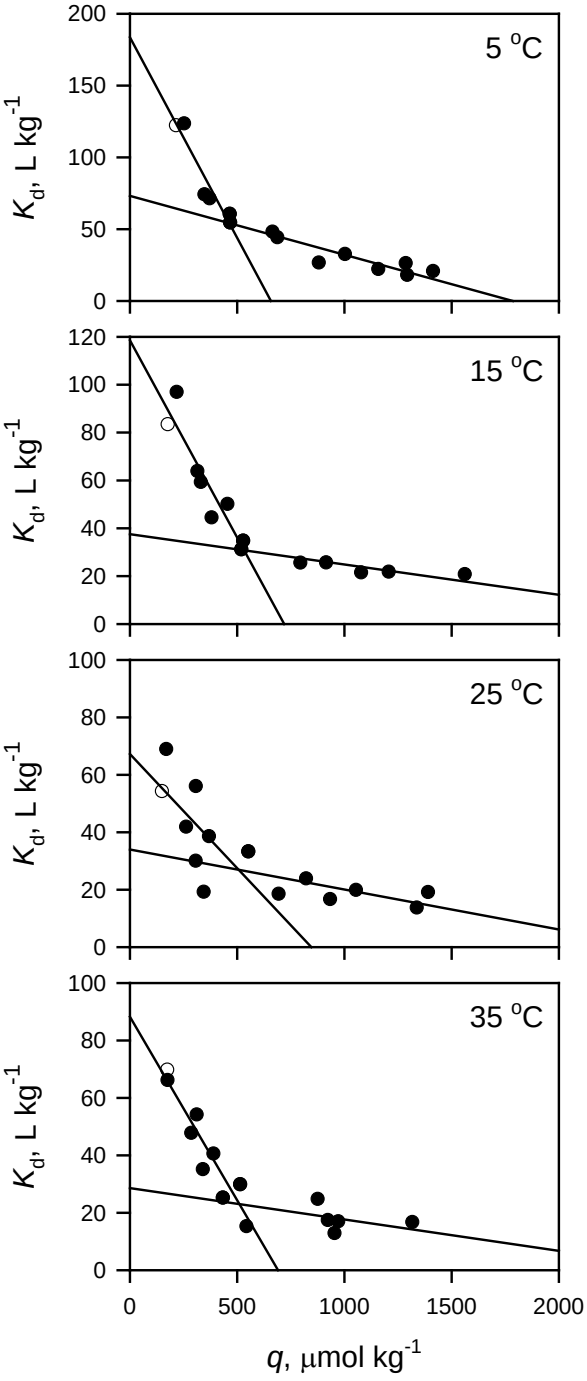

Figure 17. Application of the transformed version of the Langmuir model to K_d vs. q plots of the pH 8 antimonate adsorption isotherm data described in Fig. 15a. The adsorption of antimonate by gibbsite is described by two separate Langmuir isotherm equations (Table 5).

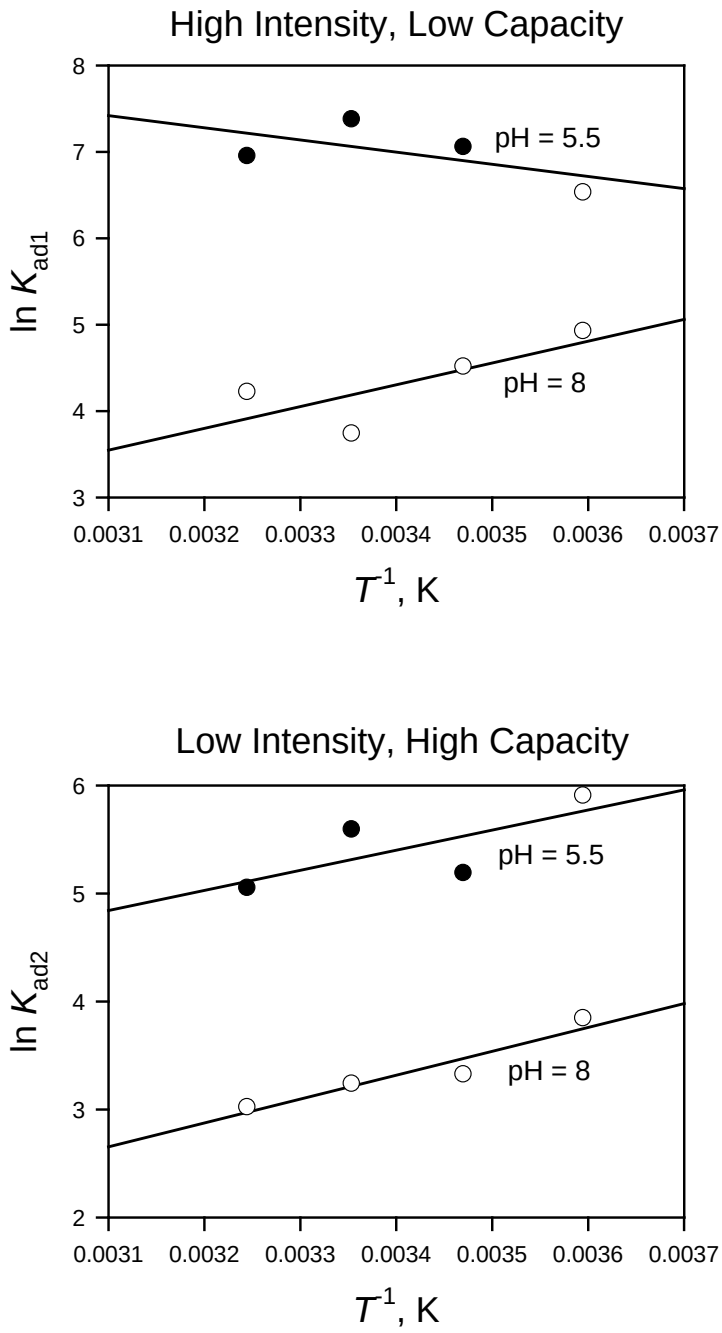

Figure 18. Temperature dependence of the Henry's Law constant for high intensity, low capacity (site type 1; $K_{ad1} = K_1 b_1$) and low intensity, high capacity (site type 2; $K_{ad2} = K_2 b_2$) for antimonate adsorption by gibbsite (K_1 and K_2, and b_1 and b_2 are adsorption constants from the two-site Langmuir equation, Eq. [7]). The lines represent the least squares linear regression analysis of the van't Hoff equation (Eq. [9]) and the ln K_{ad} vs. T^{-1} data, where T is the thermodynamic temperature.

Table 6. Thermodynamic parameters for the adsorption of antimonate by gibbsite.†

	Site type 1			Site type 2		
Temperature	ΔH_{ad}	ΔS_{ad}	ΔG_{ad}	ΔH_{ad}	ΔS_{ad}	ΔG_{ad}
°C	kJ mol^{-1}	J K^{-1}mol^{-1}	kJ mol^{-1}	kJ mol^{-1}	J K^{-1}mol^{-1}	kJ mol^{-1}
	pH 5.5					
5	11.7	97.9	–15.52	–15.5	–7.8	–13.33
15			–16.49			–13.25
25			–17.47			–13.18
35			–18.45			–13.10
	pH 8					
5	–21.0	–35.5	–11.13	–18.4	–34.9	–8.70
15			–10.78			–8.34
25			–10.42			–8.00
35			–10.07			–7.65

†Enthalpy (ΔH_{ad}) and entropy (ΔS_{ad}) of adsorption are temperature independent and computed using the van't Hoff equation (Eq. [9]) analysis of the influence of temperature on the Henry's Law constant for antimonate adsorption by site types 1 and 2 (Fig. 18). Free energy of adsorption (ΔG_{ad}) computed using Eq. [11].

Exothermic (negative ΔH_{ad}), enthalpically-driven adsorption is generally indicative of an ion exchange mechanism (adsorption increases with decreasing temperature). Thus, antimonate adsorption by gibbsite type 1 sites in pH 8, and by type 2 sites in pH 5.5 and 8, is predominately an outer-sphere surface complexation process. Antimonate adsorption by type 1 sites in pH 5.5 is endothermic (positive ΔH_{ad}) and entropically-driven (heat is absorbed during antimonate adsorption), suggesting inner-sphere complexation. Although ΔH_{ad} is positive (11.7 kJ mol^{-1}), the magnitude of ΔH_{ad} is small relative to that typically found for the inner-sphere surface complexation of ligands. Enthalpy values for the retention of specifically-adsorbed ligands by variable-charge minerals are generally <40 kJ mol^{-1}, although similar in magnitude ΔH_{ad} values have been used to infer an ion exchange mechanism (Zhang and Selim, 2008; Li et al., 2008; Ferreiro and de Bussetti, 2007). The inner-sphere adsorption of arsenate by Al and Fe oxides has been reported to generate ΔH_{ad} values of 25.11 and 17.83 kJ mol^{-1} (Helmy et al., 1996; Partey et al., 2008). Enthalpy values for the inner-sphere complexation of phosphate and 2-ketogluconate by Fe oxides range between 22 and 81.84 kJ mol^{-1} (Juang and Chung, 2004; Mezzener and Bensmaili, 2008; Mustafa et al., 2008; Journey et al., 2010). The ΔH_{ad} value computed for antimonate adsorption to the high intensity sites indicates that there is an inner-sphere component to the retention mechanism in acidic systems.

Electrostatics at the Solid-Solution Interface

Zeta potential and proton adsorption curves for gibbsite in the swamping electrolyte (KNO_3) are illustrated in Fig. 19. The KNO_3 system represents surface charging in the absence of inner-sphere complexation. For gibbsite, the isoelectric point (IEP) and the point of zero charge (pH_{pzc}) is 10.55 (Fig. 19a). This is also the common intersection point (CIP) for the zeta potential

measurements in 0.01 and 0.1 *M* KNO_3. At pH values below the pH_{pzc}, the gibbsite surface bears a net positive charge. The measured gibbsite pH_{pzc} is slightly higher than the 7.8 to 10.4 range compiled by Karamalidis and Dzombak (2010), but within the 8.7 to 11 range reported by Adekola et al. (2011). An increase in the swamping electrolyte concentration results in a decreasing zeta potential as the pH is decreased below the pH_{pzc}. Increased concentrations of electrolyte in the σ_d plane tend to shield the particle charge, decreasing the extent of charge influence in the solid-solution interface and decreasing the response (particle movement) in an electric field (Yu, 1997). As expected, the adsorbed proton concentration (Q_h) increase with decreasing pH; however, Q_h was not influenced by the background electrolyte concentration (Fig. 19b). This finding is not a "normal" response (larger Q_h at higher ionic strength), but similar to that observed by others (Yang et al., 2007; Adekola et al., 2011), due to the low surface reactivity of gibbsite.

When a ligand other than the indifferent electrolyte is present, electrophoretic mobility will reflect the adsorption mechanism. Adsorption of an anionic ligand in the is-plane will decrease the zeta potential and shift the IEP to lower pH values (additional protonation, i.e., lower pH, required for site neutralization). The adsorption of a ligand in the os-plane will not affect the IEP, relative to that in the indifferent electrolyte. However, a decrease in the zeta potential may be observed if the adsorbed ligand has higher valence than the indifferent electrolyte (providing greater negative charge to the near-surface region bounded by the particle shear plane, shielding particle charge). The proton adsorption characteristics may also be used to infer the ligand adsorption mechanism. Adsorption of an anionic ligand in the is-plane will increase Q_h in response to the addition of intrinsic negative surface charge (decreasing σ_{is}), while adsorption of a ligand in the os-plane will not have an effect on Q_h.

The presence of 10 m*M* K_2SO_4 does not appreciably change the IEP of gibbsite (Fig. 19a), relative to the KNO_3 systems, which may be due to the absence of sulfate adsorption at the IEP (Figs. 7a and 9). However, there is a negative shift in the zeta potential at pH values below the IEP as a result of sulfate adsorption. The less positive zeta potential values indicate that the adsorbed complexes of sulfate provide greater negative charge to the near-surface region bounded by the particle shear plane, relative to the background electrolyte (divalent SO_4^{2-} vs. monovalent NO_3^-). A comparison of the KNO_3 and K_2SO_4 systems indicates that sulfate adsorption results is an upward shift in Q_h which is reflective of the inner-sphere complexation of SO_4^{2-}, particularly when pH < 7 (Fig. 19b).

The IEP of gibbsite shifts to the 4.6 to 4.9 range when reacted with phosphate (Fig 20a). This is macroscopic evidence of the inner-sphere complexation of phosphate by gibbsite. This finding is consistent with the strong phosphate adsorption behavior, and the lack of an ionic strength effect (Figs. 7b and 9). A comparison of the KNO_3 and KH_2PO_4 systems indicates that phosphate adsorption results in an upward shift in Q_h which is reflective of the inner-sphere complexation of phosphate species ($H_2PO_4^-$ and HPO_4^{2-}) when pH < 10 (Fig. 20b).

Within the pH range studied (pH > 4), a gibbsite IEP in the presence of antimonate was not achieved (Fig. 21a). At all pH values, the zeta potentials are negative, reflecting the inner-sphere complexation of antimonate. A comparison of the KNO_3 and $KSb(OH)_6$ systems shows that antimonate adsorption results is an upward shift in Q_h, which indiactes the inner-sphere complexation of antimonate, particularly when pH < 8 (Fig. 21b).

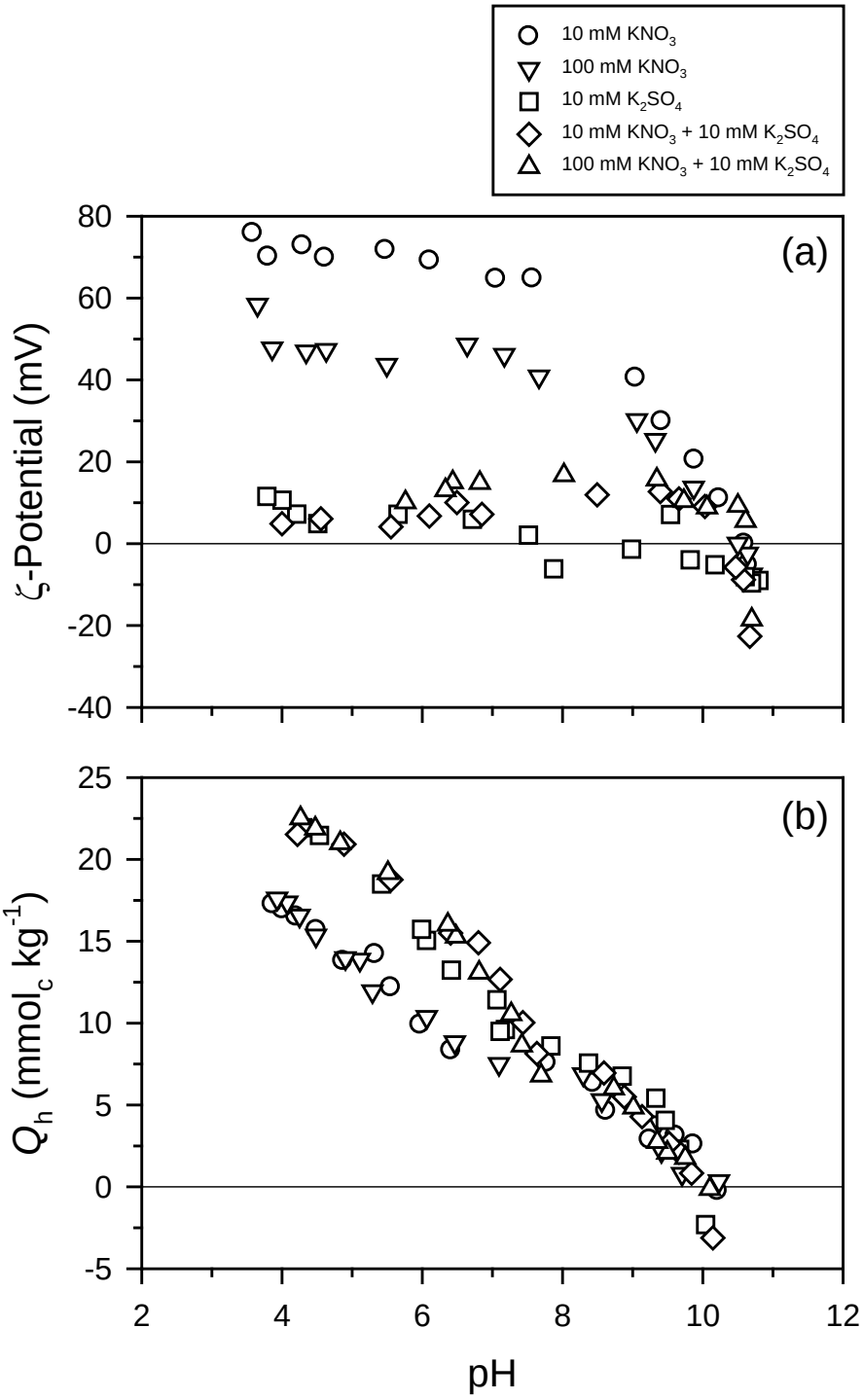

Figure 19. The influence of sulfate on gibbsite (a) zeta potential and (b) proton adsorption as a function of pH, ionic strength, and electrolyte composition.

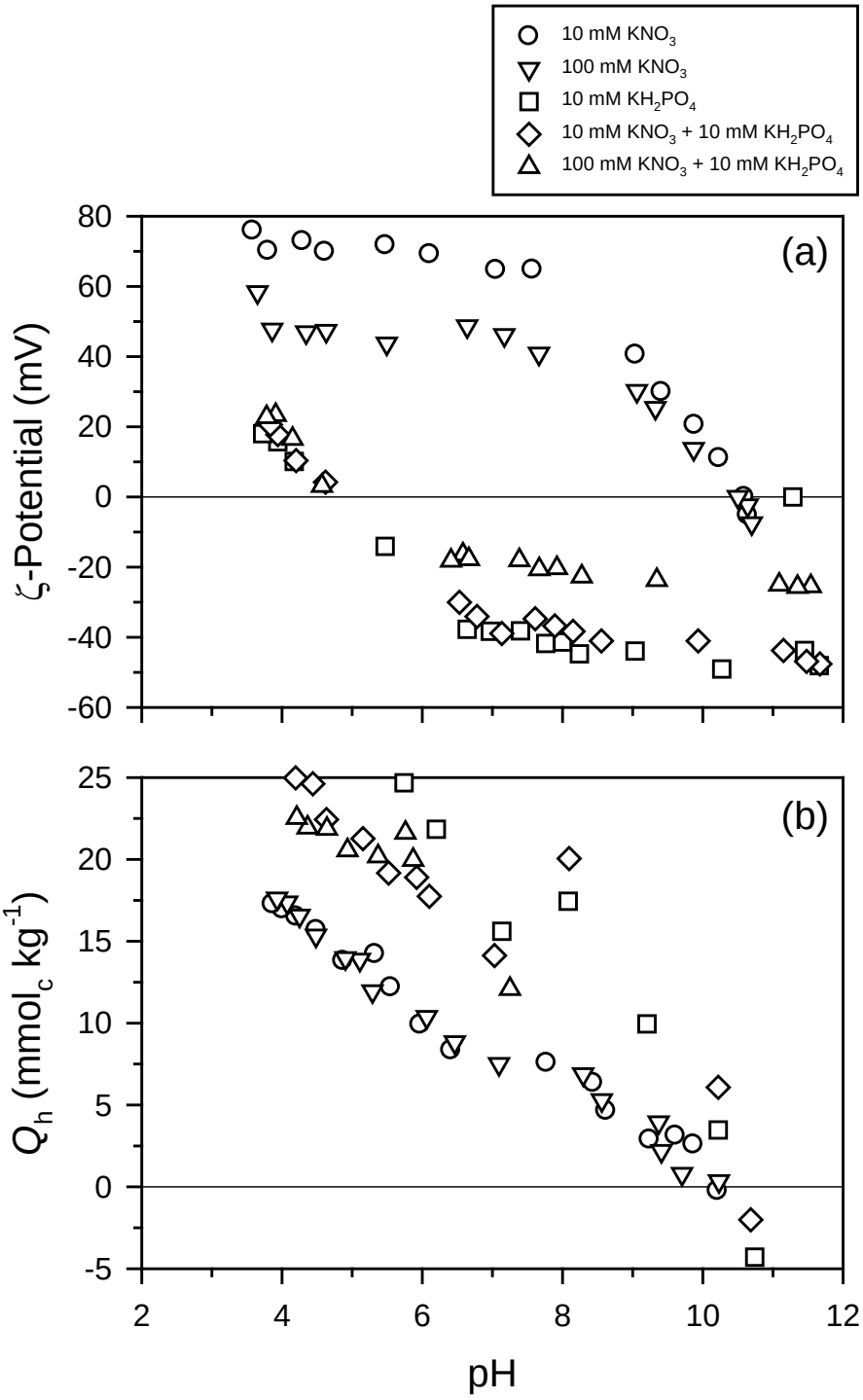

Figure 20. The influence of phosphate on gibbsite (a) zeta potential and (b) proton adsorption as a function of pH, ionic strength, and electrolyte composition.

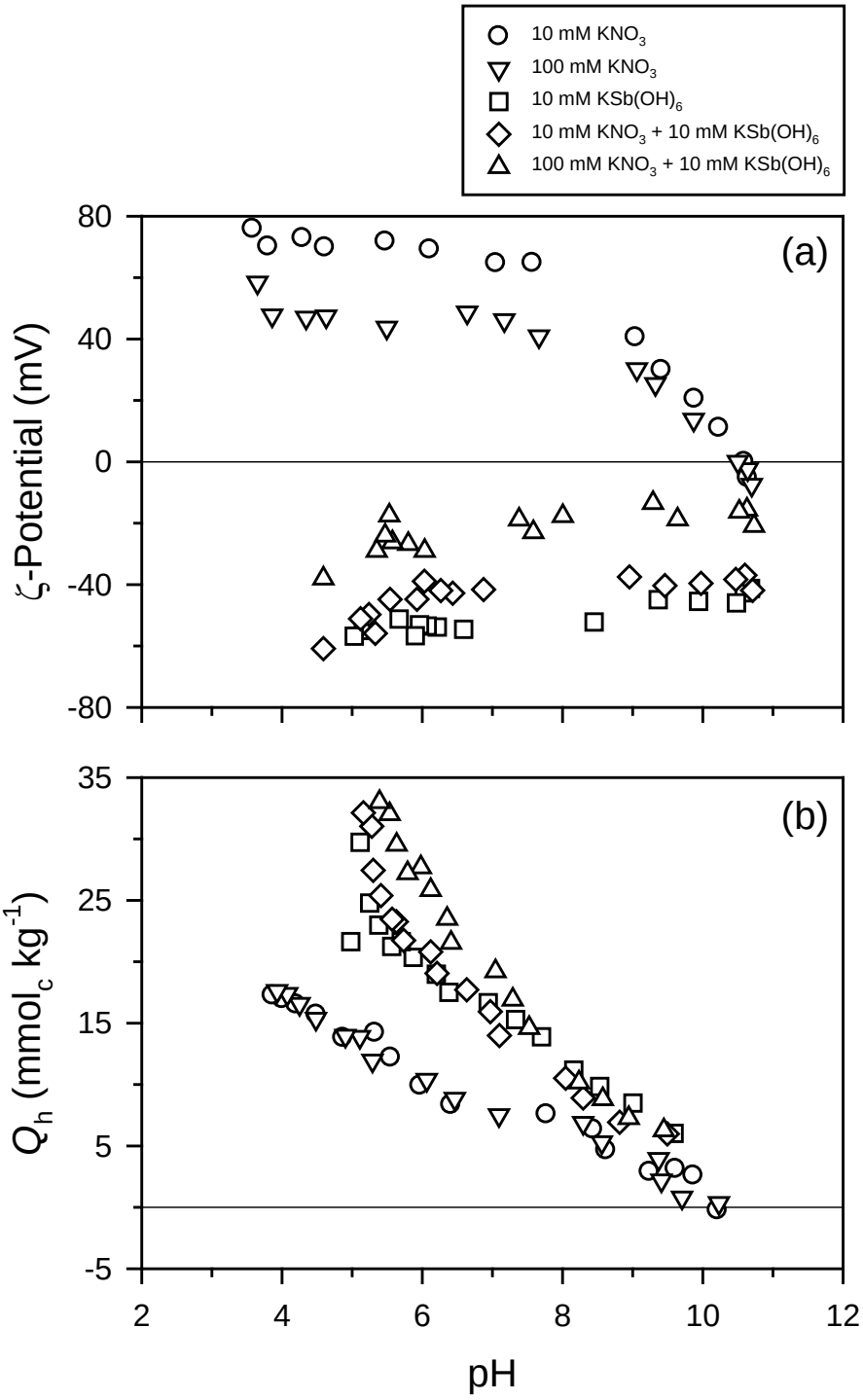

Figure 21. The influence of antimonate on gibbsite (a) zeta potential and (b) proton adsorption as a function of pH, ionic strength, and electrolyte composition.

Surface Complexation Modeling

The antimonate adsorption edge and adsorption isotherm studies, coupled with the effects of antimonate on gibbsite surface charging, indicate that antimonate retention by gibbsite occurs via a combination of inner- and outer-sphere complexation mechanisms. Specifically, antimonate retention predominately occurs via an outer-sphere mechanism ($\equiv AlOH_2^+–Sb(OH)_6^-$) in alkaline systems, with increasing inner-sphere complexation character as pH decreases into the acidic range. Spectroscopic studies indicate that the retention of antimonate by hydrous aluminum oxide, and other adsorbents with ≡AlOH surface functionality (e.g., aluminosilicates), proceeds via mono- and bidentate inner-sphere surface complexation processes ($\equiv AlOHSb(OH)_5^0$ or $\equiv AlOSb(OH)_5^-$, and $(\equiv AlO)_2Sb(OH)_4^-$) under acidic (pH 5) conditions (Ilgen and Trainor, 2012). These studies also suggest that the bidentate complex is the predominant inner-sphere species. The anion exchange, and monodentate and bidentate ligand exchange processes are illustrated in Fig. 22 and described in Eqs. [26] through [29].

Two experimental techniques were employed to generate the antimonate, sulfate, and phosphate adsorption edge data (q vs. pH) as a function of ionic strength: continuous titration beaker systems (Figs. 5 and 7) and the competitive adsorption batch systems (Fig. 9). Both data sets were used to develop the chemical models for ligand adsorption by gibbsite. Four models were evaluated for their ability to describe the antominate adsorption edge. Model A assumes that the adsorption of antimonate occurs via an outer-sphere retention process throughout the entire pH range studied, forming only the $\equiv AlOH_2^+–Sb(OH)_6^-$ surface species. Using the triple-layer SCM, coupled with the 2-pK_a approach, the adsorption of antominate is well-predicted in the pH 3 to 10 range (Fig. 23). The goodness-of-fit parameters for the beaker and batch data sets (V_Y = 3.578 and 3.073) indicate that the model satisfactorily describes the adsorption edges (Table 7). Further, the common logarithms of the intrinsic surface complexation constants for the batch and beaker systems ($\log K^{int}$ = 11.00 and 11.28) are similar. Although the outer-sphere surface complexation model describes the antimonate adsorption edge, the model tends to under predict adsorption in the acidic range (pH < 5) and in the higher ionic strength systems. This result suggests that addition surface species are required to model the antimonate adsorption in the acidic pH range.

A combined outer-sphere and inner-sphere surface complexation model is examined in Model B (Fig. 24 and Table 7). In this model, the monodentate $\equiv AlOSb(OH)_5^-$ complex is the stipulated inner-sphere species, and assumes that antimonate dissociates ($Sb(OH)_6^- = SbO(OH)_5^{2-} + H^+$) to donate H^+ to protonate the surface ($\equiv AlOH^0 + H^+ = \equiv AlOH_2^+$), creating adsorbed water which is displaced by the antominate ligand ($\equiv AlOH_2^+ + SbO(OH)_5^{2-} = \equiv AlOSb(OH)_5^- + H_2O$). The dissociation of a proton from antimonate during adsorption is proposed because its location between two highly positive cations (Al^{3+} and Sb^{5+}) is not electrostatically favored. The adsorption of antominate was well-predicted by this model in the pH 3 to 10 range. The goodness-of-fit parameters for the beaker and batch data sets (V_Y = 3.029 and 2.428) indicate that the model satisfactorily describes the adsorption edges. The common logarithms of the intrinsic surface complexation constants for the outer-sphere complex for the batch and beaker systems ($\log K^{int}$ = 10.95 and 11.23) are similar, as are the constants for the inner-sphere species ($\log K^{int}$ = –2.45 and –2.19). The outer-sphere surface complex is the predominant surface species in the pH 3 to 10 range, and in the pH > 6 range accounts for all of the adsorbed antimonate. As the pH decreases below 6, the inner-sphere species increases in

importance. This result is consistent with the adsorption reversibility and thermodynamic findings, which indicated that inner-sphere complexation becomes important in acidic systems.

The second model that considers both outer- and inner-sphere complexation of antimonate (Model C) also stipulates a monodentate, inner-sphere species ($\equiv AlOHSb(OH)_5^0$). This species differs from the $\equiv AlOSb(OH)_5^-$ species (Model B) in that a hydroxide ion, rather than an oxygen, is superimposed between the surface Al and the adsorbed Sb(V) (antimonate does not dissociate during adsorption). Like Model B, Model C provides a satisfactory description of the antimonate adsorption edge data (V_Y = 3.103 and 2.491 for the beaker and batch systems) (Fig. 25). The intrinsic complexation constants for the outer-sphere species are log K^{int} = 10.96 and 11.24 for the beaker and batch systems; the constants for the inner-sphere species for the two systems are log K^{int} = 7.53 and 7.62 (Table 7).

The outer-sphere and the inner-sphere bidentate surface complexes [$(\equiv AlO)_2Sb(OH)_4^-$] are stipulated in Model D (Table 7). Like the monodentate complex in Model B, the adsorbed antimonate donates protons to form surface-bound water, which are displaced during the ligand exchange process to form the bidentate species. The existence of a bidentate surface species is supported by the spectroscopic findings of Ilgen and Trainor (2012), and this species has been used to model antimonate adsorption by gibbsite (Rakshit et al., 2011) and goethite (Leuz et al., 2006). Model D provides a satisfactory description of the antimonate adsorption edge data (V_Y = 3.095 and 2.415 for the beaker and batch systems) (Fig. 26). The intrinsic complexation constants for the outer-sphere species are log K^{int} = 10.95 and 11.22 for the beaker and batch systems; the constants for the inner-sphere species for the two systems are log K^{int} = 0.77 and 1.08 (Table 7).

Each of the three surface complexation models that employ both an outer-sphere and an inner-sphere surface-bound antimonate (Models B, C, and D) provides a satisfactory description of the adsorption edge data. The models indicate that the outer-sphere surface species accounts for a bulk of the adsorption in the pH > 6 systems, while the inner-sphere species become increasingly important as solution pH decreases below 6. The increasing significance of an inner-sphere surface complex as solution pH decreases into the acidic range is supported by the experimental evidence. Antimonate adsorption is hysteretic in acidic systems, but reversible in the neutral to alkaline pH range (Fig. 5). Adsorption by high intensity, low capacity sites in pH 5.5 solutions is endothermic and entropically-driven (suggesting an inner-sphere component to the adsorption process). Further, proton adsorption in the presence of adsorbed antimonate deviates from that in the absence of antimonate as solution pH decreases into the neutral to acidic range (also suggesting an inner-sphere component to the adsorption process) (Fig. 21). Attempts to model the adsorption edge data without imposing an outer-sphere species were not successful. Chemical models that stipulated both a monodentate and a bidentate surface species, as inferred from spectroscopic analysis of adsorbed antimonate on gibbsite (Ilgen and Trainor, 2012), or models that only considered a single inner-sphere species, either caused convergence problems in the FITEQL program, or did not describe the adsorption edge data. The potential formation of the aqueous $KSb(OH)_6^0$ ion pair in the surface complexation modeling, as considered by Leuz et al. (2006) but discounted by Rakshit et al (2011), was also evaluated to partially explain the strong ionic strength effect on antimonite retention. However, the inclusion of this species was superfluous, as the ionic strength effect was predicted by outer-sphere adsorption alone.

In order to predict competitive adsorption in antimonate-sulfate and antimonate-phosphate systems, intrinsic constants for the retention of sulfate and phosphate must be determined. The adsorption of sulfate by gibbsite is strongly influenced by solution ionic strength (Figs. 7a and

9b) and reversible throughout the pH range studied. Sulfate adsorption does not alter the IEP of gibbsite, although zeta potentials are less positive and proton adsorption increases in pH < 7 solutions, relative to the indifferent KNO_3 electrolyte alone (Fig. 19). These experimental findings indicate that sulfate retention proceeds primarily through an outer-sphere surface complexation mechanism, an interpretation that is supported by the available literature (He et al., 1996 and 1997; Goldberg, 2010). Sulfate adsorption by gibbsite was successfully modeled by considering only outer-sphere complexation and the formation of $\equiv AlOH_2^+–SO_4^{2-}$ (Fig. 27). The goodness-of-fit parameters for the beaker and batch data sets (V_Y = 0.725 and 7.313) indicate that the model satisfactorily describes the adsorption edges (Table 7). The common logarithms of the intrinsic surface complexation constants for the batch and beaker systems are log K^{int} = 8.58 and 9.04.

Phosphate displays strong adsorption by gibbsite, with nearly complete removal of phosphate at pH values less than approximately 7 (Figs. 7b and 9c). Phosphate adsorption is independent of ionic strength, shifts the gibbsite IEP from 10.55 to 4.8, and increases proton adsorption throughout a broad pH range (relative to the KNO_3 systems) (Fig. 20). These experimental results indicate that phosphate is retained primarily by inner-sphere surface complexation mechanisms. Johnson et al. (2002) and Van Emmerik et al. (2007) reported that phosphate formed monodentate inner-sphere surface complexes on γ-Al_2O_3 and gibbsite, and that outer-sphere complexation contributed to adsorption in alkaline systems (pH > 8). The adsorption of phosphate by gibbsite has been successfully described by considering only monodentate inner-sphere complexation and the formation of $\equiv AlOPO_3^{2-}$, $\equiv AlOPO_2OH^-$, and $\equiv AlOPO(OH)_2^0$, species (Goldberg and Sposito,1984; He et al., 1997; Goldberg, 2010). Phosphate adsorption by gibbsite in the beaker and batch systems could only be predicted through the stipulation of a single outer-sphere $\equiv AlOH_2^+–HPO_4^{2-}$ species (Fig. 28). This model provides a satisfactory fit to the experimental beaker and batch adsorption edge data (V_Y = 0.439 and 2.569), with optimized log K^{int} values of 27.81 and 26.38 (Table 7). The prediction of phosphate adsorption using an inner-sphere model is also illustrated in Fig. 28. The predicted common logarithm of the intrinsic complexation constants for the reaction, $\equiv AlOH + 2H^+ + PO_4^{3-} = \equiv AlOPO_3^{2-} + 2H_2O$, in the batch and beaker systems are log K^{int} = 11.98 ± 0.04 (V_Y = 4.651) and 14.58 ± 0.02 (V_Y = 6.636). Although the goodness-of-fit parameters for the inner-sphere model are low (as are the standard deviations on log K^{int}), the model does not provide an acceptable fit to the adsorption edge data. Surface complexation models that employed either $\equiv AlOPO_2OH^-$ or $\equiv AlOPO(OH)_2^0$ species provided fits to the experimental data that were similar to $\equiv AlOPO_3^{2-}$. Models that considered multiple inner-sphere surface species, or a combination of inner- and outer-sphere surface species, caused convergence problems in the FITEQL program.

The surface complexation modeling of competitive adsorption, using the intrinsic constants obtained from single-adsorbate systems, was investigated for the direct competition antimonate-sulfate and antimonate-phosphate systems (Figs. 10 through 13). Although several models provided acceptable fits to the adsorption edge data, the model using the outer-sphere $\equiv AlOH_2^+–Sb(OH)_6^-$ and inner-sphere $(\equiv AlO)_2Sb(OH)_4^-$ species was selected to predict competitive antimonate adsorption (Model D, Table 7). This model was selected because the formation of the bidentate species on gibbsite is supported by spectroscopic evidence (Ilgen and Trainor, 2012). The outer-sphere $\equiv AlOH_2^+–SO_4^{2-}$ and $\equiv AlOH_2^+–HPO_4^{2-}$ models were used to predict sulfate and phosphate adsorption. The application of chemical models developed for single-adsorbate systems to binary-adsorbate systems has been met with limited success (Essington and

Anderson, 2008; Goldberg, 2010). Generally, the reoptimization of the intrinsic constants is necessary to provide an adequate fit to the experimental data.

The predicted direct competitive adsorption of antimonate and sulfate by gibbsite indicates that antimonate adsorption in 0.01 *M* KNO_3 is well-described, but slightly underpredicted in 0.1 *M* KNO_3 (Fig. 29a). As in the single-adsorbate systems (Fig. 26), the outer-sphere surface complex predominates throughout the pH 3 to 10 range, with the bidentate species becoming important as pH decreases below 6. The predicted adsorption of sulfate in the competitive systems is slightly underpredicted in 0.01 *M* KNO_3 and overpredicted in 0.1 *M* KNO_3. The goodness-of-fit parameter (V_Y = 16.991) is less than 20, which suggests that the modeled adsorption of antimonate and sulfate in the binary systems provide an adequate estimation of the experimental data (Herbelin and Westall, 1999). The goodness-of-fit parameter for the predicted adsorption in the binary antimonate-phosphate system is V_Y = 12.342; again suggesting that the unoptimized surface complexation model adequately describes the experimental adsorption data (Fig. 30). However, antimonate adsorption was underestimated in both the 0.01 and 0.1 *M* KNO_3 systems, while phosphate retention was over-estimated in alkaline conditions.

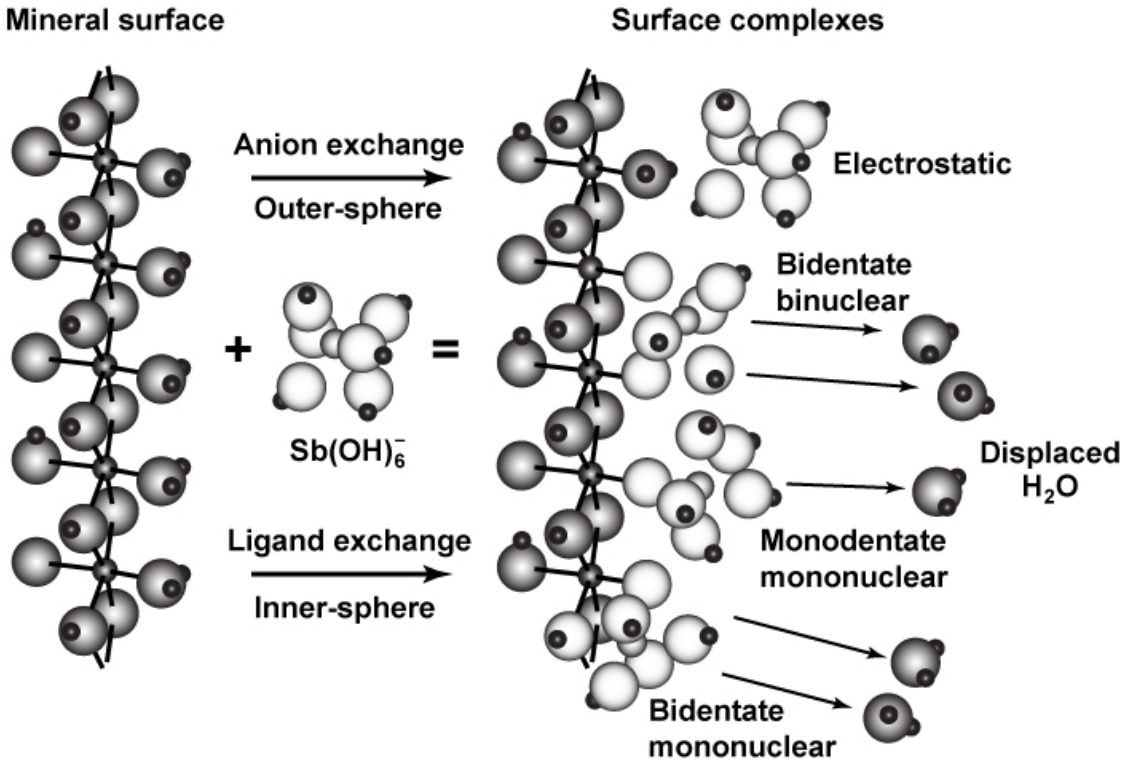

Figure 22. The anion exchange process on a metal oxide surface that results in the outer-sphere surface complexation of Sb(V), and the inner-sphere ligand exchange processes that result in the monodentate-mononuclear, bidentate-binuclear, and bidentate-mononuclear surface complexes for Sb(V) adsorption (modified from Essington, 2003).

Table 7. Surface complexation models used to describe the adsorption of antimonate, sulfate, and phosphate by gibbsite as a function of pH and ionic strength using the triple-layer formulation.

Reaction		log K^{int}† Beaker‡	log K^{int}† Batch
Antimonate Model A			
$\equiv AlOH + H^+ + Sb(OH)_6^- = \equiv AlOH_2^+–Sb(OH)_6^-$		11.00 ± 0.01	11.28 ± 0.01
	V_Y§	3.578	3.073
Antimonate Model B			
$\equiv AlOH + H^+ + Sb(OH)_6^- = \equiv AlOH_2^+–Sb(OH)_6^-$		10.95 ± 0.01	11.23 ± 0.01
$\equiv AlOH + Sb(OH)_6^- = \equiv AlOSb(OH)_5^- + H_2O$		–2.45 ± 0.12	–2.19 ± 0.14
	V_Y	3.092	2.428
Antimonate Model C			
$\equiv AlOH + H^+ + Sb(OH)_6^- = \equiv AlOH_2^+–Sb(OH)_6^-$		10.96 ± 0.01	11.24 ± 0.01
$\equiv AlOH + H^+ + Sb(OH)_6^- = \equiv AlOHSb(OH)_5^- + H_2O$		7.53 ± 0.09	7.62 ± 0.12
	V_Y	3.103	2.491
Antimonate Model D			
$\equiv AlOH + H^+ + Sb(OH)_6^- = \equiv AlOH_2^+–Sb(OH)_6^-$		10.95 ± 0.01	11.22 ± 0.01
$2\equiv AlOH + Sb(OH)_6^- = (\equiv AlO)_2Sb(OH)_4^- + 2H_2O$		0.77 ± 0.12	1.08 ± 0.14
	V_Y	3.095	2.415
Sulfate			
$\equiv AlOH + H^+ + SO_4^{2-} = \equiv AlOH_2^+–SO_4^{2-}$		8.58 ± 0.02	9.04 ± 0.02
	V_Y	0.725	7.313
Phosphate			
$\equiv AlOH + 2H^+ + PO_4^{3-} = \equiv AlOH_2^+–HPO_4^{2-}$		27.82 ± 0.05	26.38 ± 0.03
	V_Y	0.439	2.569

†Common logarithms of the intrinsic surface complexation constants (± standard deviation) optimized using FITEQL, the antimonate adsorption edge data (Figs. 5 and 9), and the gibbsite and suspension parameters described in Tables 1 and 2.
‡Adsorption edge data were obtained from the continuous titration ‘Beaker’ studies, or the competitive ‘Batch’ studies.
§Weighted sum of squares of residuals divided by the degrees of freedom.

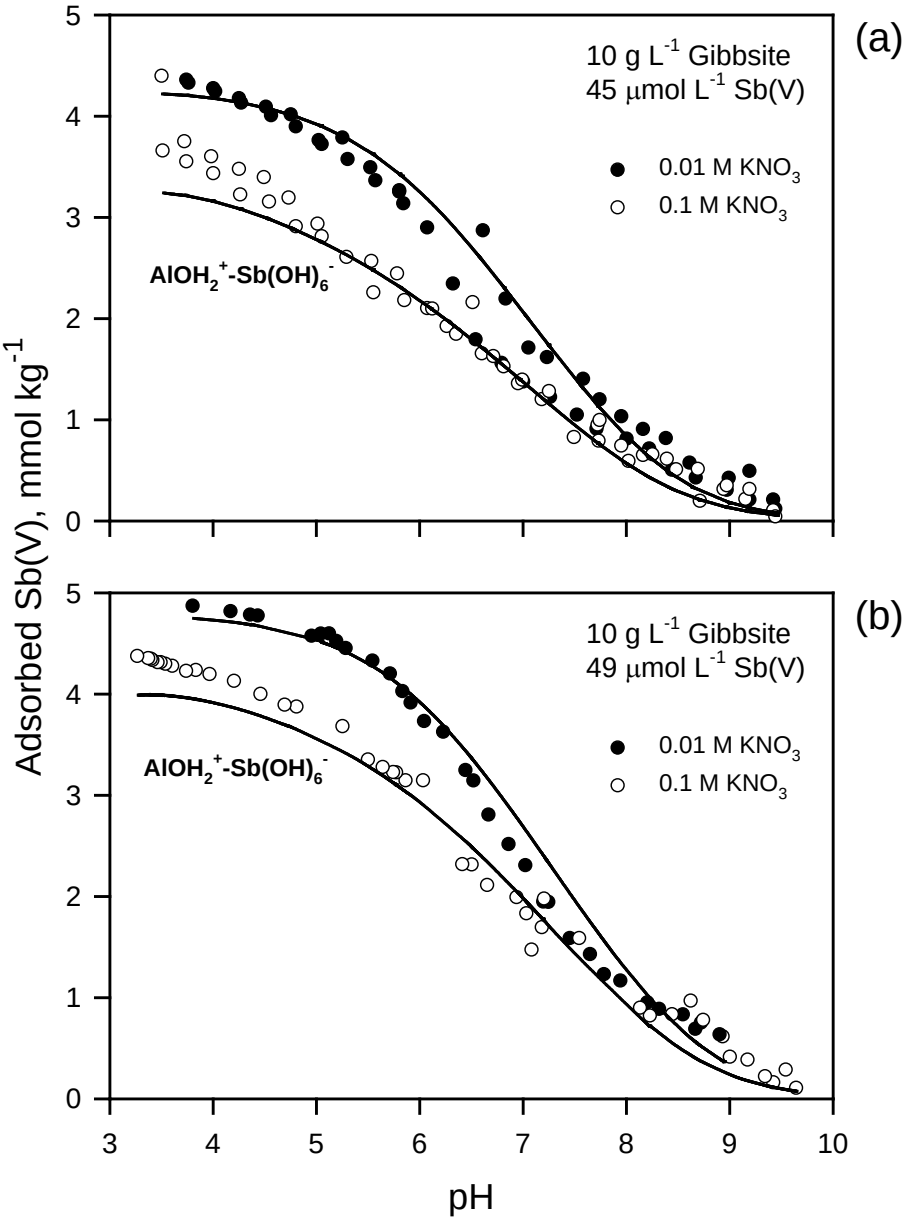

Figure 23. The adsorption of antimonate by gibbsite as a function of pH and ionic strength in (a) beaker and (b) batch systems. The lines represent the triple-layer surface complexation model fit to the experimental data using FITEQL and the chemical model described in Tables 1, 2, and 7. The solid lines show the predicted adsorption of the outer-sphere $\equiv AlOH_2^+–Sb(OH)_6^-$ species.

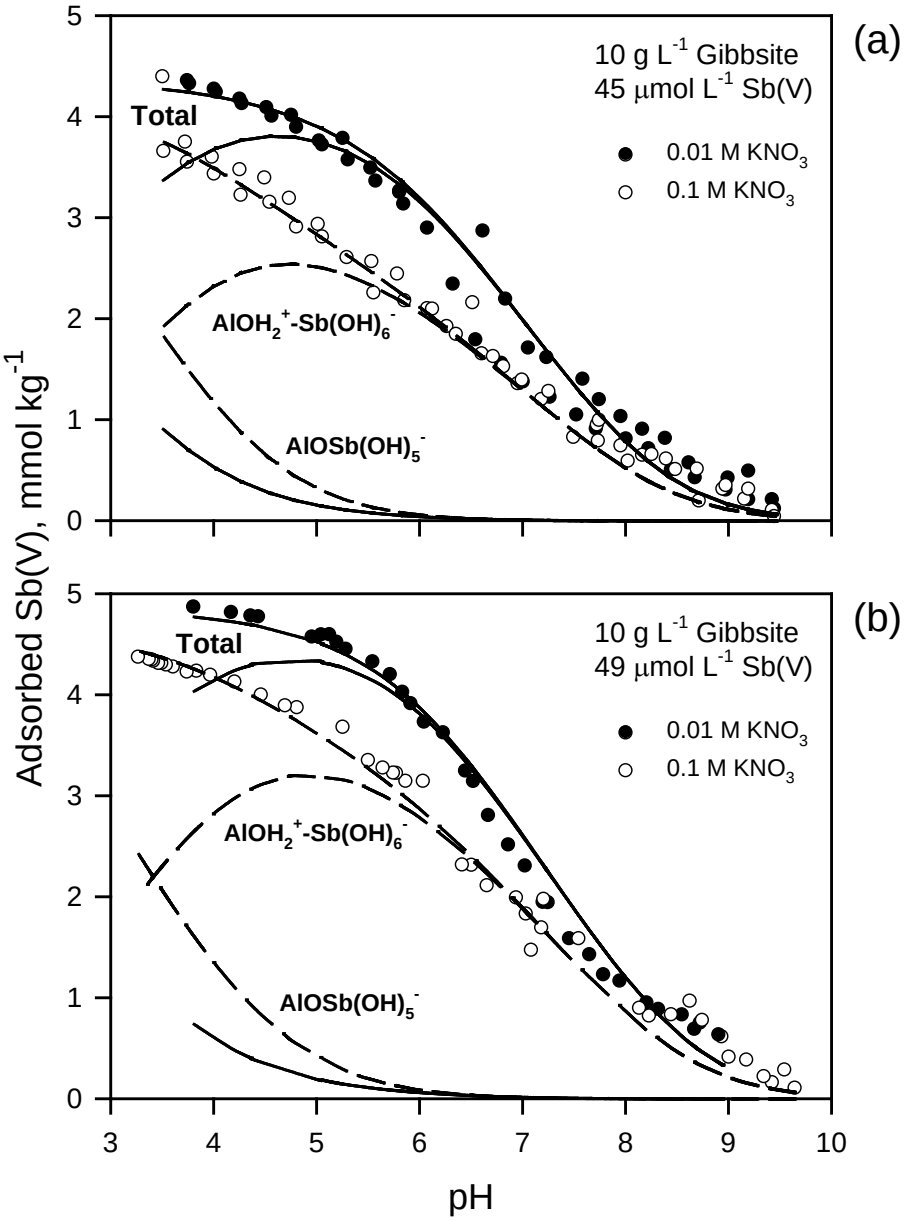

Figure 24. The adsorption of antimonate by gibbsite as a function of pH and ionic strength in (a) beaker and (b) batch systems. The lines represent the triple-layer surface complexation model fit to the experimental data using FITEQL, the outer-sphere $\equiv AlOH_2^+ – Sb(OH)_6^-$ species and the inner-sphere $\equiv AlOSb(OH)_5^-$ species, and the chemical model described in Tables 1, 2, and 7. The solid lines show the predicted adsorption in 0.01 *M* KNO_3, the dashed lines in 0.1 *M* KNO_3.

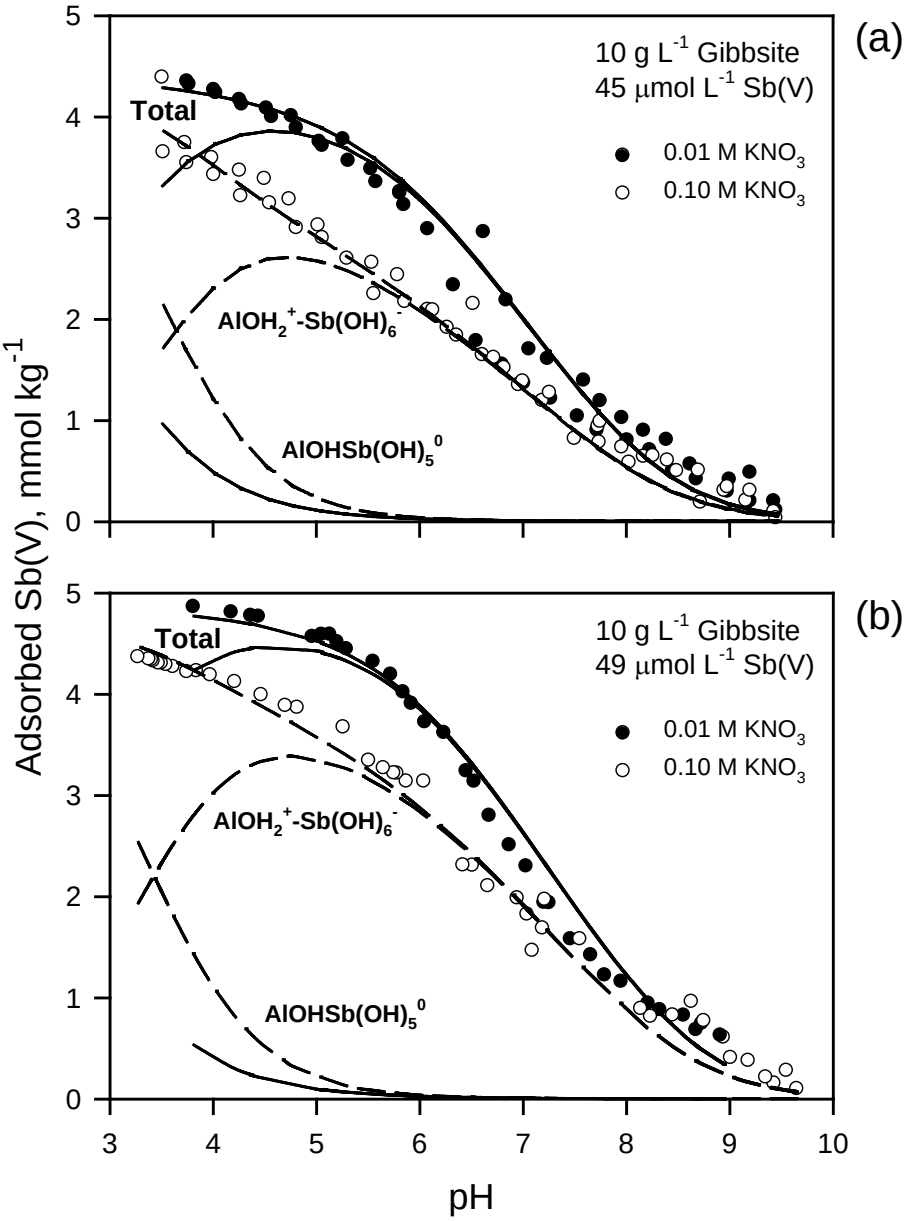

Figure 25. The adsorption of antimonate by gibbsite as a function of pH and ionic strength in (a) beaker and (b) batch systems. The lines represent the triple-layer surface complexation model fit to the experimental data using FITEQL, the outer-sphere $\equiv AlOH_2^+ – Sb(OH)_6^-$ species and the inner-sphere $\equiv AlOHSb(OH)_5^0$ species, and the chemical model described in Tables 1, 2, and 7. The solid lines show the predicted adsorption in 0.01 *M* KNO_3, the dashed lines in 0.1 *M* KNO_3.

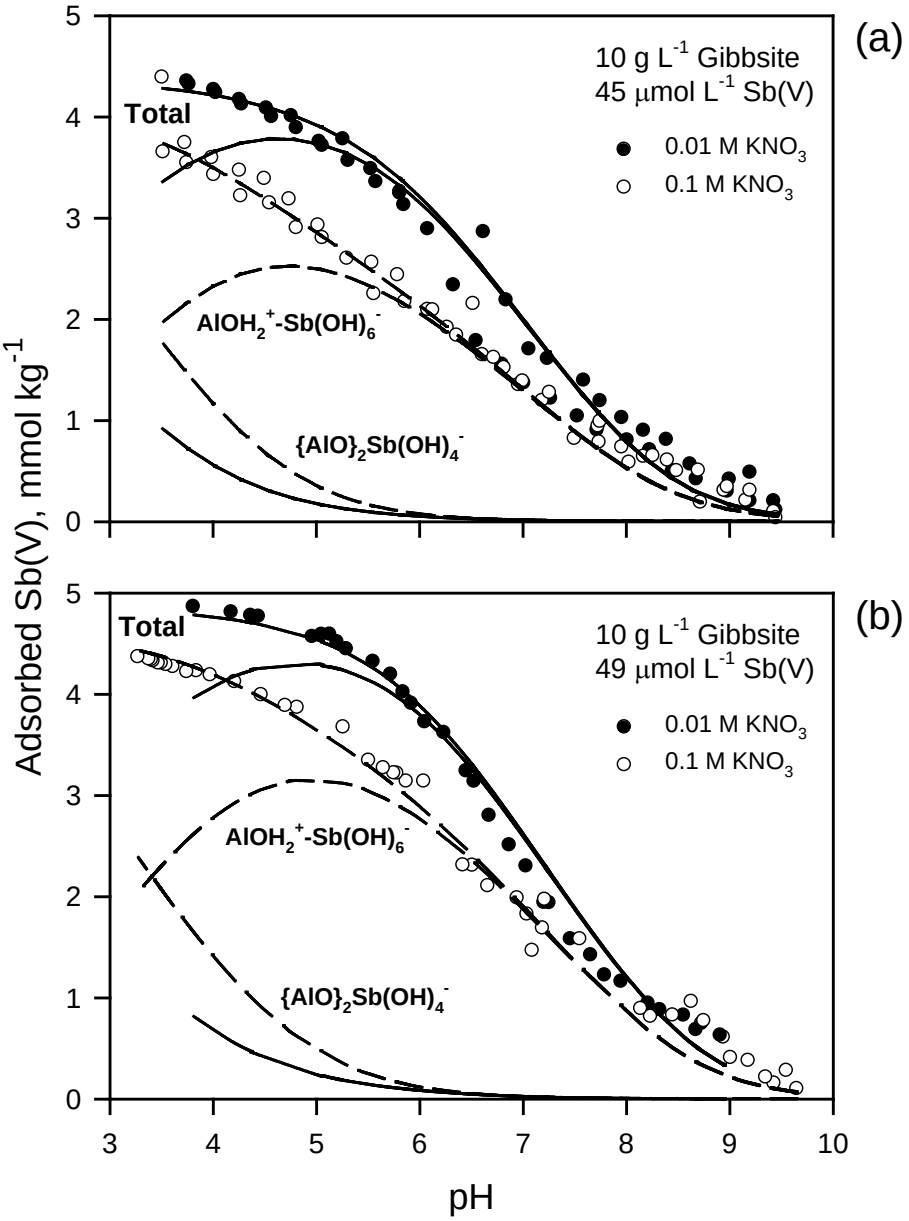

Figure 26. The adsorption of antimonate by gibbsite as a function of pH and ionic strength in (a) beaker and (b) batch systems. The lines represent the triple-layer surface complexation model fit to the experimental data using FITEQL, the outer-sphere $\equiv AlOH_2^+ – Sb(OH)_6^-$ species and the inner-sphere $(\equiv AlO)_2Sb(OH)_4^-$ species, and the chemical model described in Tables 1, 2, and 7. The solid lines show the predicted adsorption in 0.01 *M* KNO_3, the dashed lines in 0.1 *M* KNO_3.

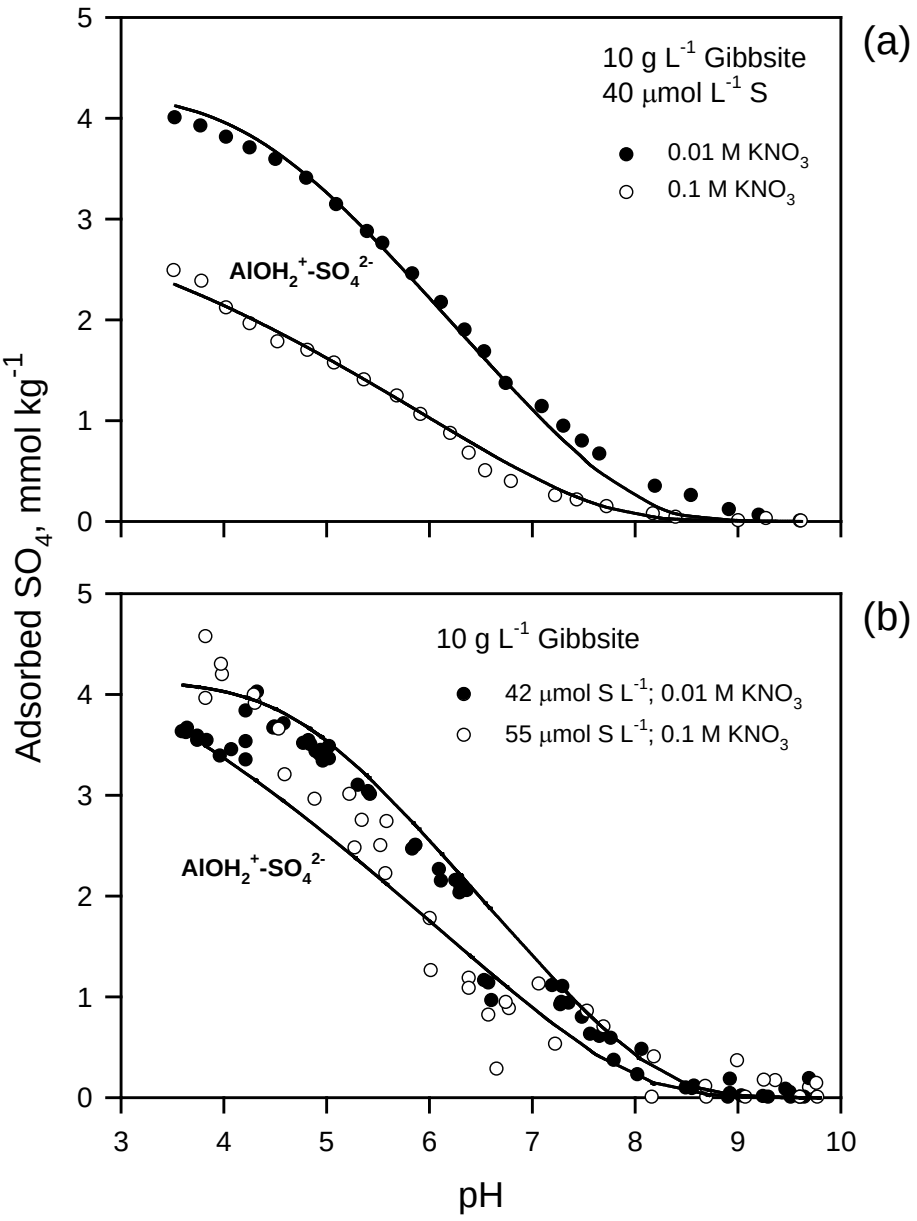

Figure 27. The adsorption of sulfate by gibbsite as a function of pH and ionic strength in (a) beaker and (b) batch systems. The lines represent the triple-layer surface complexation model fit to the experimental data using FITEQL and the chemical model described in Tables 1, 2, and 7. The solid lines show the predicted adsorption of the outer-sphere $\equiv AlOH_2^+–SO_4^{2–}$ species.

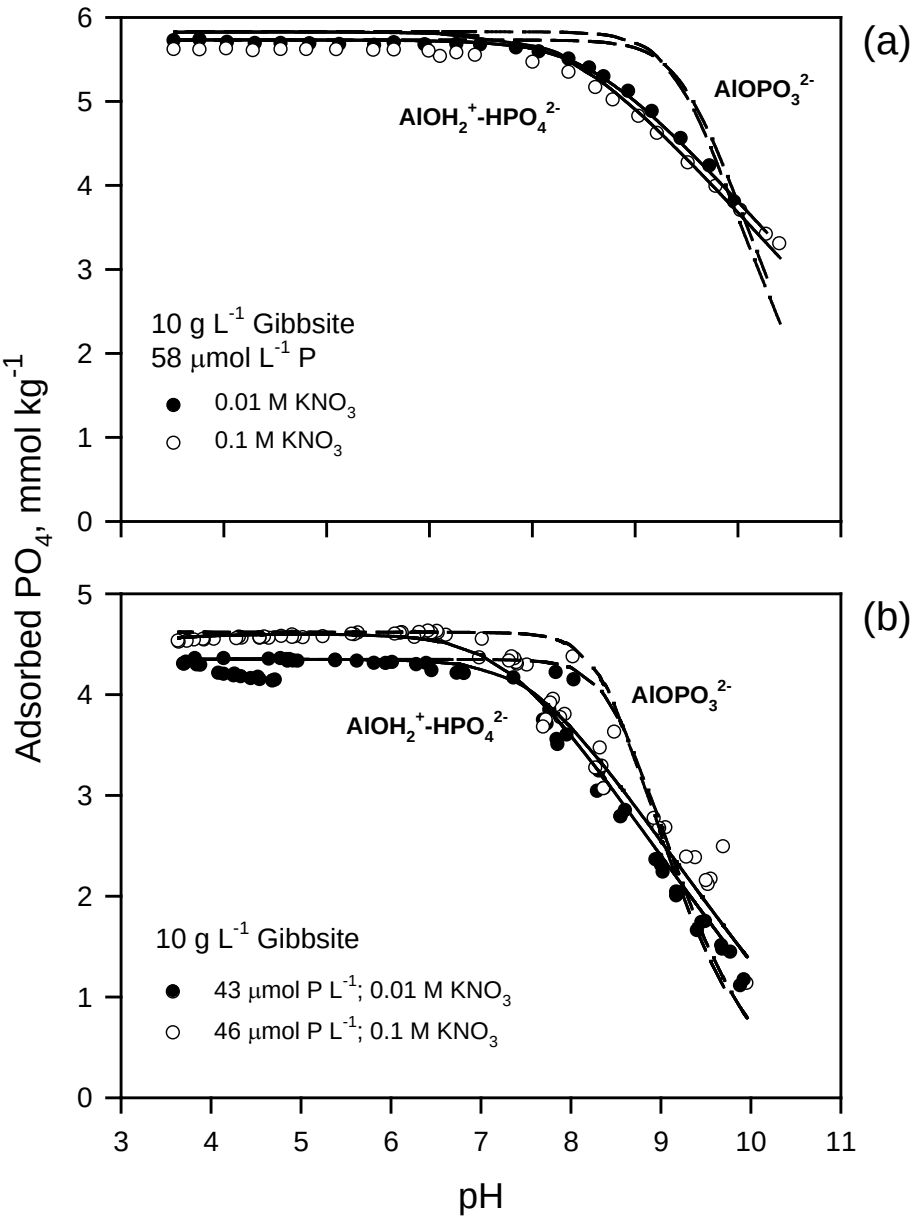

Figure 28. The adsorption of phosphate by gibbsite as a function of pH and ionic strength in (a) beaker and (b) batch systems. The lines represent the triple-layer surface complexation model fit to the experimental data using FITEQL and the chemical model described in Tables 1, 2, and 7. The solid lines show the predicted adsorption of the outer-sphere $\equiv AlOH_2^+–HPO_4^{2–}$ species; the dashed lines show the predicted adsorption of the inner-sphere $\equiv AlOPO_3^{2–}$ species.

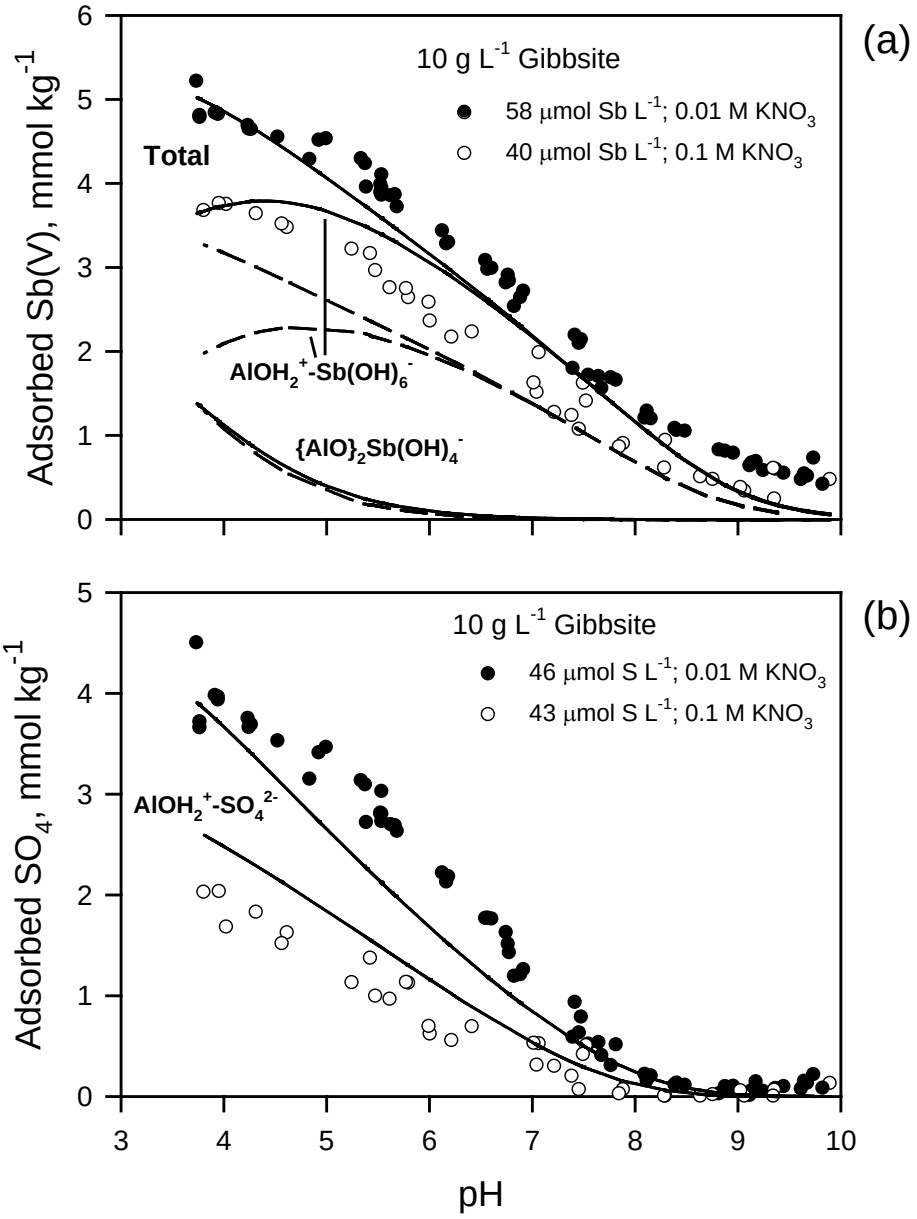

Figure 29. The adsorption of (a) antimonate and (b) sulfate by gibbsite as a function of pH and ionic strength in antimonate-sulfate direct competition systems. The lines represent the triple-layer surface complexation model predictions using the log K^{int} values optimized for non-competitive adsorption of antimonate [Model D; $\equiv AlOH_2^+ – Sb(OH)_6^-$ and $(\equiv AlO)_2Sb(OH)_4^-$ species] or sulfate ($\equiv AlOH_2^+ – SO_4^{2-}$ species) (Table 7). In (a), the solid lines show the predicted adsorption in 0.01 *M* KNO_3, the dashed lines in 0.1 *M* KNO_3. In (b) the solid lines show the predicted adsorption of the outer-sphere $\equiv AlOH_2^+ – SO_4^{2-}$ species.

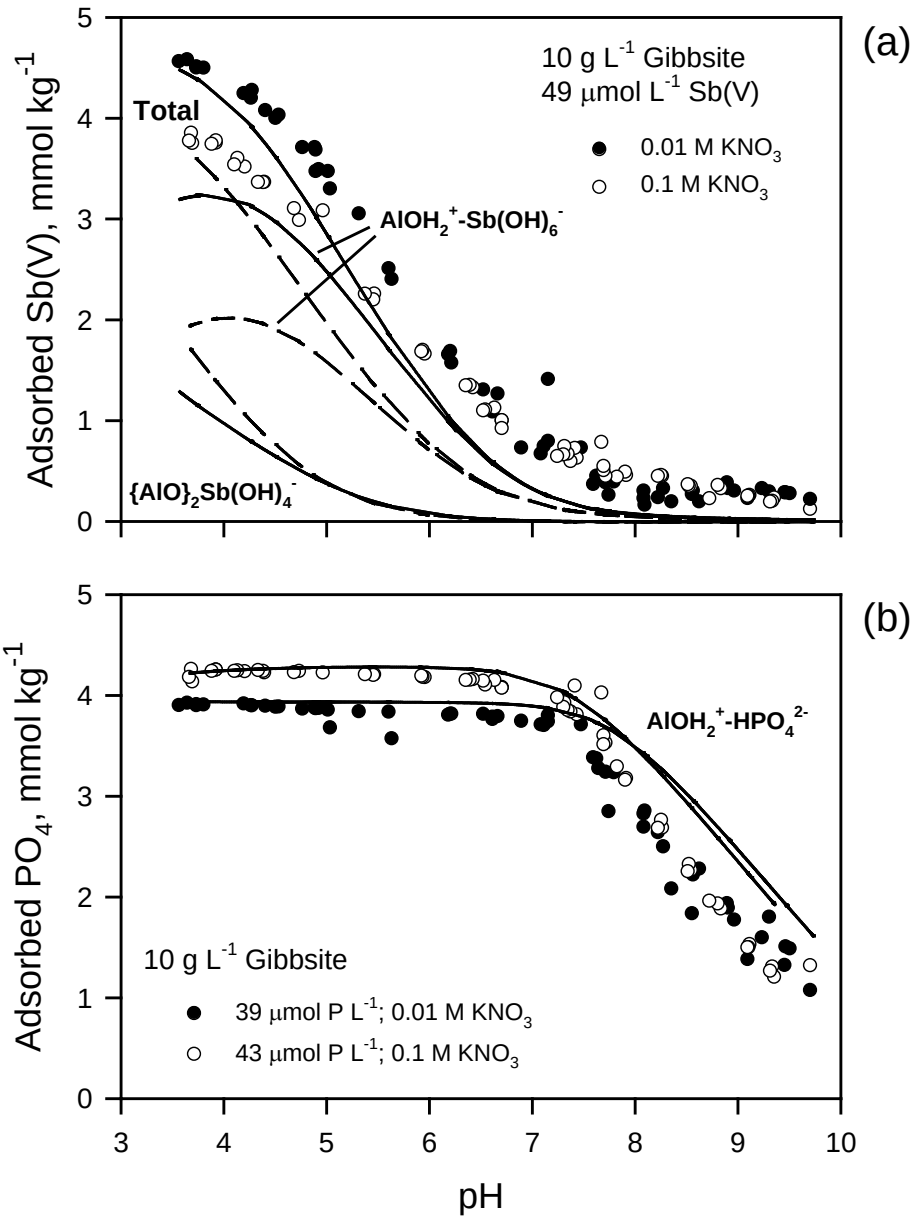

Figure 30. The adsorption of (a) antimonate and (b) phosphate by gibbsite as a function of pH and ionic strength in antimonate-phosphate direct competition systems. The lines represent the triple-layer surface complexation model predictions using the log K^{int} values optimized for non-competitive adsorption of antimonate [Model D; $\equiv AlOH_2^+ – Sb(OH)_6^-$ and $(\equiv AlO)_2Sb(OH)_4^-$ species] or phosphate ($\equiv AlOH_2^+ – HPO_4^{2-}$ species) (Table 7). In (a), the solid lines show the predicted adsorption in 0.01 *M* KNO_3, the dashed lines in 0.1 *M* KNO_3. In (b) the solid lines show the predicted adsorption of the outer-sphere $\equiv AlOH_2^+ – HPO_4^{2-}$ species.

Summary: Antimonate Adsorption by Gibbsite

Gibbsite is a ubiquitous and important mineral in soil. Throughout a broad pH range, the gibbsite surface bears a net positive change (point of zero charge is approximately 10.5), allowing for both anion and ligand retention. For this reason, gibbsite, like many other hydrous metal oxides, is considered a natural scavenger for toxins. Antimonate adsorption by gibbsite is dependent on pH and ionic strength. Adsorption is negligible in strongly alkaline environments (pH > 8), and increases with decreasing pH to an adsorption maximum in the pH 3 to 4 range. Antimonate adsorption decreases with increasing ionic strength, suggesting that anion exchange (outer-sphere surface complexation) is an important retention mechanism. The adsorption of antimonate is reversible in pH > 5 solutions; supporting the conclusion that antimonate is an exchangeable anion. However, adsorption is hysteretic (non-reversible) in pH < 5 systems, indicating that inner-sphere surface complexation becomes important with increasing acidity.

Sulfate and phosphate, which are common anions in the environment, compete with antimonate for adsorption sites at the gibbsite surface. Sulfate is primarily an exchangeable anion in moderately acidic to alkaline solutions, and specifically adsorbed in strongly acidic environments. When sulfate and antimonate are present in equal concentrations, sulfate decreases the retention of antimonite, primarily in acidic systems. However, sulfate does not substantially impact the antimonate adsorption edge (pH at which 50 % of the added antimonate is adsorbed). Phosphate is strongly retained by gibbsite, and is generally considered to be a non-exchangeable, specifically adsorbed ligand. When phosphate and antimonate are present in equal concentrations, the antimonate adsorption edge is shifted to lower pH values (decreasing adsorption throughout a broad pH range). However, phosphate does not impact the antimonate adsorption maximum in strongly acidic systems. Greater concentrations of sulfate and phosphate, as might be expected in natural environments or firing range soils treated with phosphate to stabilize lead, would be expected to have a more pronounced impact on reducing antimonate retention.

The weak, electrostatic retention of antimonate in alkaline systems, with increasing inner-sphere adsorption character with decreasing pH, was also supported by the adsorption isotherm results. A two-site Langmuir adsorption isotherm model was employed to characterize antimonate retention by gibbsite. The model allowed for the thermodynamic assessment of high intensity-low capacity (site type 1) and low intensity-high capacity (site type 2) antimonate adsorption. In alkaline systems, antimonate adsorption decreased with increasing temperature for both site types, indicating an outer-sphere (anion exchange) adsorption mechanism. In acidic solutions, adsorption by low intensity sites decreased with increasing temperature, again indicating anion exchange. However, antimonate adsorption by high intensity sites in acidic systems increased with increasing temperature, indicating an inner-sphere retention process.

Both the zeta potential and proton adsorption characteristics of gibbsite indicated that adsorbed antimonate generated negative surface charge. This response to antimonate adsorption is consistent with the formation of inner-sphere surface complexes. Based on the experimental evidence, surface complexation models were developed to predict antimonate adsorption using the triple layer model formulation. The antimonate adsorption edge as a function of ionic strength was successfully modeled by using a combination of inner- and outer-sphere mechanisms. The outer-sphere mechanism predominated under all pH and ionic strength

conditions, with the inner-sphere mechanism becoming increasingly important as solution pH decreased into the strongly acidic range. The surface complexation model, when applied to competitive antimonate-sulfate and antimonate-phosphate adsorption systems, satisfactorily predicted the antimonate adsorption edge without further optimization.

Kaolinite

Adsorption Edge: Reversibility

The adsorption of antimonate by kaolinite is dependent on solution pH, but independent of ionic strength in the beaker systems (Fig. 31). Antimonate adsorption is at a relative maximum in strongly acidic environments (pH < 4), and decreases with increasing pH to negligible levels in neutral to alkaline conditions (pH > 7). The pH-dependence of antimonate adsorption is similar to the observed by other investigators (Xi et al., 2010; Biver et al., 2011), and for other anions (Essington, 2003). Increasing antimonate retention with decreasing pH is consistent with both inner-sphere and outer-sphere adsorption mechanisms, as described in Eqs. [44] and [45]. The observation that antimonate adsorption is unaffected by ionic strength suggests that there is a significant inner-sphere component to the retention mechanism. This conclusion is also supported by desorption edge data (Fig. 31). As pH is increased from a value of 3.5, antimonate does not readily desorb from the kaolinite surface until the solution pH exceeds approximately 5 (desorption is hysteretic). At pH values above 5 desorption occurs, although desorption remains hysteretic (the slope of the adsorption and desorption edges differ).

The adsorption-desorption edge data suggest that antimonate is retained by both strong and weak reaction mechanisms at the kaolinite surface. Strong, inner-sphere complexation mechanisms (ligand exchange) appear to predominate in acidic environments, while a weak, outer-sphere mechanism (anion exchange) becomes more prevalent in slightly acidic to alkaline systems. It is not uncommon for the predominant mechanism of ligand retention (anion versus ligand exchange) to differ as a function of soil solution pH. For example, ligand exchange mechanisms may predominate in neutral to acidic systems, while anion exchange predominates in alkaline soils. This is the case for arsenate, molybdate, and sulfate retention by Fe- and Al-oxyhydroxides (Catalano et al., 2008; Goldberg et al., 2006; Leuz et al., 2006; Mansour et al., 2009), and for antimonate retention on gibbsite (previous section).

The reactive surface functional group on both gibbsite and kaolinite is the singly-coordinated aluminol (≡AlOH). Generally, the reactivity of this group is similar on both surfaces, such that ligand and metal adsorption on gibbsite has been used to predict adsorption on kaolinite (Sarkar et al., 2000; Essington and Anderson, 2008). However, antimonate adsorption by kaolinite differs from that by gibbsite. The adsorption maximum for antimonate (pH 3.5) is approximately 60 % to 65 % of the added amount for kaolinite, compared with 80 % to 95 % for gibbsite (Figs. 5 and 31). Second, antimonate retention by kaolinite is not influenced by ionic strength. Finally, antimonate retention by kaolinite is negligible in the neutral to alkaline pH range, similar to the findings of Xi et al. (2010) and Biver et al. (2011).

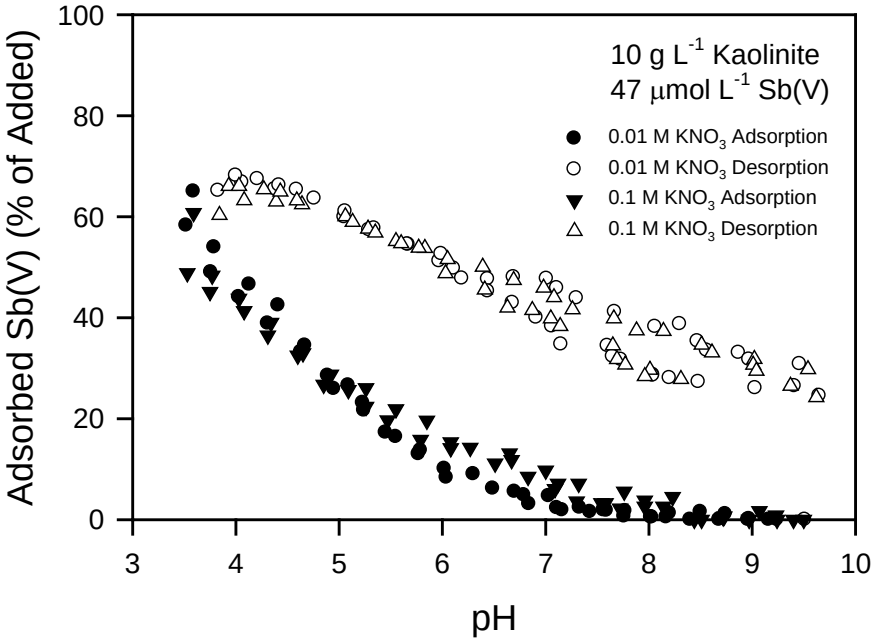

Figure 31. The adsorption (1 h equilibration) and desorption (8 h equilibration) of antimonate by kaolinite as a function of pH and ionic strength.

The difference in the magnitude of antimonate adsorbed by kaolinite and gibbsite may be ascribed to the differences in site density and surface area. The singly-coordinated ≡AlOH site density on gibbsite is approximately 8 nm^{-1} (Hiemstra et al., 1999), while that on kaolinite is 0.55 nm^{-1} (He et al., 1997). Although kaolinite (13.08 $m^2\ g^{-1}$) has a greater surface area than gibbsite (5.82 $m^2\ g^{-1}$), gibbsite has approximately six-times the number of reactive ≡AlOH surface sites (77 μmol g^{-1} for gibbsite versus 12 μmol g^{-1} for kaolinite). Based on these surface site concentrations, the total concentrations of ≡AlOH surface sites is 773 μmol L^{-1} for gibbsite and 120 μmol L^{-1} for kaolinite (Table 1). The computed concentration of antimonate adsorbed by gibbsite at pH 4 (0.01 *M* KNO_3) is approximately 43 μmol L^{-1}, (84 % of the added antimonate, Fig. 5), which accounts for less than 6 % of the available ≡AlOH sites. Similarly for kaolinite, the concentration of adsorbed antimonate at pH 4 in 10 m*M* KNO_3 is approximately 25 μmol L^{-1}, or 21 % of the available, singly-coordinated ≡AlOH sites. Thus, only a fraction of the available surface ≡AlOH groups is participating in antimonate adsorption.

The ionic strength dependence of antimonate adsorption that is absent in the kaolinite data, but present in gibbsite, appears to be a methodology artifact. Antimonate adsorption in batch systems (see *Adsorption Edge: Competitive Effects* section below) does show an ionic strength dependency. Thus, the mechanistic interpretation of the kaolinite adsorption data is consistent with that of the gibbsite data; anion exchange (outer-sphere and electrostatic) in alkaline systems, with a significant ligand exchange (inner-sphere complexation by ≡AlOH surface functional groups) component in acidic systems.

Sulfate is retained predominately by outer-sphere mechanisms by kaolinite (He et al., 1997; Essington and Anderson, 2008). Sulfate adsorption by kaolinite increases with decreasing pH, with a strong dependence on ionic strength (Fig. 32a). In addition, sulfate adsorption is reversible throughout the entire pH range studied (non-hysteretic; the adsorption and desorption edges

overlap), differing from the desorption behavior of antimonate (Fig. 31). These findings are consistent with an anion exchange mechanism and the weak, electrostatic retention of sulfate. Sulfate retention is also depressed, relative to that of antimonate, throughout the entire pH range studied and particularly in the higher ionic strength systems (Fig. 33). Despite their similar acid pK_a values (1.99 for sulfate and 2.85 for antimonate; Table 2), the retention of antimonate by kaolinite is greater than that of sulfate, less affected by ionic strength, and hysteretic.

Phosphate is retained by inner-sphere surface complexation mechanisms throughout a broad pH range (He et al., 1997; Ioannou and Dimirkou, 1997; Essington and Anderson, 2008). Phosphate retention by kaolinite is at a relative maximum at approximately pH 5, decreasing as pH increases or decreases (Fig. 32b), and follows an adsorption envelope that is similar to that observed by Chen et al. (1973) and He et al. (1997). Phosphate adsorption increases with increasing ionic strength, a finding that is not consistent with published results. Further, adsorption increases during desorption. These results may indicate that adsorption equilibrium was not achieved during the 1 h reaction period, which reportedly occurs at reaction times of 24 h or greater (Chen et al., 1973; He et al., 1997; Ioannou and Dimirkou, 1997; Essington and Anderson, 2008). Nevertheless, phosphate retention by kaolinite exceeds that of both antimonate and sulfate (Fig. 33).

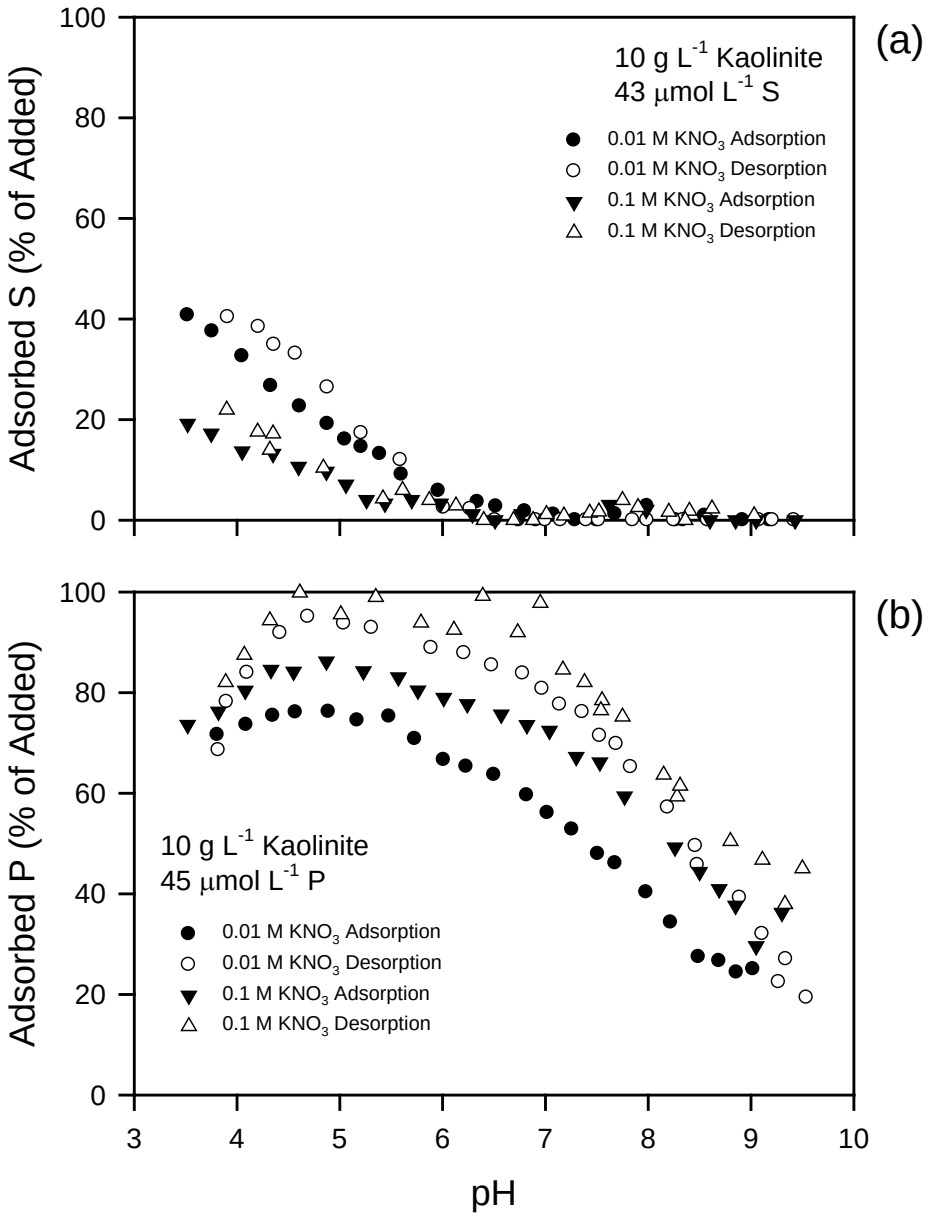

Figure 32. The adsorption and desorption of (a) sulfate and (b) phosphate by kaolinite as a function of pH and ionic strength.

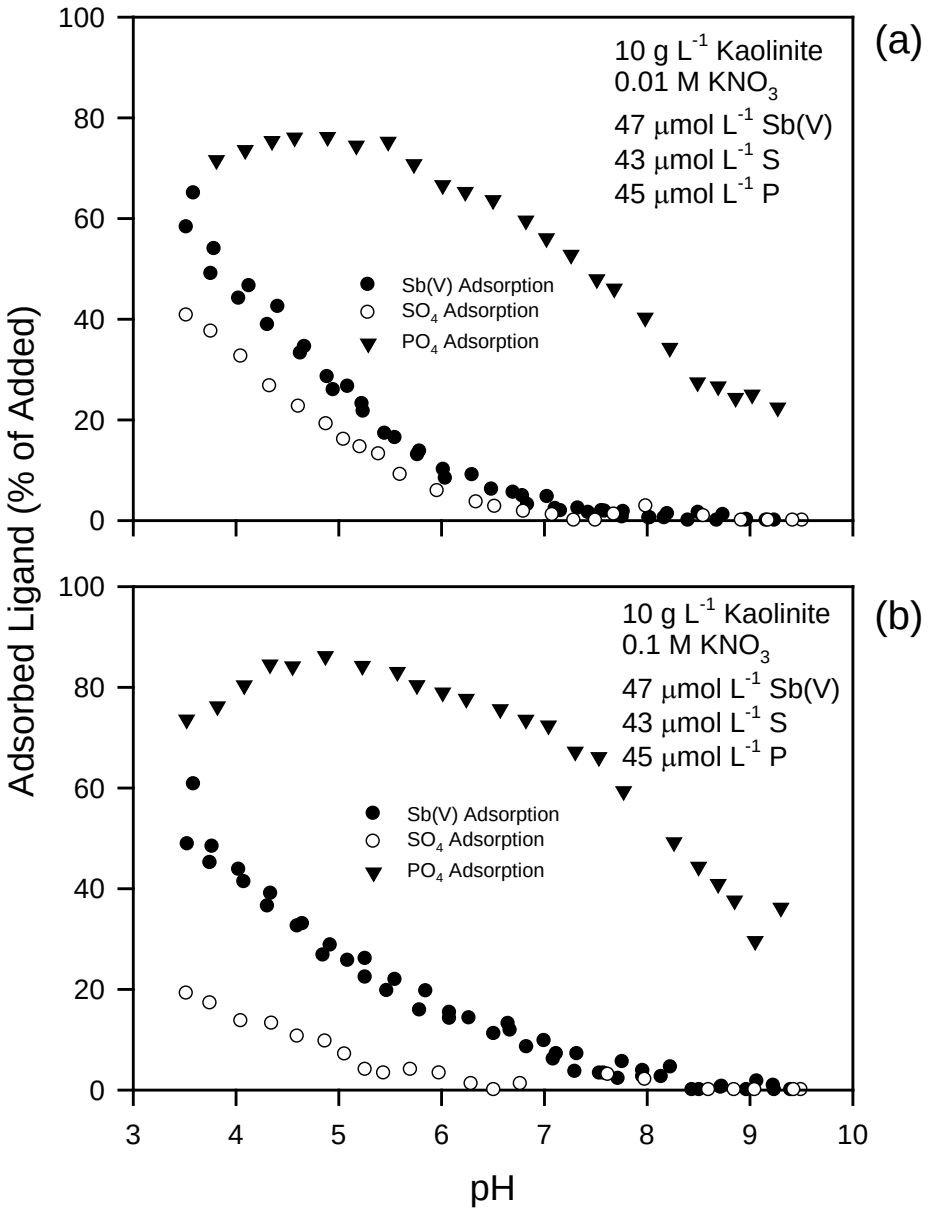

Figure 33. The adsorption antimonate, sulfate, and phosphate by kaolinite as a function of pH in (a) 10 m*M* KNO_3 and (b) 100 m*M* KNO_3 ionic media.

Adsorption Edge: Competition

The adsorption of antimonate, sulfate, and phosphate by kaolinite in the batch systems (Fig. 34) is similar to that observed in the continuous titration (beaker) systems (Figs. 31 and 32), as ligand adsorption generally increases with decreasing pH. However, antimonate retention in the batch systems decreases with increasing ionic strength (by approximately 20 % at pH 3.5), but is unaffected by ionic strength in the beaker systems. Further, phosphate adsorption is insensitive to changes in ionic strength in pH > 5 batch systems, a finding that is consistent with that of other studies (Essington and Anderson, 2008). The differing antimonate and phosphate adsorption edge results of the two experimental designs (beaker and batch) may be attributed to the differing equilibration periods. Essentially, the 1 h reaction period in the beaker systems, as determined from antimonate adsorption kinetics on gibbsite (Fig. 4), was not sufficient to achieve adsorption equilibrium in the kaolinite systems. For all three ligands, increasing the ionic strength depresses ligand retention. This affect is most apparent in strongly acidic systems. The retention of antimonate and sulfate is negligible in pH neutral and alkaline solutions, and sulfate adsorption is less than that of antimonate throughout the pH range studied. The strong ionic strength effect on antimonate and sulfate adsorption indicates that there is a weak electrostatic component to the adsorption mechanism. Phosphate retention is independent of ionic strength in pH > 5 solutions, consistent with inner-sphere surface complexation.

The inclusion of sulfate as a competing ligand does not significantly impact antimonate adsorption by kaolinite (Fig. 35), except in the strongly acidic 0.01 *M* KNO_3 solutions and in the 0.01 *M* KNO_3 system where antimonate was preadsorbed. Similarly, antimonate does not significantly reduce sulfate adsorption by kaolinite (Fig. 36), except in the strongly acidic, low ionic strength solutions. The competitive adsorption findings indicate that antimonate and sulfate compete for adsorption sites on the kaolinite surface, but only in strongly acidic and low ionic strength systems. Further, the order of competing ligand addition does not impact adsorption.

The inclusion of phosphate as a competing ligand reduces the retention of antimonate by kaolinite in both the 0.01 *M* KNO_3 and 0.1 *M* KNO_3 systems (Fig. 37). In the low ionic strength systems, the addition of phosphate shifts the antimonate adsorption edge in the preadsorbed antimonate system from 5 to 4.8, and to approximately 4.1 in the preadsorbed phosphate and direct competition systems. This indicates that the antimonate is more competitive with phosphate when preadsorbed. In the 0.1 *M* KNO_3 medium, antimonate adsorption in the preadsorbed antimonate systems is not influenced by phosphate. However, in the preadsorbed phosphate and direct competition systems, the antimonate adsorption edge is decreased by approximately one pH unit (from 5.5 to 4.5) relative to the antimonate alone systems. Further, antimonate retention in the high ionic strength and strongly acidic systems is not influenced by phosphate. The reduced impact of phosphate on antimonate retention in these systems is associated with the concomitant reduction in phosphate adsorption as solution pH decreases below approximately 4.5 (Fig 34c). In the low ionic strength systems (0.01 *M* KNO_3), the adsorption of phosphate is decreased by the addition of antimonate, primarily in the pH < 5 solutions (Fig. 38a). This effect was also present in the 0.1 *M* KNO_3 solutions, but to a lesser degree (Fig. 38b).

The impact of phosphate and sulfate on antimonate adsorption by kaolinite in the direct competition systems is compared in Fig. 39. In general, both pH and ionic strength (NO_3 concentration) influenced the competitive effects of sulfate and phosphate on antimonate

retention. Low ionic strength and acidic conditions enhanced the competitive effects of both sulfate and phosphate.

Adsorption Isotherms: Thermodynamics

The adsorption of antimonate by kaolinite in both pH 5.5 and 8, 0.01 *M* KNO_3 solutions is Langmuirian; adsorption intensity (isotherm slope) decreases with increasing surface coverage (Fig. 40a). The adsorption isotherms are linear in log-log space (Fig. 40b), indicating that the isotherms are appropriately described by the Freundlich isotherm model (Eq. [3]). Antimonate adsorption is strongly influenced by pH, as adsorption increases with increasing acidity, consistent with the adsorption edge findings described in the previous sections (Figs. 31 and 34). On average, the K_F values for antimonate adsorption at pH 5.5 and 8 were 138 and 15, which represent the surface excess of antimonate (q, in μmol kg^{-1}) when C_{eq} is unity (Table 8). Adsorption of antimonate from pH 5.5 and 8 solutions does not appear to be particularly sensitive to temperature (Fig. 40), and the Freundlich model isotherm parameters log K_F and N do not significantly differ as a function of temperature (Table 8). Further, in the pH 8 systems, antimonate adsorption is not detected in the 25°C and 35°C systems (again, consistent with the adsorption edge results).

Plots of K_d vs. q indicate that the adsorption of antimonate in pH 5.5 solutions may be described by the two-site Langmuir model (Eq. [7]; Fig. 41). Conversely, the one-site Langmuir model satisfactorily describes adsorption in pH 8 solutions (Fig. 42). For all temperatures in the pH 5.5 systems, the K_d vs. q plot may be split into two linear segments, where each segment adheres to the Langmuir model (Eq. [5]). The linear segment at low q describes high intensity and low capacity antimonate adsorption (type 1 sites); whereas at high q, low intensity and high capacity retention (type 2 sites) is described. The slope, and K_d and q intercept values obtained through the linear regression analysis of the isotherm segments in Fig. 41 were used to compute the two-site Langmuir isotherm parameters; K_1 and b_1, and K_2 and b_2, using the interpolation procedure of Sposito (1982) (Table 8). Linear regression analysis of the K_d vs. q plots in Fig. 42 was used to derive the one-site Langmuir parameters for antimonate adsorption in pH 8 systems. The K_1 and b_1 parameters describe antimonate adsorption by high intensity and low capacity sites, while K_2 and b_2 describe adsorption by low intensity and high capacity sites. The Henry's Law constants for the type 1 sites (K_{ad1}), generated from the Langmuir parameters K_1 and b_1 (Table 8), tend to increase with increasing temperature in the pH 5.5 systems (Fig. 43). However, K_{ad2} does not vary as a function of temperature. Similarly, K_{ad} does not vary as a function of temperature for adsorption in pH 8 systems.

Both the enthalpy (ΔH_{ad}) and entropy (ΔS_{ad}) of adsorption were computed for antimonate adsorption using the van't Hoff equation (Eq. [9]), as applied to the ln K_{ad} vs. T^{-1} data in Fig. 43. For high intensity, low capacity adsorption (type 1 sites) in pH 5.5, ΔH_{ad} is positive (16.68 kJ mol^{-1}) and $T\Delta S_{ad}$ is large (28.33 kJ mol^{-1} at 298 K) relative to ΔH_{ad}, indicating that antimonate adsorption is endothermic and entropically driven (Table 9). However, for pH 8, and for low intensity, high capacity adsorption (type 2 sites) in pH 5.5, ΔH_{ad} is positive, but not significantly different from zero, and $T\Delta S_{ad}$ is large relative to ΔH_{ad}, indicating that antimonate adsorption is entropically driven. For both site types, and for both pH conditions, the free energy of adsorption (ΔG_{ad}) is negative, indicating that antimonate adsorption is spontaneous.

Exothermic (negative ΔH_{ad}), enthalpically-driven adsorption is generally indicative of an ion exchange mechanism (adsorption increases with decreasing temperature). Thus, antimonate

adsorption by kaolinite in pH 8, and by type 2 sites in pH 5.5, is predominately an outer-sphere surface complexation process. Antimonate adsorption by type 1 sites in pH 5.5 is endothermic (positive ΔH_{ad}) and entropically-driven (heat is absorbed during antimonate adsorption), suggesting inner-sphere complexation. Although ΔH_{ad} is positive (16.68 kJ mol^{-1}), the magnitude of ΔH_{ad} is small relative to that typically found for the inner-sphere surface complexation of ligands. Enthalpy values for the retention of specifically-adsorbed ligands by variable-charge minerals are generally < 40 kJ mol^{-1}, although similar in magnitude ΔH_{ad} values have been used to infer an ion exchange mechanism (Zhang and Selim, 2008; Li et al., 2008; Ferreiro and de Bussetti, 2007). The inner-sphere adsorption of arsenate by Al and Fe oxides has been reported to generate ΔH_{ad} values of 25.11 and 17.83 kJ mol^{-1} (Helmy et al., 1996; Partey et al., 2008). Enthalpy values for the inner-sphere complexation of phosphate and 2-ketogluconate by Fe oxides range between 22 and 81.84 kJ mol^{-1} (Juang and Chung, 2004; Mezzener and Bensmaili, 2008; Mustafa et al., 2008: Journey et al., 2010). The ΔH_{ad} value computed for antimonate adsorption to the high intensity sites indicates that there is an inner-sphere component to the retention mechanism in acidic systems.

Table 8. Freundlich and two-site Langmuir isotherm parameters, and the Henry's Law constants (K_{ad} values) for the adsorption of antimonate by kaolinite.

	Freundlich parameters†			Two-site Langmuir parameters‡					
T, °C	log K_F	K_F	N	K_1	b_1	K_{ad1}	K_2	b_2	K_{ad2}
				pH 5.5					
5	2.063	115.6	0.633	0.2071	376	77.85	0.0199	2143	42.65
15	2.012	102.8	0.639	0.2285	314	71.85	0.0337	1206	40.68
25	2.062	115.3	0.589	0.5498	188	103.2	0.0493	1148	56.56
35	2.336	216.8	0.421	0.3150	484	152.3	0.0552	804.0	44.39
				pH 8§					
				K_L	b	K_{ad}			
5	1.077	11.9	0.828	0.0277	475.0	13.13			
15	1.276	18.9	0.639	0.0467	302.4	14.11			
25									
35									

†log K_F and N were obtained by linear regression analysis of Eq. [3]. Within pH, log K_F and N do not differ significantly at a function of temperature at $P = 0.05$.

‡K_1 and b_1 (high intensity, low capacity adsorption), and K_2, and b_2 (low intensity, high capacity adsorption) were obtained by linear regression analysis of Eq. [5] and the data presented in Fig. 41, and by employing the method of Sposito (1982); $K_{ad1} = b_1K_1$ and $K_{ad2} = b_2K_2$, for the two-site Langmuir model (Eq. [7]). Units of K_1 and K_2 are L μmol^{-1}; b_1 and b_2 are $\mu mol\ kg^{-1}$; and K_{ad1} and K_{ad2} are L kg^{-1}.

§The Langmuir parameters for antimonate adsorption in pH 8 were obtained by linear regression analysis of Eq. [5] and the data presented in Fig. 42 for the one-site Langmuir model (Eq. [4]).

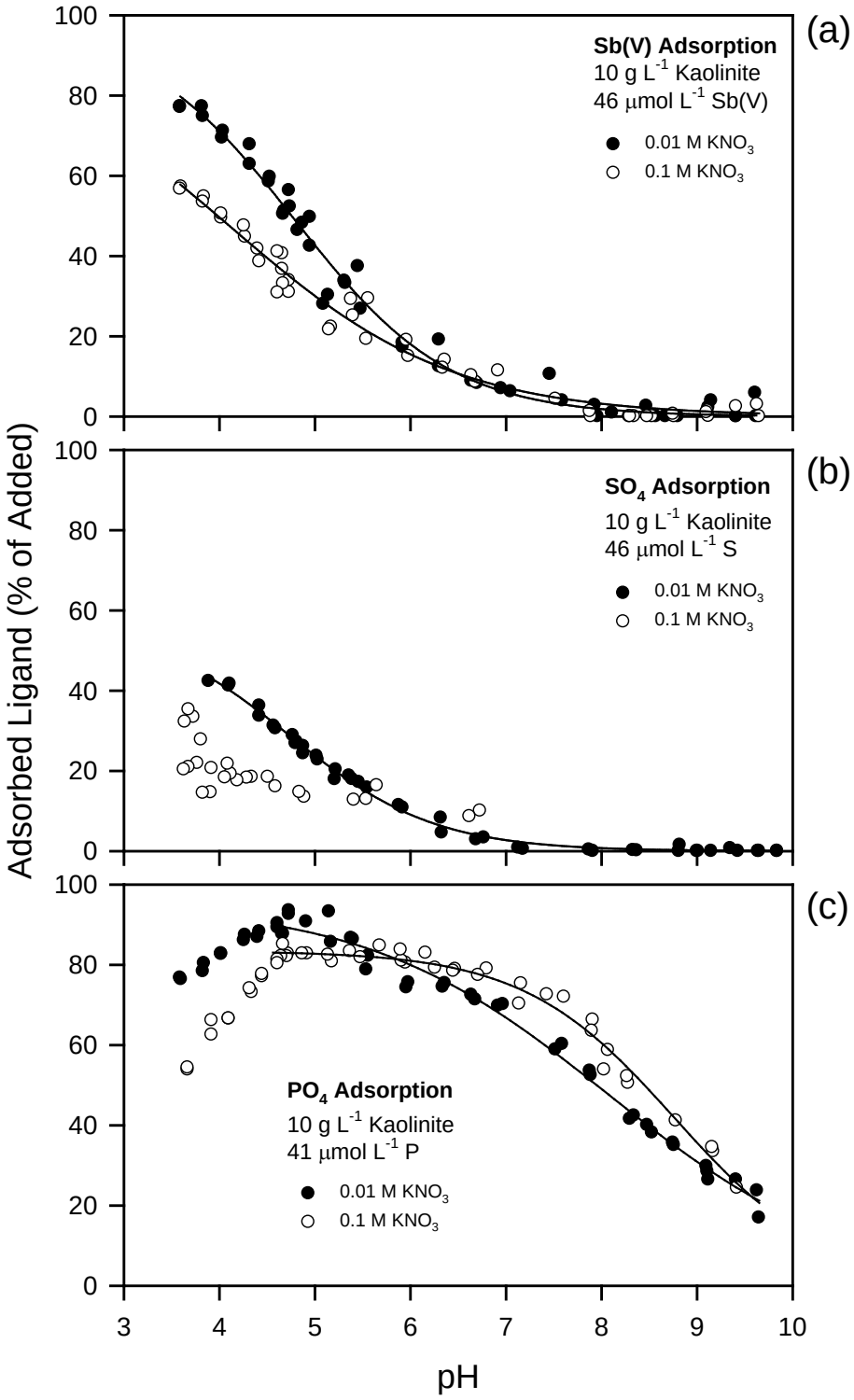

Figure 34. The adsorption of (a) antimonate, (b) sulfate, and (c) phosphate by kaolinite from batch equilibrium systems as a function of pH and ionic strength. The solid lines represent the application of Eq. [46].

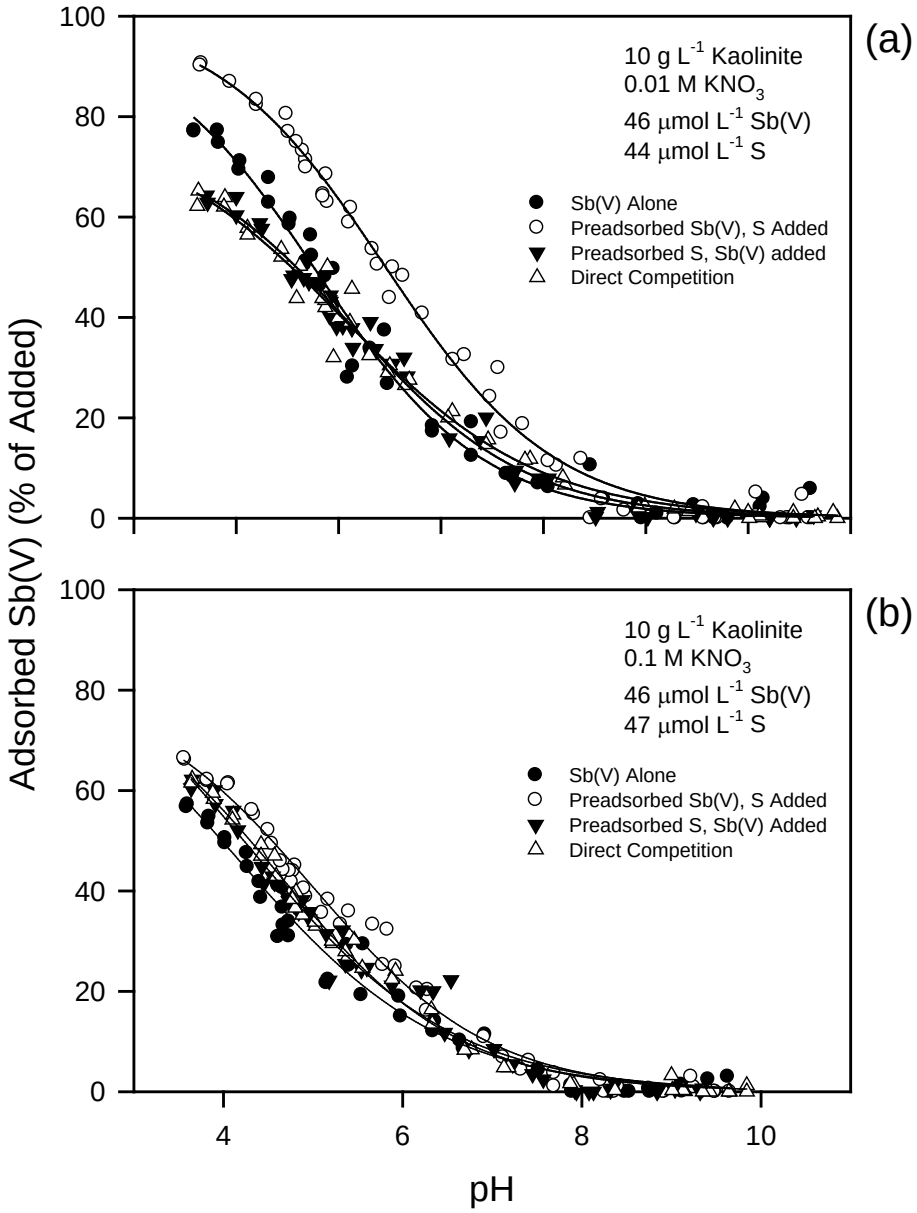

Figure 35. The competitive adsorption of antimonate by kaolinite in the presence of sulfate in (a) 10 m*M* KNO_3 and (b) 100 m*M* KNO_3 electrolyte media as a function of pH and method of sulfate addition. The solid lines represent the application Eq. [46].

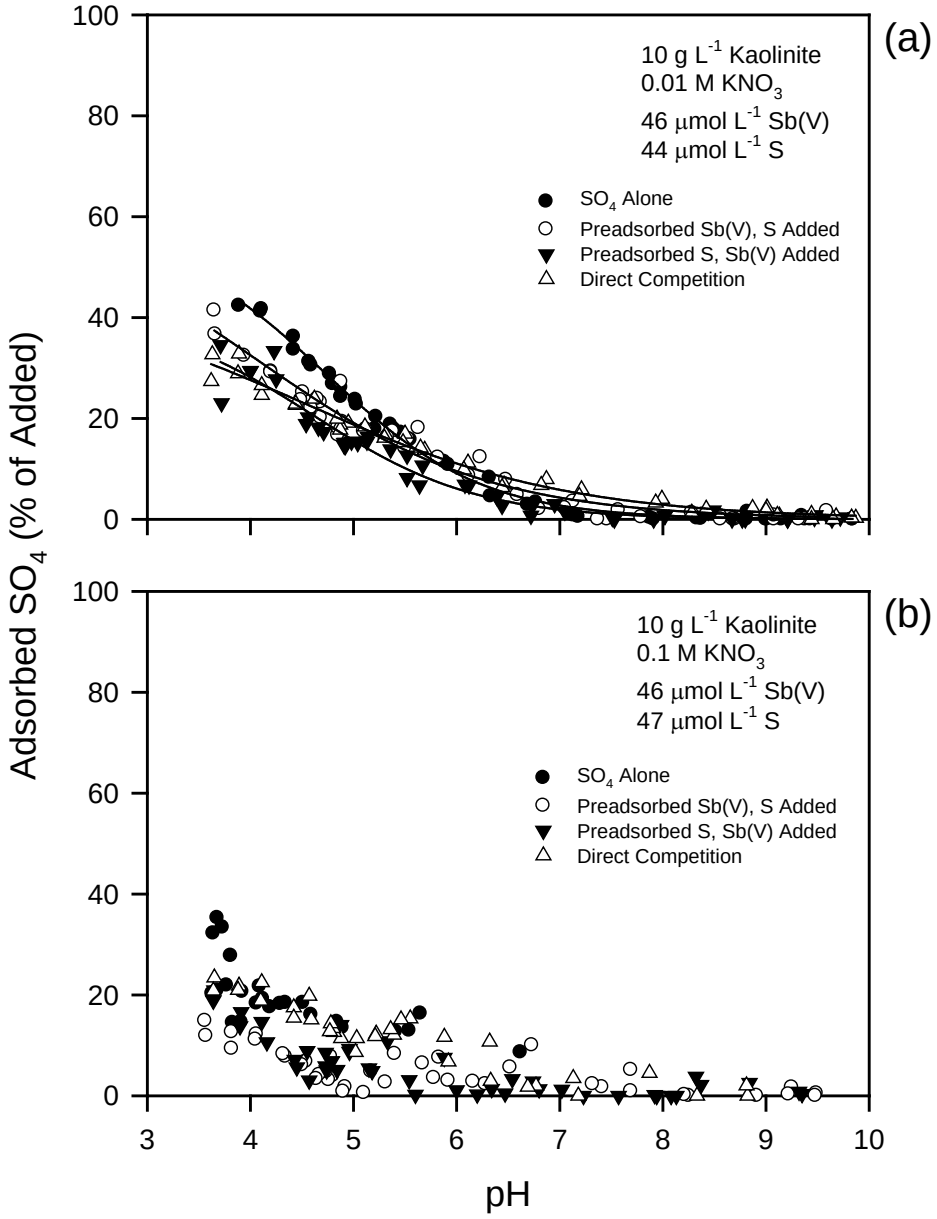

Figure 36. The competitive adsorption of sulfate by kaolinite in the presence of antimonate in (a) 10 m*M* KNO_3 and (b) 100 m*M* KNO_3 electrolyte media as a function of pH and method of antimonate addition. The solid lines represent the application Eq. [46].

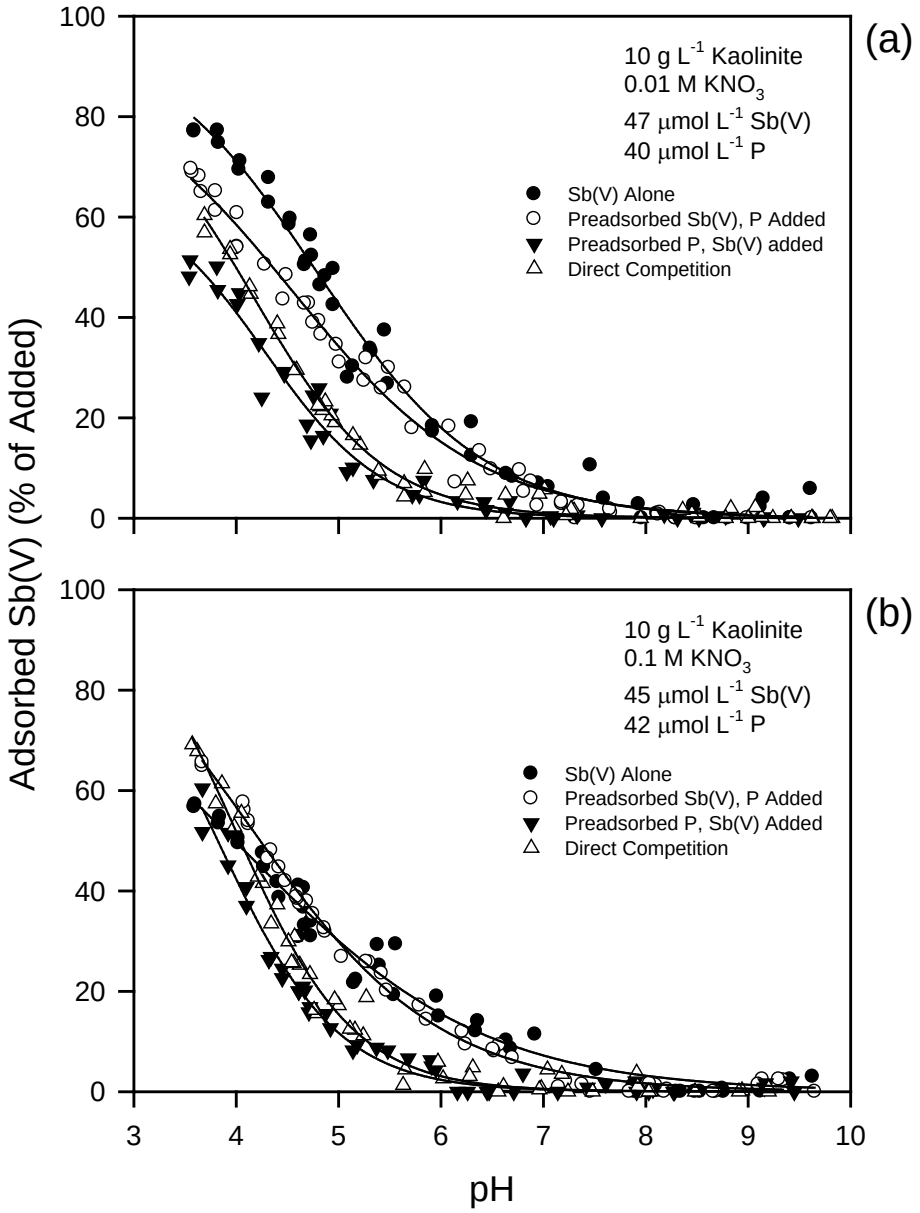

Figure 37. The competitive adsorption of antimonate by kaolinite in the presence of phosphate in (a) 10 m*M* KNO_3 and (b) 100 m*M* KNO_3 electrolyte media as a function of pH and method of phosphate addition. The solid lines represent the application Eq. [46].

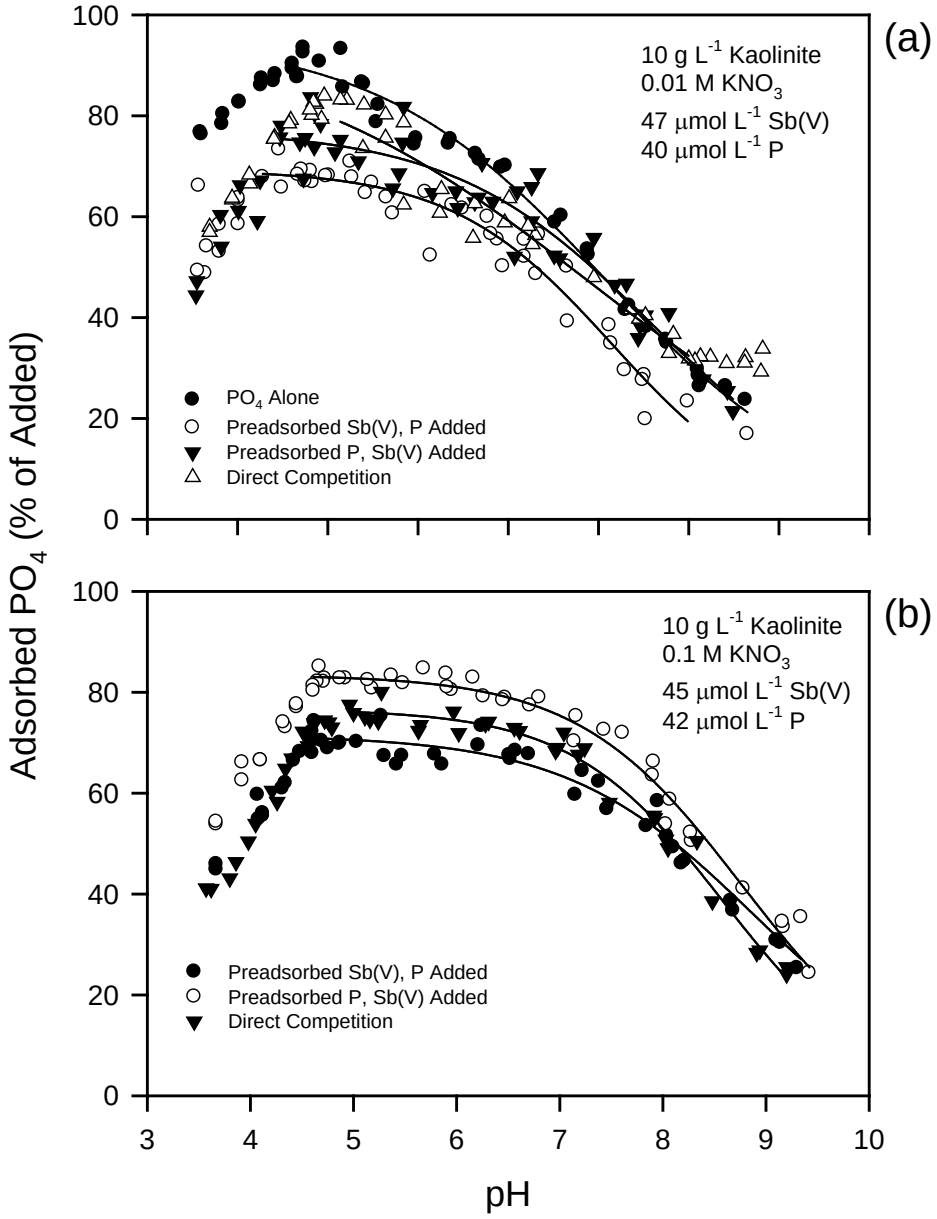

Figure 38. The competitive adsorption of phosphate by kaolinite in the presence of antimonate in (a) 10 m*M* KNO_3 and (b) 100 m*M* KNO_3 electrolyte media as a function of pH and method of antimonate addition. The solid lines represent the application Eq. [46].

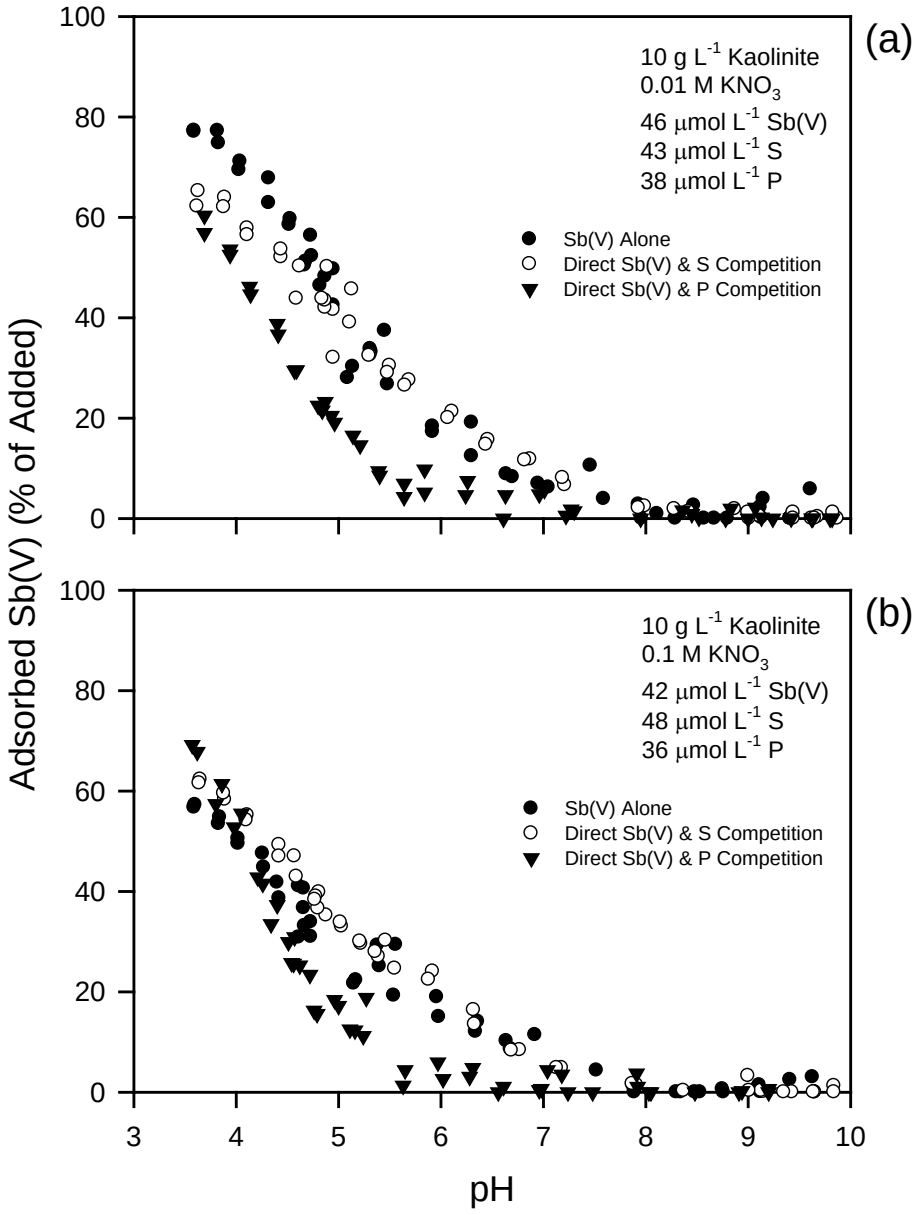

Figure 39. The competitive adsorption of antimonate by kaolinite in the presence of sulfate and phosphate in (a) 10 m*M* KNO_3 and (b) 100 m*M* KNO_3 electrolyte media as a function of pH for the direct ligand competition systems.

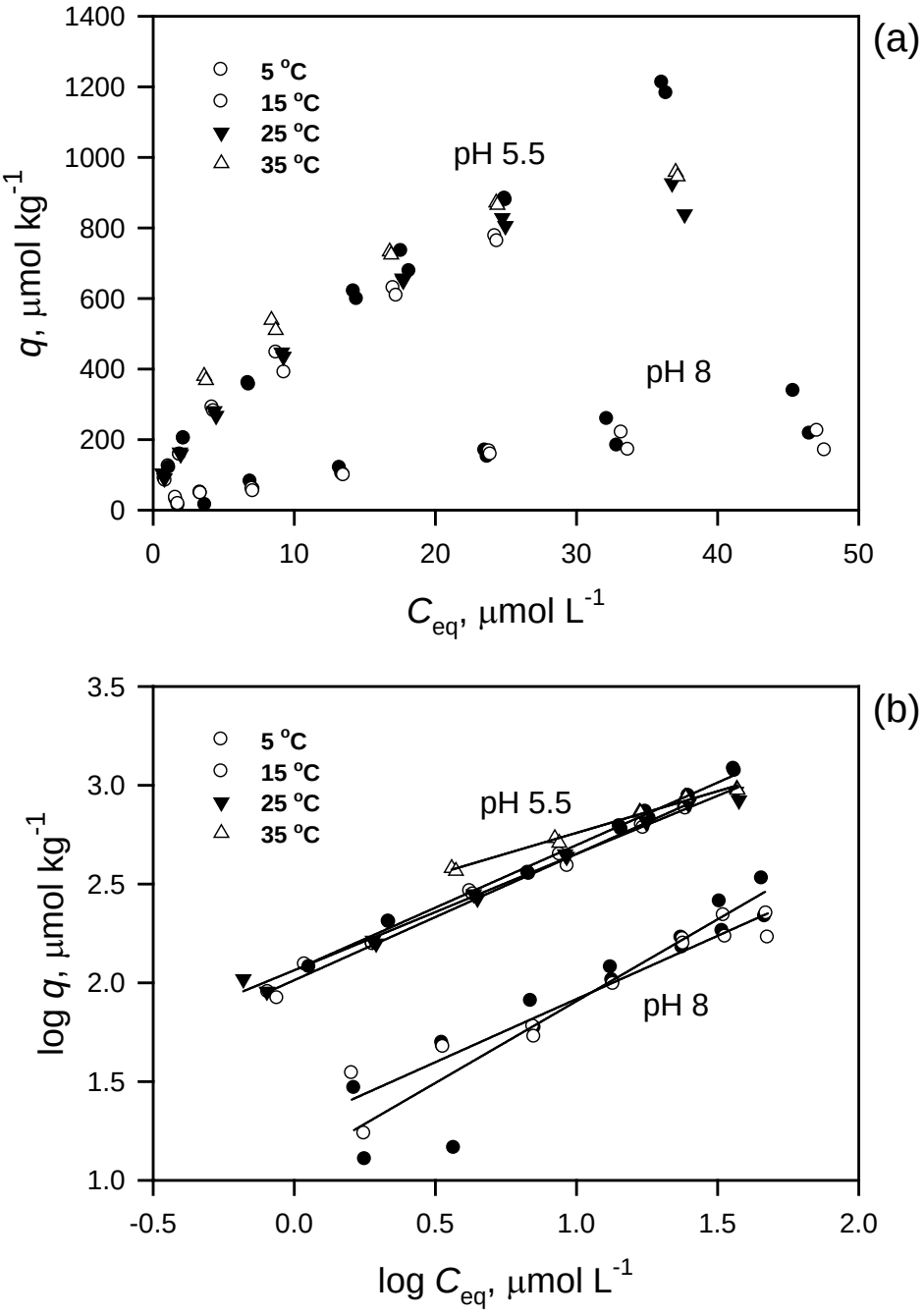

Figure 40. Adsorption isotherms, plotted in (a) normal space and (b) log-log space, illustrating the adsorption (q) of antimonate in 0.01 M KNO_3 by kaolinite (10 g L^{-1}) as a function equilibrium solution concentration (C_{eq}), pH, and temperature.

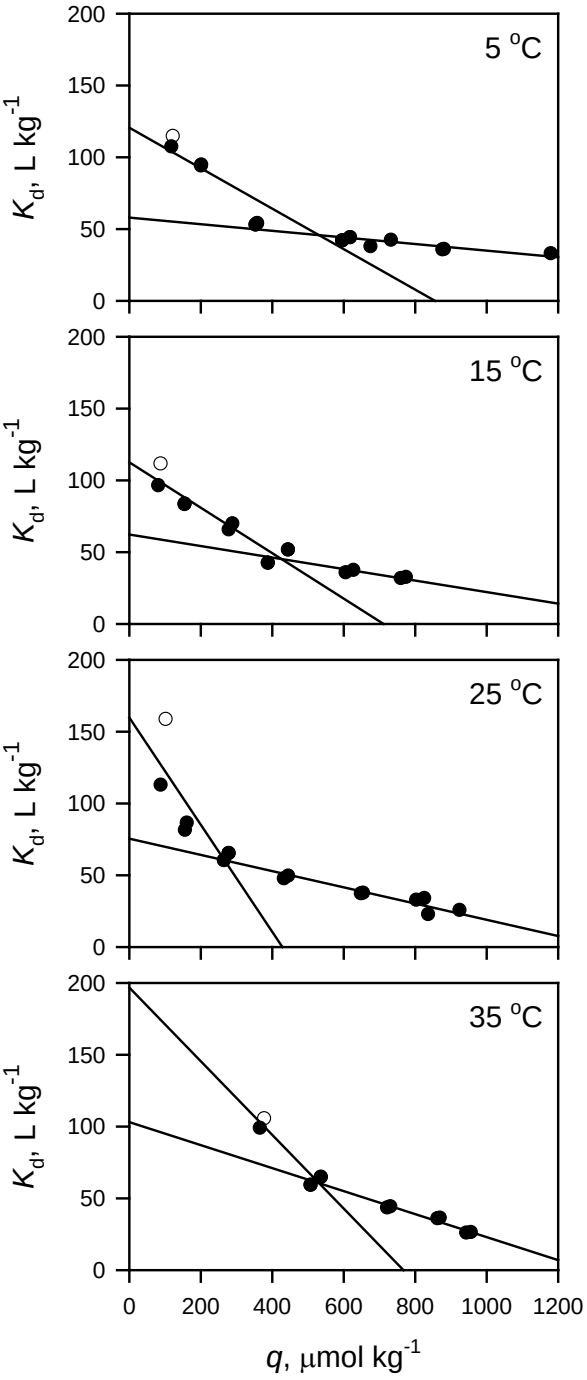

Figure 41. Application of the transformed version of the Langmuir model to K_d vs. q plots of the pH 5.5 antimonate adsorption isotherm data described in Fig. 40a. The adsorption of antimonate by kaolinite is described by two separate Langmuir isotherm equations (Table 8).

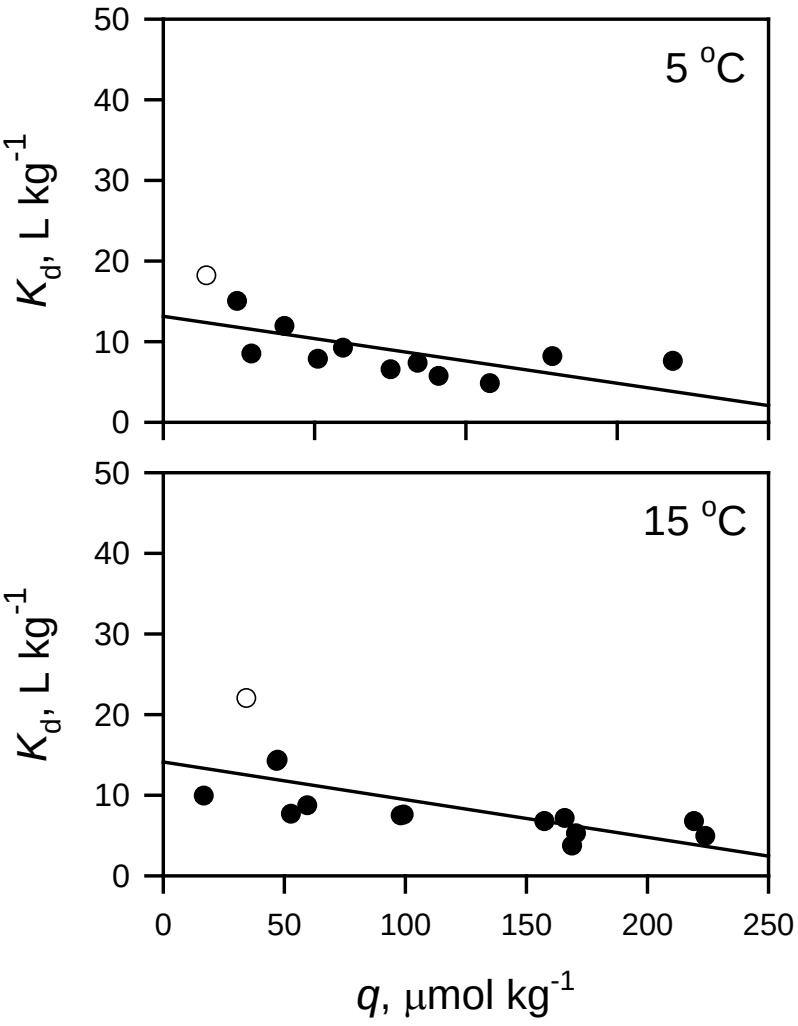

Figure 42. Application of the transformed version of the Langmuir model to K_d vs. q plots of the pH 8 antimonate adsorption isotherm data described in Fig. 40a. The adsorption of antimonate by kaolinite is described by the Langmuir isotherm equation (Table 8).

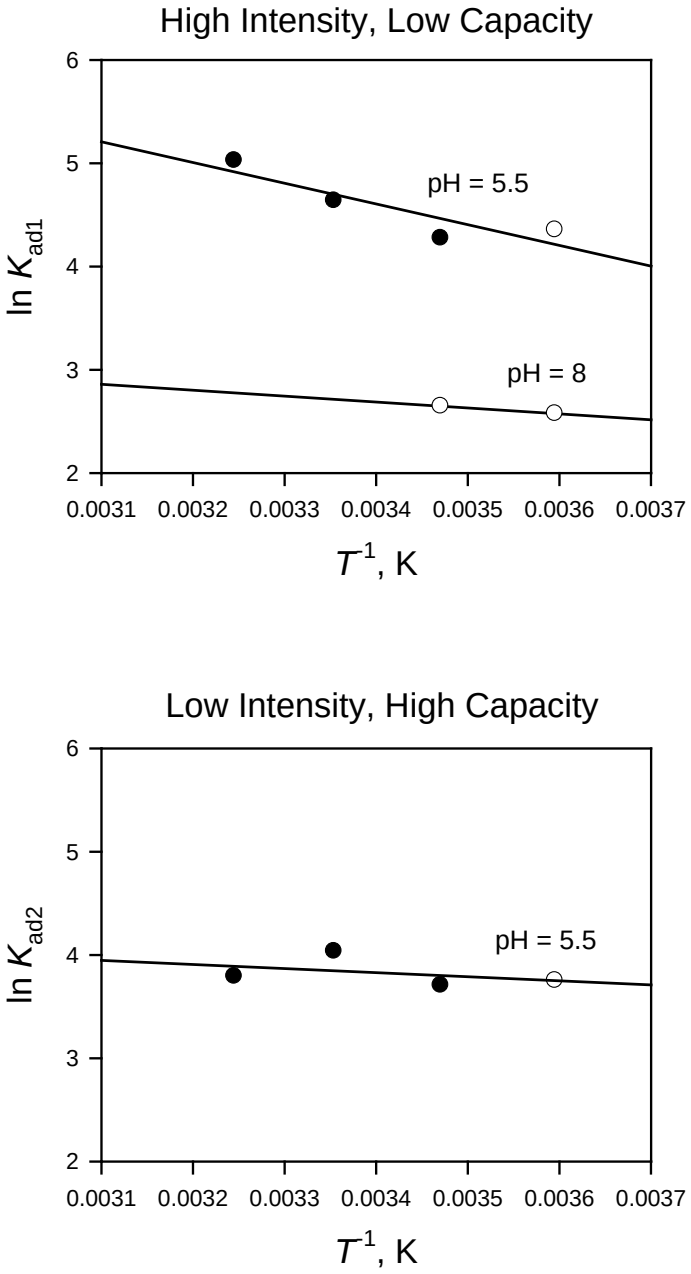

Figure 43. Temperature dependence of the Henry's Law constant for high intensity, low capacity (site type 1; $K_{ad1} = K_1 b_1$) and low intensity, high capacity (site type 2; $K_{ad2} = K_2 b_2$) for antimonate adsorption by kaolinite (K_1 and K_2, and b_1 and b_2 are adsorption constants from the two-site Langmuir equation, Eq. [7]). The lines represent the least squares linear regression analysis of the van't Hoff equation (Eq. [9]) and the ln K_{ad} vs. T^{-1} data, where T is the thermodynamic temperature.

Table 9. Thermodynamic parameters for the adsorption of antimonate by kaolinite.†

	Site type 1			Site type 2		
Temperature	ΔH_{ad}	ΔS_{ad}	ΔG_{ad}	ΔH_{ad}	ΔS_{ad}	ΔG_{ad}
°C	kJ mol^{-1}	J K^{-1}mol^{-1}	kJ mol^{-1}	kJ mol^{-1}	J K^{-1}mol^{-1}	kJ mol^{-1}
	pH 5.5					
5	16.68	95.01	–9.77	3.29‡	43.02	–8.68
15			–10.70			–9.11
25			–11.65			–9.54
35			–12.60			–9.97
	pH 8					
5	4.78‡	38.58	–5.95			
15			–6.34			

†Enthalpy (ΔH_{ad}) and entropy (ΔS_{ad}) of adsorption are temperature independent and computed using the van't Hoff equation (Eq. [9]) analysis of the influence of temperature on the Henry's Law constant for antimonate adsorption by site types 1 and 2 (Fig. 43). Free energy of adsorption (ΔG_{ad}) computed using Eq. [11].

‡ΔH_{ad} values are not significantly different from 0 based on the linear regression analysis of Fig. 43.

Electrostatics at the Solid-Solution Interface

Zeta potential and proton adsorption curves for kaolinite in the swamping electrolyte (KNO_3) are illustrated in Fig. 44. The KNO_3 system is assumed to represent surface charging in the absence of inner-sphere complexation. For kaolinite, the isoelectric point (IEP) and the point of zero charge (PZC) is 4.5 in 0.01 *M* KNO_3, shifting to 6.5 in 0.1 *M* KNO_3 (Fig. 44a). The lack of a common intersection point (CIP) for the zeta potential measurements, and an increasing IEP with increasing ionic strength, are consistent with the findings of others (Vane and Zang, 1997; Chassange et al., 2009; Kosmulski and Dahlsten, 2006). Generally, these findings for kaolinite indicate the inner-sphere complexation of potassium, although other causes have been suggested (Chassange et al., 2009). The measured kaolinite IEP (in 0.01 *M* KNO_3) is within the 2.9 to 5 range compiled by Kosmulski (2009). The adsorbed proton concentration (Q_h) increases with decreasing pH, with a CIP of approximately 4.4. However, Q_h was not influenced by the background electrolyte concentration (Fig. 44b), a result of the low surface reactivity of kaolinite.

When a ligand other than the indifferent electrolyte is present, electrophoretic mobility will reflect the adsorption mechanism. Adsorption of an anionic ligand in the is-plane will decrease the zeta potential and shift the IEP to lower pH values (additional protonation, i.e., lower pH, required for site neutralization). The adsorption of a ligand in the os-plane will not affect the IEP, relative to that in the indifferent electrolyte. However, a decrease in the zeta potential may be observed if the adsorbed ligand has higher valence than the indifferent electrolyte (providing greater negative charge to the near-surface region bounded by the particle shear plane). The proton adsorption characteristics may also be used to infer the ligand adsorption mechanism.

Adsorption of an anionic ligand in the is-plane will increase Q_h in response to the addition of intrinsic negative surface charge (decreasing σ_{is}), while adsorption of a ligand in the os-plane will not have an effect on Q_h.

The presence of K_2SO_4 results in a negative shift in the zeta potential of kaolinite when pH < 7, relative to the KNO_3 systems (Fig. 44a). At pH 4, the zeta potential shifts from +2.0 mV in 0.01 *M* KNO_3 to –20.2 mV in 0.01 *M* K_2SO_4, and to –17.1 mV in 0.01 *M* KNO_3 + 0.01 *M* K_2SO_4. Similarly, the zeta potential shifts from +12.2 mV in 0.1 *M* KNO_3 to –5.7 mV 0.1 *M* KNO_3 + 0.01 *M* K_2SO_4. The less positive zeta potential values indicate that the adsorbed complexes of sulfate provide greater negative charge to the near-surface region bounded by the particle shear plane, relative to the background electrolyte (divalent SO_4^{2-} vs. monovalent NO_3^-). Further, a charge reversal is not observed within the pH range studied when sulfate is present, which suggests the inner-sphere complexation of sulfate. A comparison of the KNO_3 and K_2SO_4 systems indicates that sulfate adsorption results is an upward shift in Q_h, also reflective of the inner-sphere complexation of SO_4^{2-}(Fig. 44b).

The presence of KH_2PO_4 also results in a negative shift in the zeta potentials of kaolinite, relative to the KNO_3 systems (Fig. 45a), which is observed when pH is less than 10. At pH 4, the zeta potential shifts from +2.0 mV in 0.01 *M* KNO_3 to –22.4 mV in 0.01 *M* KH_2PO_4, and to –23.6 mV in 0.01 *M* KNO_3 + 0.01 *M* KH_2PO_4. Similarly, the zeta potential shifts from +12.2 mV in 0.1 *M* KNO_3 to –12.2 mV 0.1 *M* KNO_3 + 0.01 *M* KH_2PO_4. A surface charge reversal was also not observed in the pH range studied, although an extrapolation of the zeta potential vs. pH curves indicates that charge reversal would occur in the pH 2 to 3 range for the three KH_2PO_4 systems. This is macroscopic evidence of the inner-sphere complexation of phosphate by kaolinite. This finding is consistent with the strong phosphate adsorption behavior, and the lack of an ionic strength effect (Fig. 34c). A comparison of the KNO_3 and KH_2PO_4 systems indicates that phosphate adsorption results is an upward shift in Q_h, which is similar in magnitude to that observed during sulfate adsorption when pH < pH_{pzc}. This is reflective of the inner-sphere complexation of phosphate species ($H_2PO_4^-$ and HPO_4^{2-}).

The influence of $KSb(OH)_6$ on the zeta-potential and Q_h at the kaolinite surface was more pronounced than that of either sulfate or phosphate (Fig. 46). The presence of $KSb(OH)_6$ results in a negative shift in the zeta potentials of kaolinite, relative to the KNO_3 systems (Fig. 46a) for all pH values less than 10. At pH 4, the zeta potential shifts from +2.0 mV in 0.01 *M* KNO_3 to –41.4 mV in 0.01 *M* $KSb(OH)_6$, and to –42.1 mV in 0.01 *M* KNO_3 + 0.01 *M* $KSb(OH)_6$. Similarly, the zeta potential shifts from +12.2 mV in 0.1 *M* KNO_3 to –22.6 mV 0.1 *M* KNO_3 + 0.01 *M* $KSb(OH)_6$. A surface charge reversal was also not observed in the pH range studied, reflecting the inner-sphere complexation of antimonate. A comparison of the KNO_3 and $KSb(OH)_6$ systems shows that antimonate adsorption results in an upward shift in Q_h, which indicates the inner-sphere complexation of antimonate, particularly when pH < 6 (Fig. 46b).

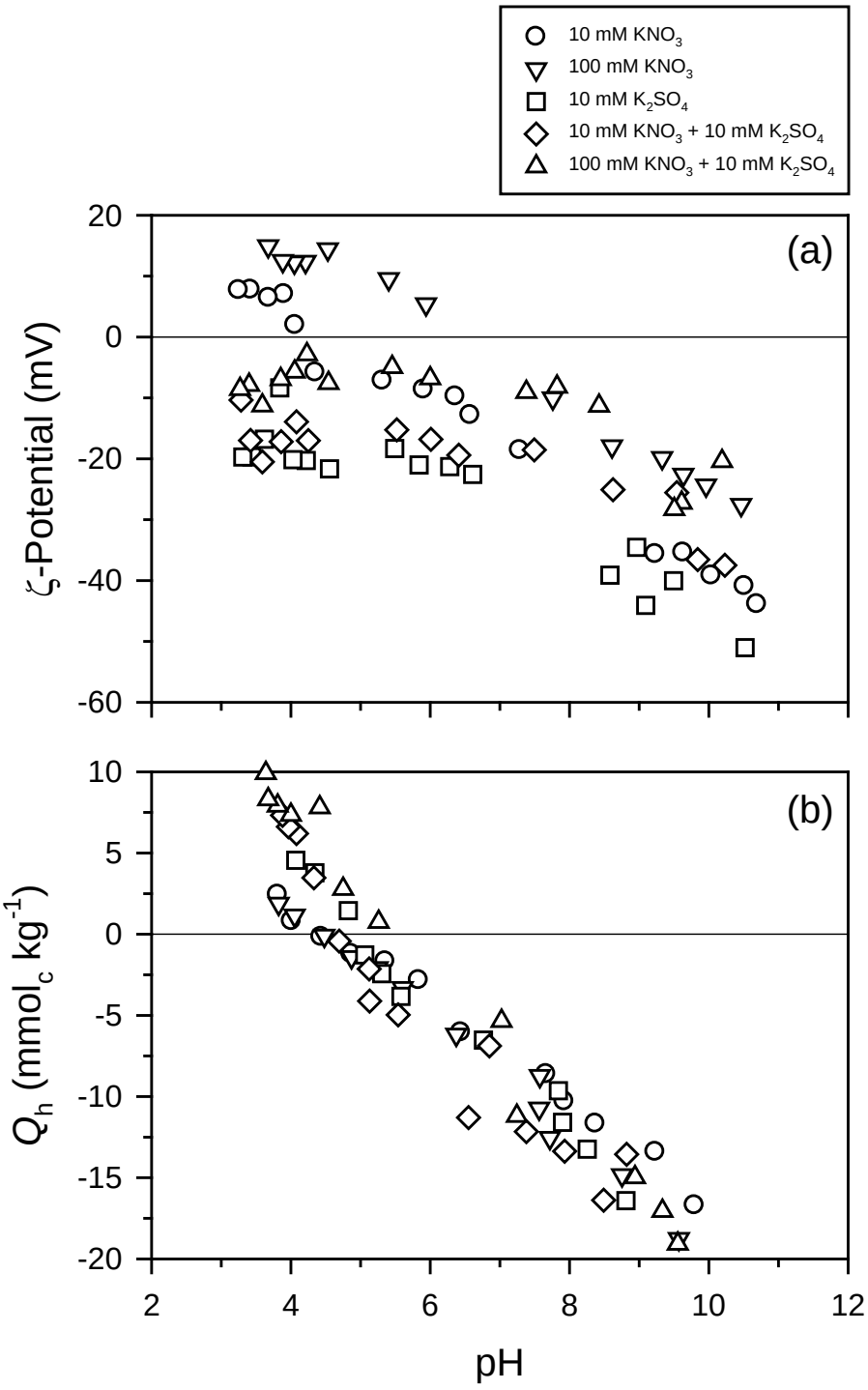

Figure 44. The influence of sulfate on kaolinite (a) zeta potential and (b) proton adsorption as a function of pH, ionic strength, and electrolyte composition.

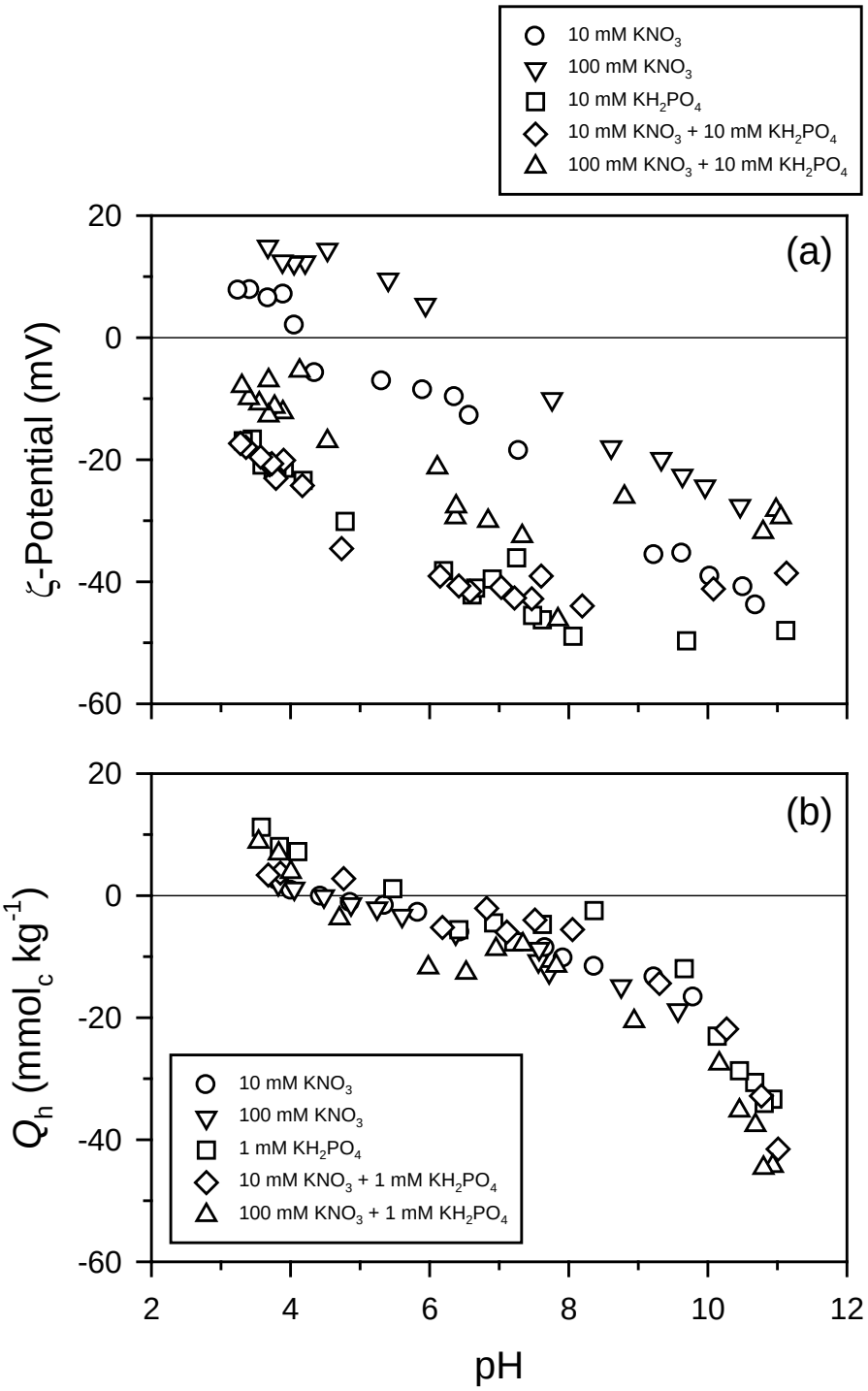

Figure 45. The influence of phosphate on kaolinite (a) zeta potential and (b) proton adsorption as a function of pH, ionic strength, and electrolyte composition.

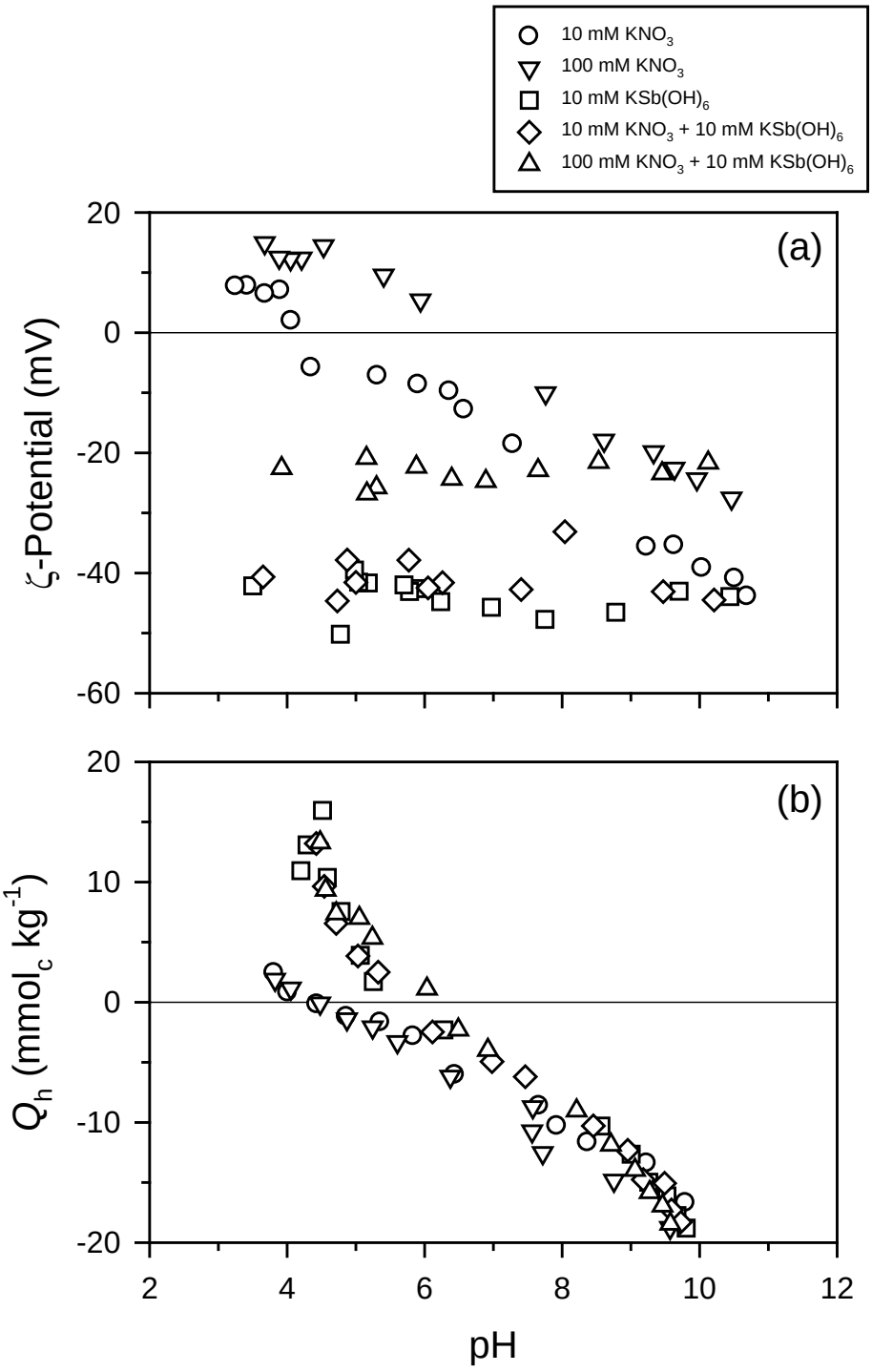

Figure 46. The influence of antimonate on kaolinite (a) zeta potential and (b) proton adsorption as a function of pH, ionic strength, and electrolyte composition.

Surface Complexation Modeling

The antimonate adsorption edge and adsorption isotherm studies, coupled with the effects of antimonate on kaolinite surface charging, indicate that antimonate retention by kaolinite occurs via a combination of inner- and outer-sphere complexation mechanisms. Specifically, antimonate retention predominately occurs via an outer-sphere mechanism ($\equiv AlOH_2^+ – Sb(OH)_6^-$) in neutral to slightly acidic systems, with increasing inner-sphere complexation character as pH is decreased into the strongly acidic range. Spectroscopic studies indicate that the retention of antimonate by hydrous aluminum oxides and kaolinite (with ≡AlOH surface functionality) proceeds via mono- and bidentate inner-sphere surface complexation processes ($\equiv AlOSb(OH)_5^-$ and $(\equiv AlO)_2Sb(OH)_4^-$) under acidic (pH 5) conditions (Ilgen and Trainor, 2012). These studies also suggest that the bidentate complex is the predominant inner-sphere species. The anion exchange, and monodentate and bidentate ligand exchange processes are illustrated in Fig. 22 and described in Eqs. [26] through [29].

Two experimental techniques were employed to generate the antimonate, sulfate, and phosphate adsorption edge data (q vs. pH) as a function of ionic strength: continuous titration beaker systems (Figs. 31 and 32) and the competitive adsorption batch systems (Fig. 34). Both data sets were used to develop the chemical models for ligand adsorption by kaolinite. Four models were evaluated for their ability to describe the antominate adsorption edge. Model A assumes that the adsorption of antimonate occurs via a combination of outer- and inner-sphere retention processes, forming $\equiv AlOH_2^+ – Sb(OH)_6^-$ and the monodentate $\equiv AlOSb(OH)_5^-$ surface species. Using the triple-layer SCM, coupled with the 2-pK_a approach, the adsorption of antominate was well-predicted in the pH 3 to 10 range (Figs. 47 and 48). The goodness-of-fit parameters for the beaker and batch data sets (V_Y = 3.850 and 2.823) indicate that the model satisfactorily describes the adsorption edges (Table 10). Further, the common logarithms of the intrinsic surface complexation constants for the batch and beaker systems (log K^{int} = 10.59 and 11.02 for $\equiv AlOH_2^+ – Sb(OH)_6^-$ formation; log K^{int} = 0.34 and 0.64 for $\equiv AlOSb(OH)_5^-$ formation) are similar. The monodentate complex is the predominant surface species in the more acidic systems; while the outer-sphere complex predominates at higher pH values.

Model B also employs a combination of outer- and inner-sphere surface species, forming $\equiv AlOH_2^+ – Sb(OH)_6^-$ and the bidentate $(\equiv AlO)_2Sb(OH)_4^-$ species (Fig. 49; Table 10). The model could only be applied to the batch systems, as there was no convergence in FITEQL for the beaker systems. The adsorption of antominate is well-predicted by this model in the pH 3 to 10 range. The goodness-of-fit parameters for the batch data set (V_Y = 5.213) indicates that the model satisfactorily describes the adsorption edges. The common logarithms of the intrinsic surface complexation constants for the outer-sphere complex is log K^{int} = 11.17; and that for the bidentate species is log K^{int} = 5.01. The bidentate complex is the predominant surface species in the pH < 4.5 (0.01 M KNO_3) and < 5.5 (0.1 M KNO_3) range; while the outer-sphere complex predominates at higher pH values. Relative to Model A (outer-sphere and monodentate inner-sphere surface complexes; Figs. 47 and 48), Model B under predicts antimonate adsorption when pH < 4.5.

In addition to the two models that consider both outer- and inner-sphere complexation of antimonate (Models A and B), surface complexation models that consider only inner-sphere complexation of antimonate by kaolinite also provide satisfactory descriptions of the adsorption edge data. Model C employed a combination of mono- and bidentate surface species

($\equiv AlOSb(OH)_5^-$ and $(\equiv AlO)_2Sb(OH)_4^-$), as inferred from spectroscopic analysis of adsorbed antimonate on hydrous aluminum oxides (Ilgen and Trainor, 2012). The adsorption of antominate is well-predicted in the pH 3 to 10 range (Figs. 50 and 51). The goodness-of-fit parameters for the beaker and batch data sets (V_Y = 2.510 and 4.056) indicate that the model satisfactorily describes the adsorption edges (Table 10). Further, the common logarithms of the intrinsic surface complexation constants for the batch and beaker systems (log K^{int} = 0.25 and 1.12 for $\equiv AlOSb(OH)_5^-$ formation; log K^{int} = 5.14 and 5.06 for $(\equiv AlO)_2Sb(OH)_4^-$ formation) are similar. For the beaker systems, the bidentate species is predicted to predominate throughout the pH range studied. However, in the batch systems, the monodentate complex is the predominant surface species. Model D employs only the bidentate surface complex (Fig. 52). This model satisfactorily describes the antimonate adsorption edge (V_Y = 2.876), but only converged for the beaker systems (Table 10). The common logarithms of the intrinsic surface complexation constant is log K^{int} = 5.33 for $(\equiv AlO)_2Sb(OH)_4^-$ formation.

The surface complexation models that employ both an outer-sphere and an inner-sphere surface-bound antimonate (Models A and B) provide a satisfactory description of the adsorption edge data. The models indicate that the inner-sphere surface species account for a bulk of the adsorption in the pH < 4 to 5 systems, while the outer-sphere species predominates as solution pH increases. The increasing significance of an inner-sphere surface complex as solution pH decreases into the strongly acidic range is supported by the experimental evidence. Antimonate adsorption is hysteretic in pH < 5 systems, becoming reversible with increasing pH (Fig. 31). Adsorption by high intensity, low capacity sites in pH 5.5 solutions is endothermic and entropically-driven (suggesting an inner-sphere component to the adsorption process). Further, both the zeta potential and proton adsorption data suggest an inner-sphere component to the adsorption process (Fig. 46).

In order to predict competitive adsorption in antimonate-sulfate and antimonate-phosphate systems, intrinsic constants for the retention of sulfate and phosphate must be determined. The adsorption of sulfate by kaolinite is strongly influenced by solution ionic strength (Figs. 32a and 34b) and is reversible throughout the pH range studied. Sulfate adsorption does not result in a charge reversal on the kaolinite surface, and proton adsorption increases in pH < 5 solutions, relative to the indifferent KNO_3 electrolyte alone (Fig. 44). These experimental findings indicate that sulfate retention proceeds primarily through an outer-sphere surface complexation mechanism, but that an inner-sphere mechanism increases in importance as solutions become strongly acidic. Sulfate adsorption by kaolinite was successfully modeled by considering only outer-sphere complexation and the formation of $\equiv AlOH_2^+–SO_4^{2-}$ (Fig. 53). The goodness-of-fit parameters for the beaker and batch data sets (V_Y = 1.051 and 2.629) indicate that the model satisfactorily describes the adsorption edges (Table 10). The common logarithms of the intrinsic surface complexation constants for the batch and beaker systems are log K^{int} = 7.11 and 7.66.

Phosphate displays strong adsorption by kaolinite, relative to antimonate and sulfate (Figs. 32b and 34c). Phosphate adsorption is independent of ionic strength (batch data), shifts the kaolinite IEP from 4.4 to the 2 to 3 range, and increases proton adsorption throughout a broad pH range (relative to the KNO_3 systems) (Fig. 45). These experimental results indicate that phosphate is retained primarily by inner-sphere surface complexation mechanisms. Johnson et al. (2002) and Van Emmerik et al. (2007) reported that phosphate formed monodentate inner-sphere surface complexes on γ-Al_2O_3 and gibbsite, and that outer-sphere complexation contributed to adsorption in alkaline systems (pH > 8). The adsorption of phosphate by kaolinite has been successfully described by considering combination of monodentate inner-sphere and outer-

sphere and the formation of $\equiv AlOPO_3^{2-}$, $\equiv AlOPO_2OH^-$, and $\equiv SiOH_2^+–PO_4^{3-}$ species (He et al., 1997). Phosphate adsorption by kaolinite in the beaker and batch systems could only be predicted by considering the outer-sphere species, $\equiv AlOH_2^+–PO_4^{3-}$ and $\equiv AlOH_2^+–HPO_4^{2-}$, and the monodentate $\equiv AlOPO(OH)_2^0$ species (Figs. 54 and 55). For the beaker studies, the 0.01 and 0.1 *M* KNO_3 systems were optimized separately in FITEQL. The chemical model provides a satisfactory fit to the experimental beaker adsorption edge data (V_Y = 0.503 and 0.898 for 0.01 and 0.1 *M* KNO_3) (Table 10). For the batch studies, the two ionic strength conditions were optimized concurrently by FITEQL, resulting in a goodness-of-fit parameter of V_Y = 2.664. Surface complexation models that considered multiple inner-sphere surface species (including $\equiv AlOPO_2OH^-$ and $\equiv AlOPO_3^{2-}$), or a combination of inner- and outer-sphere surface species, would not converge in FITEQL.

The surface complexation modeling of competitive adsorption, using the intrinsic constants obtained from single-adsorbate systems, was investigated for the direct competition antimonate-sulfate and antimonate-phosphate systems (Figs. 35 through 38). Although several models provided acceptable fits to the adsorption edge data, the model using the outer-sphere $\equiv AlOH_2^+–Sb(OH)_6^-$ and monodentate inner-sphere $\equiv AlOSb(OH)_5^-$ species was selected to predict competitive antimonate adsorption (Model A, Table 10). This model was selected because it considered both inner- and outer-sphere surface complexation, generated a lower goodness-of-fit parameter relative to the other models, described antimonate adsorption in strongly acidic systems, and satisfactorily described both the beaker and batch data sets. The outer-sphere $\equiv AlOH_2^+–SO_4^{2-}$ and the mixed outer- and inner-sphere phosphate complexation models were used to predict sulfate and phosphate adsorption (Table 10). The application of chemical models developed for single-adsorbate systems to binary-adsorbate systems has been met with limited success (Essington and Anderson, 2008; Goldberg, 2010). Generally, the reoptimization of the intrinsic constants is necessary to provide an adequate fit to the experimental data.

The predicted direct competitive adsorption of antimonate and sulfate by gibbsite indicates that antimonate adsorption is generally overpredicted (Fig. 56a). As in the single-adsorbate systems (Fig. 48), the inner-sphere surface complex predominates when pH < 5. The predicted adsorption of sulfate in the competitive systems is underpredicted throughout the entire pH range (Fig. 56b). The goodness-of-fit parameter (V_Y = 20.273), reflecting the poor fit of the model to the sulfate adsorption edge (Herbelin and Westall, 1999). As indicated above, reoptimization of the intrinsic constants is often necessary to improve model prediction (Sarkar et al., 1999; Essington and Anderson, 2008). Reoptimization of the sulfate adsorption constant greatly improved the model predictions of both antimonate and sulfate competitive adsorption (V_Y = 1.630, Fig. 57). The optimized common logarithm of the intrinsic surface complexation constant for $\equiv AlOH_2^+–SO_4^{2-}$ formation is log K^{int} = 10.46. The reoptimization of the sulfate and antimonate adsorption constants leads to a V_Y of 0.7104 (Fig. 58). The reoptimized surface complexation constants (as log K^{int}) are 10.76 for $\equiv AlOH_2^+–SO_4^{2-}$, 11.27 for $\equiv AlOH_2^+–Sb(OH)_6^-$ (compared to 11.02 unoptimized), and 0.71 for $\equiv AlOSb(OH)_5^-$ (compared to 0.64 unoptimized).

The goodness-of-fit parameter for the predicted adsorption in the binary antimonate-phosphate system is V_Y = 28.805 (Fig. 59). The surface complexation model provides a poor prediction of both antimonate and phosphate adsorption. Antimonate adsorption is overpredicted throughout a broad pH range, suggesting that the mechanism of phosphate retention employed in the model (outer-sphere) is inappropriate. Indeed, the predicted adsorption of antimonate in the competitive systems is similar to that measured in the noncompetitive systems (compare Fig. 59 to Fig. 48). In order for the surface complexation model to predict a decrease in the inner-sphere

retention of antimonate, the competing surface complexation of phosphate must also proceed through an inner-sphere mechanism. Because phosphate is modeled to form outer-sphere complexes, there is little difference between the predicted inner-sphere complexation of antimonate in the competitive and non-competitive systems. Attempts to reoptimize the adsorption constants were unsuccessful, as FITEQL would not converge, or overflow errors would occur.

Table 10. Surface complexation models used to describe the adsorption of antimonate, sulfate, and phosphate by kaolinite as a function of pH and ionic strength using the triple-layer formulation.

		log K^{int}†	
Reaction		Beaker‡	Batch
Antimonate Model A			
$\equiv AlOH + H^+ + Sb(OH)_6^- = \equiv AlOH_2^+–Sb(OH)_6^-$		10.59 ± 0.05	11.02 ± 0.05
$\equiv AlOH + Sb(OH)_6^- = \equiv AlOSb(OH)_5^- + H_2O$		0.34 ± 0.04	0.64 ± 0.04
	V_Y§	3.850	2.823
Antimonate Model B			
$\equiv AlOH + H^+ + Sb(OH)_6^- = \equiv AlOH_2^+–Sb(OH)_6^-$		NC	11.17 ± 0.02
$2\equiv AlOH + Sb(OH)_6^- = (\equiv AlO)_2Sb(OH)_4^- + 2H_2O$		NC	5.01 ± 0.03
	V_Y	NC	5.213
Antimonate Model C			
$\equiv AlOH + Sb(OH)_6^- = \equiv AlOSb(OH)_5^- + H_2O$		0.25 ± 0.74	1.12 ± 0.02
$2\equiv AlOH + Sb(OH)_6^- = (\equiv AlO)_2Sb(OH)_4^- + 2H_2O$		5.14 ± 0.04	5.06 ± 0.09
	V_Y	2.510	4.056
Antimonate Model D			
$2\equiv AlOH + Sb(OH)_6^- = (\equiv AlO)_2Sb(OH)_4^- + 2H_2O$		5.33 ± 0.02	NC
	V_Y	2.876	NC
Sulfate			
$\equiv AlOH + H^+ + SO_4^{2-} = \equiv AlOH_2^+–SO_4^{2-}$		7.11 ± 0.07	7.66 ± 0.04
$\equiv AlOH + H^+ + NO_3^- = \equiv AlOH_2^+–NO_3^-$		6.49 ± 0.09	6.67 ± 0.04
	V_Y	1.051	2.629
Phosphate¶			
	0.01 *M* KNO_3	0.1 *M* KNO_3	
$\equiv AlOH + H^+ + PO_4^{3-} = \equiv AlOH_2^+–PO_4^{3-}$	17.74 ± 0.08	18.55 ± 0.09	17.12 ± 0.06
$\equiv AlOH + 2H^+ + PO_4^{3-} = \equiv AlOH_2^+–HPO_4^{2-}$	24.07 ± 0.07	25.06 ± 0.07	24.67 ± 0.03
$\equiv AlOH + 3H^+ + PO_4^{3-} = \equiv AlOPO(OH)_2^0 + H_2O$	27.65 ± 0.33	29.39 ± 0.08	27.86 ± 0.61
$\equiv AlOH + H^+ + NO_3^- = \equiv AlOH_2^+–NO_3^-$			7.10 ± 0.05
V_Y	0.5032	0.8975	2.664

†Common logarithms of the intrinsic surface complexation constants (± standard deviation) optimized using FITEQL, the antimonate adsorption edge data (Figs. 31 and 34), and the kaolinite and suspension parameters described in Tables 1 and 2.
‡Adsorption edge data were obtained from the continuous titration 'Beaker' studies, or the competitive 'Batch' studies. NC = no convergence of FITEQL.
§Weighted sum of squares of residuals divided by the degrees of freedom.
¶The 0.01 and 0.1 *M* KNO_3 systems were optimized separately for the phosphate Beaker studies.

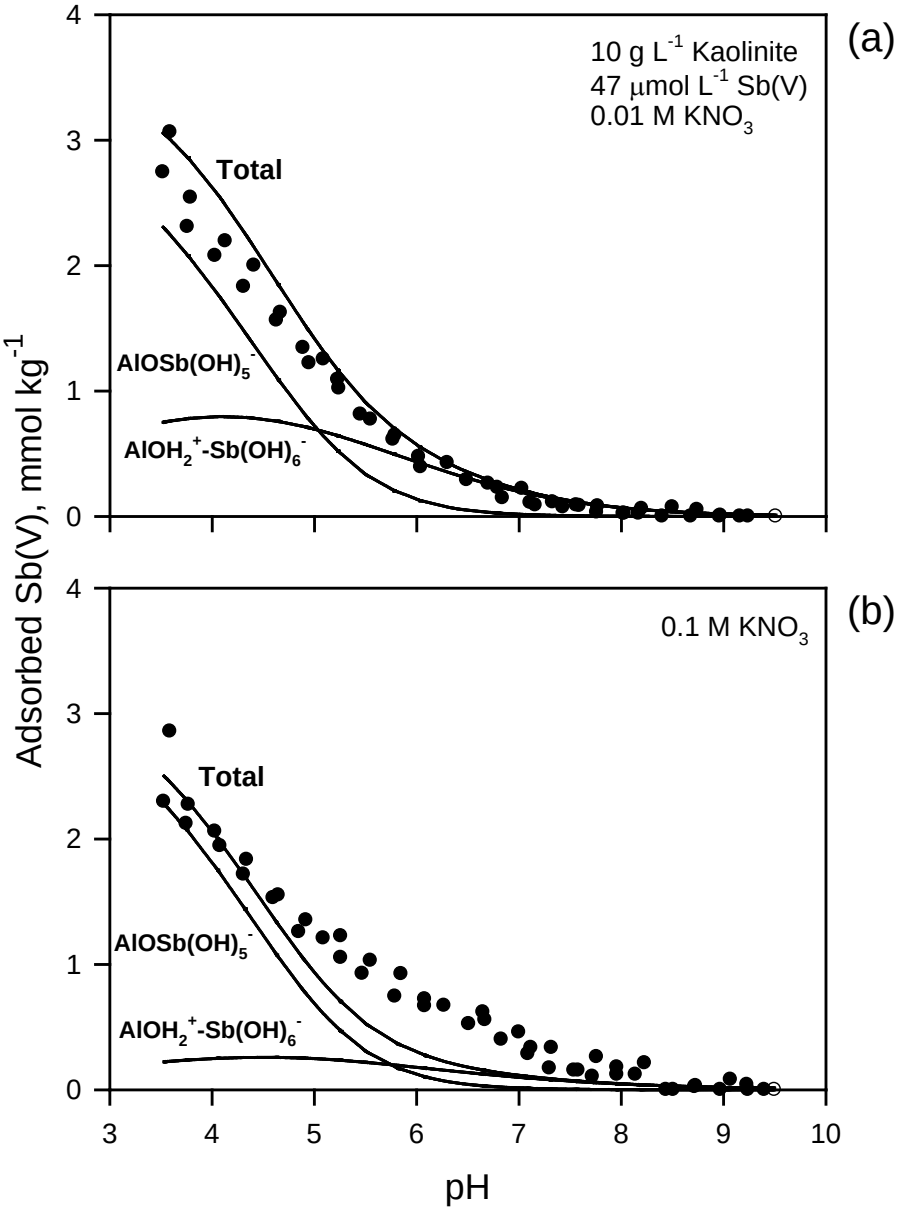

Figure 47. The adsorption of antimonate by kaolinite as a function of pH in the beaker systems in (a) 0.01 *M* KNO_3 and (b) 0.1 *M* KNO_3. The lines represent the triple-layer surface complexation model fit to the experimental data using FITEQL, the outer-sphere $\equiv AlOH_2^+–Sb(OH)_6^-$ species and the monodentate inner-sphere $\equiv AlOSb(OH)_5^-$ species, and the chemical model described in Tables 1, 2, and 10.

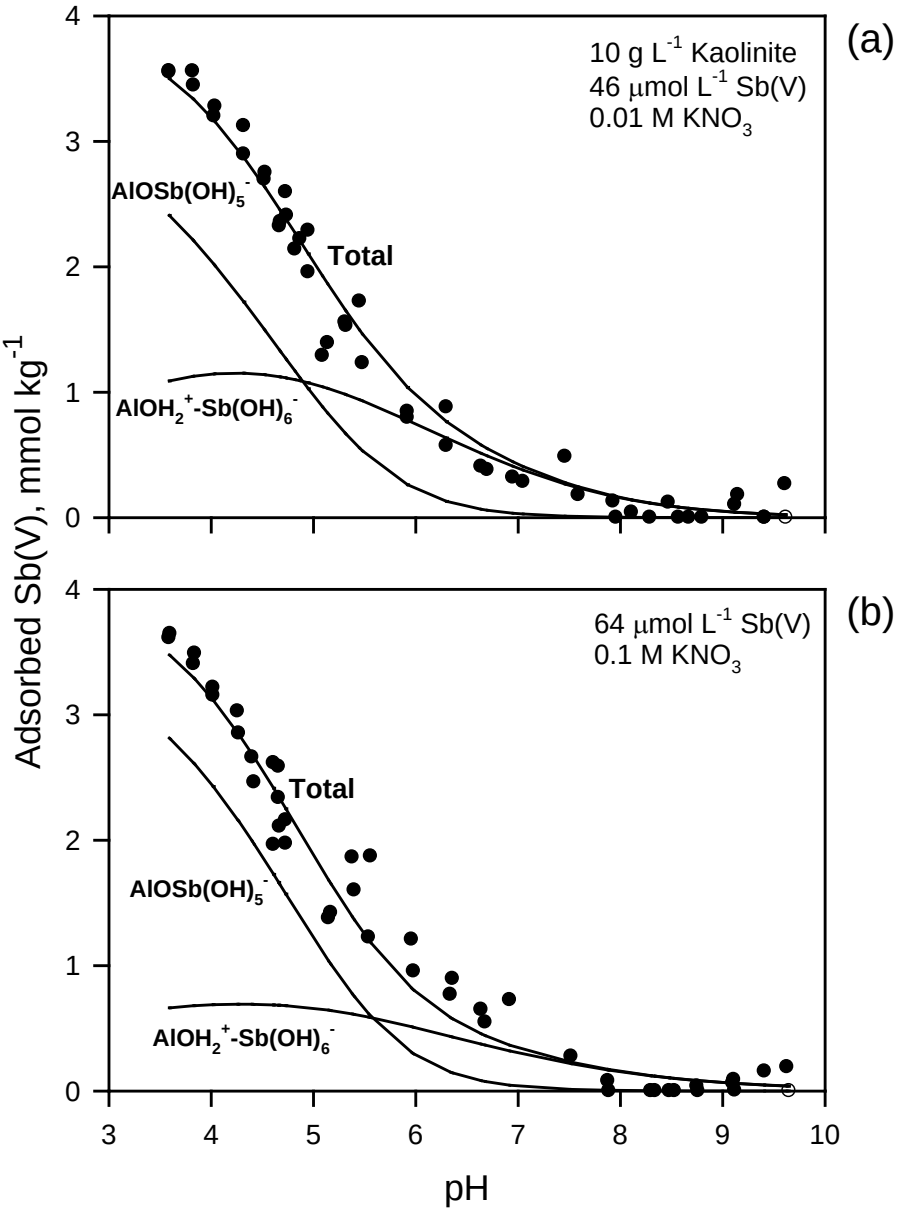

Figure 48. The adsorption of antimonate by kaolinite as a function of pH in the batch systems in (a) 0.01 *M* KNO_3 and (b) 0.1 *M* KNO_3. The lines represent the triple-layer surface complexation model fit to the experimental data using FITEQL, the outer-sphere $\equiv AlOH_2^+ – Sb(OH)_6^-$ species and the monodentate inner-sphere $\equiv AlOSb(OH)_5^-$ species, and the chemical model described in Tables 1, 2, and 10.

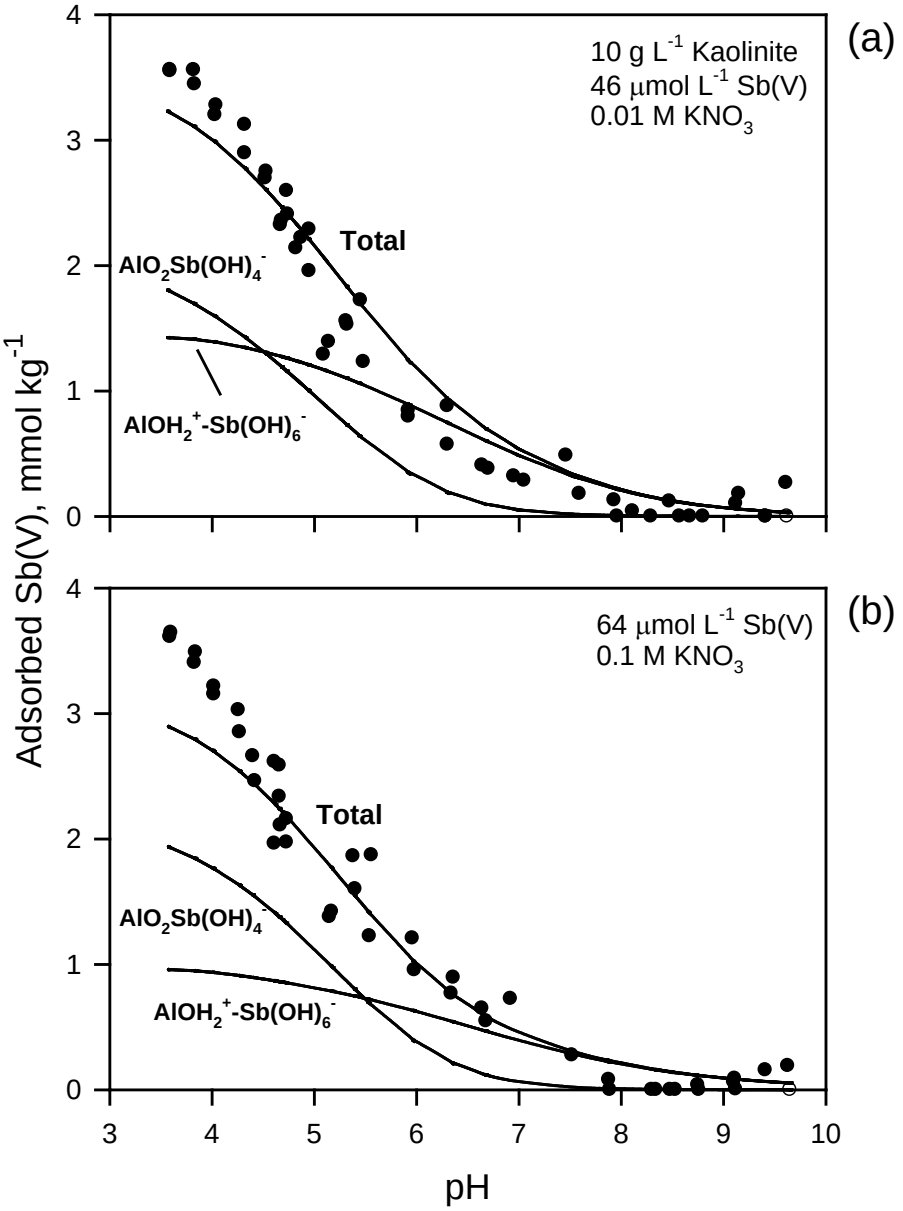

Figure 49. The adsorption of antimonate by kaolinite as a function of pH in the batch systems in (a) 0.01 *M* KNO_3 and (b) 0.1 *M* KNO_3. The lines represent the triple-layer surface complexation model fit to the experimental data using FITEQL, the outer-sphere $\equiv AlOH_2^+–Sb(OH)_6^-$ species and the bidentate inner-sphere $(\equiv AlO)_2Sb(OH)_4^-$ species, and the chemical model described in Tables 1, 2, and 10.

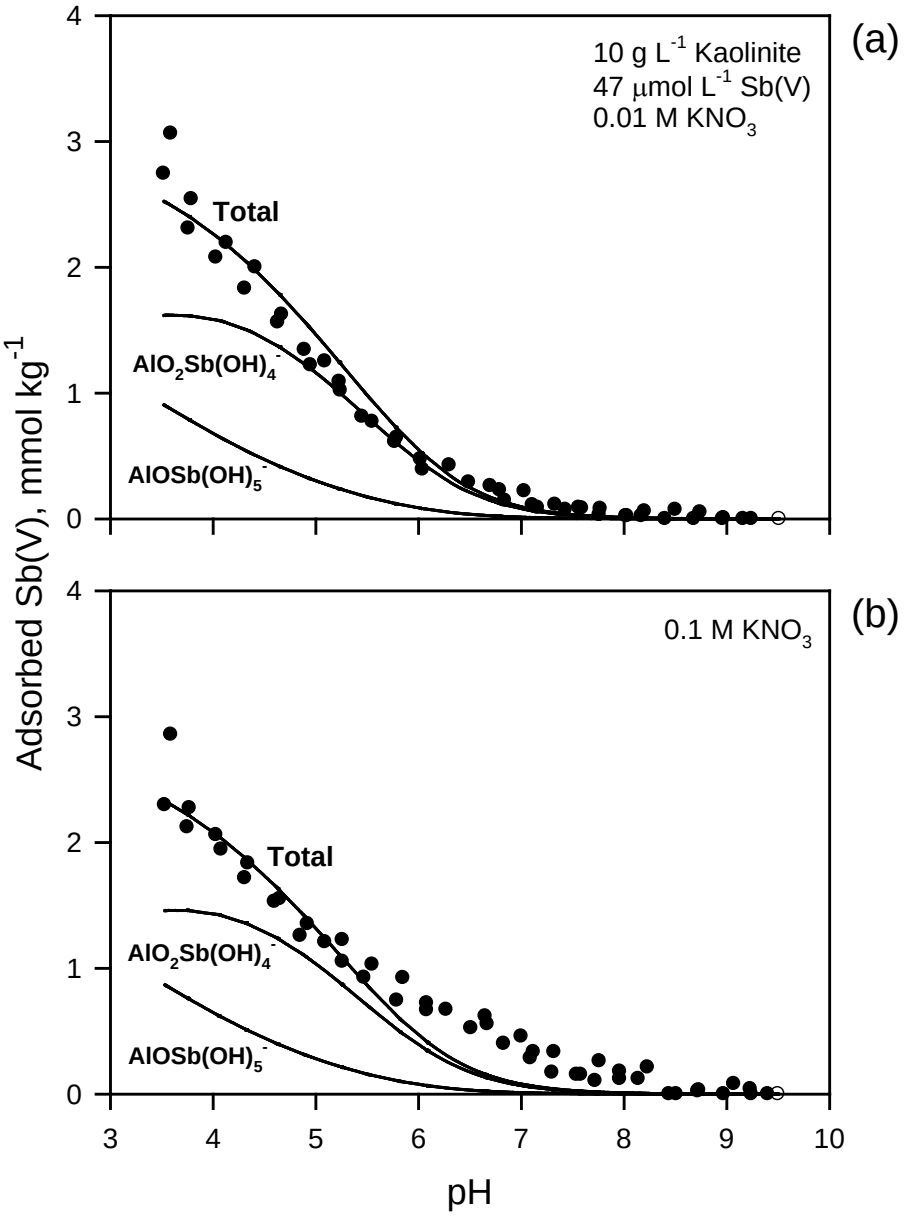

Figure 50. The adsorption of antimonate by kaolinite as a function of pH in the beaker systems in (a) 0.01 *M* KNO_3 and (b) 0.1 *M* KNO_3. The lines represent the triple-layer surface complexation model fit to the experimental data using FITEQL, the monodenate inner-sphere $\equiv AlOSb(OH)_5^-$ species and the bidentate inner-sphere $(\equiv AlO)_2Sb(OH)_4^-$ species, and the chemical model described in Tables 1, 2, and 10.

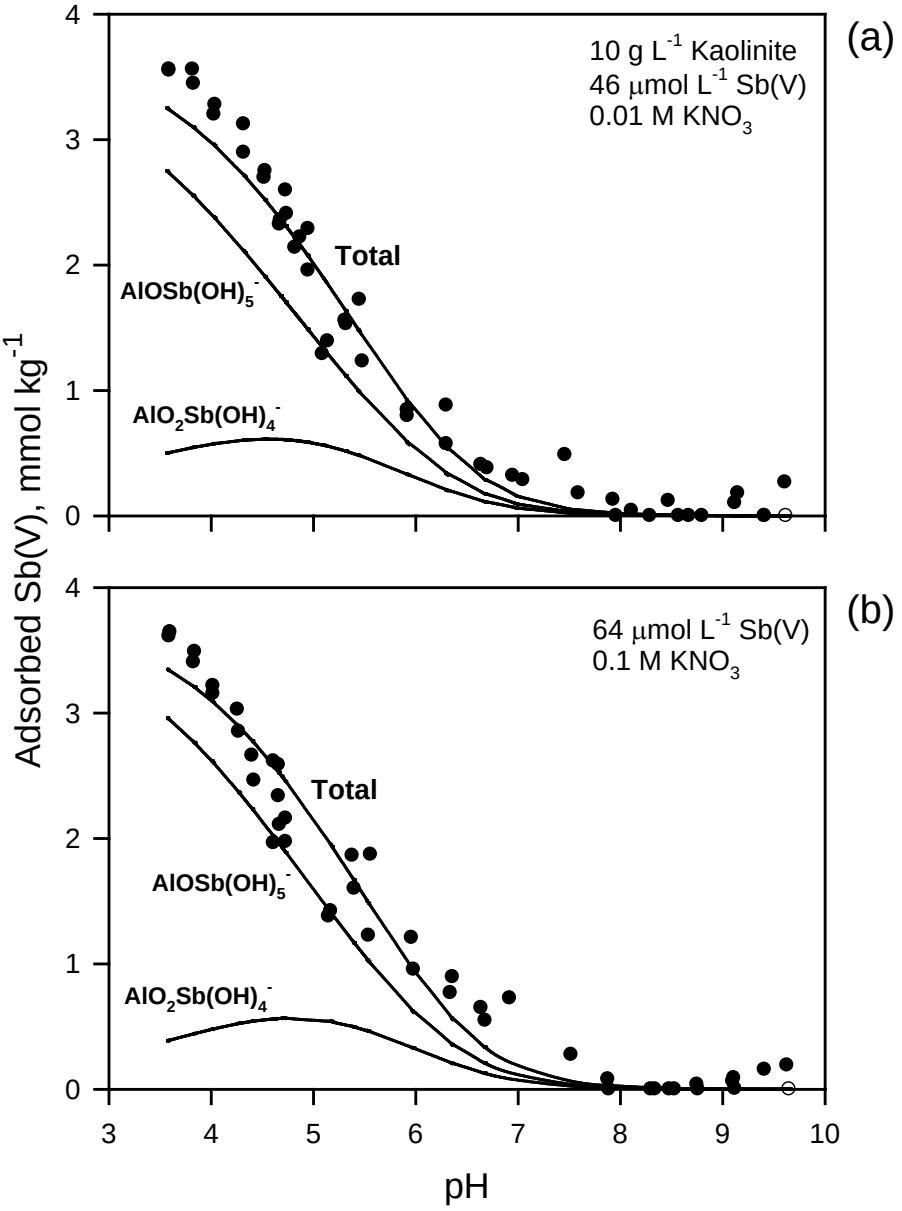

Figure 51. The adsorption of antimonate by kaolinite as a function of pH in the batch systems in (a) 0.01 *M* KNO_3 and (b) 0.1 *M* KNO_3. The lines represent the triple-layer surface complexation model fit to the experimental data using FITEQL, the monodenate inner-sphere $\equiv AlOSb(OH)_5^-$ species and the bidentate inner-sphere $(\equiv AlO)_2Sb(OH)_4^-$ species, and the chemical model described in Tables 1, 2, and 10.

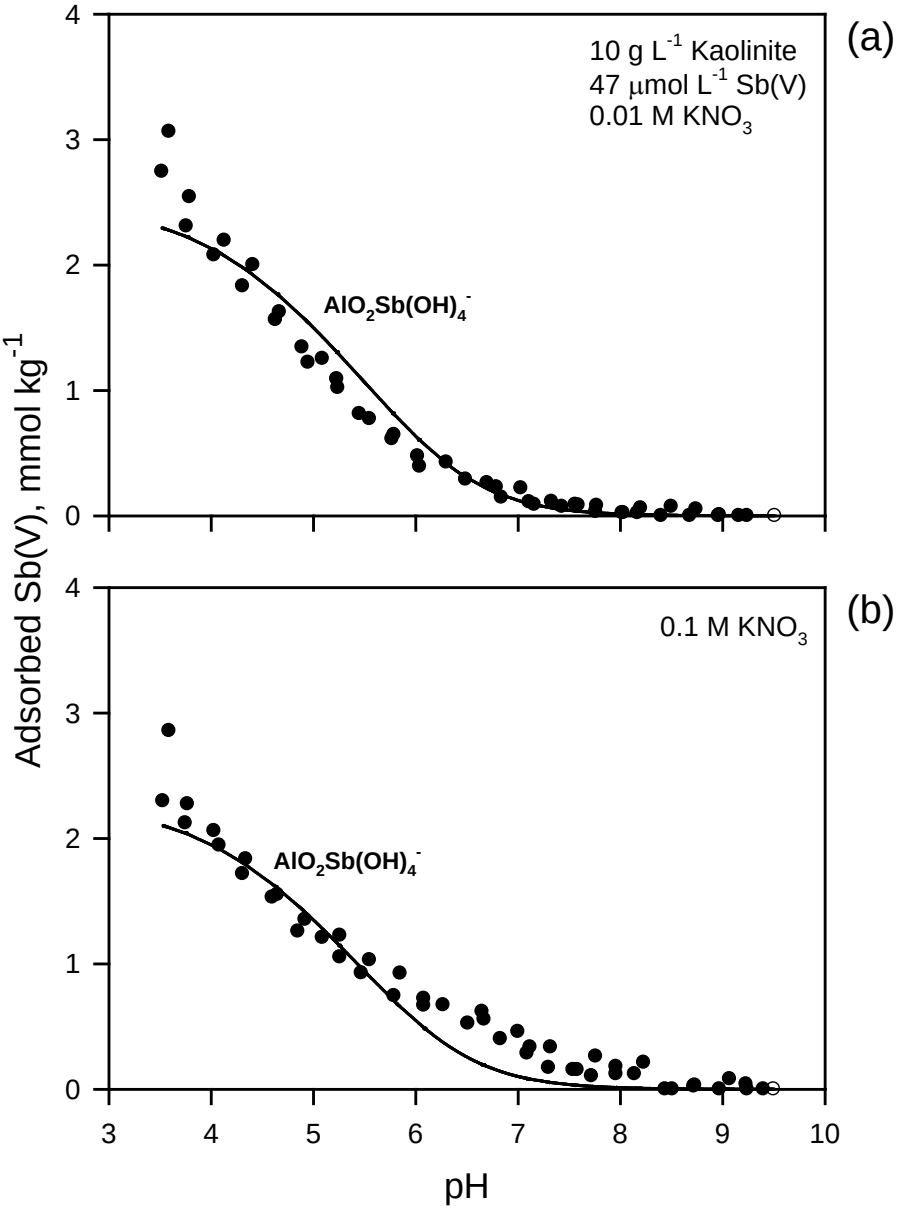

Figure 52. The adsorption of antimonate by kaolinite as a function of pH in the beaker systems in (a) 0.01 *M* KNO_3 and (b) 0.1 *M* KNO_3. The lines represent the triple-layer surface complexation model fit to the experimental data using FITEQL, the bidentate inner-sphere $(\equiv AlO)_2Sb(OH)_4^-$ species, and the chemical model described in Tables 1, 2, and 10.

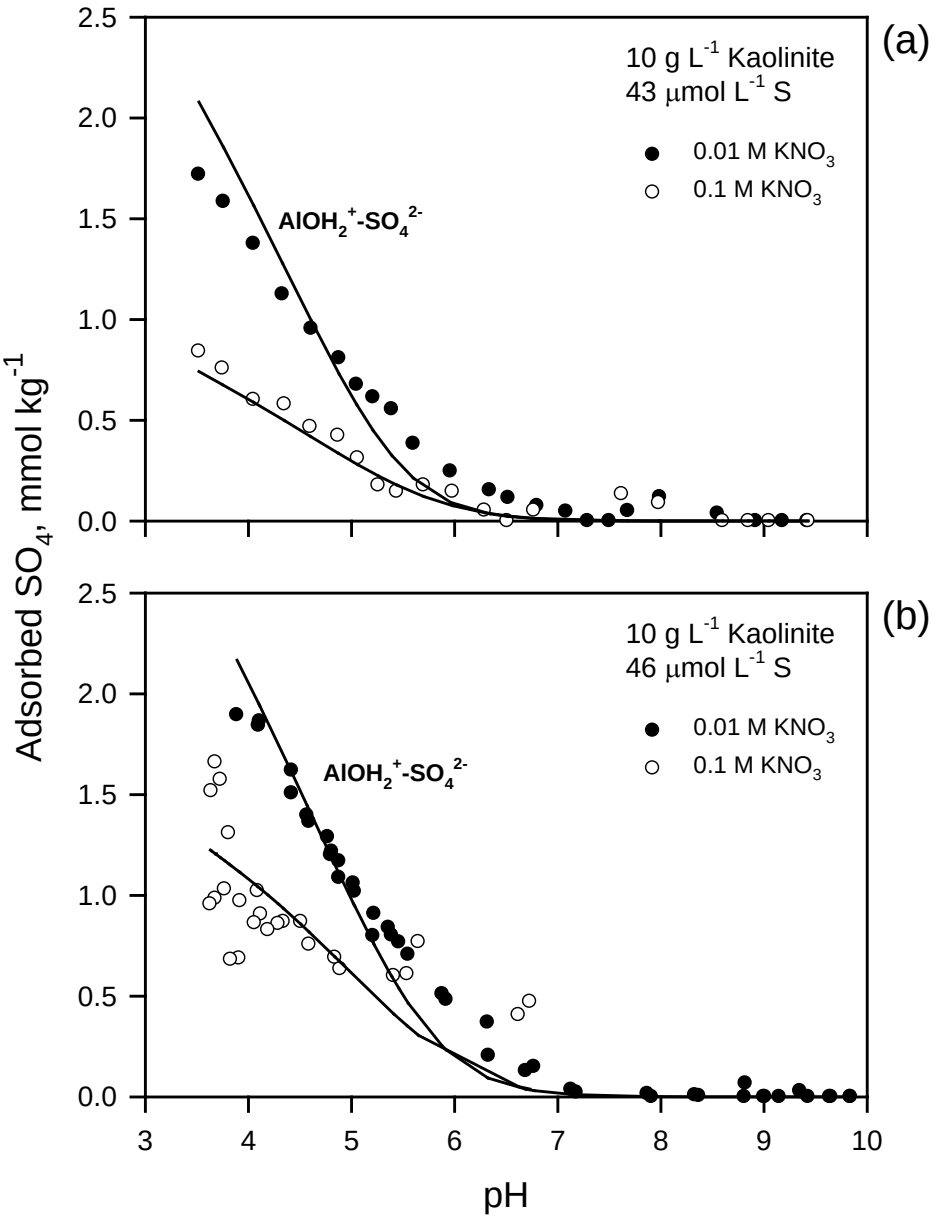

Figure 53. The adsorption of sulfate by kaolinite as a function of pH and ionic strength in (a) beaker and (b) batch systems. The lines represent the triple-layer surface complexation model fit to the experimental data using FITEQL and the chemical model described in Tables 1, 2, and 10. The solid lines show the predicted adsorption of the outer-sphere $\equiv AlOH_2^+–SO_4^{2-}$ species.

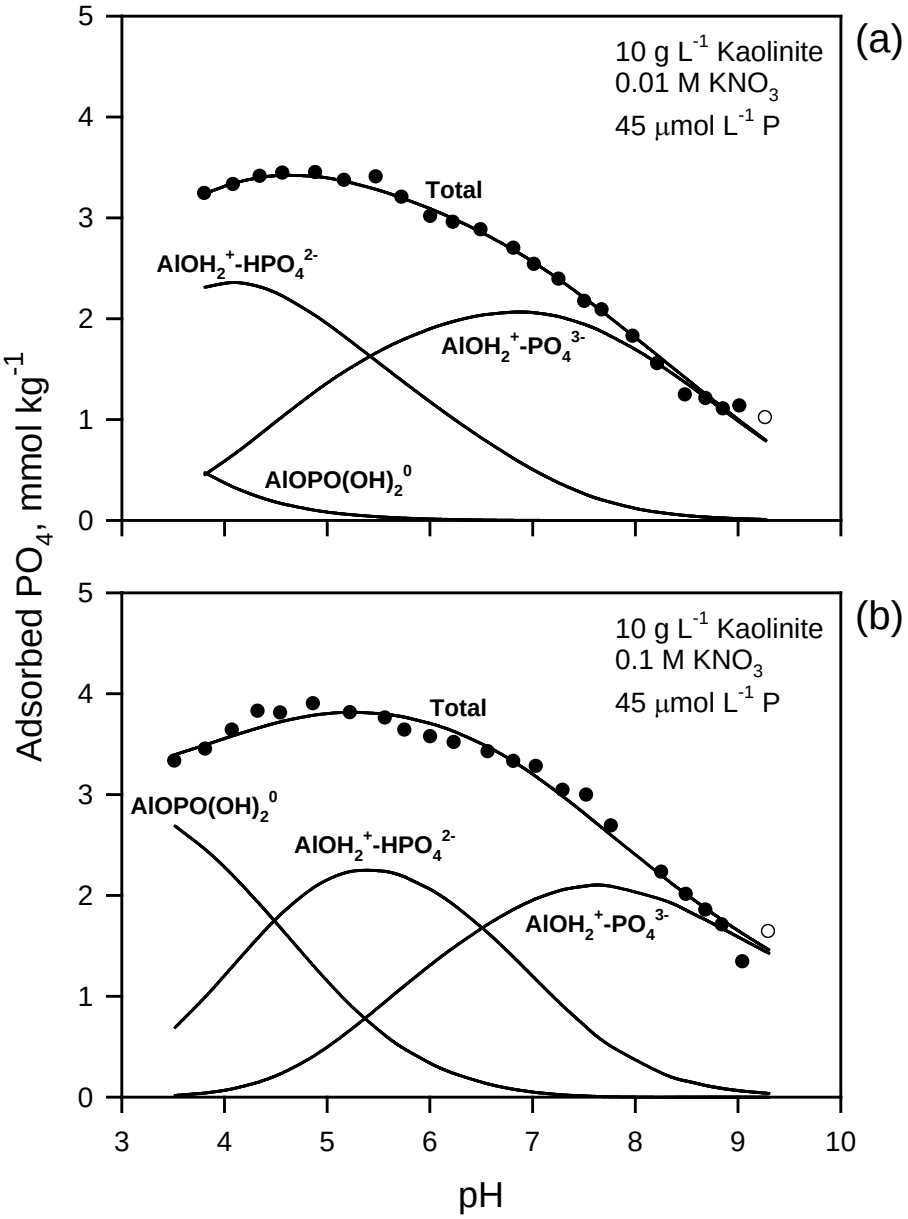

Figure 54. The adsorption of phosphate by kaolinite as a function of pH in the beaker systems in (a) 0.01 *M* KNO_3 and (b) 0.1 *M* KNO_3. The lines represent the triple-layer surface complexation model fit to the experimental data using FITEQL and the chemical model described in Tables 1, 2, and 10. The solid lines show the predicted adsorption of the outer-sphere $\equiv AlOH_2^+–PO_4^{3–}$ and $\equiv AlOH_2^+–HPO_4^{2–}$ species, and the inner-sphere $\equiv AlOPO(OH)_2^0$ species.

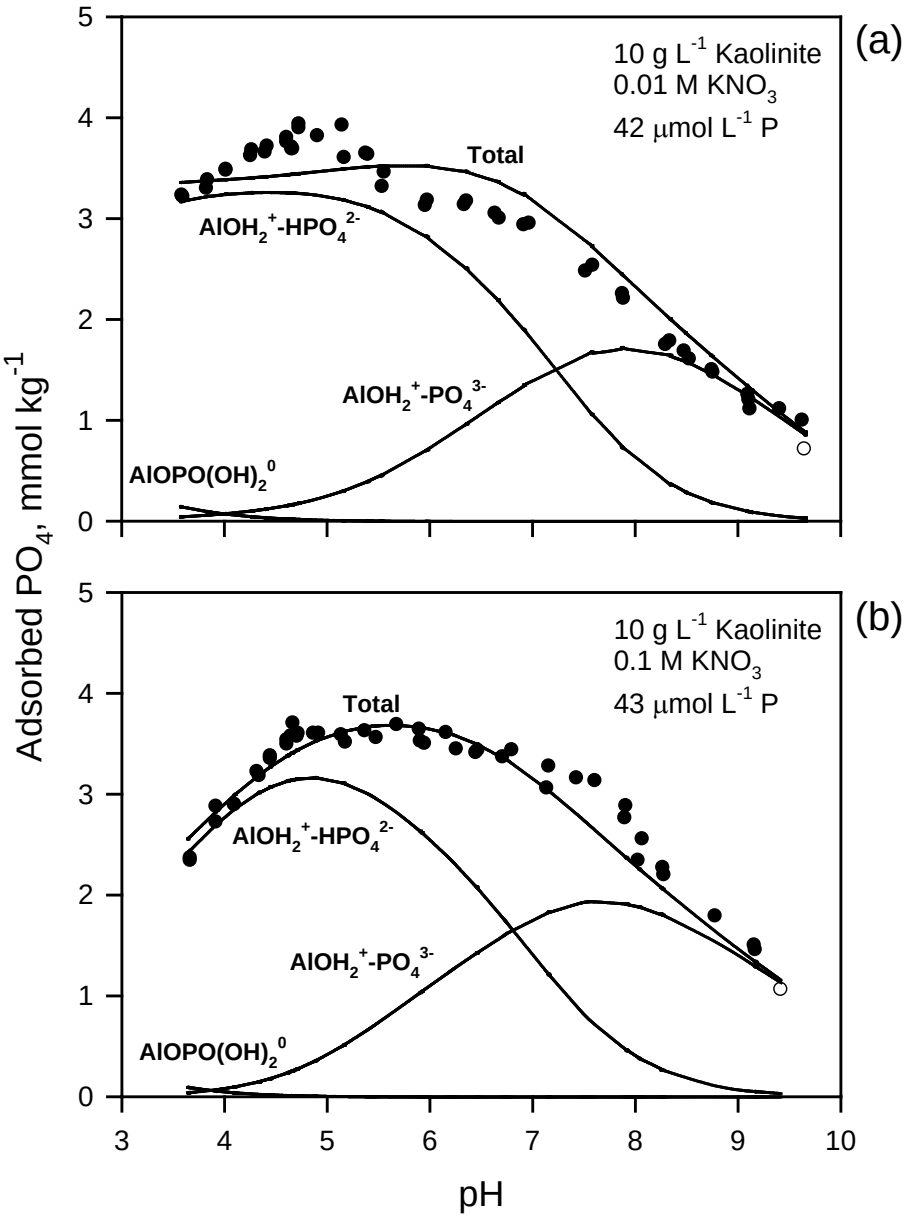

Figure 55. The adsorption of phosphate by kaolinite as a function of pH in the batch systems in (a) 0.01 *M* KNO_3 and (b) 0.1 *M* KNO_3. The lines represent the triple-layer surface complexation model fit to the experimental data using FITEQL and the chemical model described in Tables 1, 2, and 10. The solid lines show the predicted adsorption of the outer-sphere $\equiv AlOH_2^+–PO_4^{3-}$ and $\equiv AlOH_2^+–HPO_4^{2-}$ species, and the inner-sphere $\equiv AlOPO(OH)_2^0$ species.

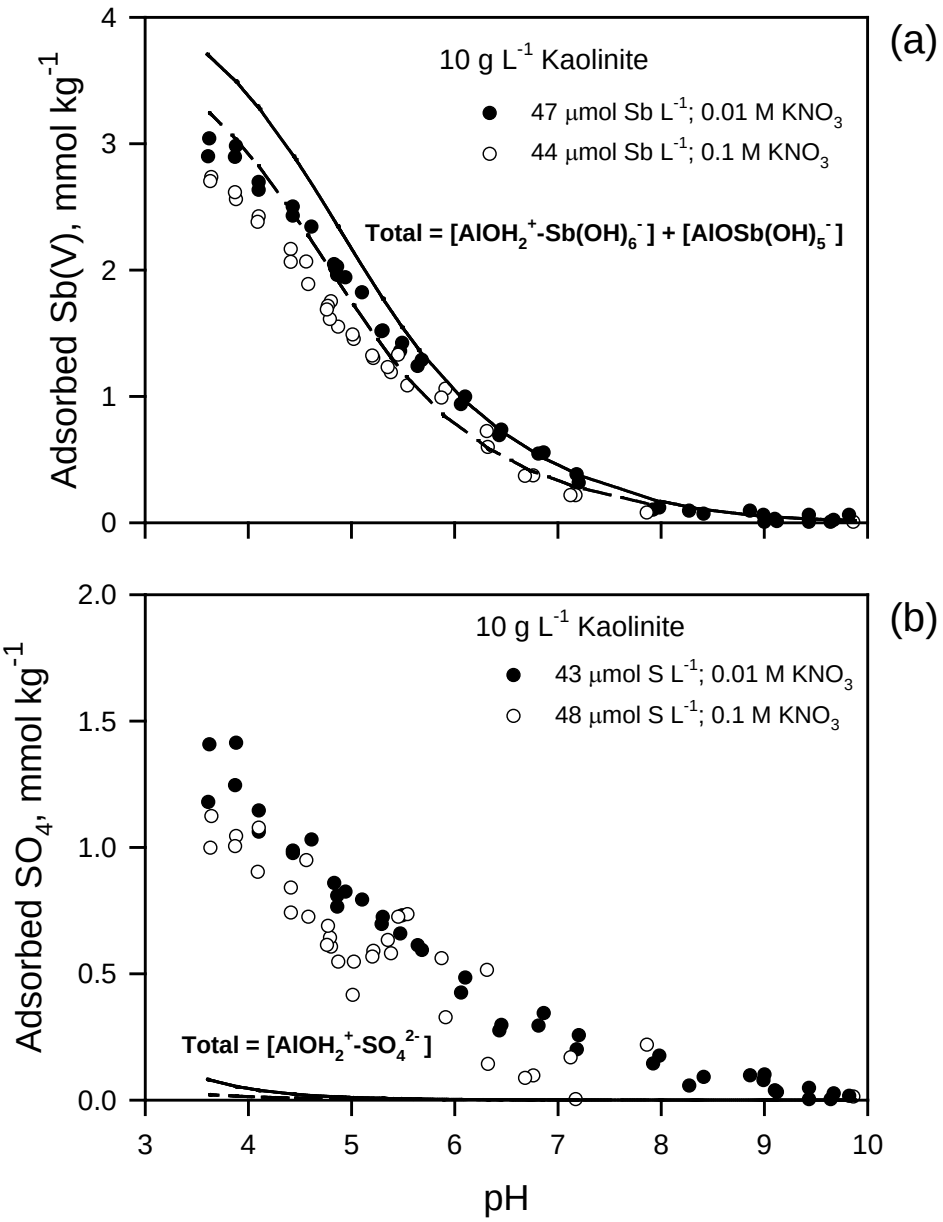

Figure 56. The adsorption of (a) antimonate and (b) sulfate by kaolinite as a function of pH and ionic strength in antimonate-sulfate direct competition systems. The lines represent the triple-layer surface complexation model predictions using the log K^{int} values optimized for non-competitive adsorption of antimonate [Model A; $\equiv AlOH_2^+ – Sb(OH)_6^-$ and $\equiv AlOSb(OH)_5^-$ species] and sulfate ($\equiv AlOH_2^+ – SO_4^{2-}$ species) (Table 10). The solid lines show the predicted adsorption in 0.01 *M* KNO_3, the dashed lines in 0.1 *M* KNO_3.

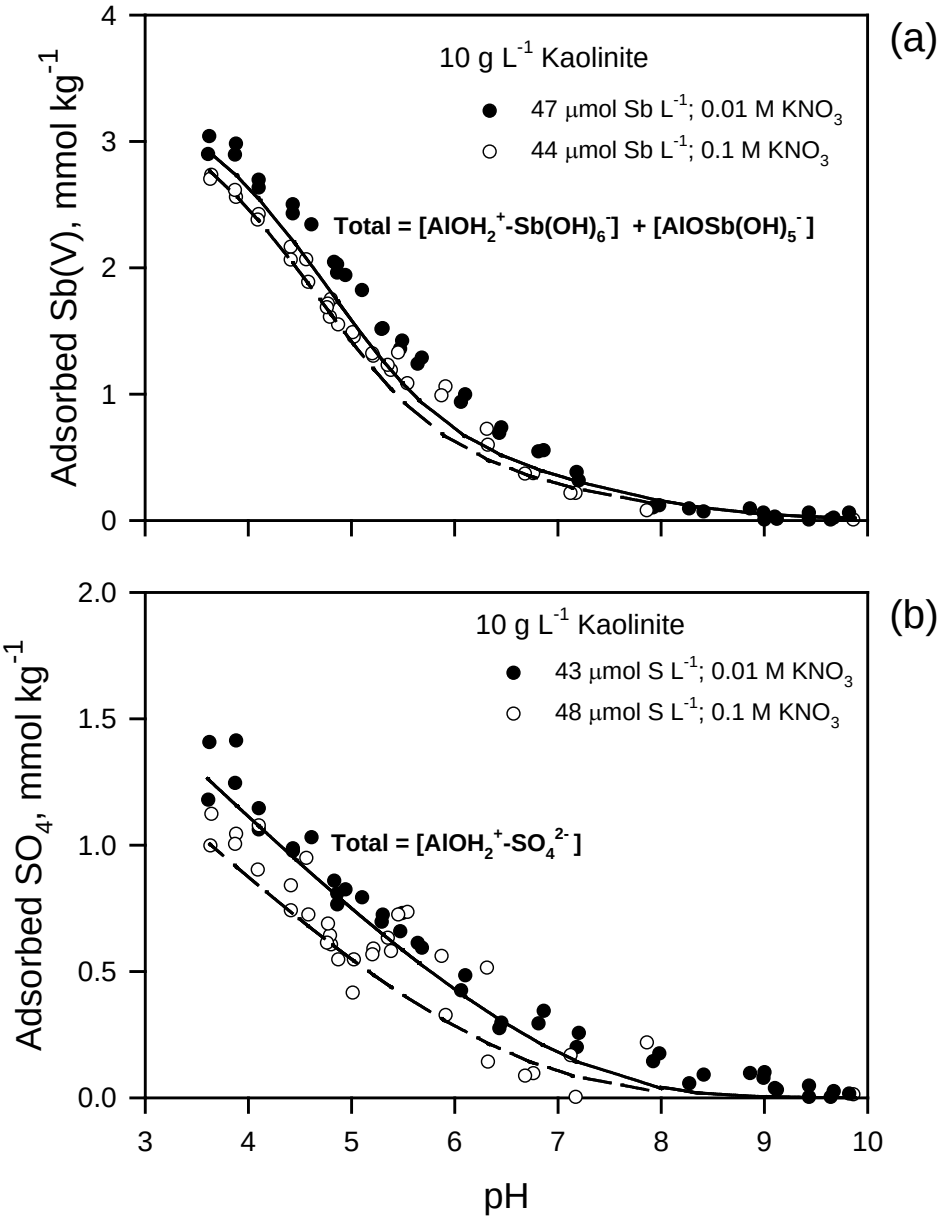

Figure 57. The adsorption of (a) antimonate and (b) sulfate by kaolinite as a function of pH and ionic strength in antimonate-sulfate direct competition systems. The lines represent the triple-layer surface complexation model predictions using the log K^{int} values optimized for non-competitive adsorption of antimonate [Model A; $\equiv AlOH_2^+ – Sb(OH)_6^-$ and $\equiv AlOSb(OH)_5^-$ species] and reoptimized for sulfate ($\equiv AlOH_2^+ – SO_4^{2-}$ species) for competitive adsorption (Table 10). The solid lines show the predicted adsorption in 0.01 *M* KNO_3, the dashed lines in 0.1 *M* KNO_3.

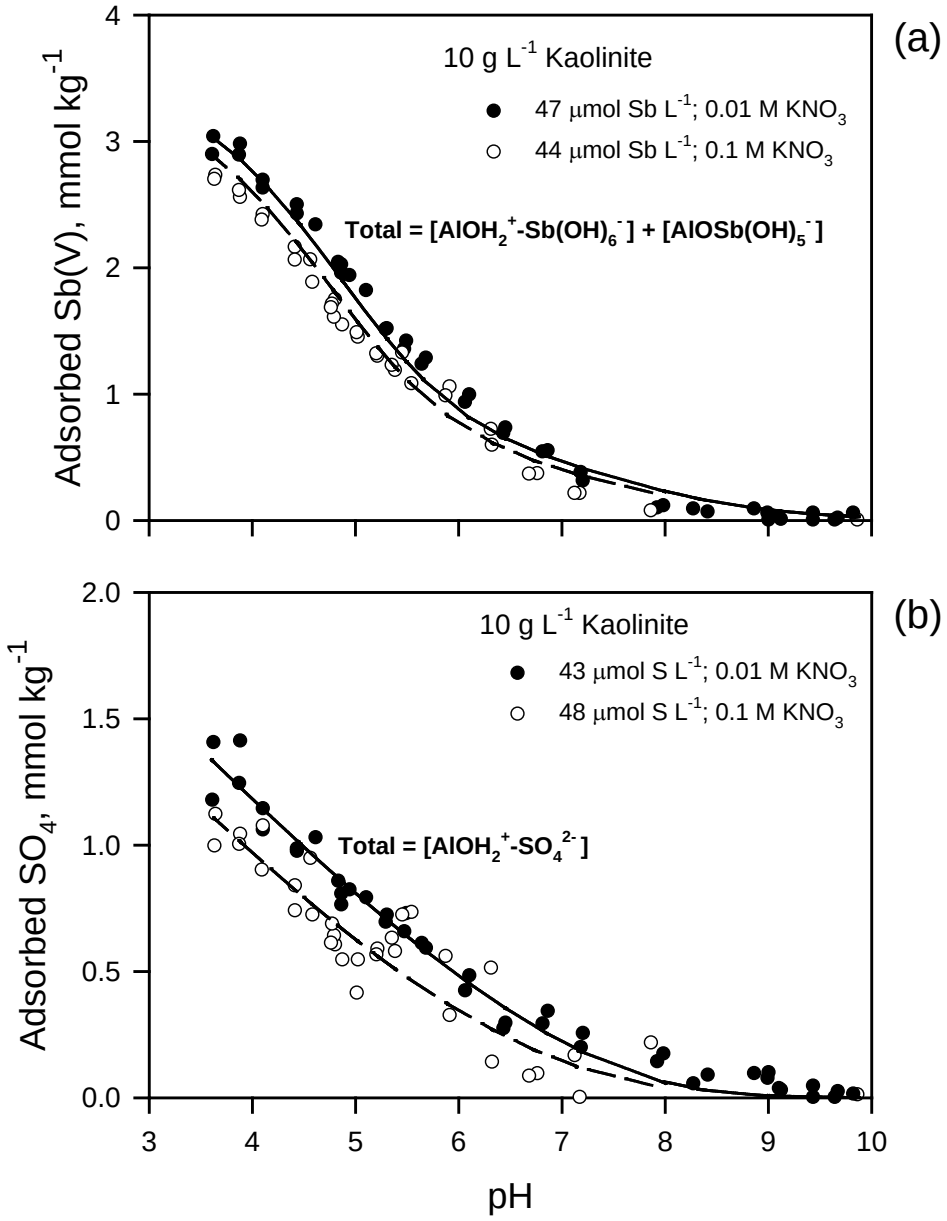

Figure 58. The adsorption of (a) antimonate and (b) sulfate by kaolinite as a function of pH and ionic strength in antimonate-sulfate direct competition systems. The lines represent the triple-layer surface complexation model predictions using the log K^{int} values reoptimized for competitive adsorption of antimonate [Model A; $\equiv AlOH_2^+ – Sb(OH)_6^-$ and $\equiv AlOSb(OH)_5^-$ species] and sulfate ($\equiv AlOH_2^+ – SO_4^{2-}$ species) (Table 10). The solid lines show the predicted adsorption in 0.01 *M* KNO_3, the dashed lines in 0.1 *M* KNO_3.

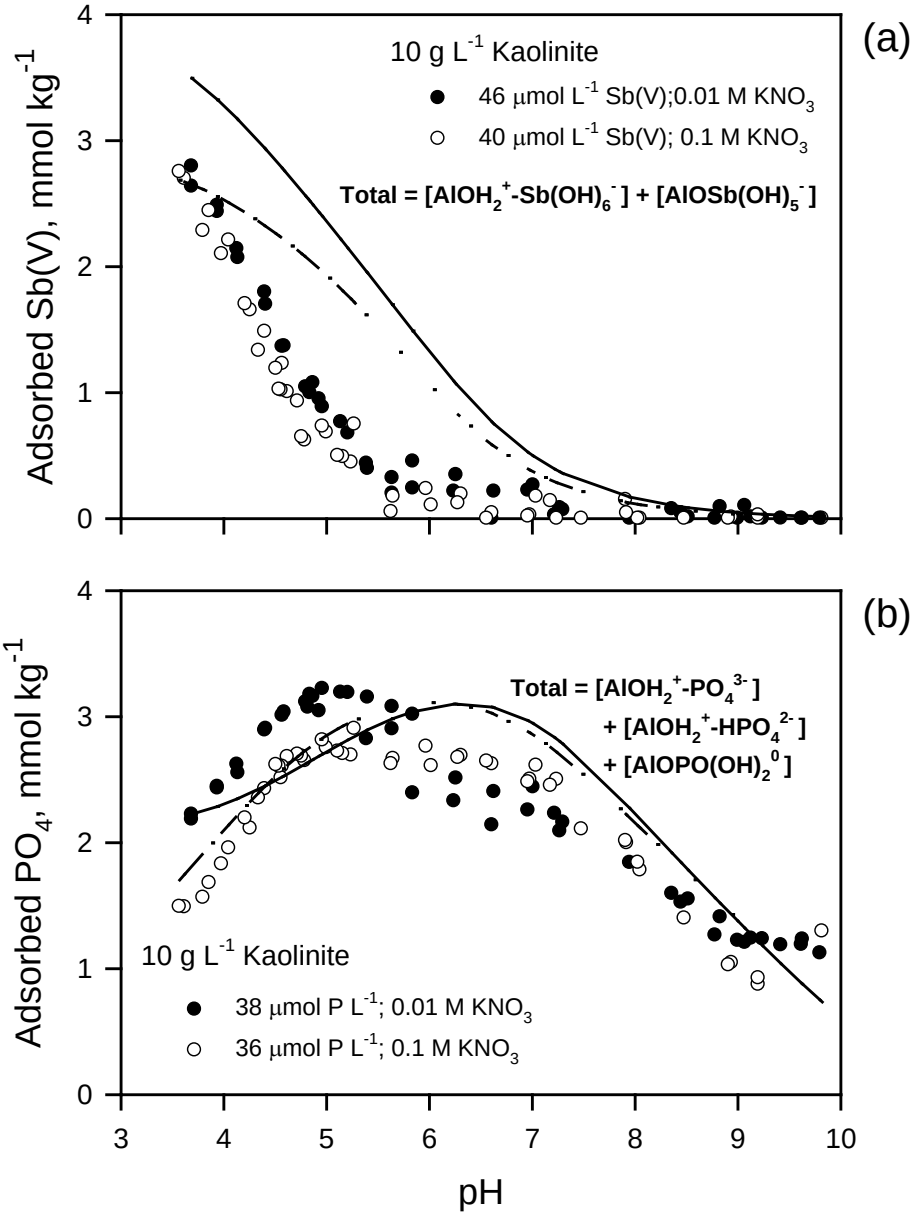

Figure 59. The adsorption of (a) antimonate and (b) phosphate by kaolinite as a function of pH and ionic strength in antimonate-phosphate direct competition systems. The lines represent the triple-layer surface complexation model predictions using the log K^{int} values optimized for non-competitive adsorption of antimonate [Model A; $\equiv AlOH_2^+–Sb(OH)_6^-$ and $\equiv AlOSb(OH)_5^-$ species] or phosphate ($\equiv AlOH_2^+–HPO_4^{2-}$, $\equiv AlOH_2^+–PO_4^{3-}$, and $\equiv AlOPO(OH)_2^0$ species) (Table 10). The solid lines show the predicted adsorption in 0.01 *M* KNO_3, the dashed lines in 0.1 *M* KNO_3.

Summary: Antimonate Adsorption by Kaolinite

Kaolinite is perhaps the most ubiquitous aluminosilicate mineral in soil. Kaolinite generally displays low surface reactivity. Throughout a broad pH range, the kaolinite surface bears a net negative change (point of zero charge is approximately 4.5). However, not all surface functional groups bear net negative charge at pH values above the pH_{pzc}, as kaolinite surface charge is derived from three sources. The isomorphic substitution of Al^{3+} for Si^{4+} in the crystal structure lends a permanent negative charge to the surface. Generally, this negative structural charge is small and satisfied by exchangeable cations on the planar surface of the mineral. The mineral edges bear charge through the protonation and deprotonation of singly-coordinated silanol (≡SiOH) and aluminol (≡AlOH) functional groups. The silanol group is primarily responsible for metal adsorption, as positive charge via protonation ($\equiv SiOH_2^+$) only becomes predominant at pH values less than 2. However, the aluminol group bears a net positive charge ($\equiv AlOH_2^+$) and the ability to attract anions throughout a broad pH range, with a pH_{pzc} of approximately 8.5.

Antimonate adsorption by kaolinite is dependent on pH and ionic strength. Adsorption is negligible in neutral to alkaline environments (pH > 6), and increases with decreasing pH. Antimonate adsorption decreases with increasing ionic strength, suggesting that anion exchange (outer-sphere surface complexation) is an important retention mechanism. The adsorption of antimonate is reversible in pH > 5 solutions; supporting the conclusion that antimonate is an exchangeable anion. However, adsorption is hysteretic (non-reversible) in pH < 5 systems, indicating that inner-sphere surface complexation becomes important with increasing acidity.

Sulfate is a common anion in the environments and generally does not compete with antimonate for adsorption sites at the kaolinite surface. Sulfate is primarily an exchangeable anion in moderately acidic to alkaline solutions, and specifically adsorbed in strongly acidic environments. When sulfate and antimonate are present in equal concentrations, sulfate decreases the retention of antimonite, primarily in pH < 4 systems. However, sulfate does not impact antimonate adsorption when pH > 4.5. Phosphate is more strongly retained by kaolinite then either antimonate or sulfate, with an adsorption edge that plateaus in the pH 4.5 to 6 range. Phosphate is generally considered to be a non-exchangeable, specifically adsorbed ligand. When phosphate and antimonate are present in equal concentrations, the antimonate adsorption edge is shifted to lower pH values (decreasing adsorption throughout a broad pH range). Greater concentrations of sulfate and phosphate, as might be expected in natural environments or firing range soils treated with phosphate to stabilize lead, would be expected to have a more pronounced impact on reducing antimonate retention.

The weak, electrostatic retention of antimonate in alkaline systems, with increasing inner-sphere adsorption character with decreasing pH, is also supported by the adsorption isotherm results. A two-site Langmuir adsorption isotherm model was employed to characterize antimonate retention by kaolinite in pH 5.5 solutions; whereas the one-site Langmuir was used to characterize adsorption in pH 8 systems. The model allowed for the thermodynamic assessment of high intensity-low capacity (site type 1) and low intensity-high capacity (site type 2) antimonate adsorption. In alkaline systems, antimonate adsorption is negligible in 25°C and 35°C systems, and adsorption is not influenced by temperature, indicating an outer-sphere (anion exchange) adsorption mechanism. In acidic solutions, adsorption by low intensity sites is not influenced by temperature, again indicating anion exchange. However, antimonate adsorption by

high intensity sites in acidic systems increases with increasing temperature, indicating an inner-sphere retention process.

Both the zeta potential and proton adsorption characteristics of kaolinite indicated that adsorbed antimonate generates negative surface charge. This response to antimonate adsorption is consistent with the formation of inner-sphere surface complexes. Based on the experimental evidence, surface complexation models were developed to predict antimonate adsorption using the triple layer model formulation. The antimonate adsorption edge as a function of ionic strength is successfully modeled by using a combination of inner- and outer-sphere mechanisms. The inner-sphere mechanism predominated under strongly acidic conditions, with the outer-sphere mechanism becoming increasingly important as solution pH increased into the moderately acidic (pH > 5) range. The surface complexation model, when applied to competitive antimonate-sulfate adsorption, overestimated antimonate adsorption and required reoptimization. Similarly, when applied to competitive antimonate-phosphate, the model overestimated antimonate retention.

Goethite

Adsorption Edge: Reversibility

The initial studies examining antimonate adsorption by goethite involved identical experimental conditions to those of the gibbsite and kaolinite evaluations, most notably a 10 g L^{-1} solid-to-solution ratio and a 50 μmol L^{-1} initial ligand concentration. These experimental conditions resulted in near complete removal of antimonate by goethite throughout a broad pH range (Fig. 60a). In general, the concentrations of reactive ≡FeOH goethite surface sites (27.23 μmol m^{-2}) are reported to be similar in magnitude to that of the ≡AlOH sites on gibbsite (13.28 μmol m^{-2}) (Sahai and Sverjensky, 1997; Lützenkirchen et al., 2002; Sverjensky, 2003). However, the higher specific surface area of goethite (34.24 m^2 g^{-1}) relative to that of gibbsite (5.82 m^2 g^{-1}), coupled with the higher concentration of reactive goethite sites, results in a goethite surface that is potentially more reactive than that of gibbsite (932.4 μmol g^{-1} ≡FeOH sites on goethite vs. 77.29 μmol g^{-1} ≡AlOH sites on gibbsite). Therefore, the higher goethite adsorption capacity for antimonate can be ascribed to the high adsorption capacity of the goethite surface, relative to gibbsite. This finding is also consistent with the observed correlation of antimony retention with the iron oxide content of soils (Mok and Wai, 1990; Chen et al., 2003; Gal et al., 2006; Ritchie et al., 2013). To account for the goethite adsorption capacity, differing solid-to-solution ratios and initial ligand concentrations were evaluated. The 2.5 g L^{-1} solid-to-solution ratio with an initial antimonate concentration of 50 μmol L^{-1} provided satisfactory results in the beaker systems (Fig. 60b). However, the low solid-to-solution ratio proved to be problematic in the competitive adsorption (batch) systems. The 5 g L^{-1} solid-to-solution ratio with an initial antimonate concentration of 500 μmol L^{-1} provided satisfactory results in both the beaker and batch systems (Fig. 60c).

Antimonate adsorption by goethite is a function of pH and independent of ionic strength (Fig. 60). Adsorption is at a relative minimum in strongly alkaline systems, where approximately 40 % of the added antimonate is adsorbed, and increases with decreasing pH. Near complete removal of antimonate is observed at pH values less than 6. Antimonate desorption is hysteretic (non-reversible) throughout the pH range studied. These findings indicate that antimonate adsorption by goethite occurs predominately through a ligand exchange (inner-sphere) mechanism at all pH values. These findings differ from those of Leuz et al. (2006). They

observed a strong ionic strength dependence on antimonate adsorption by goethite, leading them to conclude that an anion exchange (outer-sphere) mechanism was important in pH > 6 solutions.

The goethite adsorption edge findings are consistent with the results of surface spectroscopy studies. Using Mössbauer spectroscopy, Ambe et al. (1986) and Ambe (1987) concluded that antimonate adsorption by hematite (α-Fe_2O_3) occurred via monodentate, inner-sphere complexation at pH 4. McComb et al. (2007) examined antimonate adsorption using ATR-IR and also concluded that the mechanism of retention by amorphous iron oxide was monodentate, inner-sphere complexation under acidic conditions. Scheinost et al. (2006) (using goethite) and Mitsunobu et al. (2010) (using ferrihydrite) employed EXAFS to examine antimonate retention mechanisms in pH 3.5 and 7.5 systems. They concluded that both monodentate and bidentate inner-sphere surface complexation were involved in the retention of antimonate. Ritchie et al. (2013) examined Sb-contaminated sediment using EXAFS and concluded that Sb(V) was retained by bidentate inner-sphere complexation on iron oxides.

Sulfate adsorption by goethite increases with decreasing pH, with a strong dependence on ionic strength (Fig. 61a). In addition, sulfate adsorption was reversible throughout the entire pH range studied (non-hysteretic; the adsorption and desorption edges overlap), differing from the desorption behavior of antimonate (Fig. 60). These findings are consistent with an anion exchange mechanism and the weak, electrostatic retention of sulfate with the goethite surface. Sulfate retention is also depressed, relative to that of antimonate, throughout the entire pH range studied and particularly in the higher ionic strength system (Fig. 62). Despite their similar acid pK_a values (1.99 for sulfate and 2.85 for antimonate; Table 2), the retention of sulfate by goethite is less than that of antimonate, affected by ionic strength, and non-hysteretic. Phosphate retention by goethite is similar to that of antimonate (Fig. 61b). Adsorption is at a relative minimum in strongly alkaline systems, and increases with decreasing pH. Nearly complete removal of the added phosphate occurs in strongly acid (pH < 4) systems. Phosphate desorption is also hysteretic. The phosphate adsorption edge is similar to the of antimonate, indicating that the two ligands have similar affinities for the goethite surface (Fig. 62).

Adsorption Edge: Competition

The adsorption of antimonate, sulfate, and phosphate by goethite in the batch systems (Fig. 63) is similar to that observed in the continuous titration (beaker) systems (Figs. 60 and 61). Ligand adsorption increases with decreasing pH, the retention of sulfate decreases with increasing ionic strength, and the adsorption of antimonate and phosphate are not influenced by the ionic media. Sulfate adsorption is less than that of either antimonate or phosphate throughout the pH 3 to 10 range, irrespective of ionic strength. Antimonate and phosphate adsorption is complete at pH values below approximately 5.

The inclusion of sulfate as a competing ligand did not significantly impact antimonate adsorption by goethite (Fig. 64). However, sulfate adsorption is sharply reduced in the presence of antimonate (Fig. 65), irrespective of the order of ligand addition. Antimonate has a higher affinity for adsorption on goethite than sulfate, indicating that it is a stronger competitor. For example, in 0.01 *M* KNO_3 at pH 4 the density of adsorbed Sb(V) is approximately 2.44 μmol m^{-2} (~100 % of the added antimonate), while that of sulfate is 0.69 μmol m^{-2} (~60 % of the added sulfate) (Figs. 64 and 65). The large reduction in sulfate retention that occurs when in competition with antimonate may result from the direct competition for adsorption sites, or from electrostatic effects that result from the change in surface charge that arises from the adsorption

of antimonate. The site density of singly-coordinated ≡FeOH groups is 3.45 sites nm^{-2}, or 5.73 μmol m^{-2} (Table 1). Without any interaction, the total site occupation of coadsorbed antimonate and sulfate would be 3.13 μmol m^{-2} (2.44 plus 0.69 μmol m^{-2}) at pH 4, a value that is below the total site density (assuming monodentate complexation). Therefore, the direct competition of antimonate and sulfate for adsorption sites should be minimal. However, the inner-sphere complexation of antimonate at the goethite surface neutralizes positive surface charge (e.g., $\equiv FeOH_2^+ + Sb(OH)_6^- = \equiv FeOSb(OH)_5^- + H^+ + H_2O$), decreasing the electrostatic adsorption of sulfate (Fig. 65). Thus, the changing electrostatics at the solid-solution interface is responsible for the reduced retention of sulfate in the competitive systems.

The inclusion of phosphate as a competing ligand reduces the retention of antimonate by goethite in both the 0.01 *M* KNO_3 and 0.1 *M* KNO_3 systems (Fig. 66). This effect is most pronounced in the preadsorbed phosphate and direct competition systems, where antimonate adsorption is negligible in pH > 7 solutions. Antimonate is more competitive with phosphate for goethite surface sites when preadsorbed. In alkaline to highly alkaline systems, the retention of phosphate is not strongly impacted by antimonate (Fig. 67). Phosphate adsorption increases as pH decreases from approximately 10, achieving a relative maximum value in the pH 7 to 8 range. Phosphate adsorption then decreases with an additional decrease in pH. This decrease is most pronounced in the preadsorbed antimonate system, followed by the direct competition and preadsorbed phosphate systems. The decrease in phosphate retention with decreasing pH below 8 also corresponds to the pH range where antimonate adsorption becomes significant. The phosphate adsorption behavior in the competitive antimonate systems is also similar to that observed when in competition with citrate and arsenate; ligands that also form inner-sphere surface complexes (Geelhoed et al., 1998 and 1999; Hiemstra and Van Riemsdijk, 1999)

Both antimonate and phosphate have high affinity for the goethite surface. If only monodentate surface complexes are formed, the density of adsorbed Sb(V) at pH 4 (0.01 *M* KNO_3) is 2.31 μmol m^{-2} (~100 % of the added antimonate, Fig. 66), while that of phosphate is 2.32 μmol m^{-2} (~100 % of the added phosphate, Fig 67). Without any interaction, the total site occupation of coadsorbed antimonate and phosphate would be approximately 4.6 μmol m^{-2} at pH 4, a value that approaches the total site density (5.73 μmol m^{-2}). If bidentate antimonate and phosphate surface complexes are formed, a retention mechanism that is supported in the literature for both ligands, the occupied sites would exceed the available site concentration. Therefore, competition of antimonate and phosphate for adsorption sites occurs.

The competitive adsorption findings indicate that phosphate is strongly preferred by the goethite ligand exchange sites in alkaline (pH > 7) systems, relative to antimonate. The inner-sphere complexation of phosphate species contributes negative charge to the goethite surface, reducing the outer-sphere (electrostatic) complexation of antimonate. Greater proton concentration (lower pH) is required to overcome this effect; thus, the antimonate adsorption edge shifts to lower values. In the pH < 6 range, antimonate effectively competes with phosphate for the fixed number of adsorption sites, reducing phosphate retention.

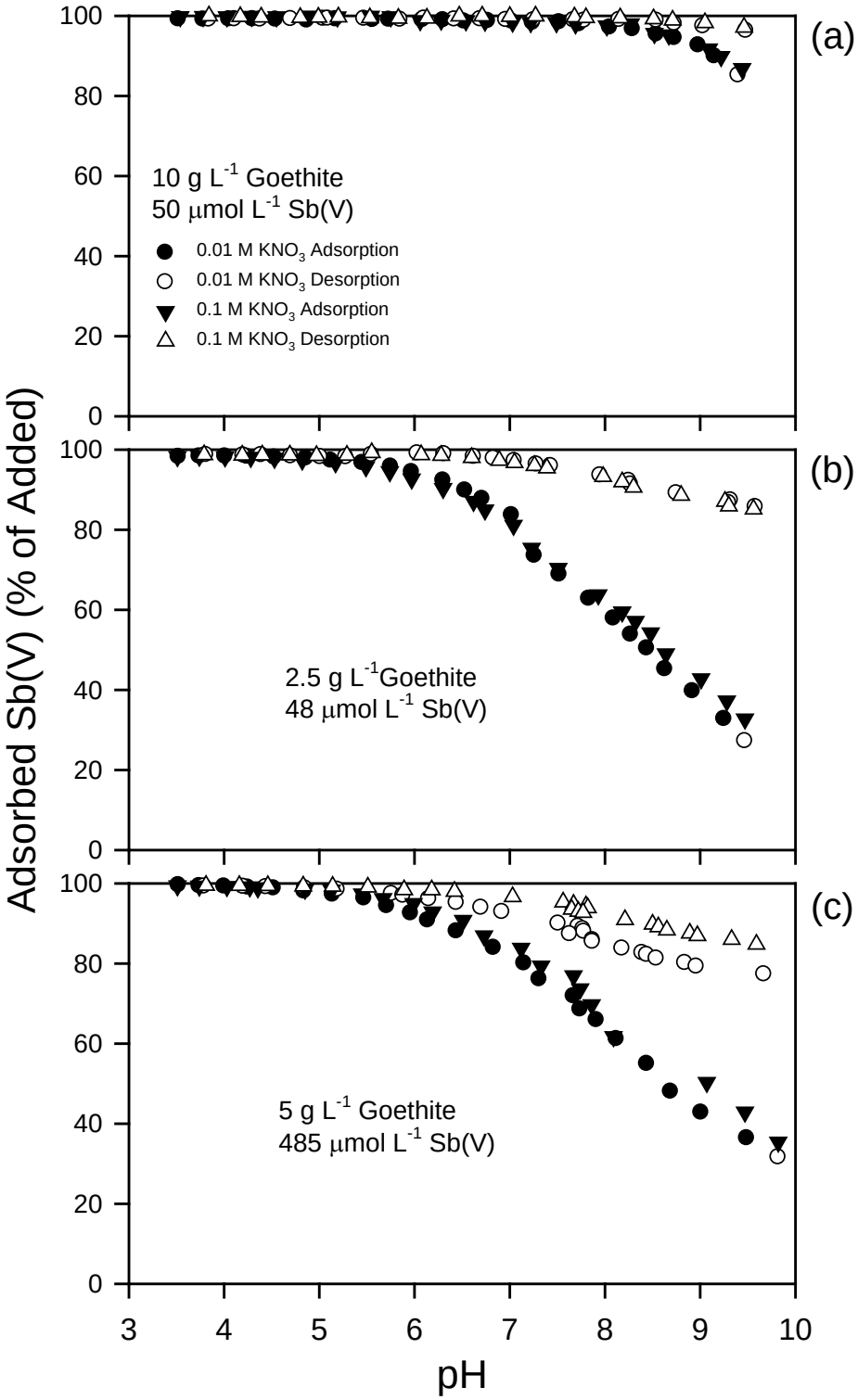

Figure 60. The adsorption of antimonate by goethite as a function of solid-to-solution ratio and initial antimonate concentration: (a) 10 g L^{-1} goethite and 50 μmol L^{-1} Sb(V); (b) 2.5 g L^{-1} goethite and 48 μmol L^{-1} Sb(V); (c) 5 g L^{-1} goethite and 485 μmol L^{-1} Sb(V).

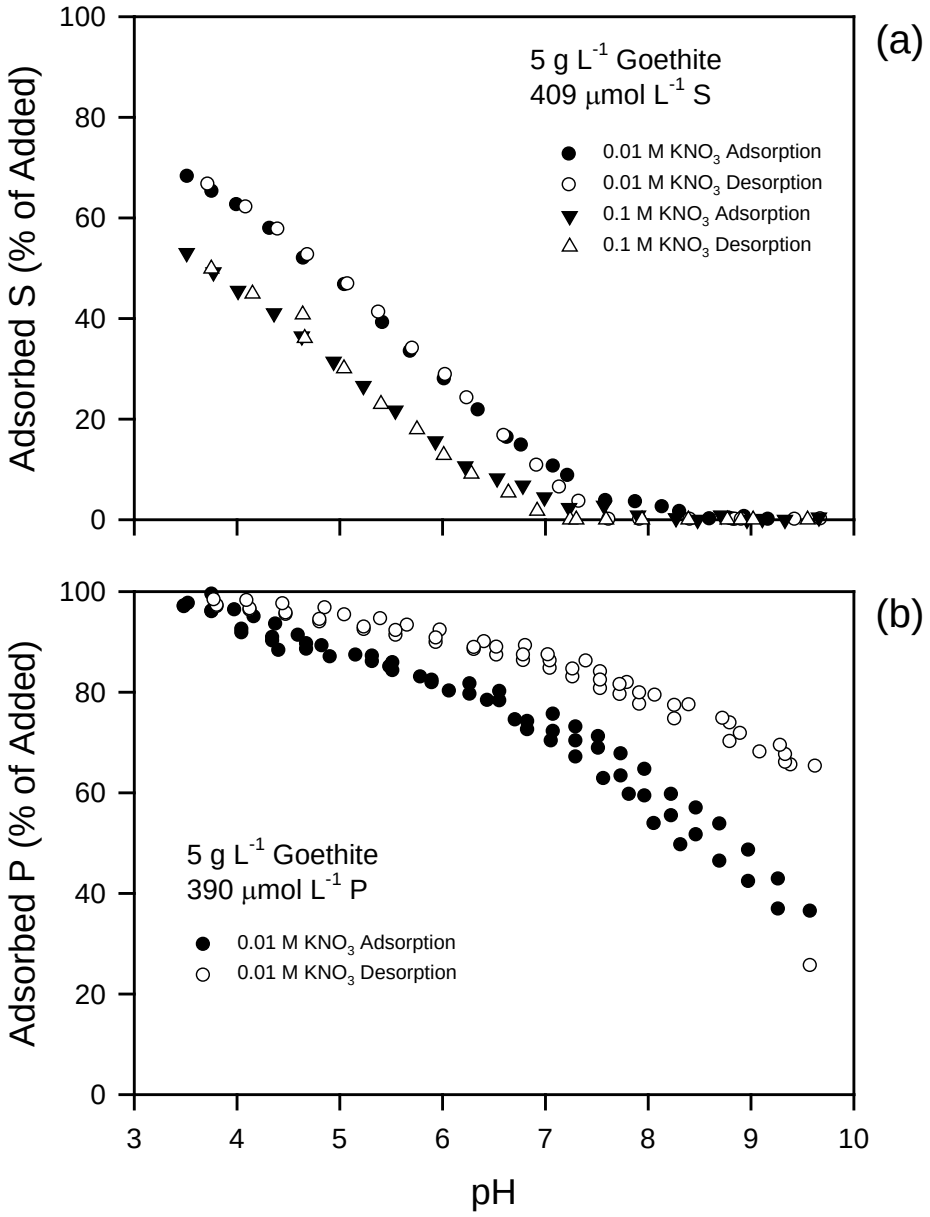

Figure 61. The adsorption and desorption of (a) sulfate and (b) phosphate by goethite as a function of pH and ionic strength.

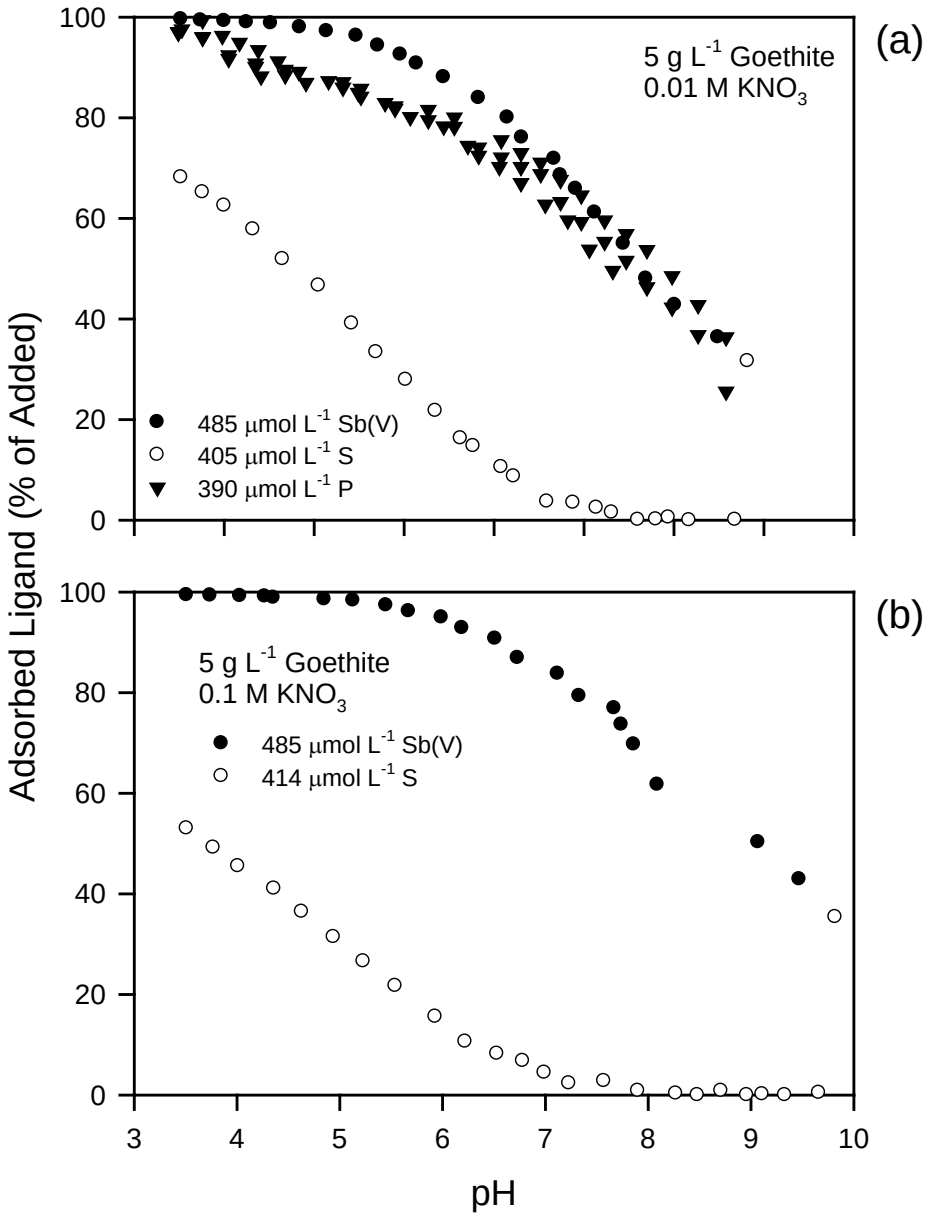

Figure 62. The adsorption antimonate, sulfate, and phosphate by goethite as a function of pH in (a) 10 m*M* KNO_3 and (b) 100 m*M* KNO_3 ionic media.

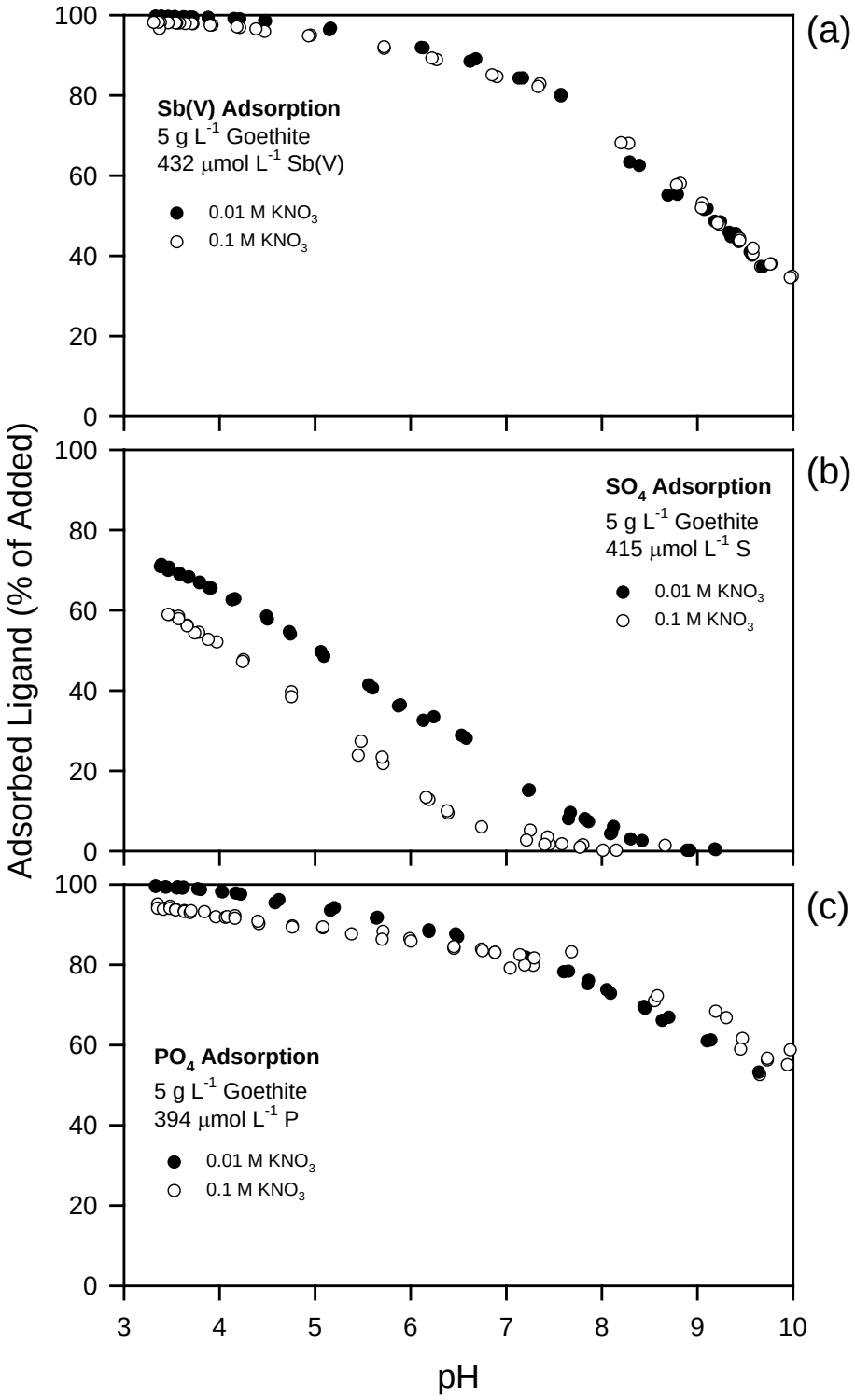

Figure 63. The adsorption of (a) antimonate, (b) sulfate, and (c) phosphate by goethite from batch equilibrium systems as a function of pH and ionic strength.

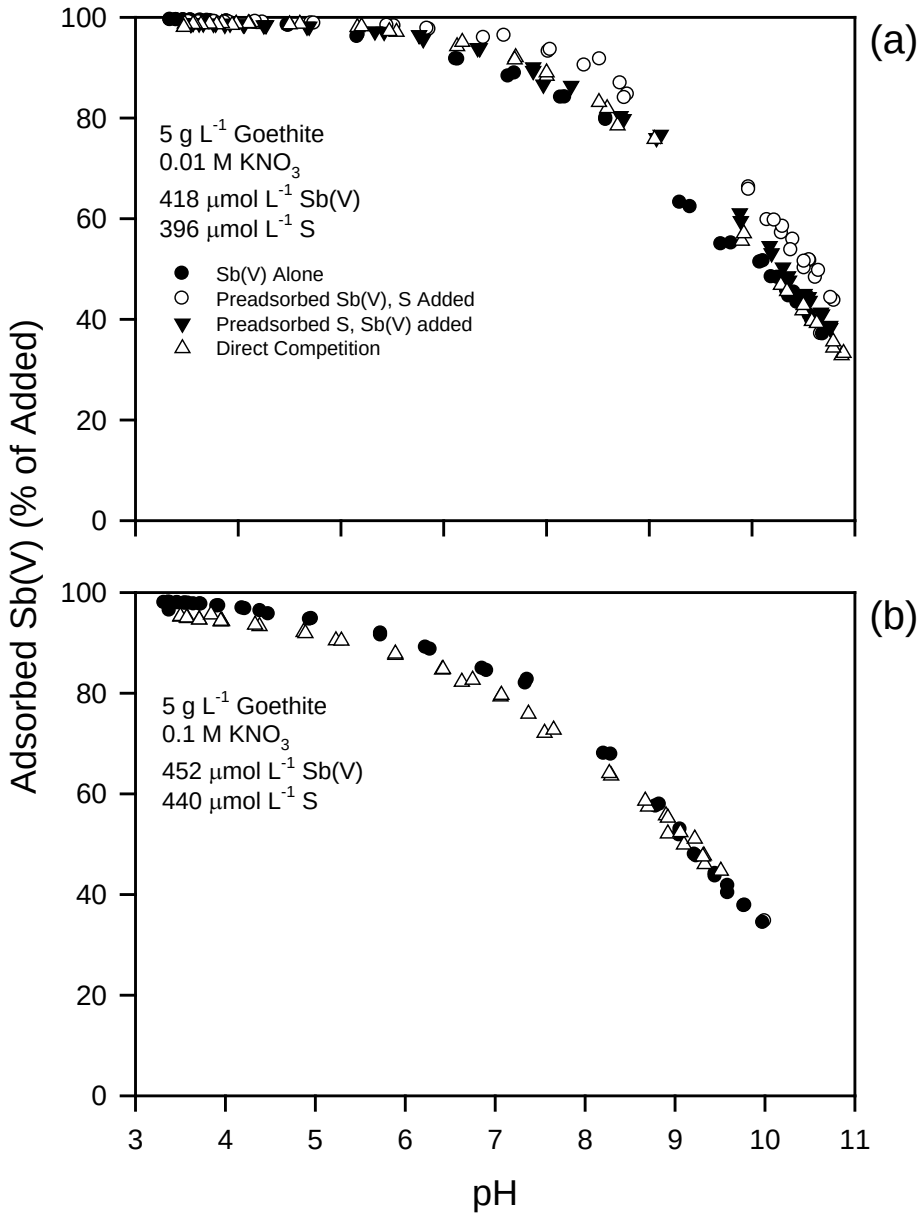

Figure 64. The competitive adsorption of antimonate by goethite in the presence of sulfate in (a) 10 m*M* KNO_3 and (b) 100 m*M* KNO_3 electrolyte media as a function of pH and method of sulfate addition.

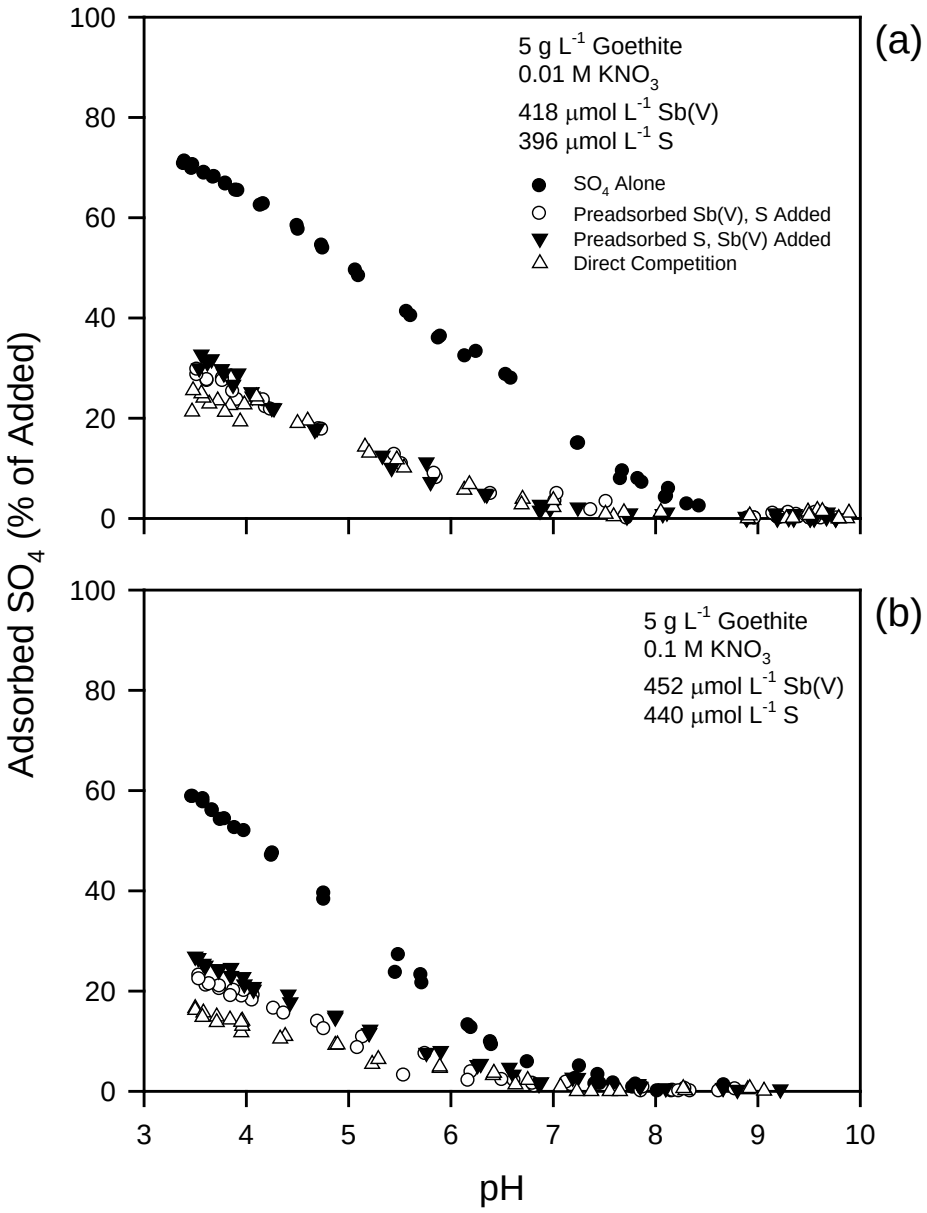

Figure 65. The competitive adsorption of sulfate by goethite in the presence of antimonate in (a) 10 m*M* KNO_3 and (b) 100 m*M* KNO_3 electrolyte media as a function of pH and method of antimonate addition.

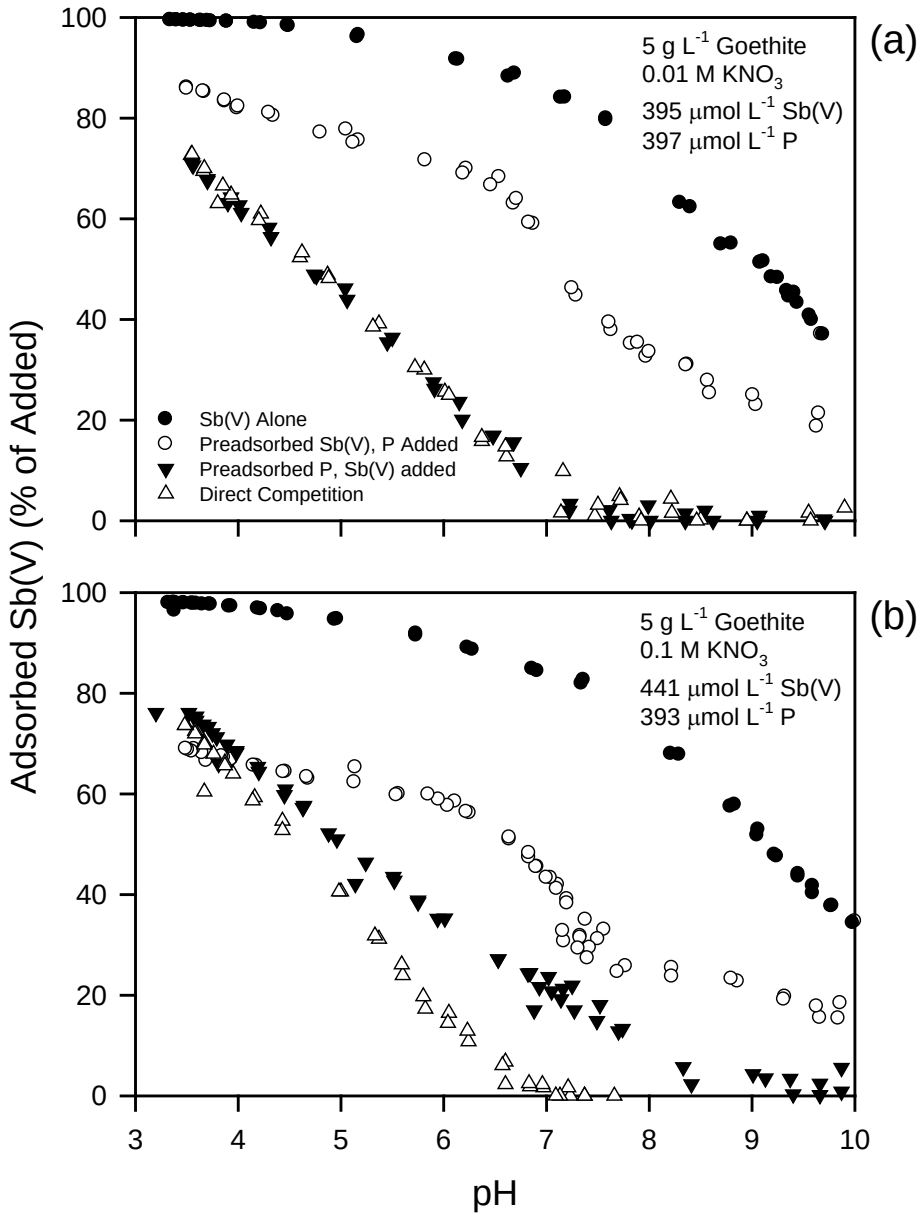

Figure 66. The competitive adsorption of antimonate by goethite in the presence of phosphate in (a) 10 m*M* KNO_3 and (b) 100 m*M* KNO_3 electrolyte media as a function of pH and method of phosphate addition.

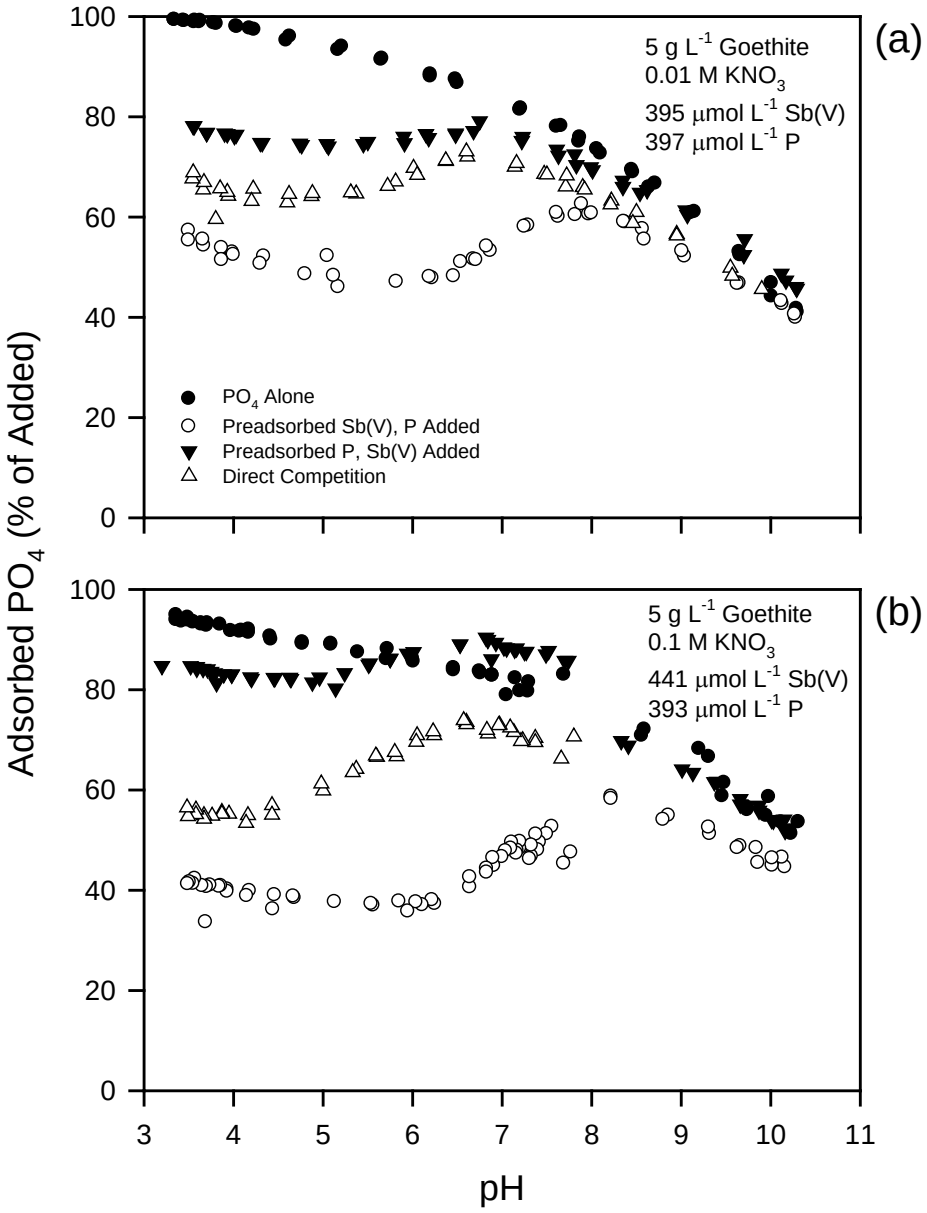

Figure 67. The competitive adsorption of phosphate by goethite in the presence of antimonate in (a) 10 m*M* KNO_3 and (b) 100 m*M* KNO_3 electrolyte media as a function of pH and method of antimonate addition.

Adsorption Isotherms: Thermodynamics

The adsorption of antimonate by goethite in both pH 5.5 and 8, 0.01 *M* KNO_3 solutions is Langmuirian; adsorption intensity (isotherm slope) decreases with increasing surface coverage (Fig. 68a). The pH 5.5 isotherms are not linear in log-log space (Fig. 68b), indicating that the Freundlich equation (Eq. [3]) is not an appropriate model for describing the adsorption isotherms. However, the pH 8 adsorption isotherms are linear in log-log space, indicating that the isotherms may be described by the Freundlich isotherm model. Antimonate adsorption is strongly influenced by pH, as adsorption increases with increasing acidity, consistent with the adsorption edge findings described in the previous section (Fig. 60). On average, the K_F value for antimonate adsorption at pH 8 was 98, which represent the surface excess of antimonate (q, in mmol kg^{-1}) when C_{eq} is unity (Table 11). The log K_F values do not vary significantly as a function of temperature. Adsorption of antimonate from both the pH 5.5 and 8 solutions tends to increase with increasing temperature.

Plots of K_d vs. q indicate that the adsorption data may also be described by the one-site Langmuir model (Eq. [4]; Figs. 69 and 70). Linear regression analysis of the K_d vs. q plots was used to derive the one-site Langmuir parameters for antimonate adsorption in the pH 5.5 and 8 systems (Table 11). The Henry's Law constants (K_{ad} values) generated from the Langmuir parameters K_L and b, tended to increase with increasing temperature in both pH systems (Table 11 and Fig. 71). Both the enthalpy (ΔH_{ad}) and entropy (ΔS_{ad}) of adsorption were computed for antimonate adsorption using the van't Hoff equation (Eq. [9]), as applied to the ln K_{ad} vs. T^{-1} data in Fig. 71. For adsorption in pH 5.5, ΔH_{ad} is positive (21.59 kJ mol^{-1}) and $T\Delta S_{ad}$ is large (49.16 kJ mol^{-1} at 298 K) relative to ΔH_{ad}, indicating that antimonate adsorption is endothermic and entropically driven (Table 12). Similarly, adsorption in pH 8 is endothermic (ΔH_{ad} = 16.61 kJ mol^{-1}) and entropically driven ($T\Delta S_{ad}$ = 34.56 kJ mol^{-1} at 298 K). For both pH conditions, the free energy of adsorption (ΔG_{ad}) is negative, indicating that antimonate adsorption is spontaneous.

Endothermic (positive ΔH_{ad}) and entropically-driven (heat is absorbed) adsorption is generally indicative of inner-sphere complexation (adsorption increases with increasing temperature). The ΔH_{ad} value for antimonate adsorption in pH 5.5 and 8 (21.6 and 16.6 kJ mol^{-1}) are similar in magnitude to ΔH_{ad} values typically found for the inner-sphere surface complexation of ligands. Enthalpy values for the retention of specifically-adsorbed ligands by variable-charge minerals are generally <40 kJ mol^{-1}, although similar in magnitude ΔH_{ad} values have been used to infer an ion exchange mechanism (Zhang and Selim, 2008; Li et al., 2008; Ferreiro and de Bussetti, 2007). The inner-sphere adsorption of arsenate by Al and Fe oxides has been reported to generate ΔH_{ad} values of 25.11 and 17.83 kJ mol^{-1} (Helmy et al., 1996; Partey et al., 2008). Enthalpy values for the inner-sphere complexation of phosphate and 2-ketogluconate by Fe oxides range between 22 and 81.84 kJ mol^{-1} (Juang and Chung, 2004; Mezzener and Bensmaili, 2008; Mustafa et al., 2008; Journey et al., 2010).

Table 11. Freundlich and Langmuir isotherm parameters, and the Henry's Law constants (K_{ad} values) for the adsorption of antimonate by goethite.

	Freundlich parameters†			Langmuir parameters‡		
T, °C	log K_F	K_F	N	K_L	b	K_{ad}
	pH 5.5					
5				465.59	71.61	33339
15				650.68	71.68	46641
25				1357.5	73.71	100057
35				893.00	78.32	69939
	pH 8					
5	1.971	93.54	0.417	12.510	67.32	842.2
15	1.892	77.98	0.341	18.647	56.54	1054
25	1.919	82.99	0.291	28.607	59.99	1716
35	2.141	138.4	0.437	20.010	77.29	1547

†log K_F and N were obtained by linear regression analysis of Eq. [3]. The log K_F and N values do not differ significantly as a function of temperature at $P = 0.05$. The Freundlich model was not used to describe antimonate adsorption in pH 5.5 systems.
‡K_L and b were obtained by linear regression analysis of Eq. [5] and the data presented in Figs. 69 and 70 for the one-site Langmuir model (Eq. [4]). Units of K_L are L mmol^{-1}; b are mmol kg^{-1}; and K_{ad} are L kg^{-1}.

Table 12. Thermodynamic parameters for the adsorption of antimonate by goethite.†

Temperature	ΔH_{ad}	ΔS_{ad}	ΔG_{ad}
°C	kJ mol^{-1}	J K^{-1}mol^{-1}	kJ mol^{-1}
	pH 5.5		
5			–24.27
15			–25.91
25	21.59	164.9	–27.56
35			–29.21
	pH 8		
5			–15.21
15			–16.36
25	16.61	115.9	–17.50
35			–18.65

†Enthalpy (ΔH_{ad}) and entropy (ΔS_{ad}) of adsorption are temperature independent and computed using the van't Hoff equation (Eq. [9]) analysis of the influence of temperature on the Henry's Law constant for antimonate adsorption (Fig. 71). Free energy of adsorption (ΔG_{ad}) computed using Eq. [11].

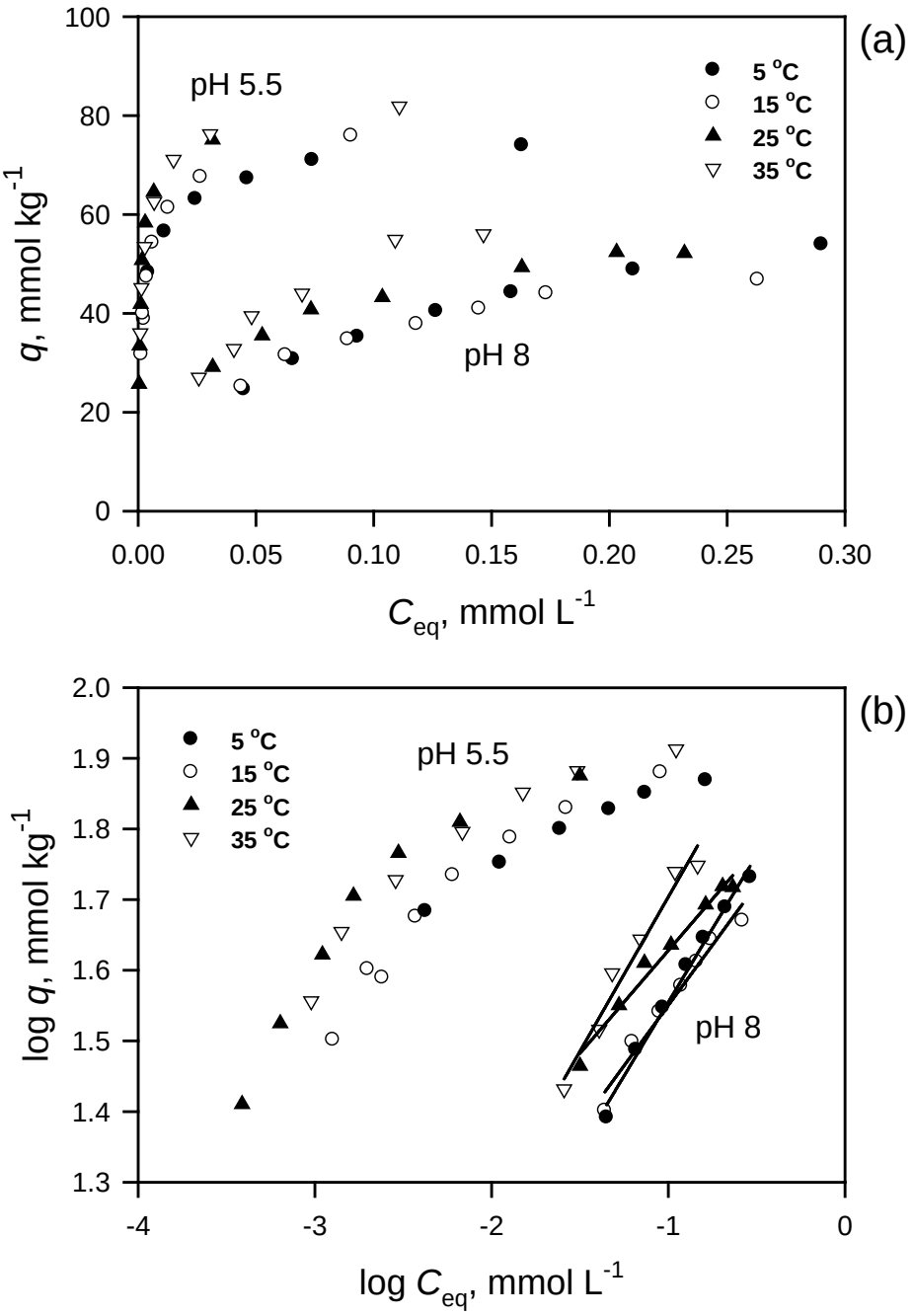

Figure 68. Adsorption isotherms, plotted in (a) normal space and (b) log-log space, illustrating the adsorption (q) of antimonate in 0.01 M KNO_3 by goethite (5 g L^{-1}) as a function equilibrium solution concentration (C_{eq}), pH, and temperature.

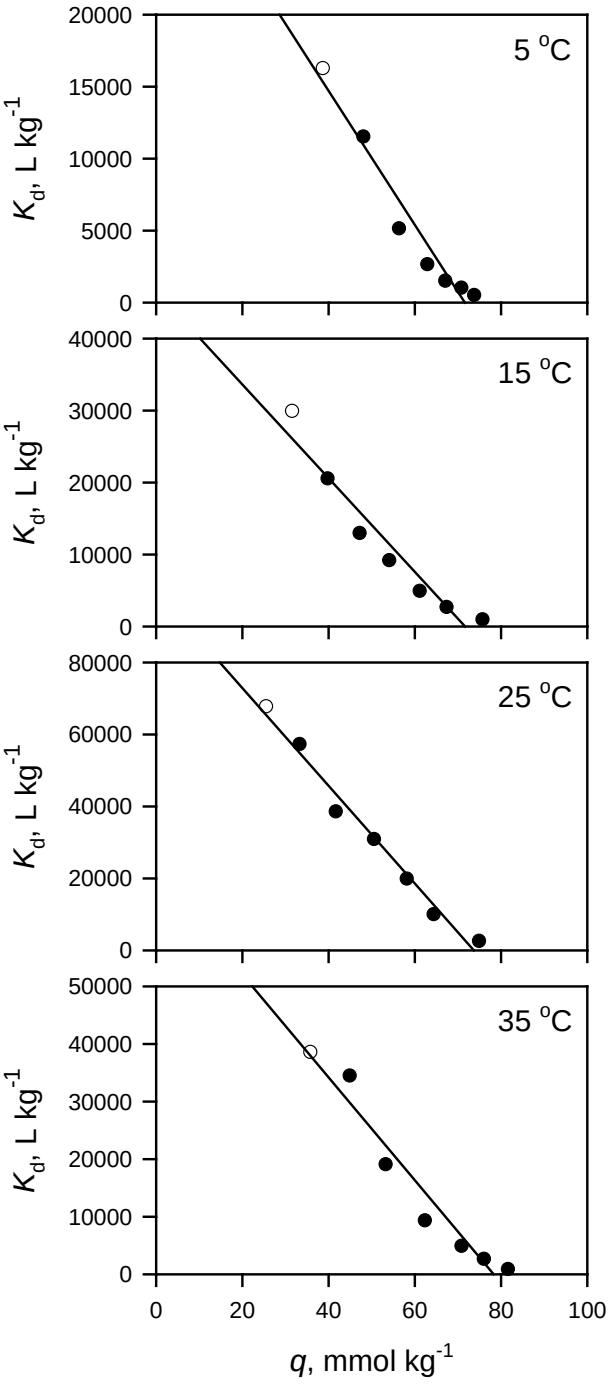

Figure 69. Application of the transformed version of the Langmuir model to K_d vs. q plots of the pH 5.5 antimonate adsorption isotherm data described in Fig. 68a. The adsorption of antimonate by goethite is described by the Langmuir isotherm equations (Table 11).

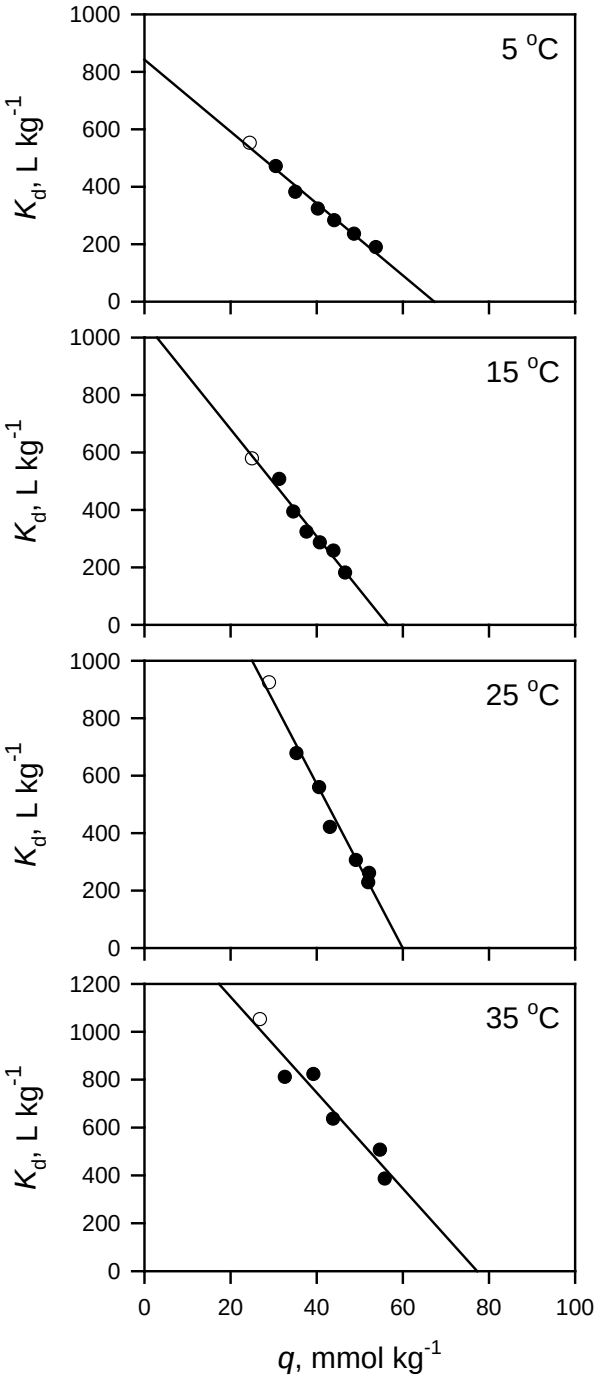

Figure 70. Application of the transformed version of the Langmuir model to K_d vs. q plots of the pH 8 antimonate adsorption isotherm data described in Fig. 68a. The adsorption of antimonate by goethite is described by the Langmuir isotherm equations (Table 11).

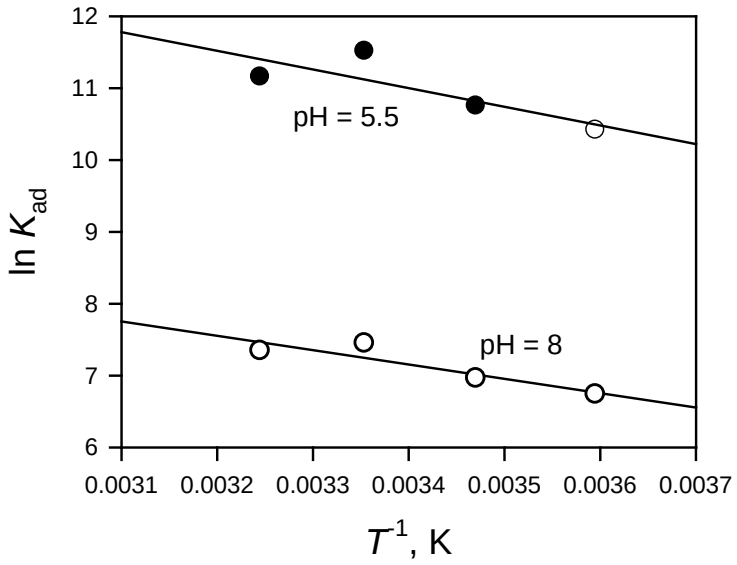

Figure 71. Temperature dependence of the Henry's Law constant for antimonate adsorption by goethite ($K_{ad} = K_L b$). The adsorption constants (K_L and b) where obtained from the application of the Langmuir equation (Eq. [7]). The lines represent the least squares linear regression analysis of the van't Hoff equation (Eq. [9]) and the ln K_{ad} vs. T^{-1} data, where T is the thermodynamic temperature.

Electrostatics at the Solid-Solution Interface

Zeta potential and proton adsorption curves for geothite in the swamping electrolyte (KNO_3) are illustrated in Fig. 72. The KNO_3 system represents surface charging in the absence of inner-sphere complexation. For goethite, the isoelectric point (IEP) and the point of zero charge (pH_{pzc}) is 9.8 (Fig. 72a). This is also the common intersection point (CIP) for the zeta potential measurements in 0.01 and 0.1 *M* KNO_3. At pH values below the pH_{pzc}, the goethite surface bears a net positive charge. The measured goethite pH_{pzc} is within the 6.7 to 10.2 range reported by Kosmulski (2009). An increase in the swamping electrolyte concentration results in a decreasing zeta potential as the pH is decreased below the pH_{pzc}. Increased concentrations of electrolyte in the σ_d plane tend to shield the particle charge, decreasing the extent of charge influence in the solid-solution interface and decrease the response (particle movement) in an electric field (Yu, 1997). As expected, the adsorbed proton concentration (Q_h) increased with decreasing pH and with increasing ionic strength (Fig. 72b). The point of zero salt effect (pH_{pzse}), and the corresponding point of net proton charge (pH_{pznpc}) of the goethite sample is approximately 9.

When a ligand other than the indifferent electrolyte is present, electrophoretic mobility will reflect the adsorption mechanism. Adsorption of an anionic ligand in the is-plane will decrease the zeta potential and shift the IEP to lower pH values (additional protonate, i.e., lower pH, required for site neutralization). The adsorption of a ligand in the os-plane will not affect the IEP, relative to that in the indifferent electrolyte. However, a decrease in the zeta potential may be observed if the adsorbed ligand has higher valence than the indifferent electrolyte (providing greater negative charge to the near-surface region bounded by the particle shear plane).

In the presence of 10 m*M* K_2SO_4 alone, or with 10 m*M* KNO_3, the zeta potential of goethite is generally negative for all pH values studied (Fig. 72a). However, the 100 m*M* KNO_3 + 10 m*M* K_2SO_4 solution does not appreciably change the IEP of goethite (Fig. 72a), relative to the KNO_3 systems, which may be due to the absence of sulfate adsorption at the IEP (Figs. 61a and 63). However, there is a negative shift in the zeta potential at pH values below the IEP and as a result of sulfate adsorption, similar to that observed by Juang and Wu (2002). The less positive zeta potential values indicate that the adsorbed complexes of sulfate provide greater negative charge to the near-surface region bounded by the particle shear plane, relative to the background electrolyte (divalent SO_4^{2-} vs. monovalent NO_3^-). The IEP of goethite shifts to the 3 to 4 range when reacted with phosphate (Fig 73). This is macroscopic evidence of the inner-sphere complexation of phosphate by goethite. This finding is consistent with the strong phosphate adsorption behavior, and the lack of an ionic strength effect (Figs. 61b and 63), and similar to that observed by Tejedor-Tejedor and Anderson (1990), Arai and Sparks (2001), and Antelo et al. (2005). Within the pH range studied (pH > 4), a goethite IEP in the presence of antimonate was not achieved (Fig. 74). At all pH values, the zeta potentials are negative, reflecting the inner-sphere complexation of antimonate.

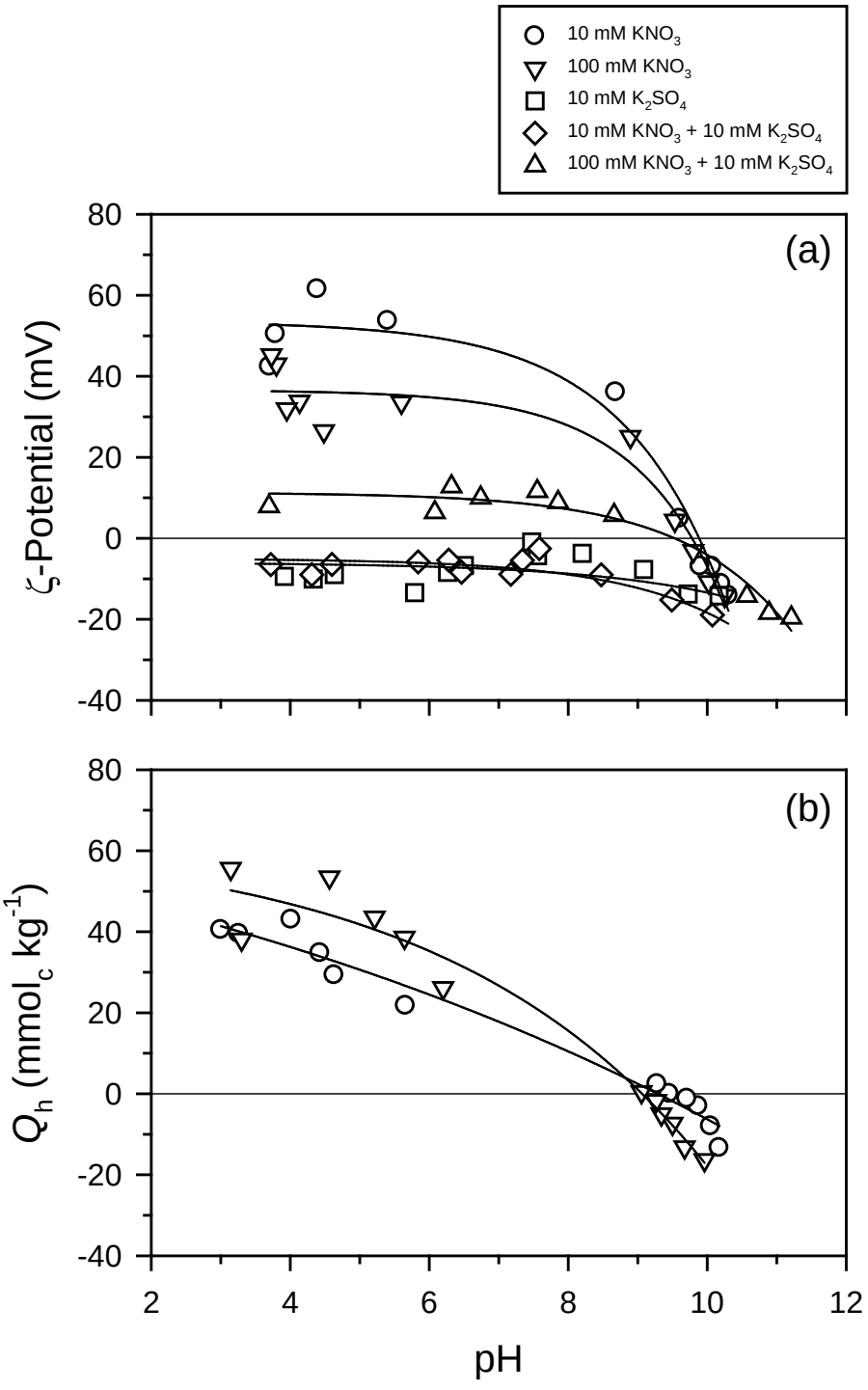

Figure 72. The influence of nitrate and sulfate on goethite (a) zeta potential and (b) proton adsorption as a function of pH, ionic strength, and electrolyte composition.

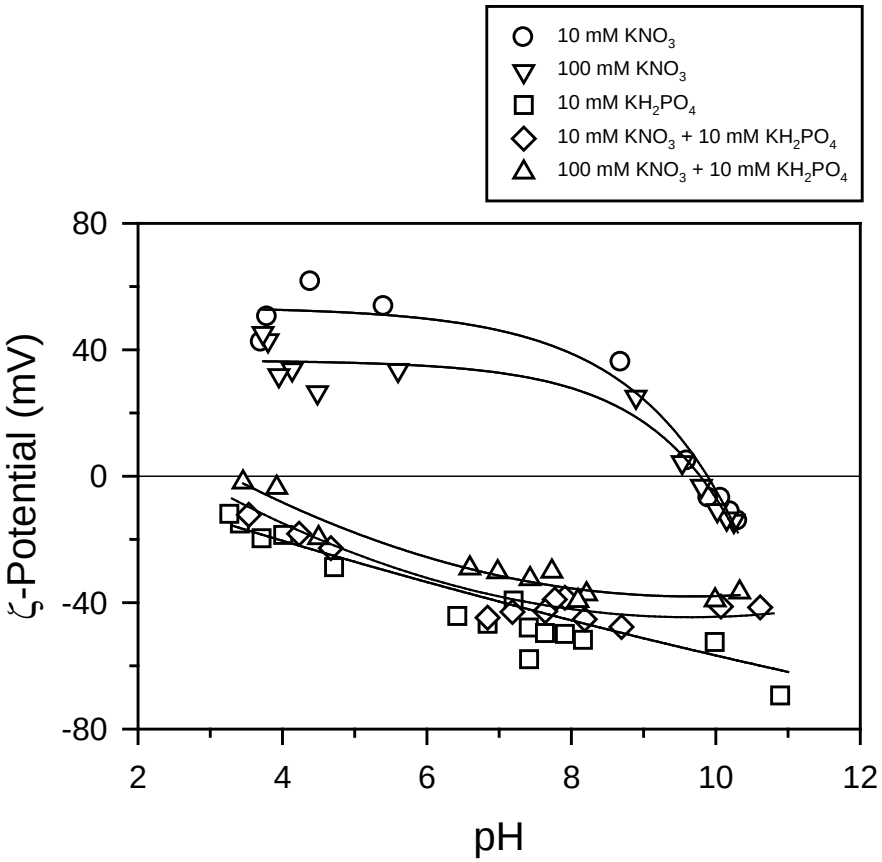

Figure 73. The influence of nitrate and phosphate on goethite zeta potential as a function of pH, ionic strength, and electrolyte composition.

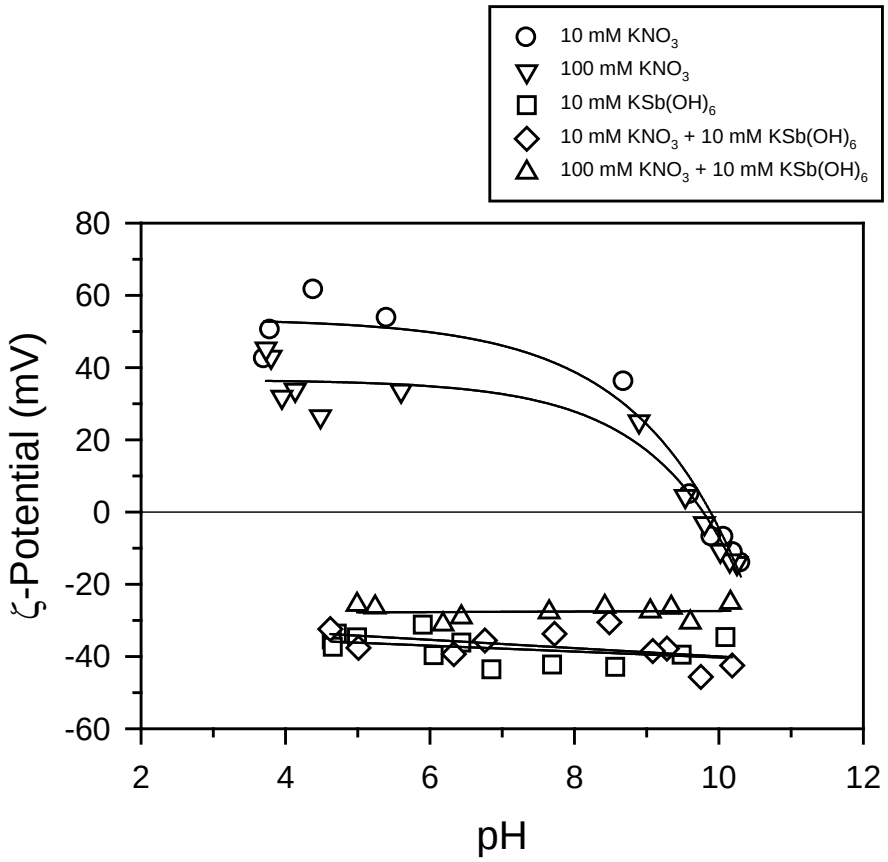

Figure 74. The influence of nitrate and antimonate on goethite zeta potential as a function of pH, ionic strength, and electrolyte composition.

Surface Complexation Modeling

The antimonate adsorption edge and adsorption isotherm studies, coupled with the effects of antimonate on goethite surface charging, indicate that antimonate retention by goethite occurs predominantly via an inner-sphere complexation mechanism. Spectroscopic studies indicate that the retention of antimonate by hydrous iron oxides with ≡FeOH surface functionality proceeds via mono- and bidentate inner-sphere surface complexation processes ($\equiv FeOHSb(OH)_5^0$ or $\equiv FeOSb(OH)_5^-$, and $(\equiv FeO)_2Sb(OH)_4^-$). Using Mössbauer spectroscopy, Ambe et al. (1986) and Ambe (1987) concluded that antimonate adsorption by hematite (α-Fe_2O_3) occurred via monodentate, inner-sphere complexation at pH 4. McComb et al. (2007) examined antimonate adsorption using ATR-IR and also concluded that the mechanism of retention by amorphous iron oxide was monodentate, inner-sphere complexation under acidic conditions. Scheinost et al. (2006) (using goethite) and Mitsunobu et al. (2010) (using ferrihydrite) employed EXAFS to examine antimonate retention mechanisms in pH 3.5 and 7.5 systems. They concluded that both monodentate and bidentate inner-sphere surface complexation were involved in the retention of antimonate. Similarly, Ritchie et al. (2013) examined Sb-contaminated sediment with EXAFS and concluded that Sb(V) was bound to Fe-oxides by bidentate, inner-sphere complexation. Leuz et al. (2006) imposed a bidentate surface complex to model antimonate adsorption by goethite. However, the bidentate model did not adequately describe the effect of ionic strength on adsorption.

Two experimental techniques were employed to generate the antimonate, sulfate, and phosphate adsorption edge data (q vs. pH) as a function of ionic strength: continuous titration beaker systems (Fig. 60) and the competitive adsorption batch systems (Figs. 63). Both data sets were used to develop the chemical models for ligand adsorption by goethite. Several models were evaluated for their ability to describe the antimonate adsorption edge, similar to those described in Tables 7 and 10 for antimonate adsorption by gibbsite and kaolinite. The only model that would describe the antimonate adsorption edge on goethite involved the monodentate $\equiv FeOSb(OH)_5^-$ complex as the stipulated inner-sphere species and the outer-sphere $\equiv FeOH_2^+ – Sb(OH)_6^-$ species. The adsorption of antimonate is generally well-predicted by this model in the pH 3 to 10 range (Figs. 75 and 76). The goodness-of-fit parameter for the beaker data set (V_Y = 9.634) indicates that the model satisfactorily describes the adsorption edges. However, the model over predicts antimonate adsorption in the batch systems, yielding a correspondingly high goodness-of-fit parameter (V_Y = 29.672). The common logarithm of the intrinsic surface complexation constants for the outer-sphere complex is $\log K^{int} = 13.35$. The constant for the inner-sphere species is $\log K^{int} = 3.26$ (Table 13).

The outer-sphere surface complex is the predominant surface species in the pH > 4 range in the 0.01 M KNO_3 systems. While in the higher ionic strength systems (0.1 M KNO_3), the outer-sphere complex predominates in pH >5 solutions. The inner-sphere species is predicted to account for greater than 20 % of the adsorbed antimonate in the pH < 8 range. This result is consistent with the adsorption reversibility and thermodynamic findings, which indicated that inner-sphere complexation is important throughout the pH range studied. Antimonate adsorption is hysteretic in both acidic and alkaline systems (Fig. 60), with less that 20 % of the adsorbed antimonate released during desorption, and only in the pH > 9 solutions. Adsorption in pH 5.5 and 8 solutions is endothermic and entropically-driven, suggesting that the inner-sphere surface complex is an important component to the adsorption process. Further, a charge reversal is not

observed in the zeta potential measurements, again suggesting an inner-sphere component to the adsorption process (Fig. 74).

In order to predict competitive adsorption in antimonate-sulfate and antimonate-phosphate systems, intrinsic constants for the retention of sulfate and phosphate must be determined. The adsorption of sulfate by goethite is strongly influenced by solution ionic strength (Figs. 61a and 63b) and reversible throughout the pH range studied. Sulfate adsorption does not alter the IEP of goethite, although zeta potentials are reduced relative to the nitrate systems (Fig. 72a). These experimental findings are consistent with the available literature (Hansmann and Anderson, 1985; Geelhoed et al., 1997; Rietra et al., 1999; Juang and Wu, 2002). However, spectroscopic evidence suggests that sulfate may also form inner-sphere surface complexes (Hug, 1997; Eggleston et al., 1998; Peak et al., 1999), particularly in acidic solutions. Sulfate adsorption by goethite was modeled by considering a combination of inner- and outer-sphere surface species, $\equiv FeOH_2^+–SO_4^{2-}$ and $\equiv FeOSO_3^-$ (Figs. 77 and 78; Table 13). The goodness-of-fit parameters for the beaker and batch data sets (V_Y = 119.91 and 119.88) indicate that the adsorption data are not well-described by the model. However, other models, including $\equiv FeOH_2^+–SO_4^{2-}$ alone and $\equiv FeOSO_3^-$ alone, did not provide suitable descriptions of the adsorption edge data. The common logarithms of the intrinsic surface complexation constants for the beaker system are log K^{int} = 10.78 ($\equiv FeOH_2^+–SO_4^{2-}$) and 5.67 ($\equiv FeOSO_3^-$). For the batch system, log K^{int} = 10.99 ($\equiv FeOH_2^+–SO_4^{2-}$) and 6.01 ($\equiv FeOSO_3^-$).

Phosphate displays strong adsorption by goethite (Figs. 61b and 63c). Phosphate adsorption is independent of ionic strength and shifts the goethite IEP from 9.8 to the 3 to 4 range (relative to the KNO_3 systems) (Fig. 73). These experimental results indicate that phosphate is retained primarily by inner-sphere surface complexation mechanisms. Spectroscopic evidence indicates that the bidentate adsorbed phosphate species [$(\equiv FeO)_2PO_2^-$ and $(\equiv FeO)_2PO(OH)^0$] predominate on hydrous ferric hydroxides (Tededor-Tejedor and Johnson, 1990; Arai and Sparks, 2001; Luengo et al., 2006; Khare et al., 2007). Successful surface complexation model descriptions of phosphate adsorption by hydrous ferric hydroxides also involves bidentate species (Tadanier and Eick, 2002; Antelo et al., 2010). The adsorption of phosphate by goethite is successfully described by considering a combination of mono- and bidentate species [$\equiv FeOPO_2OH^-$ and $(\equiv FeO)_2PO_2^-$) (Figs. 79 and 80; Table 13). The model provides a reasonable fit to the experimental beaker adsorption edge data (V_Y = 41.627), with optimized log K^{int} values of 23.90 and 28.74 for the $\equiv FeOPO_2OH^-$ and $(\equiv FeO)_2PO_2^-$ species. For the batch systems, predicted log K^{int} values of 25.62 and 27.61 were determined for $\equiv FeOPO_2OH^-$ formation in 0.01 and 0.1 *M* KNO_3 solutions, and log K^{int} values of 31.18 and 32.99 were obtained for $(\equiv FeO)_2PO_2^-$ formation. The goodness-of-fit parameters for the 0.01 and 0.1 *M* KNO_3 batch systems (V_Y = 35.455 and 8.191) indicated a relatively good fit of the model to the experimental adsorption edge data.

The predicted direct competitive adsorption of antimonate and sulfate by goethite indicates that antimonate adsorption in both the 0.01 and 0.1 *M* KNO_3 systems is well-described (Fig. 81). However, the adsorption of sulfate was overestimated, particularly in the pH < 5 solutions where the inner-sphere $\equiv FeOSO_3^-$ species is the predominant adsorbed sulfate complex (Figs. 77 and 78). The poor prediction of sulfate adsorption results in large goodness-of-fit parameters for competitive adsorption, V_Y = 554.51 and 579.58 for the 0.01 and 0.1 *M* KNO_3 systems. Although the application of chemical models developed for single-adsorbate systems to binary-adsorbate systems has been met with limited success (Essington and Anderson, 2008; Goldberg, 2010), the reoptimization of the intrinsic constants is generally necessary to provide an adequate

fit to the experimental data. For the reoptimized binary antimonate-sulfate systems, the adsorption of sulfate is successfully predicted by assuming only the formation of the outer-sphere $\equiv FeOH_2^+–SO_4^{2-}$ species (Fig. 82). Although only the log K^{int} for $\equiv FeOH_2^+–SO_4^{2-}$ formation was optimized, the predicted adsorption of antimonate is also improved, particularly in 0.1 *M* KNO_3. The reoptimized log K^{int} for $\equiv FeOH_2^+–SO_4^{2-}$ formation is 12.33 (V_Y = 25.533) in the 0.01 *M* KNO_3 system, and in the 0.1 *M* KNO_3 system was 12.88 (V_Y = 10.701).

Both antimonite and phosphate adsorption are poorly predicted in the binary antimonate-phosphate systems (Fig. 83), yielding large goodness-of-fit parameters (V_Y = 3725 and 6737 for 0.01 and 0.1 *M* KNO_3). The retention of both antomonate and phosphate are overpredicted, indicating that the chemical models used to describe ligand adsorption are inadequate. Attempts to reoptimize the adsorption constants were unsuccessful, as FITEQL would not converge, or overflow errors would occur.

Table 13. Surface complexation models used to describe the adsorption of antimonate, sulfate, and phosphate by goethite as a function of pH and ionic strength using the triple-layer formulation.

		log K^{int}†	
Reaction		Beaker‡	Batch
Antimonate Model			
$\equiv FeOH + H^+ + Sb(OH)_6^- = \equiv FeOH_2^+–Sb(OH)_6^-$		13.35 ± 0.02	13.35 ± 0.02
$\equiv FeOH + Sb(OH)_6^- = \equiv FeOSb(OH)_5^- + H_2O$		3.26 ± 0.04	3.26 ± 0.04
	V_Y§	9.634	29.67
Sulfate Model			
$\equiv FeOH + H^+ + SO_4^{2-} = \equiv FeOH_2^+–SO_4^{2-}$		10.78 ± 0.01	10.99 ± 0.01
$\equiv FeOH + H^+ + SO_4^{2-} = \equiv FeOSO_3^- + H_2O$		5.67 ± 0.01	6.01 ± 0.01
	V_Y	119.91	119.88
Phosphate Model			
0.01 *M* KNO_3			
$\equiv FeOH + 2H^+ + PO_4^{3-} = \equiv FeOPO_2OH^- + H_2O$		23.90 ± 0.02	25.62 ± 0.02
$2\equiv FeOH + 2H^+ + PO_4^{3-} = (\equiv FeO)_2PO_2^- + 2H_2O$		28.74 ± 0.02	31.18 ± 0.02
	V_Y	41.627	35.455
0.1 *M* KNO_3			
$\equiv FeOH + 2H^+ + PO_4^{3-} = \equiv FeOPO_2OH^- + H_2O$			27.62 ± 0.02
$2\equiv FeOH + 2H^+ + PO_4^{3-} = (\equiv FeO)_2PO_2^- + 2H_2O$			32.99 ± 0.03
	V_Y		8.191

†Common logarithms of the intrinsic surface complexation constants (± standard deviation) optimized using FITEQL, the antimonate adsorption edge data (Figs. 61 and 63), and the goethite and suspension parameters described in Tables 1 and 2.
‡Adsorption edge data were obtained from the continuous titration ‘Beaker’ studies, or the competitive ‘Batch’ studies.
§Weighted sum of squares of residuals divided by the degrees of freedom.

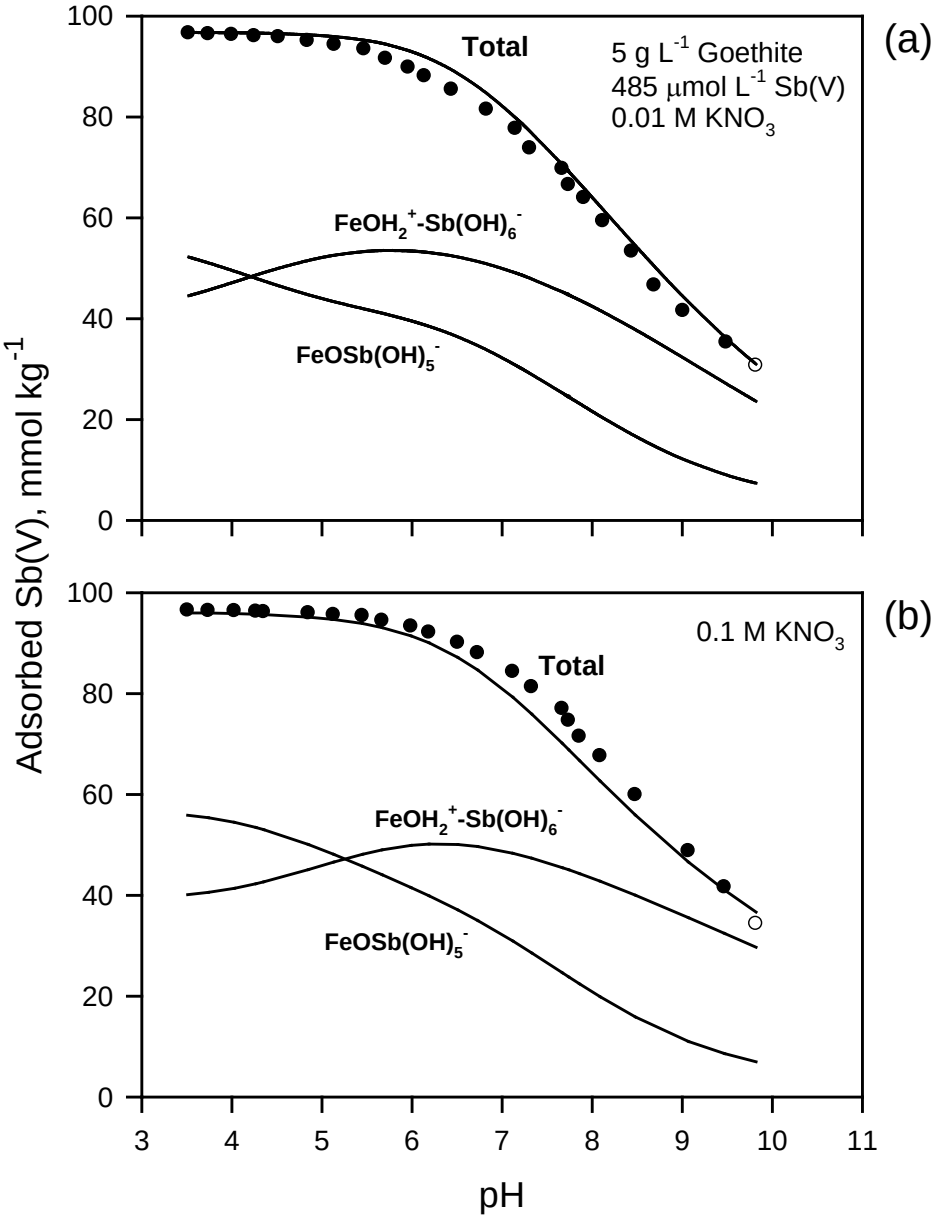

Figure 75. The adsorption of antimonate by goethite as a function of pH in the beaker systems in (a) 0.01 *M* KNO_3 and (b) 0.1 *M* KNO_3. The lines represent the triple-layer surface complexation model fit to the experimental data using FITEQL and the chemical model described in Tables 1, 2, and 13. The solid lines show the predicted adsorption of the outer-sphere $\equiv FeOH_2^+–Sb(OH)_6^-$ and the inner-sphere $\equiv FeOSb(OH)_5^-$ species.

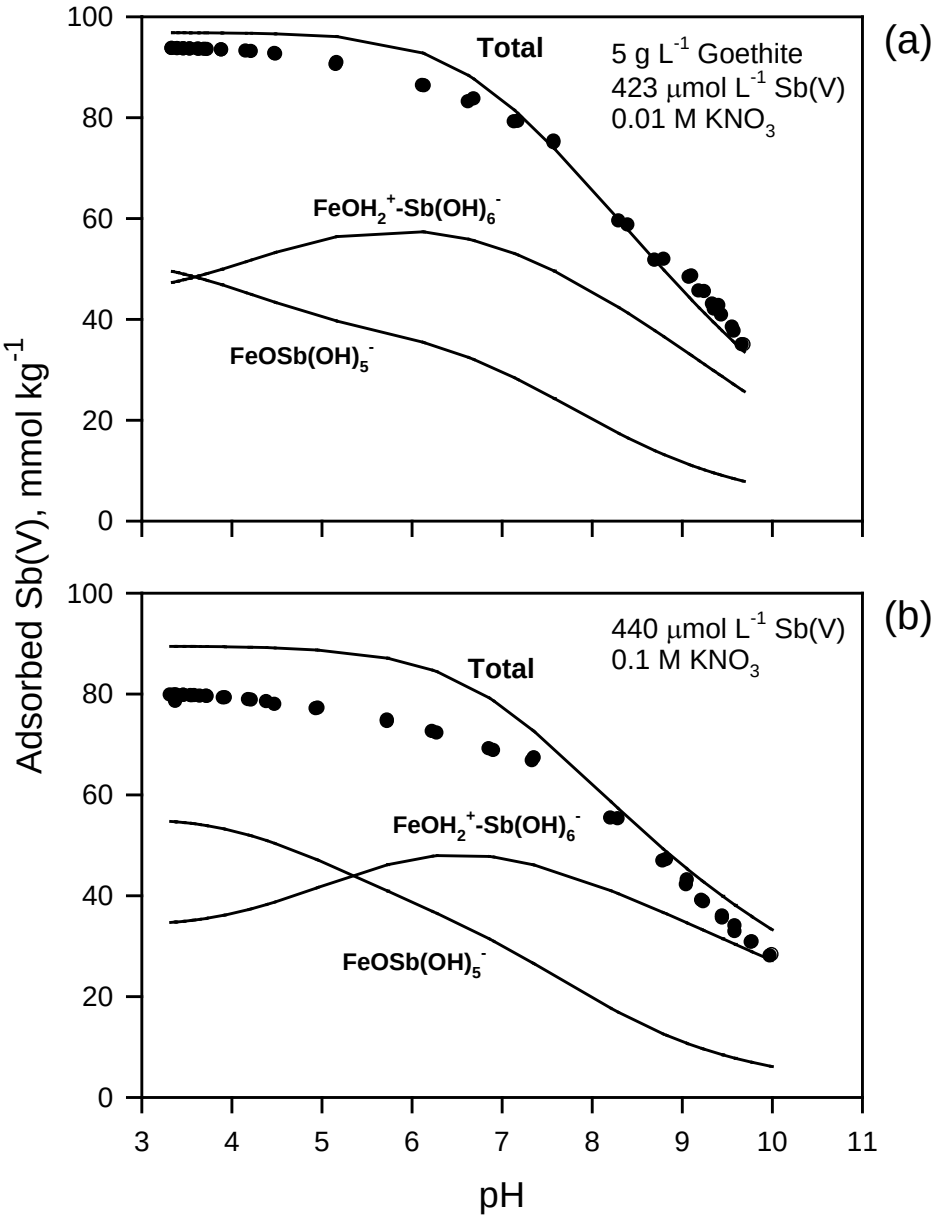

Figure 76. The adsorption of antimonate by goethite as a function of pH in the batch systems in (a) 0.01 *M* KNO_3 and (b) 0.1 *M* KNO_3. The lines represent the triple-layer surface complexation model fit to the experimental data using FITEQL and the chemical model described in Tables 1, 2, and 13. The solid lines show the predicted adsorption of the outer-sphere $\equiv FeOH_2^+–Sb(OH)_6^-$ and the inner-sphere $\equiv FeOSb(OH)_5^-$ species.

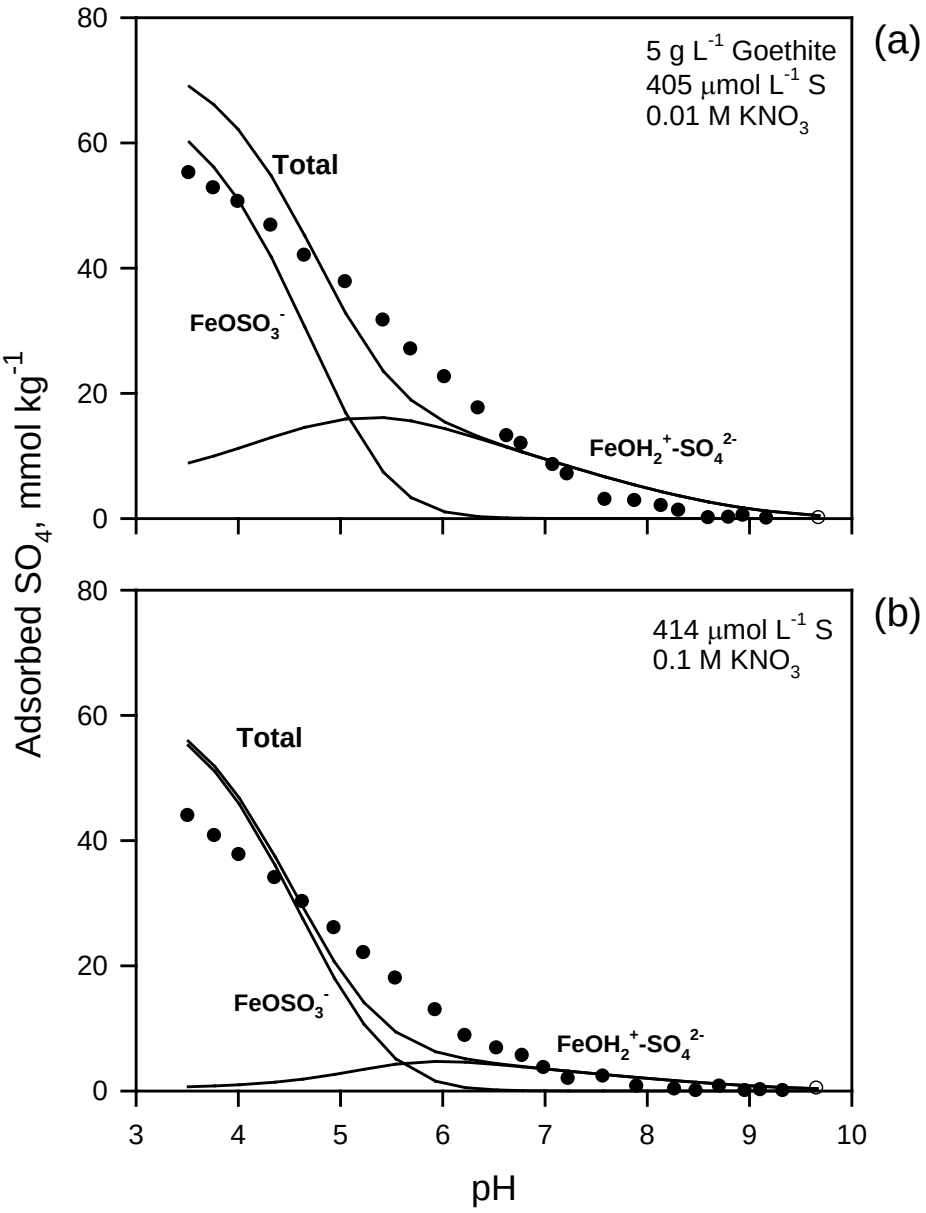

Figure 77. The adsorption of sulfate by goethite as a function of pH in the beaker systems in (a) 0.01 *M* KNO_3 and (b) 0.1 *M* KNO_3. The lines represent the triple-layer surface complexation model fit to the experimental data using FITEQL and the chemical model described in Tables 1, 2, and 13. The solid lines show the predicted adsorption of the outer-sphere $\equiv FeOH_2^+–SO_4^{2-}$ and the inner-sphere $\equiv FeOSO_3^-$ species.

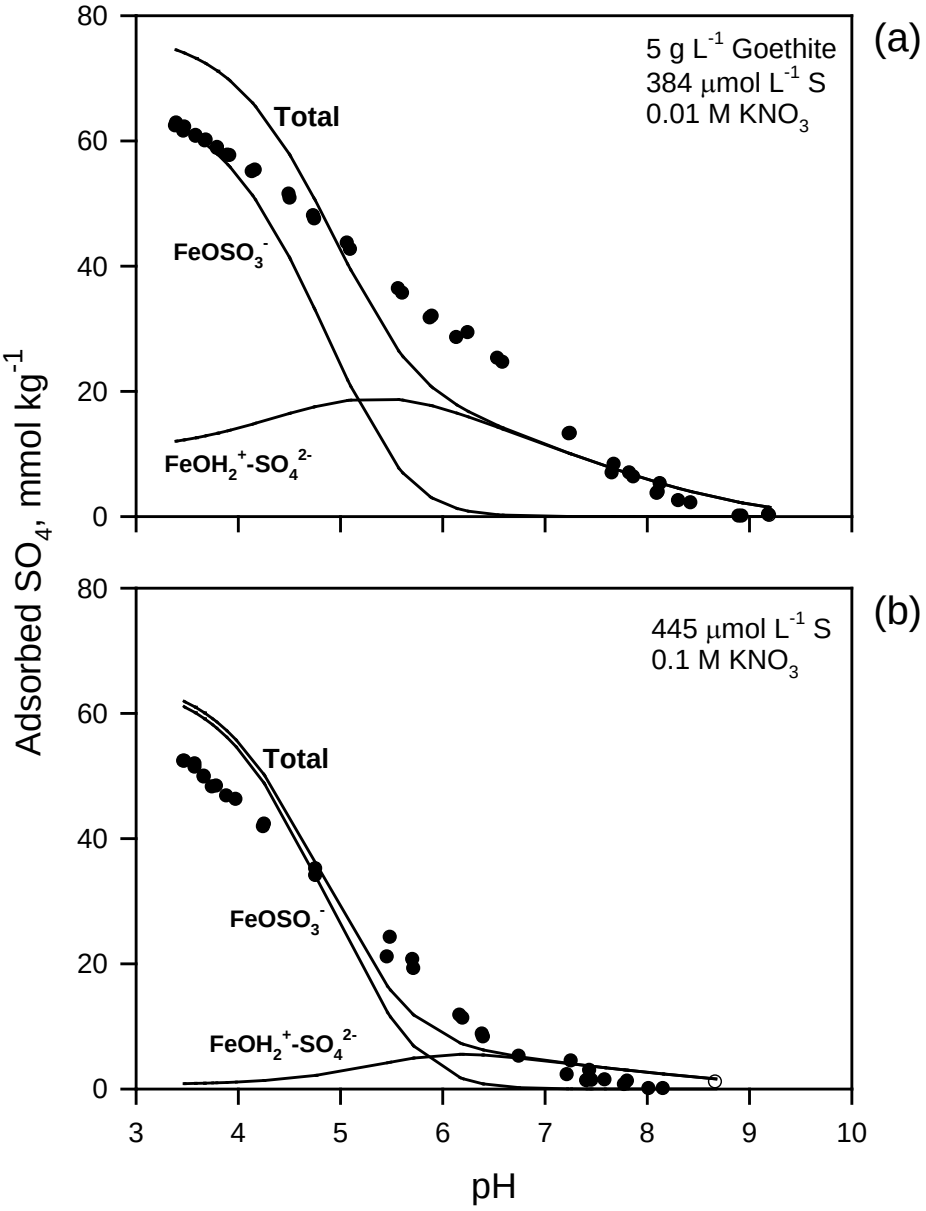

Figure 78. The adsorption of sulfate by goethite as a function of pH in the batch systems in (a) 0.01 *M* KNO_3 and (b) 0.1 *M* KNO_3. The lines represent the triple-layer surface complexation model fit to the experimental data using FITEQL and the chemical model described in Tables 1, 2, and 13. The solid lines show the predicted adsorption of the outer-sphere $\equiv FeOH_2^+–SO_4^{2–}$ and the inner-sphere $\equiv FeOSO_3^-$ species.

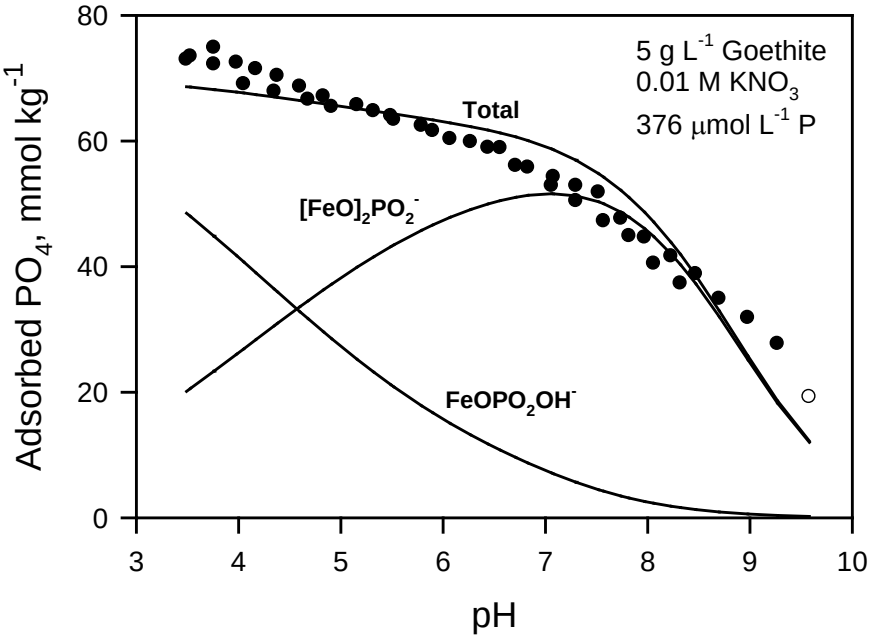

Figure 79. The adsorption of phosphate by goethite as a function of pH in the 0.01 *M* KNO_3 beaker system. The lines represent the triple-layer surface complexation model fit to the experimental data using FITEQL and the chemical model described in Tables 1, 2, and 13. The solid lines show the predicted adsorption of the inner-sphere monodentate $\equiv FeOPO_2OH^-$ and bidentate $(\equiv FeO)_2PO_2^-$ species.

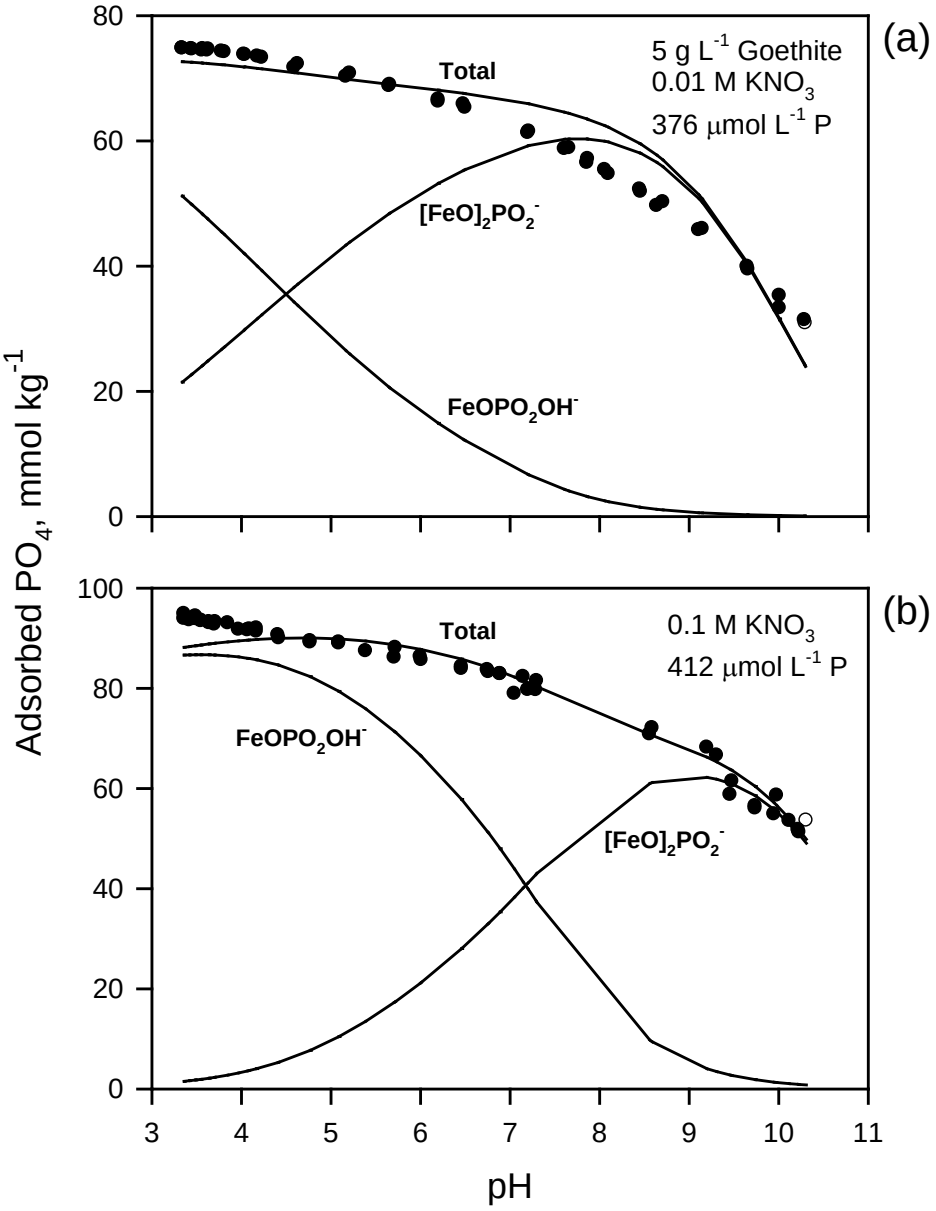

Figure 80. The adsorption of phosphate by goethite as a function of pH in the batch systems in (a) 0.01 *M* KNO_3 and (b) 0.1 *M* KNO_3. The lines represent the triple-layer surface complexation model fit to the experimental data using FITEQL and the chemical model described in Tables 1, 2, and 13. The solid lines show the predicted adsorption of the inner-sphere monodentate $\equiv FeOPO_2OH^-$ and bidentate $(\equiv FeO)_2PO_2^-$ species.

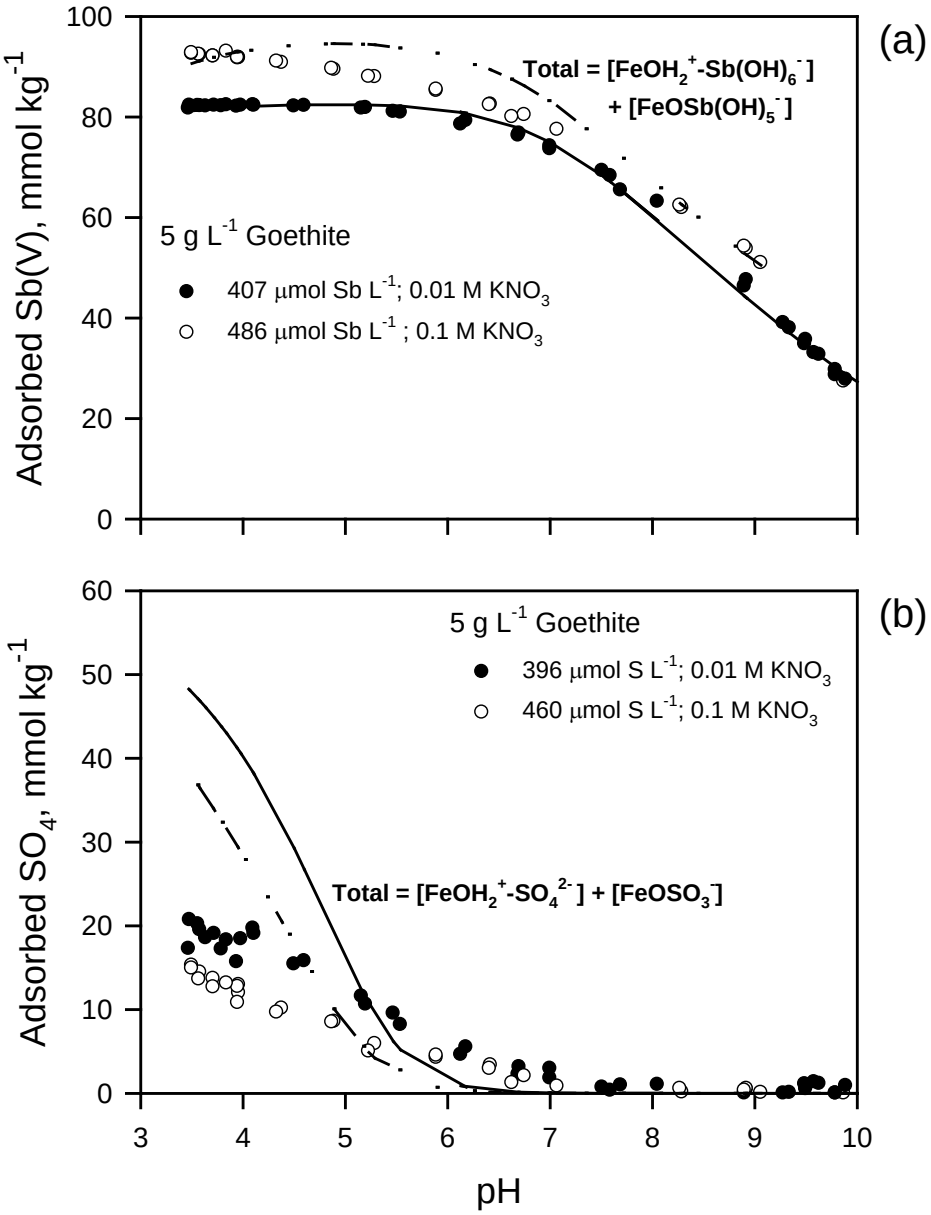

Figure 81. The adsorption of (a) antimonate and (b) sulfate by goethite as a function of pH and ionic strength in antimonate-sulfate direct competition systems. The lines represent the triple-layer surface complexation model predictions using the log K^{int} values optimized for non-competitive adsorption of antimonate [$\equiv FeOH_2^+ – Sb(OH)_6^-$ and $\equiv FeOSb(OH)_5^-$ species] and sulfate ($\equiv FeOSO_3^-$ and $\equiv FeOH_2^+ – SO_4^{2-}$ species) (Table 13). The solid lines show the predicted adsorption in 0.01 *M* KNO_3, the dashed lines in 0.1 *M* KNO_3.

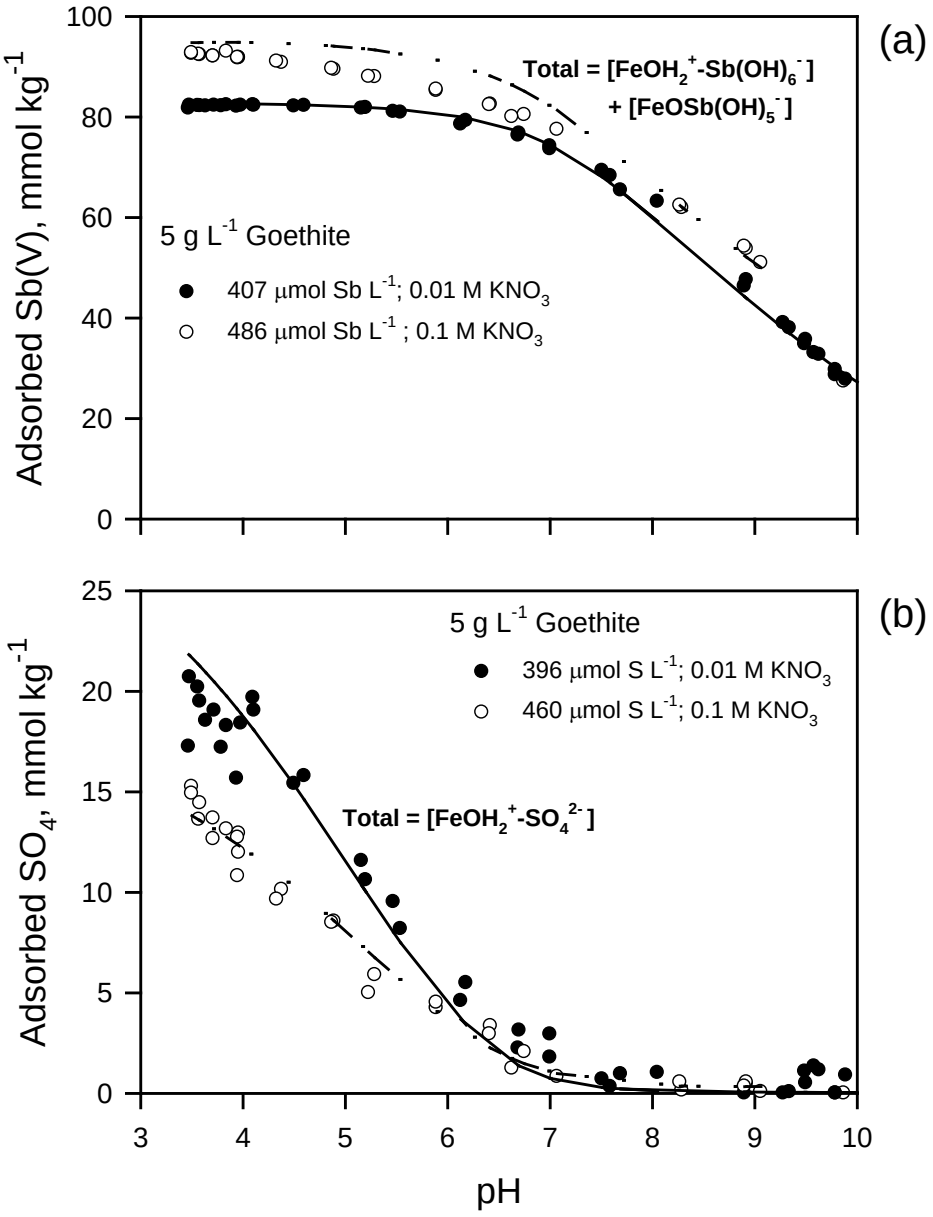

Figure 82. The adsorption of (a) antimonate and (b) sulfate by goethite as a function of pH and ionic strength in antimonate-sulfate direct competition systems. The lines represent the triple-layer surface complexation model predictions using the log K^{int} values optimized for non-competitive adsorption of antimonate [$\equiv FeOH_2^+ – Sb(OH)_6^-$ and $\equiv FeOSb(OH)_5^-$ species] and reoptimized for sulfate ($\equiv FeOH_2^+ – SO_4^{2-}$ species) for competitive adsorption. The solid lines show the predicted adsorption in 0.01 *M* KNO_3, the dashed lines in 0.1 *M* KNO_3.

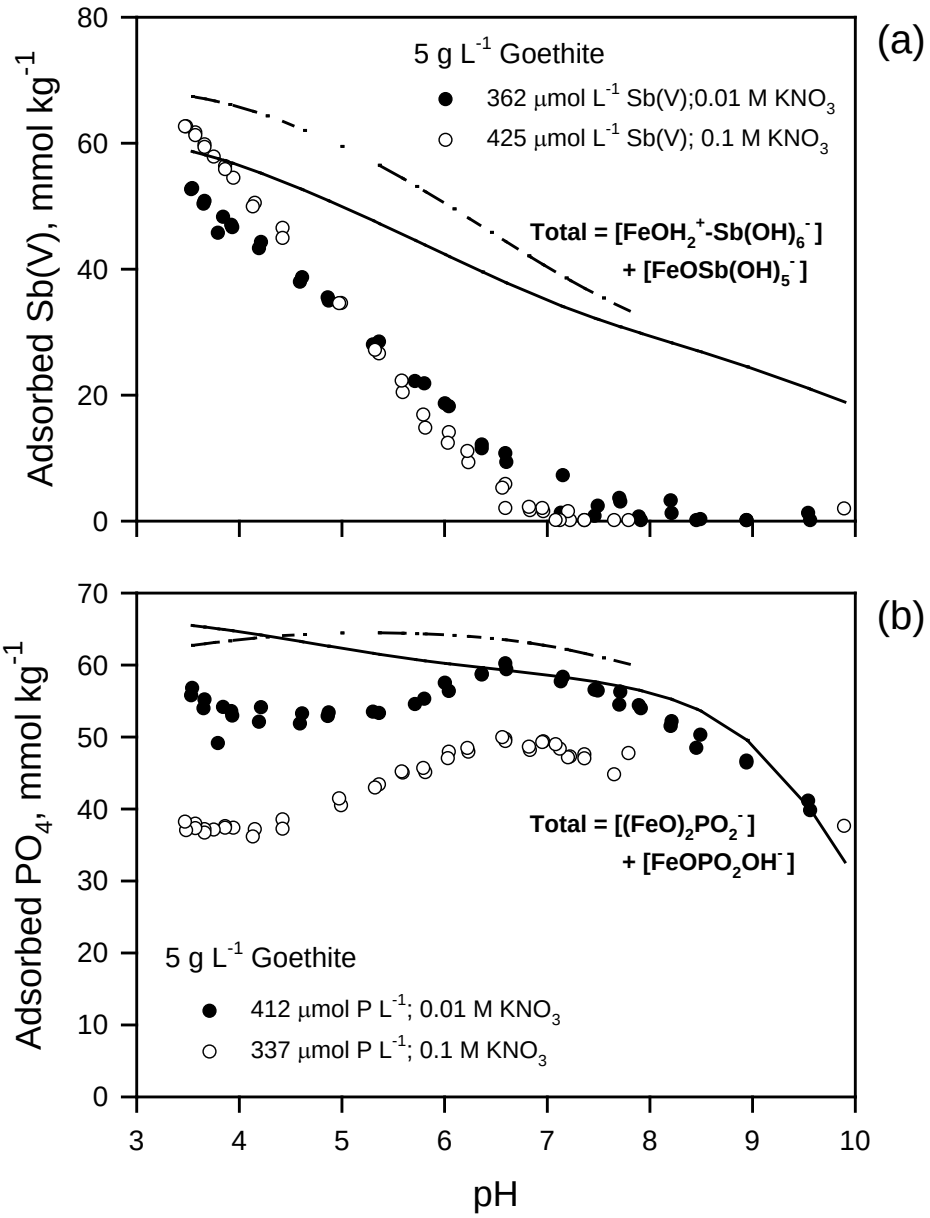

Figure 83. The adsorption of (a) antimonate and (b) phosphate by goethite as a function of pH and ionic strength in antimonate-phosphate direct competition systems. The lines represent the triple-layer surface complexation model predictions using the log K^{int} values optimized for non-competitive adsorption of antimonate [$\equiv FeOH_2^+ – Sb(OH)_6^-$ and $\equiv FeOSb(OH)_5^-$ species] and phosphate [$(\equiv FeO)_2PO_2^-$ and $\equiv FeOPO_2OH^-$ species) (Table 13). The solid lines show the predicted adsorption in 0.01 *M* KNO_3, the dashed lines in 0.1 *M* KNO_3.

Summary: Antimonate Adsorption by Goethite

Goethite is a ubiquitous and important mineral in soil. Throughout a broad pH range, the goethite surface bears a net positive change (point of zero charge is approximately 9.8), allowing for both anion and ligand retention. For this reason, goethite, like many other hydrous metal oxides, is considered a natural scavenger for toxins. Goethite displays a high capacity for antimonate adsorption. Antimonate adsorption by goethite is dependent on pH and independent of ionic strength. The complete removal of antimonate by goethite occurs in acidic to neutral solutions, and adsorption decreases with increasing pH. Antimonate adsorption is not affected by ionic strength, suggesting that ligand exchange (inner-sphere surface complexation) is an important retention mechanism. The adsorption of antimonate is not reversible; further supporting the conclusion that antimonate is a specifically-adsorbed ligand.

Sulfate and phosphate are common anions in the environments, but only phosphate competes with antimonate for adsorption sites at the goethite surface. Sulfate adsorption increases with increasing ionic strength and with decreasing pH. Sulfate adsorption is negligible when pH > 7 and reversible, indicating that it is primarily an exchangeable anion. When sulfate and antimonate are present in equal concentrations, sulfate does not influence antimonate retention. However, sulfate retention is substantially decreased in the presence of antimonate. Phosphate is strongly retained by goethite with an adsorption edge that is similar to that of antimonate. Phosphate is also considered to be a non-exchangeable, specifically adsorbed ligand. When phosphate and antimonate are present in equal concentrations, the antimonate adsorption edge is shifted to lower pH values (decreasing adsorption throughout a broad pH range), and adsorption is negligible above pH 7. The adsorption of phosphate is reduced concomitantly with the increasing retention of antimonate below pH 7. Greater concentrations of phosphate, as might be expected in firing range soils treated with phosphate to stabilize lead, would be expected to have a more pronounced impact on reducing antimonate retention.

The strong, inner-sphere retention of antimonate throughout a broad pH range was also supported by the adsorption isotherm results. The one-site Langmuir adsorption isotherm model was employed to characterize antimonate retention by goethite. The model allowed for the thermodynamic assessment of antimonate adsorption. In both acidic and alkaline systems, antimonate adsorption increases with increasing temperature, and is endothermic (positive ΔH_{ad}) and entropically-driven (heat is absorbed), indicating an inner-sphere (ligand exchange) retention mechanism.

The zeta potential characteristics of goethite indicated that adsorbed antimonate generated negative surface charge. This response to antimonate adsorption is consistent with the formation of inner-sphere surface complexes. Based on the experimental evidence, surface complexation models were developed to predict antimonate adsorption using the triple layer model formulation. The antimonate adsorption edge as a function of ionic strength was successfully modeled by using a combination of inner- and outer-sphere mechanisms. The outer-sphere mechanism predominated under neutral and alkaline pH conditions, with the inner-sphere mechanism becoming increasingly important as solution pH decreased into the strongly acidic range. However, the surface complexation model, when applied to competitive antimonate-sulfate and antimonate-phosphate adsorption systems, did not satisfactorily predicted the antimonate adsorption edge without further optimization.

Birnessite

Adsorption Edge and Competitive Adsorption

Hydrous manganese (Mn) oxides are surface-reactive and important sinks for metals and ligands in soils and sediment. Birnessite (MnO_2) is a common Mn oxide, consisting of layered sheets of edge-linked $Mn^{IV}O_6$ octahedra. Naturally-occurring manganese oxide solids are generally microcrystalline, poorly ordered, and impure, leading to an abundance of reactive surface functional groups. The surface reactivity of birnessite arises from cation vacancies in the Mn octahedral layer and from the substitution of Mn^{III} for Mn^{IV} (resulting in negative structural charge), and from the protonation and deprotonation of singly- and doubly-coordinated surface hydroxyl groups. Commonly, the negative structural charge is satisfied by exchangeable cations that reside between the Mn octahedral layers. The surface hydroxyl groups are scavengers for metal ions, primarily through proton exchange processes. Due to the large amount of negative structural charge, and the presence of undercoordinated surface hydroxyls ($\equiv MnOH^{-0.33}$ and $\equiv Mn_2O^{-0.67}$), birnessite has negative surface charge throughout a broad pH range (point of zero charge < 3), and is generally considered to have a low capacity to adsorb anions.

The adsorption of both antimonate and phosphate occurs at pH values above the point of zero charge of birnessite (surface charge is negative), indicating that they form inner-sphere surface complexes. However, sulfate was not adsorbed in the pH range studied, and is essentially repelled by the birnessite surface (data not shown). The adsorption of antimonate by birnessite is both pH and ionic strength dependent (Fig. 84a). Adsorption increases from a minimum at pH 10 to near complete removal of antimonate at pH values below approximately 6. Antimonate adsorption also increases with increasing ionic strength, as the adsorption edge shifts from approximately pH 6.9 to 7.4. Similar adsorption behavior is observed for phosphate (Fig. 84b). Adsorption increases from a minimum in the pH 9 to 10 range, to a maximum in the pH 3 to 4 range. Further, phosphate adsorption also increases with increasing ionic strength (the adsorption edge shifts from pH 6.9 to 7.6). This ionic strength effect for ligands, such as phosphate, is observed for adsorption at pH values above the point of zero charge (Yao and Millero, 1996; Arai and Sparks, 2001; Mustafa et al., 2006; Rahnemaie et al., 2007; Antelo et al., 2010). Hiemstra and Van Riemsdijk (1999) attribute the effect to a smaller repulsive interaction between the negatively charged surface and the anion caused by enhanced electrolyte screening of the particle surface charge. The ionic strength effect has been interpreted to indicate the inner-sphere (Hiemstra and Van Riemsdijk, 1999; Antelo et al., 2010) or the outer-sphere (Yao and Millero, 1996) ligand adsorption of phosphate. However, Aria and Sparks (2001) argued that the adsorption mechanism (inner- vs. outer-sphere) could not be ascertained from this type of macroscopic data.

The electrolyte screening effect is evidenced by the zeta potential of birnessite as a function of pH and ionic strength (Fig. 85). The zeta potential of birnessite in indifferent electrolyte (KNO_3 or K_2SO_4) is negative throughout the pH 3 to 11 range (IEP < 3), and is generally invariant with changing pH. Further, the zeta potential becomes more positive with increasing ionic strength, averaging –28.18 mV in the 10 m*M* KNO_3 (or K_2SO_4) systems and –20.41 mV in the 100 m*M* KNO_3 systems (illustrating the screening effect). The presence of antimonate or phosphate does not influence the zeta potential of birnessite in the pH range studied (Figs. 86 and 87). The average zeta potential is –29.43 mV for 10 m*M* KH_2PO_4 and –29.52 mV for 10 m*M* KNO_3 + 10 m*M* KH_2PO_4 suspensions, compared to –28.14 mV for 10 m*M* KNO_3. The average zeta potential is –20.52 mV for 100 m*M* KNO_3 + 10 m*M* KH_2PO_4 suspensions, compared to –

21.33 mV for 100 m*M* KNO_3. For the antimonate suspensions, the average zeta potential is –34.26 mV for 10 m*M* $KSb(OH)_6$ and –29.60 mV for 10 m*M* KNO_3 + 10 m*M* $KSb(OH)_6$, compared to –28.14 mV for 10 m*M* KNO_3. The average zeta potential is –20.57 mV for 100 m*M* KNO_3 + 10 m*M* $KSb(OH)_6$ suspensions, compared to –21.33 mV for 100 m*M* KNO_3. The impact of specifically adsorbed antimonate or phosphate on the IEP of birnessite could not be evaluated, as the IEP is outside the range of the adsorption experiments (IEP < 3).

Both antimonate and phosphate have similar affinities for the birnessite surface, although antimonate appears to adsorb more strongly than phosphate (Fig. 84). This is supported by the competitive adsorption findings. The influence of phosphate on antimonate adsorption is negligible, irrespective of the initial state of the suspensions (Fig. 88). However, the inclusion of antimonate as a competing ligand decreases the retention of phosphate. The effect is more pronounced in the lower ionic strength systems, and in the preadsorbed antimonate and direct competition systems (Fig. 89). Phosphate is more competitive with antimonate in the preadsorbed phosphate suspensions. The reduction in phosphate retention that occurs when in competition with antimonate may result from the direct competition for adsorption sites, or from electrostatic effects resulting from the change in surface charge that arises from the adsorption of antimonate. The total concentration of available ≡MnOH surface functional groups (4.805 mmol L^{-1} in the birnessite suspensions, Table 1) far exceeds the initial concentration of added ligand (~ 0.08 mmol L^{-1}). However, because the suspension pH is greater than the IEP of birnessite, the concentration of positively-charged $\equiv MnOH_2^+$ sites (required for both anion and ligand exchange) may only be a minor fraction of the total sites. The concentration of these sites is dependent on both pH and ionic strength. Site concentration decreases with decreasing ionic strength and with increasing pH. The greater impact of antimonate on phosphate retention in the 0.01 *M* KNO_3 suspensions, in comparison to that in 0.1 *M* KNO_3, illustrates the ionic strength effect on $\equiv MnOH_2^+$ concentration. However, the cause of the competition remains unknown.

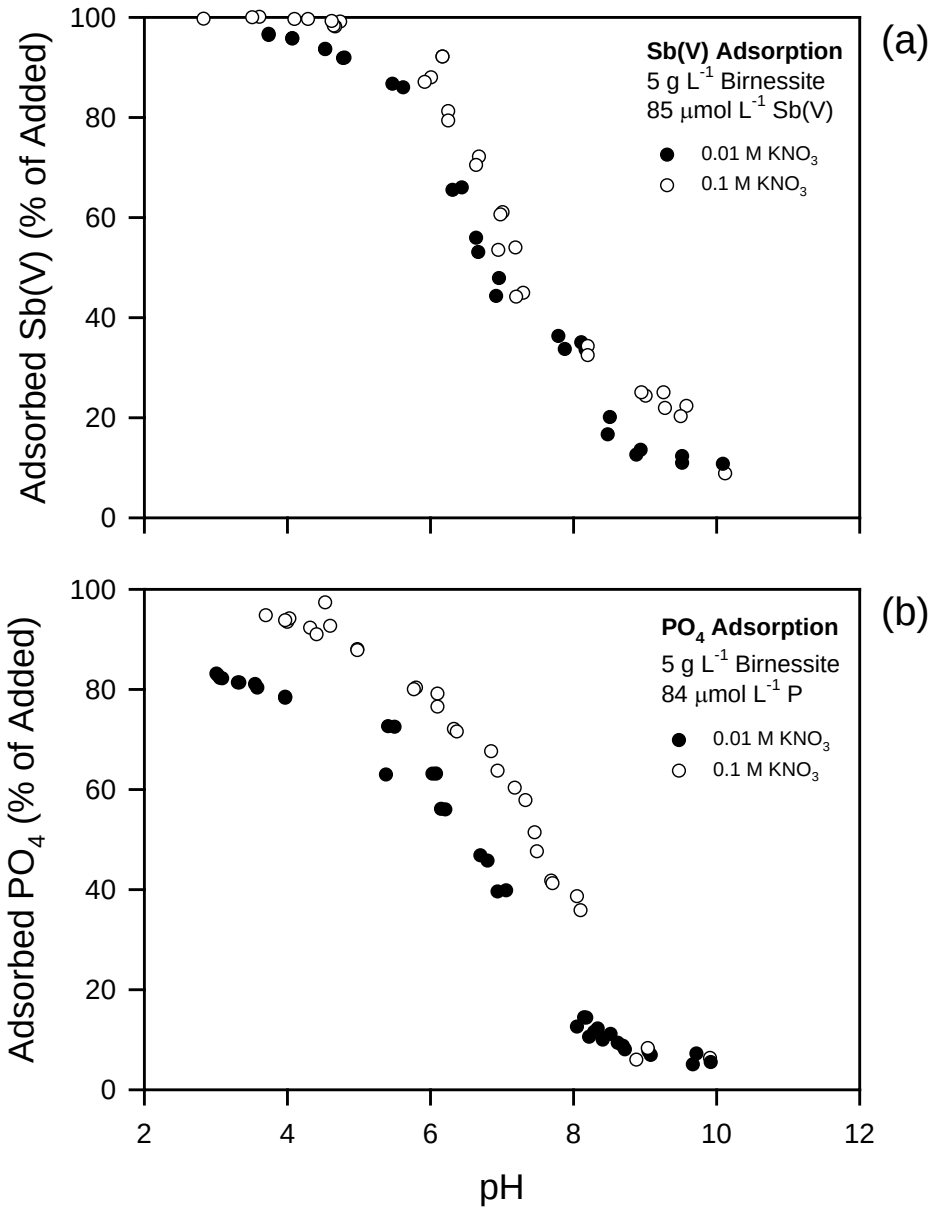

Figure 84. The adsorption of (a) antimonate and (b) phosphate by birnessite as a function of pH and ionic strength.

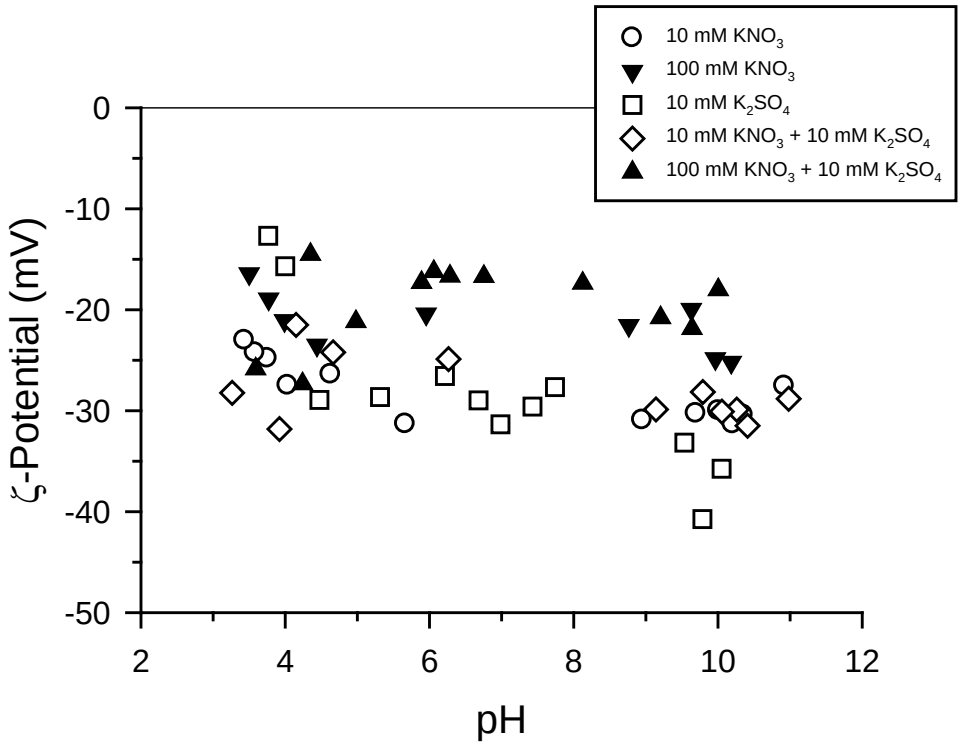

Figure 85. The influence of nitrate and sulfate on the zeta potential of birnessite as a function of pH, ionic strength, and electrolyte composition.

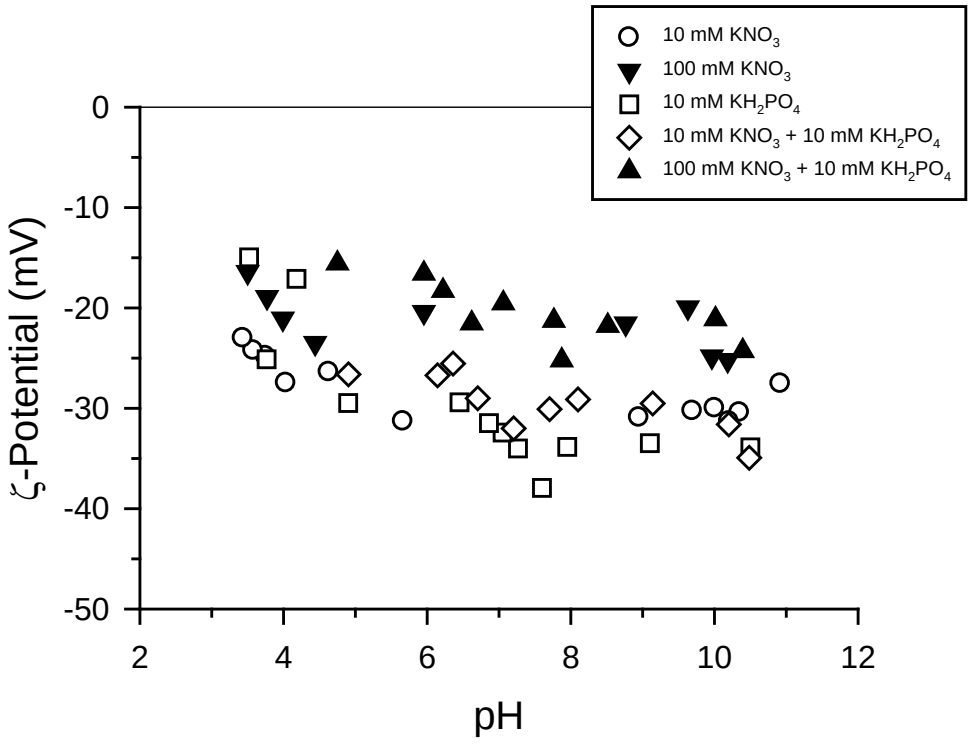

Figure 86. The influence of nitrate and phosphate on the zeta potential of birnessite as a function of pH, ionic strength, and electrolyte composition.

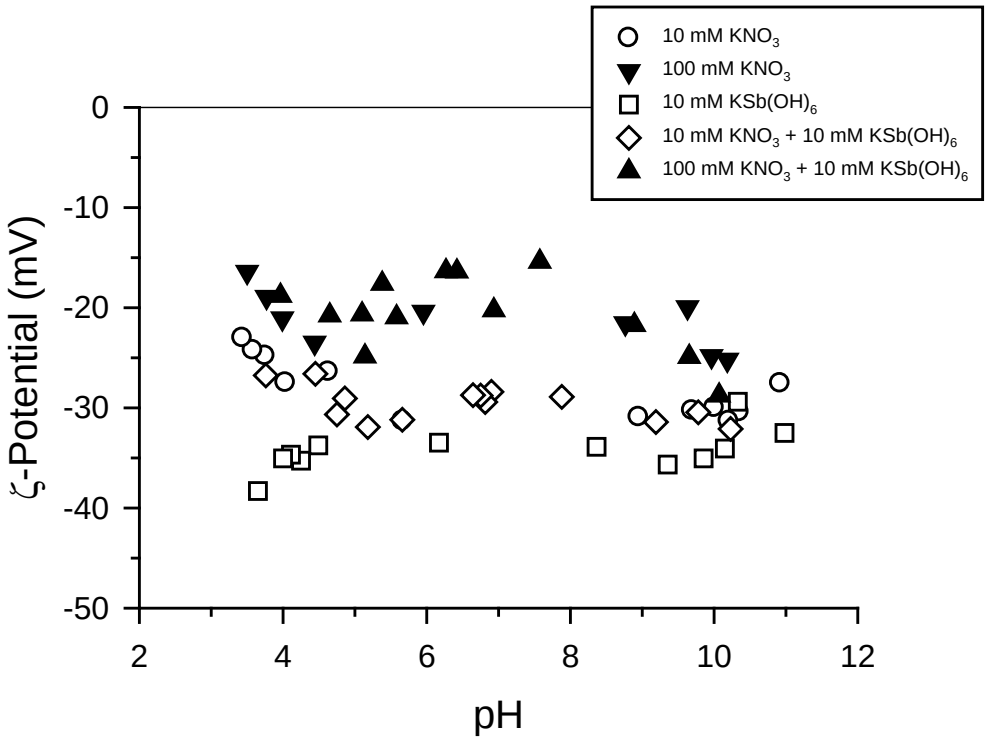

Figure 87. The influence of nitrate and antimonate on the zeta potential of birnessite as a function of pH, ionic strength, and electrolyte composition.

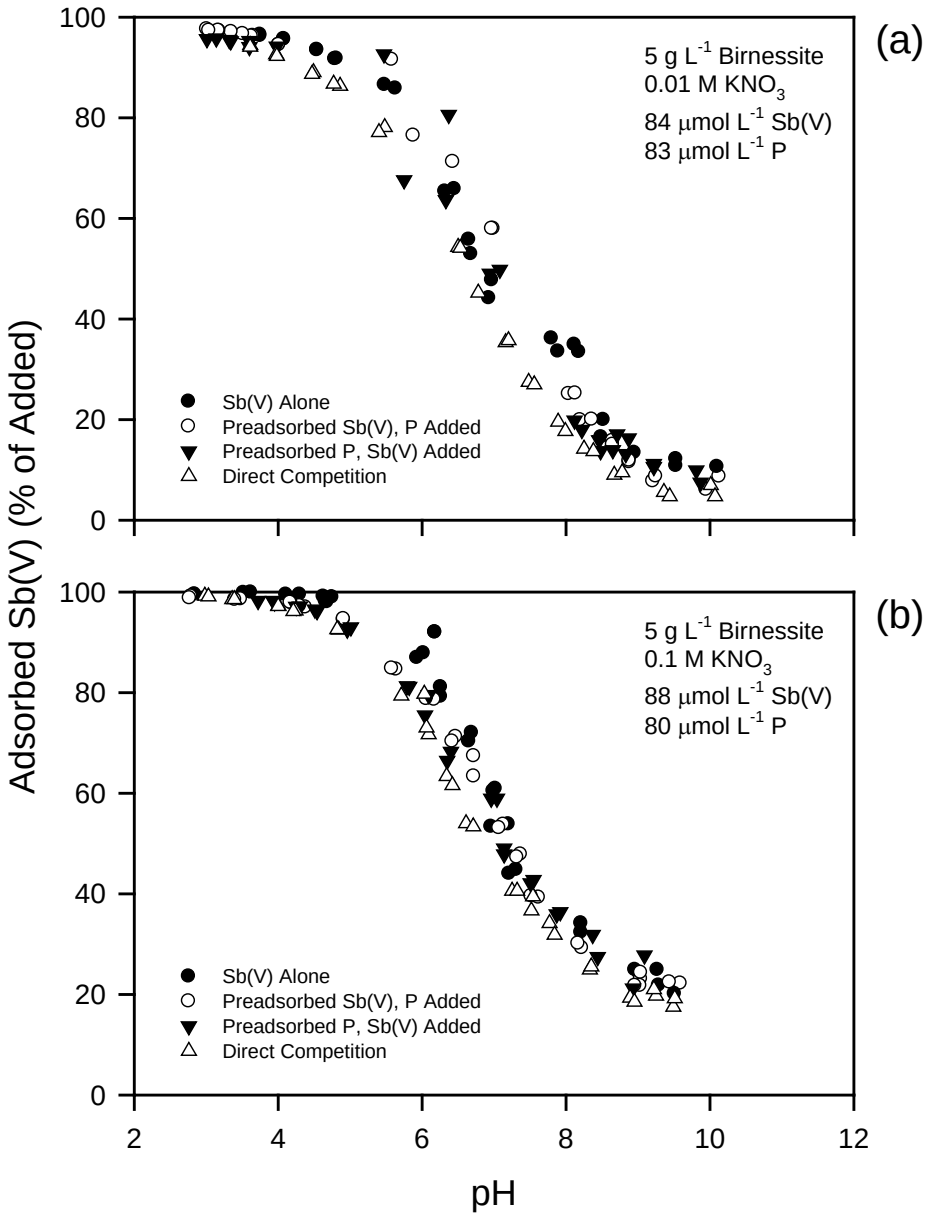

Figure 88. The competitive adsorption of antimonate by birnessite in the presence of phosphate in (a) 0.01 *M* KNO_3 and (b) 0.1 *M* KNO_3 electrolyte media as a function of pH and method of antimonate or phosphate addition.

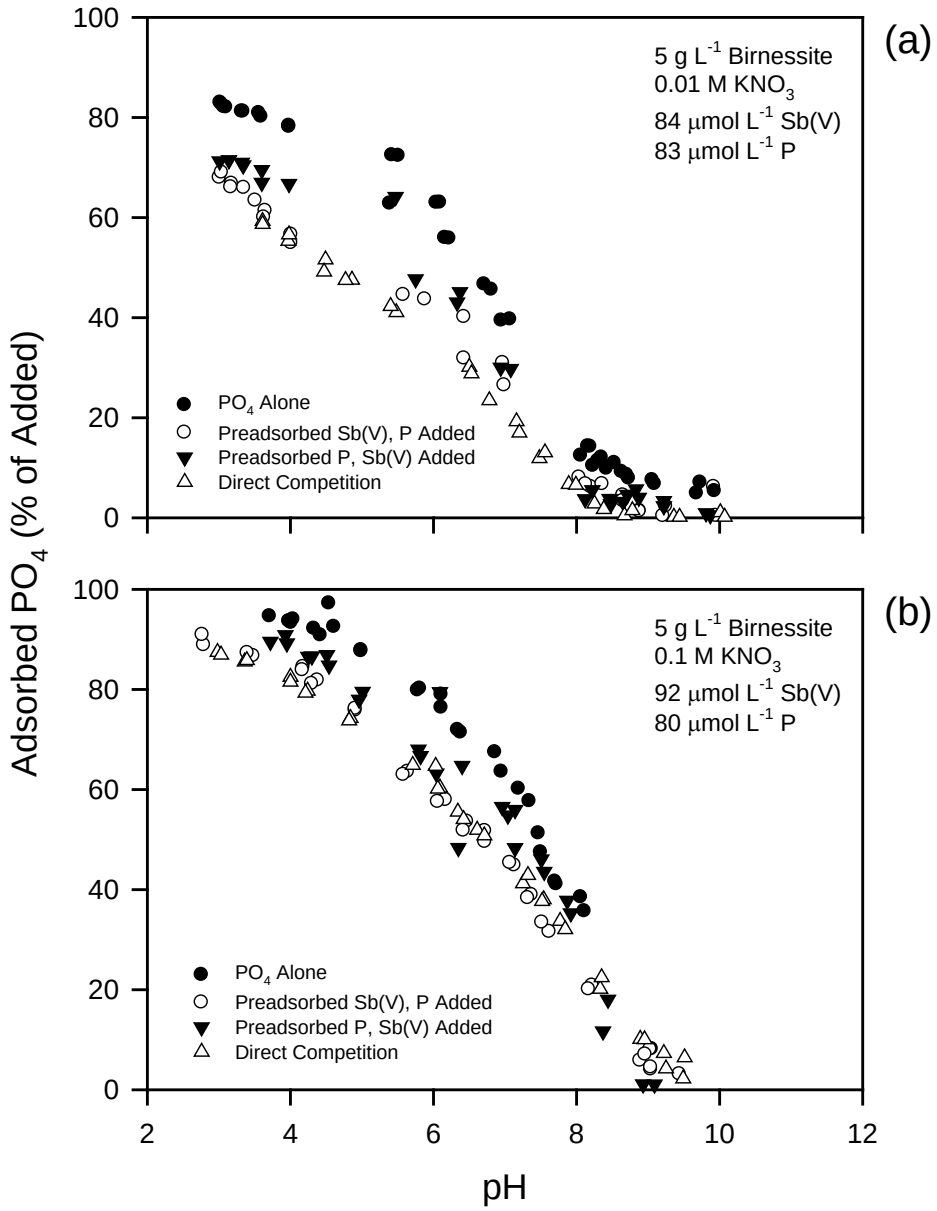

Figure 89. The competitive adsorption of phosphate by birnessite in the presence of antimonate in (a) 0.01 *M* KNO_3 and (b) 0.1 *M* KNO_3 electrolyte media as a function of pH and method of antimonate or phosphate addition.

Surface Complexation Modeling

The macroscopic adsorption edge studies do not provide sufficient evidence to indicate an adsorption mechanism for antimonate on birnessite. Outer-sphere complexation via an electrostatic interaction is sensitive to changes in ionic strength. This is due to competition with counter anions. Inner-sphere complexation is generally insensitive to changes in ionic strength, as the ligand bonds directly to surface functional groups. There is a minor impact of ionic strength on the adsorption of antimonate by birnessite (Fig. 84), as the adsorption edge shifts to a high pH value and adsorption increases with increasing ionic strength. This type of ligand adsorption behavior has been associated with both inner- and outer-sphere surface complexation. Further, surface complexation models that invoke either inner-sphere or outer-sphere adsorption reactions have been used to successfully describe adsorption at pH values above the IEP of the solid. This is particularly the case for phosphate (Antelo et al., 2010; Yao and Millero, 1996).

Several surface complexation models were evaluated for their ability to describe the antimonate adsorption edge (Table 14). The chemical model that considers only the outer-sphere $\equiv MnOH_2^+–Sb(OH)_6^-$ surface species (Model A) does not provide a satisfactory description of the adsorption edge (Fig. 90). The model predicted increased adsorption with increasing ionic strength; however, the adsorption edge was too shallow compared to the experimental data. The chemical models that considered only an inner-sphere surface complex [either the monodentate $\equiv MnOSb(OH)_5^-$ or the bidentate $(\equiv MnO)_2Sb(OH)_4^-$] provide an adequate descrition of the adsorption edge (Fig. 91). The goodness-of-fit parameter for the $\equiv MnOSb(OH)_5^-$ model is V_Y = 27.988, while that for the $(\equiv MnO)_2Sb(OH)_4^-$ model is V_Y = 29.672. Although either model provides a satisfactory fit, neither predicts the observed ionic strength effect. Both inner-sphere models predict increasing retention with decreasing ionic strength. Models that combine inner- and outer-sphere retention of antimonate are successful in describing the experimental adsorption edge and in predicting the ionic strength effect (Fig. 92, Table 14). The application of Model D, which combined the $\equiv MnOH_2^+–Sb(OH)_6^-$ and $\equiv MnOSb(OH)_5^-$ surface species, resulting in a goodness-of-fit parameter of V_Y = 9.057. The goodness-of-fit parameter for the model that combined the outer-sphere and bidentate $(\equiv MnO)_2Sb(OH)_4^-$ species (Model E) is V_Y = 8.754. In both models, the inner-sphere complex is predicted to predominate throughout a broad pH range. Both models are particularly successful in describing the adsorption edge in 0.01 *M* KNO_3. However, the steepness of the edge in 0.1 *M* KNO_3 is not as well-described.

In order to predict competitive adsorption in binary antimonate-phosphate systems, intrinsic constants for the retention of phosphate must be determined. The affinity of phosphate for the birnessite surface is similar to that of antimonate. Phosphate adsorption is dependent on ionic strength. Increasing the ionic strength from 0.01 to 0.1 *M* KNO_3 shifts the adsorption edge to a high pH value (from pH 6.9 to 7.6). Yao and Millero (1996) successfully predicted phosphate adsorption on birnessite by considering the formation of the outer-sphere complexes, $\equiv MnOH_2^+–HPO_4^{2-}$ and $\equiv MnOH_2^+–H_2PO_4^-$. This model is used to successfully described phosphate adsorption (Fig. 93, Table 14), yielding a goodness-of-fit parameter of V_Y = 9.978. The optimized log K^{int} values of 18.91 and 25.91 for $\equiv MnOH_2^+–HPO_4^{2-}$ and $\equiv MnOH_2^+–H_2PO_4^-$ formation are similar to the log K^{int} values of 19.6 and 25.1 obtained by Yao and Millero (1996).

The combined monodentate inner-sphere ($\equiv MnOSb(OH)_5^-$) and outer-sphere ($\equiv MnOH_2^+–Sb(OH)_6^-$) antimonate model (Model D) and the outer-sphere phosphate model are used to predict ligand adsorption in the binary systems. The predicted direct competitive adsorption of

antimonate and phosphate by birnessite indicates that antimonate adsorption in both the 0.01 and 0.1 *M* KNO_3 systems are overestimated (Fig. 94). Similarly, the adsorption of phosphate is overestimated. The poor prediction of both antimonate and phosphate adsorption results in a large goodness-of-fit parameter for competitive adsorption, $V_Y = 51.477$. Although the application of chemical models developed for single-adsorbate systems to binary-adsorbate systems has been met with limited success (Essington and Anderson, 2008), the reoptimization of the intrinsic constants is generally necessary to provide an adequate fit to the experimental data. For the reoptimized binary antimonate-phosphate systems, ligand adsorption is generally well-predicted, with $V_Y = 9.023$ (Fig. 95). The reoptimized log K^{int} values for $\equiv MnOH_2^+$–$Sb(OH)_6^-$, $\equiv MnOSb(OH)_5^-$, $\equiv MnOH_2^+$–HPO_4^{2-}, and $\equiv MnOH_2^+$–$H_2PO_4^-$ formation are 5.19 ± 0.01, 6.90 ± 0.02, 18.52 ± 0.03, and 25.49 ± 0.01.

Table 14. Surface complexation models used to describe the adsorption of antimonate and phosphate by birnessite as a function of pH and ionic strength using the triple-layer formulation.

Reaction		log K^{int}†
Antimonate Model A		
$\equiv MnOH + H^+ + Sb(OH)_6^- = \equiv MnOH_2^+$–$Sb(OH)_6^-$		6.10 ± 0.01
	V_Y‡	86.159
Antimonate Model B		
$\equiv MnOH + Sb(OH)_6^- = \equiv MnOSb(OH)_5^- + H_2O$		8.29 ± 0.01
	V_Y	27.988
Antimonate Model C		
$2\equiv MnOH + Sb(OH)_6^- = (\equiv MnO)_2Sb(OH)_4^- + 2H_2O$		10.76 ± 0.01
	V_Y	29.672
Antimonate Model D		
$\equiv MnOH + H^+ + Sb(OH)_6^- = \equiv MnOH_2^+$–$Sb(OH)_6^-$		5.44 ± 0.02
$\equiv MnOH + Sb(OH)_6^- = \equiv MnOSb(OH)_5^- + H_2O$		7.62 ± 0.03
	V_Y	9.057
Antimonate Model E		
$\equiv MnOH + H^+ + Sb(OH)_6^- = \equiv MnOH_2^+$–$Sb(OH)_6^-$		5.46 ± 0.01
$2\equiv MnOH + Sb(OH)_6^- = (\equiv MnO)_2Sb(OH)_4^- + 2H_2O$		10.07 ± 0.03
	V_Y	8.754
Phosphate		
$\equiv MnOH + 2H^+ + PO_4^{3-} = \equiv MnOH_2^+$–$HPO_4^{2-}$		18.91 ± 0.03
$\equiv MnOH + 3H^+ + PO_4^{3-} = \equiv MnOH_2^+$–$H_2PO_4^-$		25.91 ± 0.01
	V_Y	9.978

†Common logarithms of the intrinsic surface complexation constants (± standard deviation) optimized using FITEQL, the antimonate and phosphate adsorption edge data (Fig. 84), and the birnessite and suspension parameters described in Tables 1 and 2.
‡Weighted sum of squares of residuals divided by the degrees of freedom.

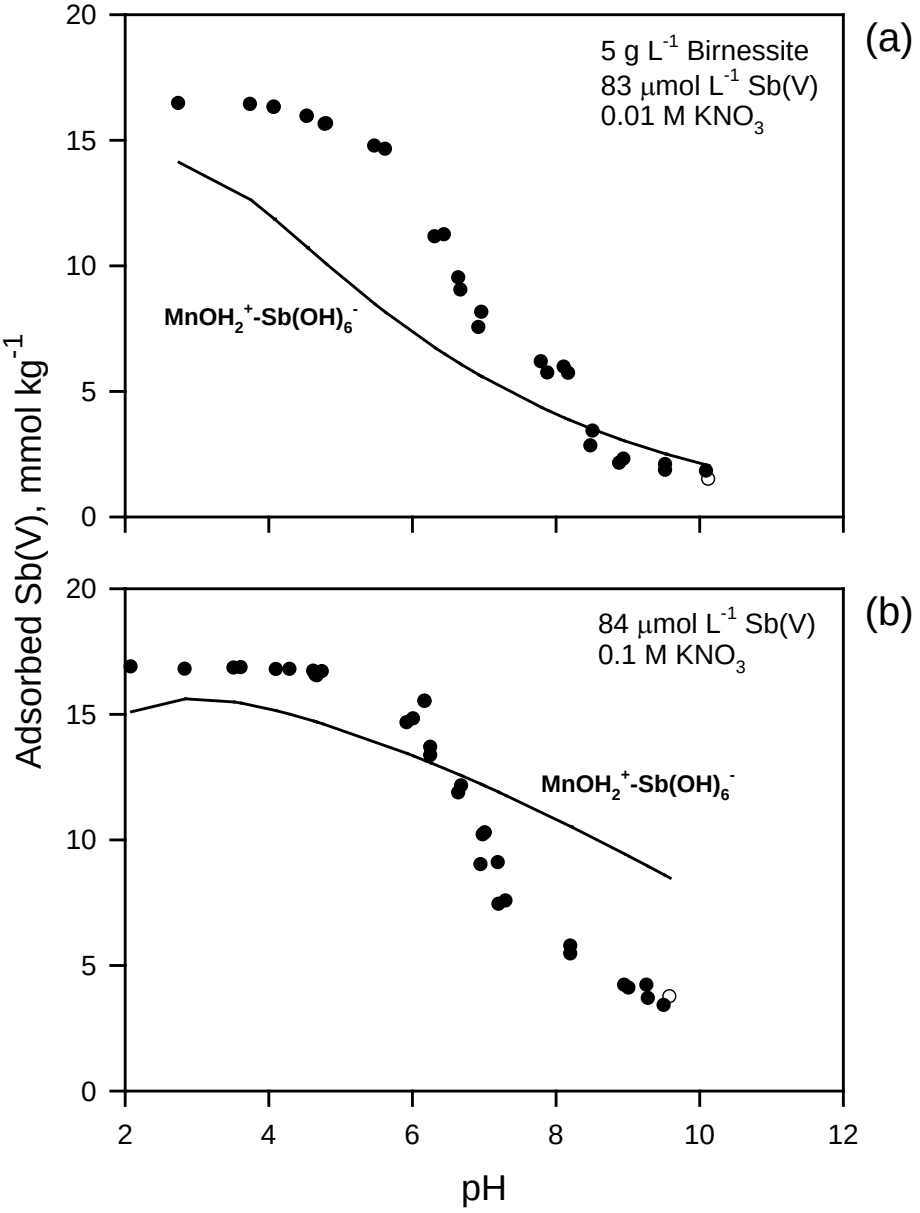

Figure 90. The adsorption of antimonate by birnessite as a function of pH and ionic strength in (a) 0.01 *M* KNO_3 and (b) 0.1 *M* KNO_3. The lines represent the triple-layer surface complexation model fit to the experimental data using FITEQL, the outer-sphere $\equiv MnOH_2^+ - Sb(OH)_6^-$ species, and chemical model A described in Table 14.

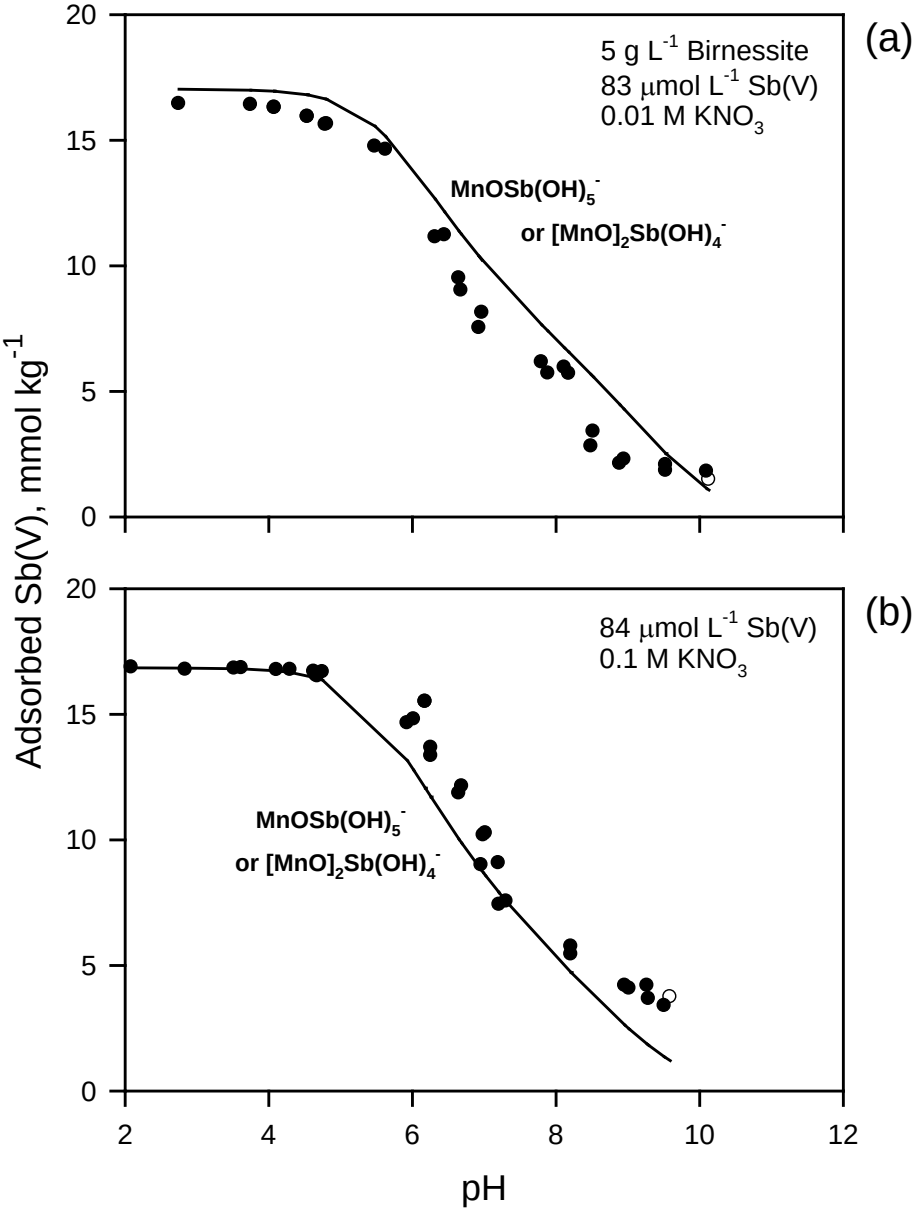

Figure 91. The adsorption of antimonate by birnessite as a function of pH and ionic strength in (a) 0.01 *M* KNO_3 and (b) 0.1 *M* KNO_3. The lines represent the triple-layer surface complexation model fit to the experimental data using FITEQL, the inner-sphere monodentate $\equiv MnOSb(OH)_5^-$ or bidentate $(\equiv MnO)_2Sb(OH)_4^-$ species, and chemical models B and C described in Table 14.

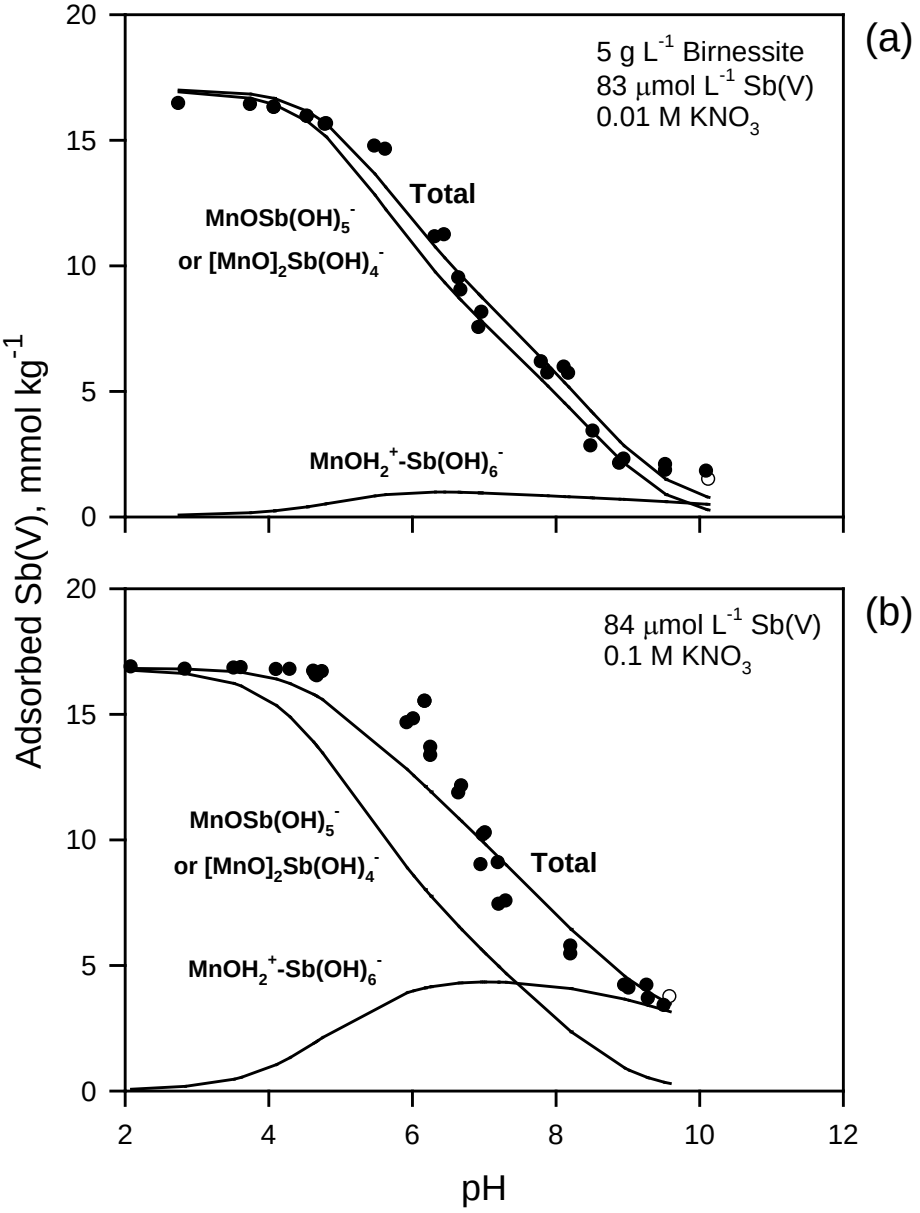

Figure 92. The adsorption of antimonate by birnessite as a function of pH and ionic strength in (a) 0.01 *M* KNO_3 and (b) 0.1 *M* KNO_3. The lines represent the triple-layer surface complexation model fit to the experimental data using FITEQL, the outer-sphere $\equiv MnOH_2^+–Sb(OH)_6^-$ species and the inner-sphere monodentate $\equiv MnOSb(OH)_5^-$ or bidentate $(\equiv MnO)_2Sb(OH)_4^-$ species, and chemical models D and E described in Table 14.

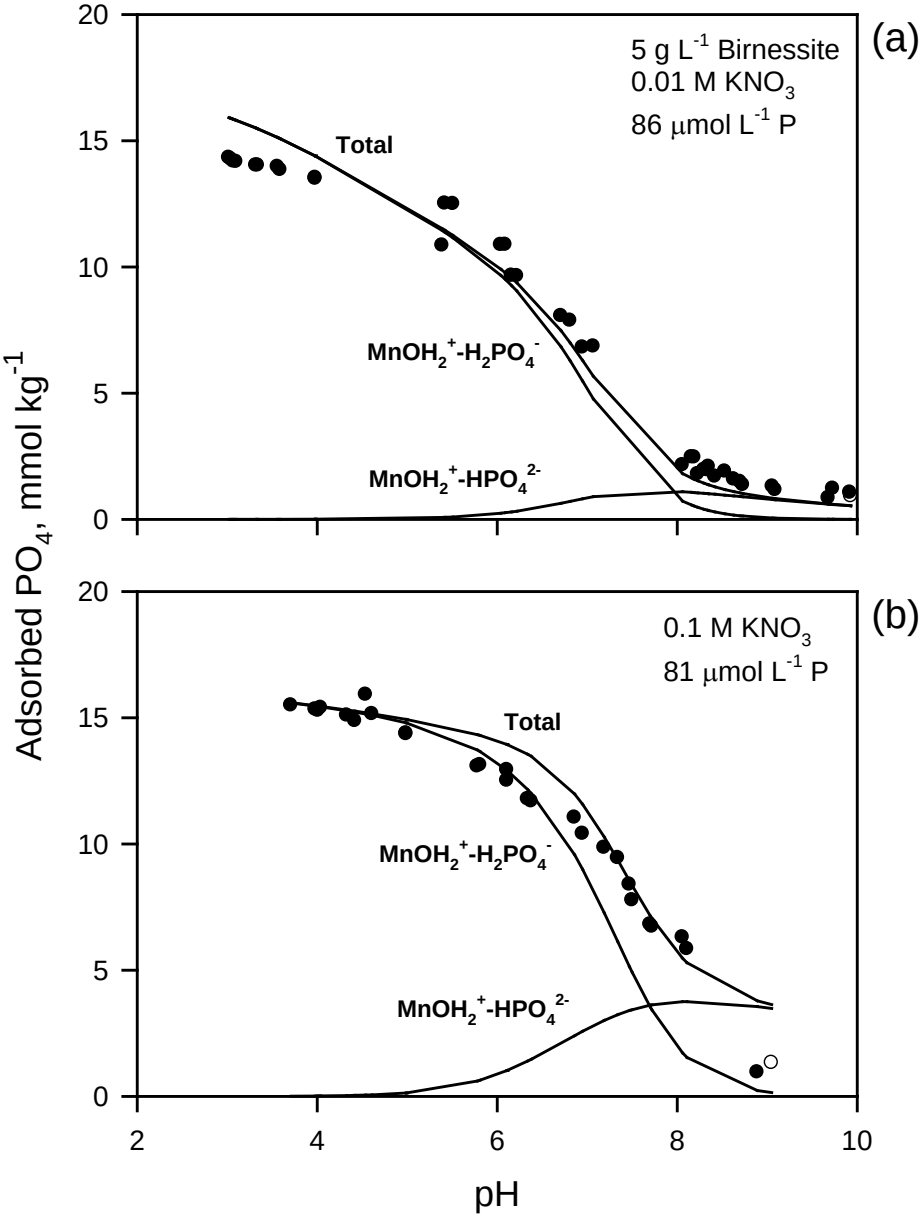

Figure 93. The adsorption of phosphate by birnessite as a function of pH and ionic strength in (a) 0.01 *M* KNO_3 and (b) 0.1 *M* KNO_3. The lines represent the triple-layer surface complexation model fit to the experimental data using FITEQL and the chemical model described in Table 14.

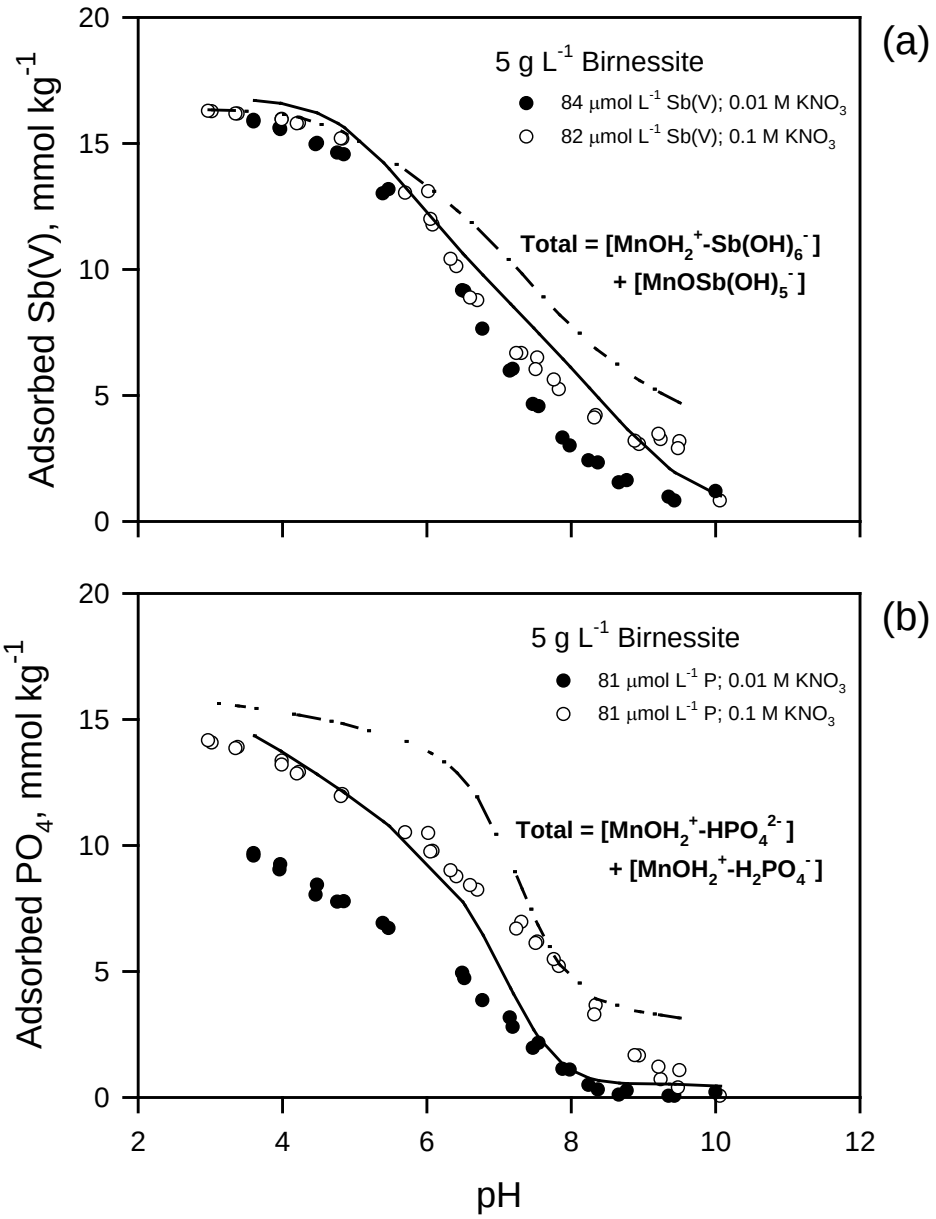

Figure 94. The adsorption of (a) antimonate and (b) phosphate by birnessite as a function of pH and ionic strength in antimonate-phosphate direct competition systems. The lines represent the triple-layer surface complexation model predictions using the log K^{int} values optimized for non-competitive adsorption of antimonate (Model D; $\equiv MnOH_2^+–Sb(OH)_6^-$ and $\equiv MnOSb(OH)_5^-$ species) or phosphate ($\equiv MnOH_2^+–HPO_4^{2-}$ and $\equiv MnOH_2^+–H_2PO_4^-$ species) (Table 14). The solid lines show the predicted adsorption in 0.01 *M* KNO_3, the dashed lines in 0.1 *M* KNO_3.

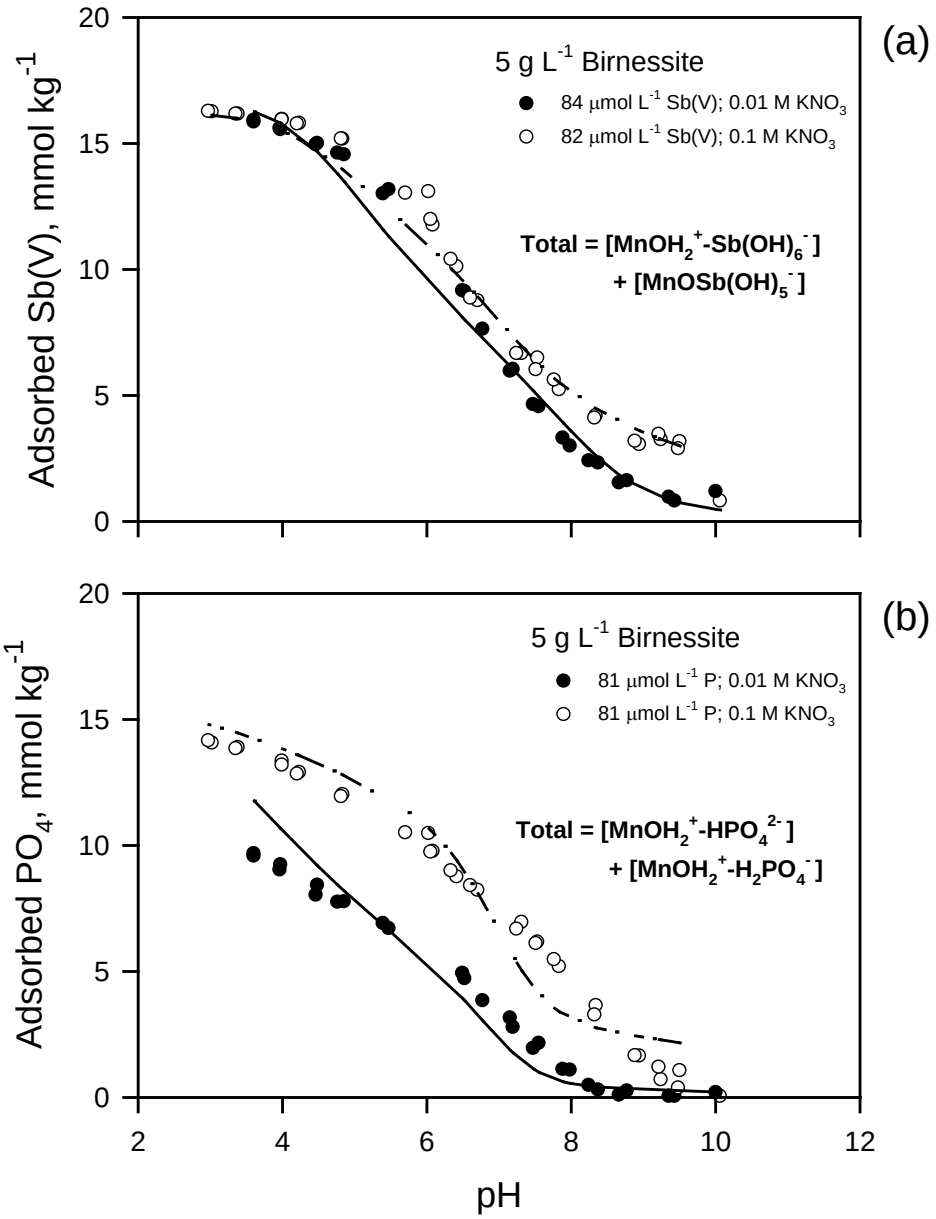

Figure 95. The adsorption of (a) antimonate and (b) phosphate by birnessite as a function of pH and ionic strength in antimonate-phosphate direct competition systems. The lines represent the triple-layer surface complexation model predictions using the reoptimized log K^{int} values of 5.19, 6.90, 18.52, and 25.49 for $\equiv MnOH_2^+ – Sb(OH)_6^-$, $\equiv MnOSb(OH)_5^-$, $\equiv MnOH_2^+ – HPO_4^{2-}$, and $\equiv MnOH_2^+ – H_2PO_4^-$ formation. The solid lines show the predicted adsorption in 0.01 *M* KNO_3, the dashed lines in 0.1 *M* KNO_3.

Summary: Antimonate Adsorption by Birnessite

Birnessite is a surface reactive mineral in soil and sediment, primarily known as a scavenger for metal cations. Throughout a broad pH range, the birnessite surface bears a net negative change (point of zero charge is approximately 2). Birnessite displays a high capacity for antimonate adsorption. Antimonate adsorption by birnessite is dependent on pH and ionic strength. The complete removal of antimonate by birnessite occurs in acidic to neutral solutions (pH < 6), and adsorption decreases with increasing pH. Antimonate adsorption increases with increasing ionic strength. This ionic strength effect is observed for ligand adsorption when the pH is greater than the IEP of the adsorbent. Similar adsorption behavior is observed for phosphate. However, birnessite has a lower affinity for phosphate than for antimonate.The ionic strength effect has also been interpreted to indicate either inner-sphere or outer-sphere surface complexation. Both adsorption mechanisms have been successfully employed in the surface complexation modeling of ligand adsorption by birnessite. Sulfate is not adsorbed by birnessite in the pH 2 to 10 range.

The inclusion of phosphate (and sulfate) in equimolar concentrations with antimonate did not impact antimonate adsorption by birnessite. However, the presence of antimonate decreases phosphate retention, particularly in the low ionic strength systems, and in preadsorbed antimonate and direct competition suspensions. This effect may be due to the greater affinity of antimonate for birnessite surface functional groups. However, adsorbed antimonate my also provide negative surface charge, interfering with the electrostatic interactions of phosphate with the surface.

Based on the experimental evidence, surface complexation models were developed to predict antimonate adsorption using the triple layer model formulation. The antimonate adsorption edge as a function of ionic strength is successfully modeled by using a combination of inner- and outer-sphere mechanisms. In general, the inner-sphere mechanism predominated over a broad range of pH conditions. Phosphate adsorption was successfully modeled by employing outer-sphere surface complexes. However, the surface complexation models, when applied to competitive antimonate-phosphate adsorption systems, did not satisfactorily predicted the antimonate or phosphate adsorption edge without further optimization.

Conclusions and Implications for Future Research/Implementation

Antimony is one of the least abundant elements in natural environments, with concentrations in uncontaminated soils that are generally less than 1 mg kg^{-1}. Elevated environmental concentrations of Sb that arise from anthropogenic sources are a concern, as this element has no known biological function, has high acute toxicity, and is known to induce chronic health effects. Antimony is listed as a priority pollutant by the U.S. Environmental Protection Agency and a priority metal by the Department of Defense (DoD). Antimony is a component of lead-based ammunition, and it is a cocontaminant with lead at DoD installations and civilian firing ranges, where soil Sb concentrations may range from < 517 mg kg^{-1} to < 17,500 mg kg^{-1}. Bullet fragments oxidize, releasing Sb in the anionic Sb(V) (antimonate) state. Antimonate [$Sb(OH)_6^-$] is not known to form discrete mineral precipitates; thus, the mechanism of retention in soil and sediment is adsorption, via anion exchange (weak electrostatic

interactions with positively-charged surfaces, outer-sphere complexation) or ligand exchange (strong covalent interactions, inner-sphere complexation). The type of adsorption mechanism dictates Sb mobility and bioaccessibility, as well as the ability to be displaced by ligands that competing for adsorption sites on soil constituents.

The objectives of this study were to characterize the adsorption of Sb(V) by minerals in soils and sediments that retain ligands. Several experiments were performed to investigate the adsorption of antimonate by gibbsite [$Al(OH)_3$], kaolinite [$Al_2Si_2O_5(OH)_4$], goethite (FeOOH), and birnessite (MnO_2) as a function pH, ionic strength, antimonate concentration, temperature, and in the presence of the competing ligands, SO_4 and PO_4. In addition to providing a characterization of antimonate adsorption behavior, the results may be interpreted to provide information on the mechanism of antimonate retention. The results are also used to develop chemical models that may be employed to predict antimonate behavior in chemically complex environments, such as soils and sediments.

The aluminol group (≡AlOH) is the ligand-reactive surface functional group on kaolinite and gibbsite. The aluminal group has relatively low affinity for Sb(V), and retention is both pH- and ionic strength-dependent. Kaolinite exhibits the lowest capacity to retain Sb(V) (1.48 mmol kg^{-1} adsorbed Sb(V) at pH 5.5), with minimal adsorption (~0 % of added Sb(V)) in pH > 7 suspensions. In pH < 4 suspensions, adsorption increases to approximately 50 % of the added Sb(V) in 0.1 I_s, and to 80 % in 0.01 I_s. Similarly, Sb(V) retention by gibbsite is pH- and I_s-dependent, with between 0 % and 10 % of the added Sb(V) retained in pH > 9 suspesions. In pH < 4 suspensions, retention increases to approximately 80 % of the added Sb(V) in 0.1 I_s, and to > 90 % in 0.01 I_s. The concentration of adsorbed Sb(V) is 4.32 mmol kg^{-1} at pH 5.5 and 1.16 mmol kg^{-1} at pH 8. The ionic strength-dependency of Sb(V) adsorption by kaolinite and gibbsite indicates that the weak, electrostatic retention of Sb(V) is an important mechanism. However, in strongly acidic suspensions (pH < 5 to 6), Sb(V) adsorption is irreversible, suggesting strong covalent bonding. The mechanistic interpretation of the adsorption edge results are supported by the adsorption isotherm and surface electrostatics results. In general, kaolinite and gibbsite Sb(V) adsorption isotherms are Langmuirian and may be described by the Freundlich and the two-site Langmuir isotherm models. In pH 8 suspensions, Sb(V) adsorption by the aluminol group increases with increasing temperature and is exothermic (ΔH_{ad} is –21.0 to –18.4 kJ mol^{-1}), indicating that the predominate retention mechanism is anion exchange. In pH 5.5 suspensions, adsorption consists of high-intensity, endothermic (ΔH_{ad} is 11.7 to 16.7 kJ mol^{-1}) and low-intensity, exothermic (ΔH_{ad} is ~0 to –15.5 kJ mol^{-1}) components, indicating covalent bonding by the aluminol functional group. Antimonate adsorption generates a negative shift in surface charge and an increase in proton adsorption, both of which are consistent with covalent bonding. Both sulfate and phosphate interfere with Sb(V) retention on kaolinite and gibbsite. The order of ligand addition has a small influence on Sb(V) adsorption. In general, preadsorbed Sb(V) is more difficult to displace from the aluminol functional group by competing ligands.

The ferrol group (≡FeOH) on goethite has a high capacity to retain Sb(V). The concentration of adsorbed Sb(V) is 88.5 mmol kg^{-1} at pH 5.5 and 67.2 mmol kg^{-1} at pH 8. Adsorption by goethite is pH-dependent, independent of ionic strength, and generally irreversible throughout the pH 3 to 10 range. Approximately 40 % of the added Sb(V) is retained by goethite in pH 10 suspensions, increasing to 100 % when pH < 6. Antimonate adsorption isotherms are Langmuirian and described by the one-site Langmuir isotherm model. Adsorption is endothermic in both pH 5.5 (ΔH_{ad} is 21.6 kJ mol^{-1}) and 8 (ΔH_{ad} is 16.6 kJ mol^{-1}) suspensions, indicating covalent bonding by the ferrol functional group. Correspondingly, Sb(V) adsorption generates a

negative shift in goethite surface charge. Antimonate adsorption by goethite is not impacted by sulfate. However, phosphate strongly inhibits Sb(V) retention, particularly when phosphate is preadsorbed or when the two ligands are in direct competition (Sb(V) adsorption is neglible above pH 7). However, preadsorbed Sb(V) is difficult to displace from the ferrol functional group by phosphate.

Like the ferrol group on goethite, the manganol group (≡MnOH) on birnessite is a scavenger for Sb(V). The concentration of adsorbed Sb(V) is 14.8 mmol kg^{-1} at pH 5.5 and 5.83 mmol kg^{-1} at pH 8. Adsorption by birnessite is pH- and ionic strength-dependent. Approximately 10 % (low I_s) to 20 % (high I_s) of the added Sb(V) was retained by birnessite in pH > 9 suspensions, increasing to 100 % when pH < 5. Antimonate adsorption generates a negative shift in birnessite surface charge, indicating covalent bonding by the manganol functional group. Antimonate adsorption by birnessite is not impacted by either sulfate or phosphate.

The experimental findings suggest that the retention of Sb(V) by kaolinite and gibbsite occurs via a combination of mechanisms. Electrostatic adsorption occurs throughout the pH 3 to 10 range; whereas, covalent bonding by the aluminol functional group becomes important in pH < 6 suspensions. The retention of antimonate by goethite and birnessite occurs predominately by covalent mechanisms. Antimonate adsorption by the mineral surfaces, as a function of pH and ionic strength, was successfully predicted by any one of several surface complexation models, including outer-sphere, monodentate or bidentate inner-sphere, or combined outer-sphere and inner-sphere (monodentate or bidentate) models. Thus, there was no unique surface complexation model that would specifically describe Sb(V) adsorption by a given surface. In general, the surface complexation models that generated the lowest goodness-of-fit parameters (V_Y) included both outer-sphere [≡*S*OH_2^+–$Sb(OH)_6^-$] and monodenate inner-sphere [≡*S*O$Sb(OH)_5^-$] complexation reactions (Table 15). The magnitude of the intrinsic constants generally reflects the observed capacities of the minerals to adsorb Sb(V). The intrinsic constants for ≡*S*OH_2^+–$Sb(OH)_6^-$ and ≡*S*O$Sb(OH)_5^-$ formation (as K^{int}) on gibbsite and kaolinite, which have a low capacity for Sb(V) retention, are orders of magnitude lower than the constants for complex formation on goethite and birnessite, which effectively immobilize Sb(V).

Table 15. Antimonate surface complexation reactions and equilibrium constants (as log K^{int}) that describe adsorption as a function of pH and ionic strength.†

Surface complexation reaction‡	Gibbsite	Kaolinite	Goethite	Birnessite
≡*S*OH_2^+ + $Sb(OH)_6^-$ = ≡*S*OH_2^+–$Sb(OH)_6^-$	3.73	3.13	6.35	7.04
≡*S*OH^0 + $Sb(OH)_6^-$ = ≡*S*O$Sb(OH)_5^-$ + H^+	–2.19	0.64	3.26	7.62
V_Y§	2.428	2.823	29.67	9.057

†The log K^{int} values where optimized using the triple layer formulation of the surface complexation model, the FITEQL computer code, and the adsorption edge data for both 0.01 and 0.1 *M* KNO_3 simultaneously.
‡*S* is Al for gibbsite and kaolinite; Fe for goethite; and Mn for birnessite.
§Goodness-of-fit parameter; the weighted sum of squares of residuals divided by the degree of freedom.

The ability of the surface complexation models to predict Sb(V) adsorption in competitive $Sb(OH)_6$ and SO_4 or $Sb(OH)_6$ and PO_4 systems, using the surface complexation constants obtained for the single-ligand systems, was also evaluated. In general, the reoptimization of the surface complexation models was required to satisfactorily predict ligand adsorption in the competitive systems. For the gibbsite systems, the single-ligand models provided satisfactory descriptions of Sb(V) adsorption in both the competitive SO_4 and PO_4 systems. The reopimization of the intrinsic constants for the mixed ligand systems resulted in an improved prediction of Sb(V) adsorption in the competitive PO_4 systems, but not in the SO_4 systems. For both the kaolinite and goethite systems, the single-ligand models did not adequately predict Sb(V) adsorption in the competitive SO_4 or PO_4 systems. Reoptimization resulted in the satisfactory prediction of Sb(V) adsorption in the SO_4 systems, but not in the PO_4 systems. The satisfactory description of Sb(V) adsorption by birnessite in the competitive PO_4 systems also required reoptimization of the intrinsic constants.

This research specifically addresses deficiencies in the scientific literature by providing an improved and detailed understanding of Sb(V) adsorption behavior by reactive soil and sediment components, and by developing the capabilities to predict Sb(V) mobility and bioavailability. The research results will help establish technically-defensible clean-up goals and priorities at DoD facilities, and will improve public and DoD site manager confidence in the management of contaminated environments. This research describes the adsorption of Sb(V) by the surface-reactive minerals that are common to soils and sediments. The results indicate that Sb(V) retention is strongly dependent on pH. Depending on the adsorbent, Sb(V) adsorption is also influenced by the ionic strength (salinity) and the presence of ligands (SO_4 and PO_4) that compete for adsorption sites. In general, Sb(V) is immobilized in strongly acidic environments, and by Fe- and Mn-rich phases (but not by Al-rich phases). The research findings also indicate that the addition of PO_4-based fertilizer amendments to immobilize lead in shooting range soils will inhibit Sb(V) adsorption, potentially enhancing Sb(V) mobility and bioaccessibility. Geochemical models that predict the distribution of Sb(V) between soluble and adsorbed phases as a function of pH and ionic environment were successfully developed. However, the application of these models to predict behavior in Sb(V)-affected environments will require site-specific chemical information and calibration.

The soil environment is a chemically-complex system where numerous chemical processes involving a multitude of reactants impact the fate and behavior of a substance. This study examined one such process affecting Sb(V) behavior; adsorption by a small number of environmentally relevant minerals as influenced by a small number of chemical variables. The interactions of Sb(V) with the reactive aluminol, ferrol, and manganol surface functional groups was examined. These functional groups are common to minerals in soil and sediment, and they readily react with ligands. In some cases, the functionality of each group is similar, irrespective of the supporting mineral. For example, the reactivity of the aluminol group located on the edge of kaolinite is similar to that on gibbsite, and surface complexation models developed to describe ligand adsorption by gibbsite have been successfully employed to predict adsorption by kaolinite. However, despite these similarilties in functional group behavior, mineral-specific characteristics and surface reactivities commonly influence ligand adsorption. Even differing preparations of the same mineral, often generating differing levels of mineral crystallinity and surface functionality, can result in differing ligand adsorption characteristics. Thus, it is vital to evaluate the interactions of Sb(V) with a variety of soil minerals to provide a critical assessment of Sb(V) fate and behavior. This is particularly the case for the hydrous metal oxides (e.g.,

goethite, hematite, ferrihydrite, and other ferric oxyhydroxides), as these minerals have the greater capacity to impact Sb(V) bioaccessibility. Although layer silicates represent a group of surface-reactive soil minerals, due to their extensive internal surface area and layer charge deficit, their surface reactivity is primarily restricted to the attraction of cations. The edge aluminol groups on layer silicates (e.g., micas, vermiculites, and smectites) are expected to have only a minor impact on Sb(V) retention, as indicated by the adsorption of Sb(V) by kaolinite. In addition to the ferric oxyhydroxides, naturally-occurring soil organic materials may exert a profound impact on the fate and behavior of substances in soil and sediment environments. The interactions of Sb(V) with these substances, in either the solid or dissolved state, has yet to be investigated.

In addition to characterizing the interactions of Sb(V) with natural mineral and organic adsorbents, as well as soil and sediments, the influence of soil solution chemistry on retention requires additional investigation. Competing ligands, such as sulfate and phosphate (and nitrate), influenced the adsorption behavior of Sb(V). The influence of varying concentrations of these and other common ions in soil (e.g., calcium, magnesium, and chloride) and organic solutes on Sb(V) adsorption behavior remains to be addressed. Most significant are the low molecular mass organic acid anions, such as citrate, oxalate, and malate. These substances occur in natural environments as microbial and plant root exudates, and form strong surface complexes with soil minerals. Their impact on Sb(V) adsorption may be similar to that of phosphate described in this study. Knowledge of the aqueous complexation chemistry of Sb(V) is also lacking. Although the pK_a value for the hydrolysis of the $Sb(OH)_5^0$ species is known, the association of $Sb(OH)_6^-$ with common soil solution cations (e.g., Ca^{2+}, Mg^{2+}, and Al^{3+}) to form soluble complexes (e.g., $CaSb(OH)_6^+$ and $MgSb(OH)_6^+$) has not been investigated (nor has the potential for Sb(V) to form sparingly-soluble precipitates with common soil cations). Significant complexation of Sb(V) in soil and sediment solutions will directly impact Sb(V) adsorption behavior. Thus, knowledge of these processes is required to develop holistic chemical models of Sb(V) behavior in soil and sediment environments.

Literature Cited

Accornero, M., L. Marini, and M. Lelli. 2008. The dissociation constant of antimonic acid at 10-40°C. J. Solution Chem. 37:785-800.

Adekola, F., M. Fédoroff, H. Geckeis, T. Kupcik, G. Lefèvre, J. Lützenkirchen, M. Plaschke, T. Preocanin, T. Rabung., and D. Schild. 2011. Characterization of acid-base properties of two gibbsite samples in the context of literature results. J. Colloid Interface Sci. 354:306-317.

Ambe, F., S. Ambe, T. Okada, and H. Sekizawa. 1986. In situ Mössbauer studies of metal oxide-aqueous solution interfaces with adsorbed cobalt-57 and antimony-119 ions. p. 403-424. *In* J.A. Davis and K.F. Hayes (eds.) Geochemical processes at mineral surfaces. ACS Symposium Series 323. ACS, Washington, DC.

Ambe, S. 1987. Adsorption-kinetics of antimony(V) ions onto α-Fe_2O_3 surfaces from an aqueous solution. Langmuir 3:489-493.

Andereae, M.O., J.F. Asmode, P., Foster, and L. Vantdack. 1981. Determination of antimony (III), antimony (V), and methylantimony species in natural waters by atomic adsorption spectrometry with hydride generation. Anal. Chem 53:1766-1771.

Antelo, J., M. Avena, S. Fiol, R. López, and F. Arce. 2005. Effects of pH and ionic strength on the adsorption of phosphate and arsenate at the goethite-water interface. J. Colloid Interface Sci. 285:476-486.

Antelo, J., S. Fiol, C. Pérez, S. Mariño, F. Arce, D. Gondar, and R. López. 2010. Analysis of phosphate adsorption onto ferrihydrite using the CD-MUSIC model. J. Colloid Interface Sci. 347:112-119.

Appel, C., L.Q. Ma, R.D. Rhue, and E. Kennelley. 2003. Point of zero charge determination in soils and minerals via traditional methods and detection of electroacoustic mobility. Geoderma 113:77-93.

Arai, Y., and D.L. Sparks. 2001. ATR-FTIR spectroscopic investigation on phosphate adsorption mechanisms as the ferrihydrite-water interface. J. Colloid. Interface Sci. 241:317-326.

Avena, M.J., and C.P. de Pauli. 1998. Proton adsorption and electrokinetics of an Argentinean montmorillonite. J. Colloid Interface Sci. 202:195-204.

Basunia, S., and S. Landsberger. 2001. Contents and leachability of heavy metals (Pb, Cu, Sb, Zn, As) in soil at the Pantex firing range, Amarillo, Texas. J. Air Waste Manag. Assoc. 51:1428-1435.

Belzile, N., Y.W. Chen, and Z.J. Wang. 2001. Oxidation of antimony (III) by amorphous iron and manganese oxyhydroxides. Chem. Geol. 174:379-387.

Bencze, S. 1994. Antimony. *In* Handbook on metals in clinical and analytical chemistry. H.G. Seiler, et al. (eds.), Marcel Dekker, New York.

Biver, M., M. Krachler, and W. Shotyk. 2011. The desorption of antimony(V) from sediments, hydrous oxides, and clay minerals by carbonate, phosphate, sulfate, nitrate, and chloride. J. Environ. Qual. 40:1143-1152.

Carlin, J.F., Jr. 2000. Antimony. U.S. Geological Survey, Mineral Commodity Summaries. USGS, Denver, CO.

Catalano, J.G., C. Park, P. Fenter, and Z. Zhang. 2008. Simultaneous inner- and outer-sphere arsenate adsorption on corundum and hematite. Geochim. Cosmchim. Acta 72:1986-2004.

Catts, J.G., and D. Langmuir. 1986. Adsorption of Cu, Pb and Zn by δMnO_2: application of the site binding-surface complexation model. Appl. Geochem. 1:255-264.

Chassagne, C., F. Mietta, and J.C. Winterwerp. 2009. Electrokinetic study of kaolinite suspensions. J. Colloid Interface Sci. 336:352-359.
Chen, Y.S.R., J.N. Butler, and W. Stumm. 1973. Adsorption of phosphate on alumina and kaolinite from dilute aqueous solutions. J. Colloid Interface Sci. 43:421-436.
Chen, B., M. Krachler, and W. Shotyk. 2003. Determination of antimony in plant and peat samples by hydride generation-atomic fluorescence spectrometry (HG-AFS). J. Anal. Atomic Spectro. 18:1256-1262.
Crecelius, E.A., M.H. Bothner, and R. Carpenter. 1975. Geochemistries of arsenic, antimony, mercury, and related elements in sediments of Puget Sound. Environ. Sci. Technol. 9:325-333.
Davis, J.A., R.O. James, and J.O. Leckie. 1978. Surface ionization and complexation at the oxide/water interface. I. Computation of electric double layer properties in simple electrolytes. J. Colloid Interface Sci. 63:480-499.
Eggleston, C.M., S. Hug., W. Stumm, B. Sulzberger, and M. Dos Santos Afonso. 1998. Surface complexation of sulfate by hematite surfaces: FTIR and STM observations. Geochim. Cosmochim. Acta 62:585-593.
Essington, M.E. 2003. Soil and water chemistry: an integrative approach. CRC Press, Boca Raton, FL.
Essington, M.E., J.E. Foss, and Y. Roh. 2004. The soil mineralogy of lead at Horace's Villa. Soil Sci. Soc. Am. J. 68:979-993.
Essington, M.E., and R.M. Anderson. 2008. Competitive adsorption of 2-ketogluconate and inorganic ligands onto gibbsite and kaolinite. Soil Sci. Soc. Am. J. 72:595-604.
Fan, J.X., Y.J. Wang, X.D. Cui, and D.M. Zhou. 2013. Sorption isotherms and kinetics of Sb(V) on several Chinese soils with different physicochemical properties. J. Soils Sed. 13:344-353.
Ferreiro, E., and S.G. de Bussetti. 2007. Thermodynamic parameters of adsorption of 1,10-phenanthroline and 2,2'-bipyridyl on hematite, kaolinite and montmorillonite. Colloids Surf. A 301:117-128.
Filella, M., and P.M. May. 2003. Computer simulation of the low-molecular-weight inorganic species distribution of antimony(III) and Antimony(V) in natural waters. Geochim. Cosmochim. Acta 67:4013-4031.
Filella, M., N. Belzile, and Y.W. Chen. 2002a. Antimony in the environment: a review focused on natural waters. I. Occurrence. Earth-Sci. Rev. 57:125-176.
Filella, M., N. Belzile, and Y.W. Chen. 2002b. Antimony in the environment: a review focused on natural waters. II. Relevant solution chemistry. Earth-Sci. Rev. 59:265-285.
Flynn, H.C., A.A. Meharg, P.K. Bowyer, and G.I. Paton. 2003. Antimony bioavailability in mine soils. Environ. Pollut. 124:93-100.
Gal, J., A.S. Hursthouse, and S.J. Cuthbert. 2006. Chemical availability of arsenic and antimony in industrial soils. Environ. Chem. Letters 3:149-153.
Gebel, T., S. Christensen, and H. Dunkelberg. 1997. Comparative and environmental genotoxicity of antimony and arsenic. Anticancer Res. 17:2603-2607.
Geelhoed, J.S., T. Hiemstra, and W.H. Van Riemsdijk. 1997. Phosphate and sulfate adsorption on goethite: single anion and competitive adsorption. Geochim. Cosmochim. Acta 61:2389-2396.
Geelhoed, J.S., T. Hiemstra, and W.H. Van Riemsdijk. 1998. Competitive interaction between phosphate and citrate on goethite. Environ. Sci. Technol. 32:2119-2123.

Geelhoed, J.S., W.H. Van Riemsdijk, and G.R. Findenegg. 1999. Simulation of the effect of citrate exudation from roots on the plant availability of phosphate adsorbed on goethite. Eur. J. Soil Sci. 50:379-390.
Goldberg, S. 1992. Use of surface complexation models in soil chemical systems. Adv. Agron. 47:233-329.
Goldberg, S. 2010. Competitive adsorption of molybdate in the presence of phosphorus and sulfur on gibbsite. Soil Sci. 175:105-110.
Goldberg, S. and G. Sposito. 1984. A chemical model of phosphate adsorption by soils: I. Reference oxide minerals. Soil Sci. Soc. Am. J. 48:772-778.
Goldberg, S., G.E. Brown, C.T. Johnston, and D.L. Suarez. 2006. Mechanism of molybdate adsorption on soil minerals evaluated using vibrational spectroscopy and surface complexation modeling. Abstr. Pap. Am. Chem. Soc. 231.
Goldberg, S., and L.J. Criscenti. 2008. Modeling adsorption of metals and metalloids by soil components. p. 216-264. IN A. Violente et al. (ed.) Biophysical-chemical processes of heavy metals and metalloids in soil environments. John Wiley & Sons, Hoboken, NJ.
Goldberg, S., and N.J. Kabengi. 2010. Bromide adsorption by reference minerals and soils. Vadose Zone J. 9:780-786.
Goldberg, S., I. Lebron, J. Seaman, and D. Suarez. 2012. Soil colloid behavior. *In* P.M. Huang, Y. Li, and M.E. Sumner (eds.) Handbook of soil science: properties and processes, second edition. CRC Press, Boca Raton, FL.
Hansmann, D.D., and M.A. Anderson. 1985. Using electrophoresis in modeling sulfate, selenite, and phosphate adsorption onto goethite. Environ. Sci. Technol. 19:544-551.
He, L.M., L.W. Zelazny, V.C. Baligar, K.D. Ritchey, and D.C. Martens. 1996. Hydroxyl-sulfate exchange stoichiometry on γ-Al_2O_3 and kaolinite. Soil Sci. Soc. Am. J. 60:442-452.
He, L.M., L.W. Zelazny, V.C. Baligar, K.D. Ritchey, and D.C. Martens. 1997. Ionic strength effects on sulfate and phosphate adsorption on γ-alumina and kaolinite: triple-layer model. Soil Sci. Soc. Am. J. 61:784-793.
Helmke, P.A. 1999. The chemical composition of soils. *In* M.E. Sumner (ed.) Handbook of soil science. CRC Press, Boca Raton, FL.
Helmy, A.K., E.A. Ferreiro, and S.G. de Bussette. 1996. Energy, enthalpy, and isosteric heat of adsorption of phosphate on hydrous Al oxide. J. Colloid Interface Sci. 183:131-134.
Herbelin, A.L., and J.C. Westall. 1999. FITEQL: a computer program for determination of chemical equilibrium constants from experimental data. Version 4.0. Rep. 99-01. Dep. of Chemistry, Oregon State Univ., Corvallis.
Hiemstra, T., and W.H. Van Riemsdijk. 1999. Surface structural ion adsorption modeling of competitive binding of oxyanions by metal (hydr)oxides. J. Colloid Interface Sci. 210:182-193.
Hiemstra, T., H. Yong, and W.H. Van Riemsdijk. 1999. Interfacial charging phenomena of aluminum (hydr)oxides. Langmuir 15:5942-5955.
Hug, S.J. 1997. In situ Fourier transform infrared measurements of sulfate adsorption on hematite in aqueous solutions. J. Colloid Interface Sci. 188:415-422.
Ilgen, A.G., and T.P. Trainor. 2012. Sb(III) and Sb(V) sorption onto Al-rich phases: hydrous Al oxide and the clay minerals kaolinite KGa-1b and oxidized and reduced nontranite NAu-1. Environ. Sci. Technol. 46:843-851.

Ioannou, A., and A. Dimirkou. 1997. Phosphate adsorption on hematite, kaolinite, and kaolinite-hematite (k-h) systems as described by a constant capacitance model. J Colloid Interface Sci. 192:119-128.

Johnson, B.B., A.V. Ivanov, O.N. Antzutkin, and W. Forsling. 2002. ^{31}P nuclear magnetic resonance study of the adsorption of phosphate and phenyl phosphates on γ-Al_2O_3. Langmuir 18:1104-1111.

Johnson, C.A., H. Moench, P. Wersin, P. Kugler, and C. Wenger. 2005. Solubility of antimony and other elements in samples taken from shooting ranges. J. Environ. Qual. 34:248-254.

Journey, J.S., R.M. Anderson, and M.E. Essington.. 2010. The adsorption of 2-ketogluconate by goethite. Soil Sci. Soc. Am. J. 74:1119-1128.

Juang, L.C., and L. Chung. 2004. Adsorption of basic dyes onto MCM-41. Chemosphere 64:1920-1928.

Juang, R.S., and W.L. Wu. 2002. Adsorption of sulfate and copper(II) on goethite in relation to the changes of zeta potentials. J. Colloid Interface Sci. 249:22-29.

Kameda, T., M. Nakamura, and T. Yoshioka. 1012. Removal of antimonate ions from an aqueous solution by anion exchange with magnesium-aluminum layered double hydroxide and the formation of brandholzite-like structure. J. Environ. Sci. Health A 47:1146-1151.

Kaplan, D.I., and A.S. Knox. 2004. Enhanced contaminant desorption induced by phosphate mineral additions to sediment. Environ. Sci. Technol. 38:3153-3160.

Karamalidis, A.K., and D.A. Dzombak. 2010. Surface complexation modeling: gibbsite. J. Wiley & Sons, Inc., Hoboken, NJ.

Khare, N., J.D. Martin, and D. Hesterberg. 2007. Phosphate bonding configuration on ferrihydrite based on molecular orbital calculations and XANES fingerprinting. Geochim Cosmochim Acta 71:4405-4415.

Kilgour, D.W., R.B. Moseley, M.O. Barnett, K.S. Savage, and P.M. Jardine. 2008. Potential negative consequences of adding phosphorus-based fertilizers to immobilize lead in soil. J. Environ. Qual. 37:1733-1740.

Kinniburgh, D.G. 1986. General purpose adsorption isotherms. Environ. Sci. Technol. 20:895-904.

Knechtenhofer, L.A., I.O. Xifra, A.C. Scheinost, H. Flühler, and R. Kretzschmar. 2003. Fate of heavy metals in a strongly acidic shooting-range soil: small-scale metal distribution and its relation to preferential water flow. J. Plant Nutri. Soil Sci. 166:84-92.

Kosmulski. M. 2009. pH-dependent surface charging and points of zero charge. IV. Update and new approaches. J. Colloid Interface Sci. 337:439-448.

Kosmulski, M., and P. Dahlsten. 2006. High ionic strength elctrokinetics of clay minerals. Colloids and surfaces A: Physiochem. Eng. Aspects 291:212-218.

Legoux, Y., G. Blain, R. Guillaumont, G. Ouzounian, L. Brillard, and M. Hussonnois. 1992. K_D measurements of activiation, fission and heavy elements in water solid phase systems. Radiochim. Acta 58-9:211-218.

Leuz, A.K., H. Monch, and C.A. Johnson. 2006. Sorption of Sb(III) and Sb(V) to goethite: influence on Sb(III) oxidation and mobilization. Environ. Sci. Technol. 40:7277-7282.

Lewis, J., J. Sjöström, U. Skyllberg, and L. Hägglund. 2010. Distribution, chemical speciation, and mobility of lead and antimony originating from small arms ammunition in a coarse-grained unsaturated surface soil. J. Environ. Qual. 39:863-870.

Li, W., G. Pan, M. Zhang, Y. Yang, H. Chen, and G. He. 2008. EXAFS studies on sorption irreversibility of Zn(II) on TiO_2: temperature dependence. J. Colloid Interface Sci. 319:385-391.

Lintschinger, J., B. Michalke, S. Schulte-Hostede, and P. Schramel. 1998. Studies on speciation of antimony in soil contaminated by industrial activity. Int. J. Environ. Anal. Chem. 72:11-25.

Li, X.D., and I. Thornton. 1993. Aresenic, antimony and bismuth in soil and pasture herbage in some metalliferous areas in England. Environ. Geochem. Health 15:135-144.

Luengo, C., M. Brigante, J. Antelo, and M. Avena. 2006. Kinetics of phosphate adsorption on goethite: comparing batch adsorption and ATR-IR measurements. J. Colloid Interface Sci. 300:511-518.

Lützenkirchen, J., J.-F. Boily, L. Lövgren, and S. Sjöberg. 2002. Limitations of the potentiometric titration technique in determining the proton active site density of goethite surfaces. Geochim. Cosmochim. Acta 66:3389-3396.

Mansour, C., G. Lefèvre, E.M. Pavageau, H. Catalette, M. Fédoroff, and S. Zanna. 2009. Sorption of sulfate ions onto magnetite. J. Colloid Interface Sci. 331:77-82.

Martell, A.E., R.M. Smith, and R.J. Motekaitis. 2004. NIST critically selected stability constants of metal complexes. NIST standard reference database 46, Version 8.0. NIST, Gaithersburg, MD.

Martínez-Lladó, X., C. Valderrama, M. Rovira, V. Martí, J. Giménez, and J. De Pablo. 2011. Sorption and mobility of Sb(V) in calcareous soils of Catalonia (NE Spain): batch and column experiments. Geoderma 160:468-476.

May, P.M., and K. Murry. 1991. JESS, a joint expert speciation system. II. The thermodynamic database. Talanta 38:1419-1426.

Mattigod, S.V., J.A. Frampton, and C.H. Lim. 1985. Effects of ion pair formation on boron adsorption by kaolinite. Clays Clay Miner. 33:433-457.

McComb, K.A., D.Craw, and A.J. McQuillan. 2007. ATR-IR spectroscopic study of antimonite adsorption to iron oxide. Langmuir 23:12125-12130.

McKenzie, R.M. 1971. Synthesis of birnessite, crytomelane, and some other oxides and hydroxides of manganese. Mineral. Mag. 38:493-502.

Melamed, R. and L.Q. Ma. 2008. Phosphate-induced lead immobilization in contaminated soils: mechanisms, assessment, and field application. In A. Violante, P.M. Huang, and G.M. Gadd (eds.) Biophyico-chemical processes of heavy metals and metalloids in soil environments. J. Wiley & Sons, Inc., Hoboken, NJ.

Mezzener, N.Y., and A. Bensmaili. 2008. Kinetics and thermodynamic study of phosphate adsorption on iron hydroxide-eggshell waste. Chem. Eng. J. 10:1016-1026.

Mitsunobu, S., T. Harada, and Y. Takahashi. 2006. Comparison of antimony behavior with that of arsenic under various soil redox conditions. Environ. Sci. Technol. 40:7270-7276.

Mitsunobu, S., Y. Takahashi, Y. Sakai, and K. Inumaru. 2009. Interaction of synthetic sulfate green rust with antimony(V). Environ. Sci. Technol. 43:318-323.

Mitsunobu, S., Y. Takahashi, Y. Terada, and M. Sakai. 2010. Antimony(V) incorporation into synthetic ferrihydrite, goethite, and natural iron oxyhydroxides. Environ. Sci. Technol. 44:3712-3718.

Mok, W.M., and C.M. Wai. 1990. Distribution and mobilization of arsenic and antimony species in the Coeur-D'Alene River, Idaho. Environ. Sci. Technol. 24:102-108.

Mustafa, S., M.I. Zaman, and S. Khan. 2006. pH effect on phosphate sorption by crystalline MnO_2. J. Colloid Interface Sci. 301:370-375.
Mustafa, S., M.I. Zaman, R. Gul, and S. Khan. 2008. Effect of Ni2+ loading on the mechanism of phosphate anion sorption by iron hydroxide. Sep. Purif. Technol. 39:108-114.
Nakamaru, Y., K. Tagami, and S. Uchida. 2006. Antimony mobility in Japanese agricultural soils and the factors affecting antimony sorption behavior. Environ. Pollut. 141:321-326.
National Research Council. 2003. Bioavailability of contaminants in soils and sediments: processes, tools, and applications. National Academy of Science, The National Academies Press, Washington, DC.
Nriagu, J.O. 1989. A global assessment of natural sources of atmospheric trace metals. Nature 338:47-49.
Nriagu, J.O., and J.M. Pacyna. 1988. Quantitative assessment of worldwide contamination of air, water and soils by trace metals. Nature 333:134-139.
Partey, F., D. Morman, S. NDur, and R. Nartey. 2008. Arsenic sorption onto laterite iron concretions: temperature effect. J. Colloid Interface Sci. 321:493-500.
Peak, D., R.G. Ford, and D.L. Sparks. 1999. An in situ ATR-FTIR investigation of sulfate bonding mechanisms on goethite. J. Colloid Interface Sci. 218:289-299.
Quentel, F., M. Filella, C. Elleouet, and C.L. Madec. 2004. Kinetic studies on Sb(III) oxidation by hydrogen peroxide in aqueous solution. Environ. Sci. Technol. 38:2843-2848.
Rahnemaie, R., T. Hiemstra, and W.H. Van Riemsdijk. 2007. Geometry, charge distribution, and surface speciatio0n of phosphate on goethite. Langmuir 23:3680-3689.
Rakshit, S., D. Sarkar, P. Punamiya, and R. Datta. 2011. Antimony sorption at gibbsite-water interface. Chemosphere 84:480-483.
Rietra, R.P.J.J., T. Hiemstra, and W.H. van Riemsdijk. 1999. Sulfate adsorption on goethite. J. Colloid Interface Sci. 218:511-521.
Ritchie, V., A.G. Ilgen, S.H. Mueller, T.P. Trainor, and R.J. Goldfarb. 2013. Mobility and chemical fate of antimony and arsenic in historic mining environments of the Kantishna Hills district, Denali National Park and Preserve, Alaska. Chem. Geol. 335:172-188.
Sahai, N., and D. Sverjensky. 1997. Evaluation of internally consistent parameters for the triple-layer model by the systematic analysis of oxide surface titration data. Geochim. Cosmochim, Acta 61:2801-2826.
Salatas, J.H., Y.W. Lowney, R.A. Pastorok, R.R. Nelson, and M.V. Ruby. 2004. Metals that drive health-based remedial decisions for soils at U.S. Department of Defense sites. Human Ecol. Risk Assess. 10:983-997.
Sarkar, D., M.E. Essington, and K.C. Misra. 1999. Adsorption of mercury(II) by variable charge surfaces of quartz and gibbsite. Soil Sci. Soc. Am. J. 63:1626-1636.
Sarkar, D., M.E. Essington, and K.C. Misra. 2000. Adsorption of mercury(II) by kaolinite. Soil Sci. Soc. Am. J. 64:1968-1975.
Scheinost, A.C., A. Rossberg, D. Vantelon, I. Xifra, R. Kretzschmar, A.K. Leuz, H. Funke, and C.A. Johnson. 2006. Quantitative antimony speciation in shooting-range soils by EXAFS spectroscopy. Geochim. Cosmochim. Acta 70:3299-3312.
Schnorr, T.M., K. Steenland, M.J. Thun, and R.A. Rinsky. 1995. Mortality in a cohort of antimony smelter workers. Am. J. Industr. Med. 27:759-770.
Schwertmann, U., and R.M. Cornell. 2000. Iron oxides in the laboratory: preparation and characterization. J. Wiley & Sons, Inc. New York, NY.

Sposito, G. 1980. Derivation of the Freundlich equation for ion exchange reactions in soils. Soil Sci. Soc. Am. J. 44:652-654.
Sposito, G. 1981. The operational definition of the zero point of charge in soils. Soil Sci. Soc. Am. J. 45:292-297.
Sposito, G. 1982. On the use of the Langmuir equation in the interpretation of "adsorption" phenomena: II. The "two-surface" Langmuir equation. Soil Sci. Soc. Am. J. 46:1147-1152.
Sposito, G. 2004. The surface chemistry of natural particles. Oxford, New York.
Spuller, C., H. Weigand, and C. Marb. 2007. Trace metal stabilization in a shooting range soil: mobility and phytotoxicity. J. Hazard. Mater. 141:378-387.
Sverjensky, D.A. 2003. Standard states for the activities of mineral surface sites and species. Geochim. Cosmochim. Acta 67:17-28.
Tadanier, C.J., and M.J. Eick. 2002. Formulating the charge-distribution multisite surface complexation model using FITEQL. Soil Sci. Soc. Am. J. 66:1505-1517.
Takaoka, M., S. Fukutani, T. Yamamoto, M. Horbiuchi, N. Satta, N. Takeda, K. Oshita, M. Yoneda, S. Morisawa, and T. Tanaka. 2005. Determination of chemical form of antimony in contaminated soil around a smelter using x-ray absorption fine structure. Anal. Sci. 21:769-773.
Takayanagi, K., and D. Cossa. 1997. Vertical distributions of Sb(III) and Sb(V) in Pavin Lake, France. Water Res. 31:671-674.
Tejedor-Tejedor, M.I., and M.A. Anderson. 1990. Protonation of phosphate on the surface of goethite as studied by CIR-FTIR and electrophoretic mobility. Langmuir 6:602-611.
Thanabalasingam, P., and W.F. Pickering. 1990.Specific sorption of antimony(III) by hydrous oxides of Mn, Fe, and Al. Water Air Soil Pollut. 49:175-185.
Tighe, M., P. Lockwood, and S. Wilson. 2005a. Adsorption of antimony(V) by floodplain soils, amorphous iron(III) hydroxide and humic acid. J. Environ. Monitor. 7:1177-1185.
Tighe, M., P. Ashley, P. Lockwood, and S. Wilson. 2005b. Soil, water, and pasture enrichment of antimony and arsenic within a coastal floodplain system. Sci. Total Environ. 347:175-186.
USEPA. 2004. 2004 Edition of the drinking water standards and health advisories. EPA 822-R-04-005. USEPA, Washington, DC.
Vane, L.M., and G.M. Zang. 1997. Effect of aqueous phase properties on clay particle zeta potential and electro-osmotic permeability: implications for electro-kinetic soil remediation processes. J. Hazard. Mater. 55:1-22.
Van Emmerick, T.J., D.E. Sandström, O.N. Antzutkin, M.J. Angove, and B.B. Johnson. 2007. 31P solid-state nuclear magnetic resonance study of the sorption of phosphate onto gibbsite and kaolinite. Langmuir. 23:3205-3213.
Watkins, R., D. Weiss, W. Dubbin, K. Peel, B. Coles, and T. Arnold. 2006. Investigations into the kinetics and thermodynamics of Sb(III) adsorption on goethite (α-FeOOH). J. Colloid Interface Sci. 303:639-646.
Wang, X., M. He, C. Lin, Y. Gao, and L. Zheng. 2012. Antimony(III) oxidation and antimony(V) adsorption reactions on synthetic manganite. Chemie der Erde 72 S4:41-47.
WHO. 2006. Guidelines for drinking water quality: incorporating first addendum. Vol. 1, Recommendations. World Health Organization, Geneva, Switzerland.
Wilson, N.J., D. Craw, and K. Hunter. 2004. Antimony distribution and environmental mobility at an historic antimony smelter site, New Zealand.

Xi, J., M. He, and C. Lin. 2010. Adsorption of antimony(V) on kaolinite as a function of pH, ionic strength and humic acid. Environ. Earth Sci. 60:715-722.
Xi, J., M. He, and C. Lin. 2011. Adsorption of antimony(III) and antimony(V) on bentonite: kinetics, thermodynamics and anion competition. Microchem. J. 97:85-91.
Xu, W., H. Wang, R. Liu, X. Zhao, and J. Qu. 2011. The mechanism of antimony(III) removal and its reactions on the surfaces of Fe-Mn binary oxide. J. Colloid Interface Sci. 363:320-326.
Xu, Y.H., A. Ohki, and S. Maeda. 2001. Adsorption and removal of antimony from aqueous solution by an activated alumina. 1. Adsorption capacity of adsorbent and effect of process variables. Toxicol. Environ. Chem. 80:133-144.
Yang, X., Z. Sun, D. Wang, and W. Forsling. 2007. Surface acid-base properties and hydration/dehydration mechanisms of aluminum (hydr)oxides. J. Colloid Interface Sci.308:395-404.
Yao, W., and F.J. Millero. 1996. Adsorption of phosphate on manganese dioxide in seawater. Environ. Sci. Technol. 30:536-541.
Yu, T.R. 1997. Chemistry of variable charge soils. Oxford, New York.
Zhang, H., and H.M. Selim. 2008. Competitive sorption-desorption kinetics of arsenate and phosphate in soils. Soil Sci. 173:3-12.

Appendix: List of Scientific/Technical Publications

Essington, M.E., and M. Stewart. 2013. Surface complexation modeling of antimonate adsorption by variable-charge minerals. *In* Annual International Meetings Abstracts [CD-ROM]. ASA, CSSA, and SSSA, Madison, WI.

Kalyn Vergeer. 2013. Adsorption of antimony by birnessite and the impact of antimony on the electrostatic surface properties of variable-charge soil minerals. MS Thesis. The University of Tennessee, Knoxville.

Essington, M., and M. Stewart. 2012. The influence of temperature on the adsorption of antimonate by soil minerals. *In* Annual International Meetings Abstracts [CD-ROM]. ASA, CSSA, and SSSA, Madison, WI.

Stewart, M. and M. Essington. 2012. The adsorption of antimonate by goethite. *In* Annual International Meetings Abstracts [CD-ROM]. ASA, CSSA, and SSSA, Madison, WI.

Vergeer, K.A., and M. Essington. 2012. Impact of antimony(V) adsorption on surface charge. *In* Annual International Meetings Abstracts [CD-ROM]. ASA, CSSA, and SSSA, Madison, WI.

Essington, M.E. 2011. Antimony(V) adsorption by variable-charged minerals. *In* Abstracts of the SERDP-ESTCP Partners in Environmental Technology Technical Symposium & Workshop (www.serdp-estcp.org/symposium). Nov. 29 – Dec. 1, 2011, Washington, D.C. p. G-170.

Stewart, M.A., and M.E. Essington. 2011. Competitive adsorption of antimonate, phosphate, and sulfate on gibbsite. *In* Annual International Meetings Abstracts [CD-ROM]. ASA, CSSA, and SSSA, Madison, WI.

Vergeer, K.A., M.A. Stewart, and M.E. Essington. 2011. Impact of antimonate on the charging characteristics of metal oxyhydroxides. *In* Annual International Meetings Abstracts [CD-ROM]. ASA, CSSA, and SSSA, Madison, WI.

Essington, M.E. 2010. Antimony(V) adsorption by variable-charged minerals. *In* Abstracts of the SERDP-ESTCP Partners in Environmental Technology Technical Symposium & Workshop (www.serdp-estcp.org/symposium). Nov. 30 – Dec. 2, 2010, Washington, D.C. p. G-243.

Essington, M.E. 2010. Geochemical modeling of speciation and the prediction of bioaccessibility: can the former lead to the latter? Geochim. Cosmochim. Acta 74(11) Supplement 1:A272. (Keynote address, Section 16c, Goldschmidt Conference)

Essington, M., and M. Stewart. 2010. The adsorption of antimony(V) by gibbsite. *In* Annual International Meetings Abstracts [CD-ROM]. ASA, CSSA, and SSSA, Madison, WI.